TiO_2-based magnetic nanocomposites with core-shell structure

Zuzanna Bielan

2020

GDAŃSK UNIVERSITY OF TECHNOLOGY
FACULTY OF CHEMISTRY

The author of the PhD dissertation: mgr inż. Zuzanna Bielan

Scientific discipline: Chemical sciences

DOCTORAL DISSERTATION

Title of PhD dissertation: TiO_2-based magnetic nanocomposites with core-shell structure

Title of PhD dissertation (in Polish): Magnetyczne nanokompozyty na bazie TiO_2 o strukturze rdzeń-otoczka

Supervisor *signature*
PhD DSc, Anna Zielińska-Jurek, Assoc. Prof. of GUT

Gdańsk, 2020

STATEMENT

The author of the PhD dissertation: Zuzanna Bielan

I, the undersigned, agree that my PhD dissertation entitled:
TiO_2-based magnetic nanocomposites with core-shell structure

may be used for scientific or didactic purposes.[1]

Gdańsk,..... .....

signature of the PhD student

Aware of criminal liability for violations of the Act of 4th February 1994 on Copyright and Related Rights (Journal of Laws 2006, No. 90, item 631) and disciplinary actions set out in the Law on Higher Education (Journal of Laws 2012, item 572 with later amendments),[2] as well as civil liability, I declare, that the submitted PhD dissertation is my own work.

I declare that the submitted PhD dissertation is my own work performed under and in cooperation with the supervision of dr hab. inż. Anna Zielińska-Jurek

This submitted PhD dissertation has never before been the basis of an official procedure associated with the awarding of a PhD degree.

All the information contained in the above thesis, which is derived from written and electronic sources is documented in a list of relevant literature in accordance with art. 34 of the Copyright and Related Rights Act.

I confirm that this PhD dissertation is identical to the attached electronic version.

Gdańsk,..... .....

signature of the PhD student

I, the undersigned, agree to include an electronic version of the above PhD dissertation in the open, institutional, digital repository of Gdańsk University of Technology, Pomeranian Digital Library, and for it to be submitted to the processes of verification and protection against misappropriation of authorship.

Gdańsk,..... .....

signature of the PhD student

[1] Decree of Rector of Gdansk University of Technology No. 34/2009 of 9th November 2009, TUG archive instruction addendum No. 8.

[2] Act of 27th July 2005, Law on Higher Education: Chapter 7, Criminal responsibility of PhD students, Article 226.

GDAŃSK UNIVERSITY OF TECHNOLOGY
FACULTY OF CHEMISTRY

Description of doctoral dissertation

The Author of the PhD dissertation: MSc Zuzanna Bielan

Title of PhD dissertation: TiO_2-based magnetic nanocomposites with core-shell structure

Title of PhD dissertation in Polish: Magnetyczne nanokompozyty na bazie TiO_2 o strukturze rdzeń-otoczka

Language of PhD dissertation: English

Supervision: PhD DSc, Anna Zielińska-Jurek, Assoc. Prof. of GUT

Date of doctoral defense:

Keywords of PhD dissertation in Polish: Fe_3O_4, fotokataliza heterogeniczna, separacja magnetyczna, fotokatalizator magnetyczny

Keywords of PhD dissertation in English: Fe_3O_4, heterogeneous photocatalysis, magnetic separation, magnetic photocatalyst

Summary of PhD dissertation in Polish: Tematyka badawcza pracy doktorskiej obejmuje preparatykę i charakterystykę fotokatalizatorów, ze szczególnym uwzględnieniem modyfikowanych fotokatalizatorów tlenku tytanu(IV), które znajdują zastosowanie do degradacji zanieczyszczeń organicznych niepodatnych na rozkład biologiczny. Celem pracy doktorskiej było opracowanie metody otrzymywania i charakterystyka nanokompozytów typu rdzeń magnetyczny – otoczka (TiO_2) aktywnych fotokatalitycznie pod wpływem promieniowania UV i Vis. Zastosowanie metody mikroemulsyjnej do otrzymywania nanokompozytów magnetycznych umożliwiło wytworzenie pożądanej struktury, w której

rdzeń nanokompozytu stanowił tlenek żelaza(II) diżelaza(III) (Fe_3O_4), pokryty warstwą inertnej krzemionki oraz warstwą fotokatalizatora TiO_2. Drugim z aspektów naukowych pracy było uzyskanie zwiększonej aktywności fotokatalitycznej otrzymanych nanokompozytów w świetle UV/Vis, jak i świetle widzialnym poprzez modyfikację powierzchni TiO_2 platyną oraz miedzią, jak również wprowadzenie do struktury krystalicznej defektów tytanowych. Otrzymane nanokompozyty zastosowano do efektywnej degradacji uporczywych zanieczyszczeń organicznych obecnych w płynie pozabiegowym po procesie szczelinowania hydraulicznego oraz karbamazepiny, powszechnie stosowanego leku przeciwpadaczkowego, zaliczanego do grupy środków farmaceutycznych stanowiących zanieczyszczenie środowiska wodnego.

Summary of PhD dissertation in English: The main aim of the doctoral dissertation was preparation and characterization of photocatalysts, with particular emphasis on modified titanium (IV) oxide photocatalysts, which can be applied for the degradation of organic pollutants not susceptible to biodegradation. A particularly important aspect of the work was the development of preparation method of nanocomposites with the magnetic core-shell and photocatalyst shell (TiO_2) structure, photocatalytic active under UV/Vis radiation. The use of the microemulsion method for the preparation of magnetic nanocomposites allowed for the creation of the desired structure, in which the core of the nanocomposite was iron (II) diiron (III), (Fe_3O_4), covered with a layer of inert silica and TiO_2 photocatalyst. The second scientific aspect of the work was to increase the photocatalytic activity of the obtained nanocomposites in UV/Vis light and visible light by modifying the titanium(IV) oxide surface with platinum and copper, as well as introducing titanium defects into the crystal structure of TiO_2. The obtained nanocomposites were used for the effective degradation of persistent organic pollutants present in flowback water after the hydraulic fracturing process and carbamazepine, a commonly used antiepileptic drug, classified as a pharmaceutical pollutant of the aquatic environment.

Acknowledgements

Throughout my journey with PhD studies, I received much encouragement and support words from lots of people. If I start to list them all here, definitely there would not be enough space. Nonetheless, I will try.

I would like to express my sincere thanks to:

- Prof. Anna Zielińska-Jurek, for being my supervisor during MSc and PhD studies, all effort put in checking my manuscripts' scribbles and awakening my love to photocatalysis.

- Prof. Ewa Kowalska and Prof. Bunsho Ohtani from Institute for Catalysis (ICAT), Hokkaido University in Sapporo, Japan, for the opportunity for being the part of "Ohtani Laboratory family", all advices, help and support.

- Prof. Tomasz Klimczuk and Zuzanna Ryżyńska, for magnetic properties measurements.

- Dr. Izabela Wysocka, for being the best *senpai* I could dream of.

- Szymon Dudziak, for all scientific discussions with tea and pizza and all common-sense arguments.

- My "Basement Photocat Children" as well as co-workers from Department of Process Engineering and Chemical Technology, especially (in alphabetic order): Natalia Czaplicka, Prof. Jacek Gębicki, Prof. Jan Hupka, Anna Grzegórska, Marta Kowalkińska, Izabela Malinowska, Dr. Aleksandra Małachowska, Eryka Mrotek, Małgorzata Lech, Łukasz Pałys, Dr. Andrzej Rogala and Agnieszka Sulowska, for unforgettable experiences, which accumulated during these five years. And for feeding cats.

- My friends from around the world, especially (in alphabetic order): Fitri Rizki Amalia, Kanae Aoki, Paulina & Majk Bąba, Rafał Borawski, Bartłomiej Cieślik, Guangyi Chen, Marlena Czajkowska, Yuto Doi, Maya Endo-

Kimura, Artur Jędrzak, Linfu Jiang, Pradudnet Ketwong, Róża & Adam Kubiak, Yumin Li, Łukasz Małecki, Tharishinny Raja Mogan, Yang Shen, Paweł Sosnowski, Marina Takahashi, Kunlei Wang, Wojciech Wojnowski, Dong Zhang and Chunyu Zhao, for notorious questions when *finally* I will finish my PhD studies. This work is a milestone in this direction!

⇨ My family, especially my Mum, Grandparents, Godmother with her husband and daughters and their families. When all I wanted was to lie in bed for the rest of my life due to sadness, exhaustion and hate to what I was doing, they were next to me.

⇨ Finally, Dr. Przemysław Tyszkiewicz. If we had not met in December 2016, this work would never have been written and I would not have been where and who I am now.

Thank you very much.

ありがとう ございます

This dissertation was accomplished within the Sonata-12 project titled: „Studies on preparation, physicochemical characterization of TiO_2 nanocomposites based on spinel and hexagonal ferrites for the oxidation of organic compounds in the aqueous phase" financed by the National Science Centre in Poland, project no. 2016/23/D/ST5/01021.

NATIONAL SCIENCE CENTRE
POLAND

Abbreviations and acronyms

AO	Ammonium oxalate
AOTs	Advanced Oxidation Technologies
BET	Specific surface area determined using Brunauer-Emmett-Teller method [m^2/g]
BQ	1,4-Benzoquinone
CB	Conduction band
CCB	Central composite design
COD	Chemical oxygen demand [mgO_2/dm^3]
CTAB	Hexadecyltrimethylammonium bromide, surfactant
DAD	Photodiode array detector
DAP	Decahedral anatase particles
e^-	Electron
E_{fb}	Flat band energy [eV]
Eg	Band gap energy [eV]
EPR	Electron paramagnetic resonance spectroscopy
FP6	Commercially available titanium(IV) dioxide (Showa Denko K.K., Japan)

GC-MS	Gas chromatography with mass spectrometry
h^+	Hole
HPLC	High-performance liquid chromatography
IEP	Isoelectric point
LC-TOFMS	Liquid chromatography-quadrupole time of flight mass spectrometry
LSPR	Localized Surface Plasmon Resonance
M	Metal nanoparticle
M_s	Saturation magnetization [Am^2/kg]
OAP	Octahedral anatase particles
P25	Commercially available titanium(IV) dioxide (Evonik, Germany)
POPs	Persistant organic pollutants
SN	Silver nitrate
ST01	Commercially available titanium(IV) dioxide (Ishihara Sangyo, Japan)
ST41	Commercially available titanium(IV) dioxide (Ishihara Sangyo, Japan)
STEM	Scanning transmission electron microscope
t-BuOH	*tert*-butanol
TIP	Titanium isopropoxide, TiO_2 organic precursor

TBT	Titanium n-butoxide, TiO_2 organic precursor
TEOS	Tetraethyl orthosilicate
Ti_i	Titanium interstitials
TOC	Total organic carbon [mg/dm^3]
UV	Ultraviolet light
VB	Valence band
Vis	Visible light
V_o	Oxygen vacancies
V_{Ti}	Titanium vacancies
XPS	X-ray photoelectron spectroscopy
XRD	X-ray powder diffraction

Contents

Chapter 1

Introduction

Nowadays, about 3,000 different active substances are used in the European Union in the production of pesticides, painkillers, antibiotics, contraceptives, beta-blockers, lipid regulators, sedatives and drugs. Some of the widely used pharmaceuticals (antiepileptic carbamazepine) as well as analgesic and anti-inflammatory drugs (ibuprofen, diclofenac, ketoprofen, naproxen), have been detected in lakes, rivers and sewage treatment plants in concentrations ranging from 5 to 3500 ng/dm^3 [1]. In this regard, the use of Advanced Oxidation Technologies - AOTs, which use the strongest oxidizing properties of hydroxyl radicals – 2.80 V [2], enable the complete mineralization and removal of persistent compounds that are difficult or not susceptible to degradation using traditional methods of wastewater treatment.

Photocatalysis is one of the AOTs, consisting of the acceleration of a chemical reaction that occurs with the use of electromagnetic radiation (infrared, ultraviolet or visible light). Materials, capable of absorbing a radiation quantum with simultaneous activation and thus, promoting a chemical reaction are called photocatalysts, most of which are semiconductors. Among a wide range of semiconductors used in photocatalytic reactions [3, 9], titanium(IV) oxide (TiO_2) is the most widespread due to its advantages, e.g. high oxidizing potential, high chemical stability over a wide pH range, and relatively low price [10]. The first paper on the application of TiO_2 as a potential photocatalyst was reported in 1972 when Honda and Fujishima published their work about the photocatalytic decomposition of water using titanium(IV) oxide electrode [11]. Four years later, in 1976, Carey et al. for the first time studied photodegradation of biphenyls and chlorobiphenyls in the presence of TiO_2 [12]. Titanium(IV) oxide may occur in three polymorphs: tetragonal anatase and rutile as well as orthorhombic brookite [13]. The most stable one is rutile, with anatase and brookite converted into it through

high-temperature thermal treatment [14]. Commercially available titanium(IV) oxide is usually a mixture of crystalline and non-crystalline phases [15]. Studies show that biphasic TiO_2, consisting of anatase and rutile, achieves higher photocatalytic activity than monophasic one, due to the synergistic effect that extends the lifetime of photogenerated charge carriers [16]. In recent years, many studies focused on TiO_2 different structures and morphology. Nonetheless, despite different shape and polymorphic composition, which enhance the photocatalytic activity, TiO_2-based photocatalysis possess some limitations that impede commercialization. The major limitations discussed in the doctoral dissertation and challenges are presented in Figure 1.

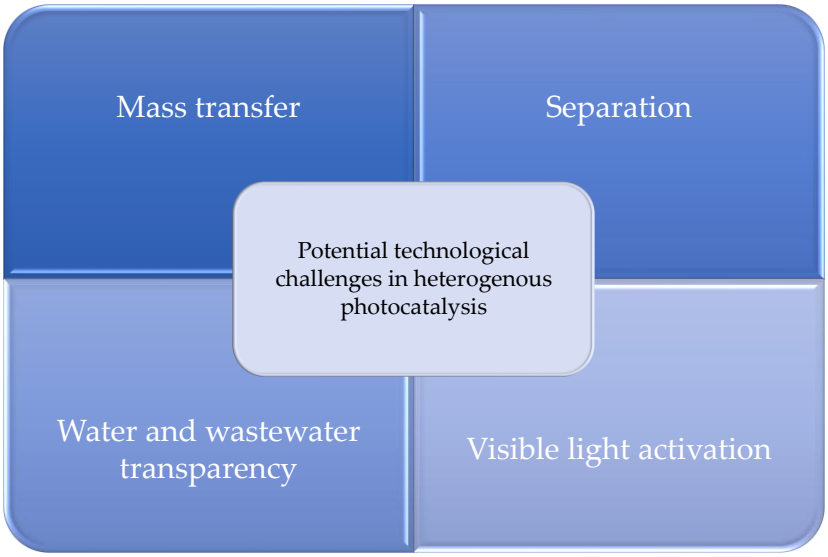

Figure 1. Potential technological problems and challenges in heterogeneous photocatalysis.

Mass transport in heterogeneous photocatalysis at the air/water/solid interface is primarily dependent on the interface between the phases. The larger the contact surface, the more efficient the photocatalytic process will be. The proper interfacial contact size, when carrying the process where the photocatalyst is suspended in the

aqueous phase, can be ensured by nanometric particle size, aeration as well as the mixing of the system.

The photocatalyst's particle size is closely related to its specific surface area. The number of active centres on which the adsorption of pollutants occurs depends on the development of the surface area. Usually, the smaller the particle sizes, the better the photocatalytic properties are observed. Addamo et al. [17] studied the effect of calcination temperature on the crystallites' size as well as the specific surface area and photocatalytic activity in the 4-nitrophenol degradation reaction. They found that the increase in calcination temperature from 120 °C to 500 °C caused a three-fold decrease in specific surface area. On the other hand, the exceptionally high specific surface area increases the incidence of crystal defects which favour the recombination of electrons and holes, thereby reducing the photocatalytic activity [18].

Aeration of photocatalysts suspension is mainly used to provide dissolved oxygen in the system, which is necessary to generate reactive oxygen species. The most optimal oxygen concentration is above 1 mg/dm^3 [19]. Aeration and mixing of the photocatalyst suspension lead to the dispersion of the semiconductor particles throughout the entire reactor volume and, thus to an increase in the surface contact between photocatalyst and pollutant molecules. However, it should be noted, that intense mixing and aeration could also lead to turbulent flow and, consequently, to a disturbance in the transparency of the system and a decrease in photocatalytic activity.

The depth of UV light penetration into the photocatalyst suspension is limited by the strong absorption of titanium(IV) oxide and the properties of dissolved organic pollutants [20]. Also, energy losses due to light reflection from the photocatalyst surface, transmission and heat losses are inevitable and mostly affect process efficiency [21]. Therefore, appropriate reactor construction, forcing radiation of a thin, transparent layer and enabling penetration of radiation deep into the aqueous phase could cause an increase in TiO_2 photocatalytic activity.

To the major challenges of the photocatalytic process belongs the limitations related to the wide band gap of TiO_2, which differs in the range of 3.0-3.2 eV, for rutile and anatase, respectively [22]. Therefore, photoexcitation of TiO_2 is possible

almost only in UV light ($\lambda \leq 388$ nm), and use of solar radiation is highly limited, which generates high costs due to application of energy-consuming light sources in photocatalysis. It is assumed that only 3-5% of sunlight could be used in the process of photocatalysis using pure TiO_2. Also, unfavourable recombination of generated by photo-excitation electrons and holes causes a significant reduction in the quantum efficiency of the photocatalytic process [23].

In order to increase the activity of titanium(IV) oxide in visible light (400-800 nm) range, various methods of doping and surface modification are used, including:

- Doping with non-metals, e.g. N [24], C [25], F [26], Cl [27], S [28], I [29];
- Surface modification with noble and semi-noble metals, e.g. Ag [30], Au [31], Mo [32], Fe [33], Pt [34], Pd [35];
- Sensitization with dyes [36, 37];
- Heterojunction with other semiconductors [38 - 40];
- Introduction of intrinsic crystal defects [41 - 43];

Among the used methods, surface modification with noble and semi-noble metals is the most commonly applied. Wysocka et al. [44] obtained mono- (Pt, Ag, Cu) and bimetal- (Cu/Ag, Ag/Pt, Cu/Pt) modified TiO_2 photocatalysts, where TiO_2 matrix was commercially available ST01 (fine anatase particles). Metal ions were reduced using the chemical as well as the thermal treatment method. The highest photocatalytic activity in hydrogen evolution was observed for TiO_2-based nanocomposite modified with Pt and Cu. Klein et al. [45] prepared TiO_2-P25 modified with Pt, Pd, Ag and Au using radiolysis. Obtained photocatalysts were further immobilized on a glass plate and used for toluene removal from the gas phase. The highest photoactivity was noticed for TiO_2 modified with 0.1 % of Pt. In turn, Janczarek et al. [46] proposed a method of obtaining Ag- and Cu-modified decahedral anatase particles (DAP) by photodeposition. Au/Ag modified DAP, together with octahedral anatase particles (OAP) were also characterized by Wei et al. [47]. It was found that selective deposition of metals nanoparticles on {001} facets of TiO_2 results in significant photocatalytic process improvement under visible light irradiation.

Metals nanoparticles have unique properties compared to bulk material or isolated atoms. Depending on the shape and size, metal nanoparticles possess better

optical, electrical and magnetic properties [48]. Furthermore, transition metal nanoparticles, such as Ag, Au, Pt, due to the presence of localized surface plasmon resonance, can absorb visible light. Localized Surface Plasmon Resonance (LSPR) is a collective oscillation of electrons caused by an external electric field. The field inside the nanoparticles, created under the influence of an electromagnetic wavelength, sets electrons in the conductivity band in motion. The presence of electrons affects the formation of a negative charge on one side of the particle, while a positive one on the other side. If the frequency of the exciting light is the same as the oscillation frequency, the quantum of light excites the oscillating vibrations of the particle [49,50]. Metal nanoparticles' deposition on the surface of titanium(IV) oxide allows the activation of the semiconductor in the visible range. Metals deposited on the TiO_2 surface could also increase photocatalytic activity by reducing the electron-hole recombination and generating charge carriers due to light interaction as well as increasing the efficiency of interfacial charge transfer [51 - 55]. Differences between photoactivation of non-modified and metal-modified TiO_2 are presented in Figure 2 a-c in the reaction of phenol photodegradation in UV and Vis light.

Noble metals deposited on titanium(IV) oxide are also characterized by high Schottky barrier and therefore act as electron traps, facilitating charge carriers separation. They are also able to react with holes, electrons and oxygen [52], as it is presented in the equations (1-3):

$$M + e^- \rightarrow M^- \quad (1)$$

$$M^- + O_2 \rightarrow O_2^- + M \quad (2)$$

$$M + H^+ \rightarrow M^+ \quad (3)$$

Moreover, the efficiency of titanium(IV) oxide activation is significantly influenced by the amount of deposited metal and its particle size [56]. Larger particles (above 100 nm) and high metal concentration could block active sites on the TiO_2 surface and accelerate the recombination of electron-hole pairs [57].

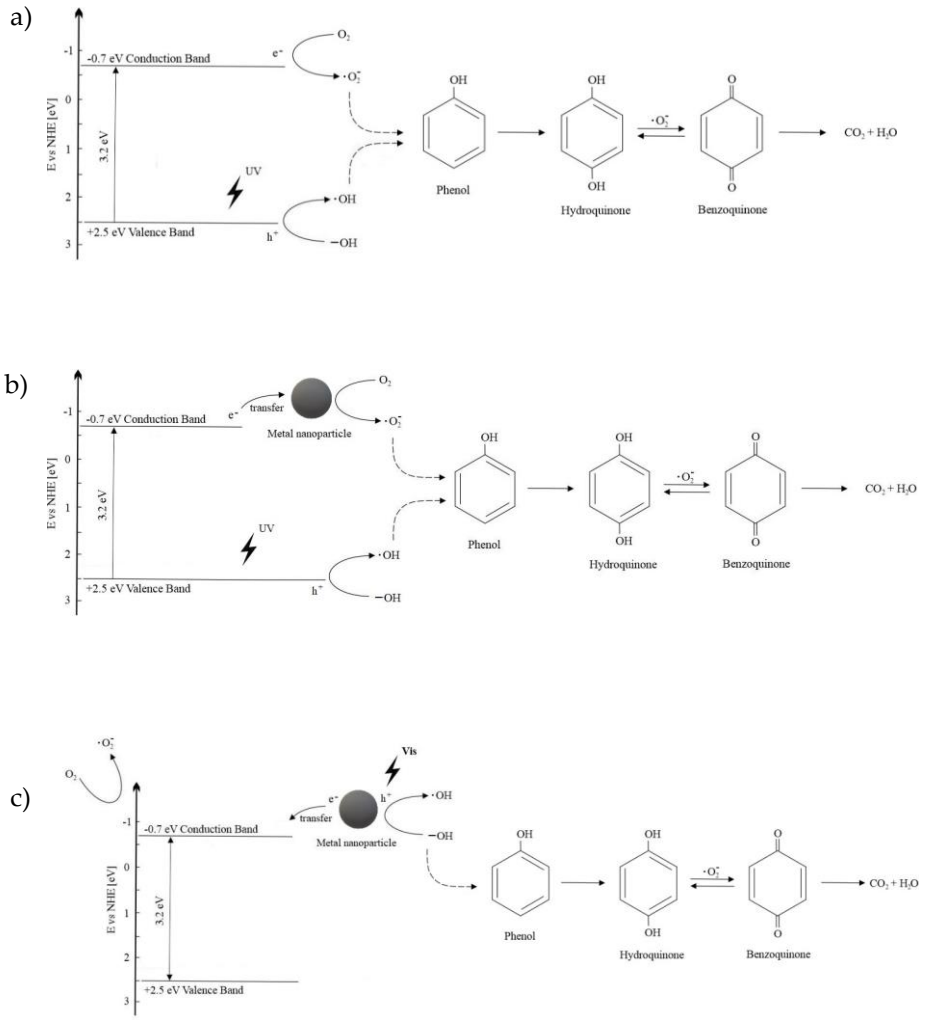

Figure 2. Schematic illustration of the mechanism of phenol degradation in UV light in the presence of non-modified (a) and metal-modified TiO_2 (b) as well as Vis light activation in the presence of metal-modified TiO_2 (c).

Another possibility of increasing the TiO_2 photoactivity is an introduction of intrinsic defects to its crystal structure. Titanium and oxygen vacancies, surface disorders as well as the formation of Ti-OH bonds, could extend the light absorption to the visible region without any external dopant introduction. Ti^{3+} defected (commonly known as blue titania) and reduced TiO_2 (black titania) are widely described in the literature [58 - 59]. Lettieri et al. [60] obtained blue TiO_2 from commercially available titanium(IV) oxide – P25 by a simple solvent reflux thermal treatment method. The formed surface and sub-surface oxygen vacancies allowed for narrowing the bandgap energy (Eg) to about 2.3 eV and, as a consequence, increasing the photoactivity in visible light range. In turn, the yellow colour of the TiO_2 photocatalyst suggests the formation of titanium vacancies (V_{Ti}) or titanium interstitials (Ti_i), which are the most rarely investigated from all the titania defects. Titanium removal from the crystal structure (as it is presented in Figure 3 for anatase polymorph) could be caused by nucleation and growth of TiO_2 nanoparticles in the presence of UV light [41]. V_{Ti} are also responsible for p-type properties of TiO_2 and lowering its Fermi level due to acceptor-type centres forming [61 - 62].

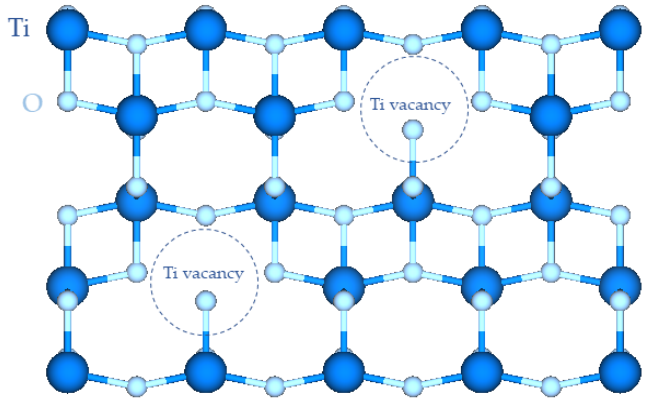

Figure 3. Atomic structure of anatase TiO_2 with formed titanium vacancies.

At the end of the 20th century, along with the growing interest in TiO_2 photocatalysis and its use for the purification of both gas [63] and liquid [64] phases,

the problem with the photocatalyst's recovery and reuse became a very important issue in photocatalysis, especially in a technological scale. The main reason for the separation process limitations and, consequently, its effectiveness is the nanometric size of the titanium(IV) oxide [65]. Recover of the suspended photocatalysts from the batch reactor could be carried out with the use of ultrafiltration [66]. However, such a solution is expensive and significantly increases the costs of the photocatalysis process. Another method that completely excludes the separation process is TiO_2 immobilization on support. Titanium(IV) oxide nanoparticles could be deposited on solid material, such as glass, sand, ceramic balls, zeolites, activated carbon, optical fibres [67 - 69]. Immobilization could be carried out by dip-coating, controlled immersion of the carrier in the photocatalyst suspension [70]. Nevertheless, TiO_2 solidification leads to a decrease in its photocatalytic activity caused by specific surface area reduction [71]. Comparison studies of the photodegradation activity between suspended and immobilized TiO_2 in the formic acid degradation reaction were conducted by Dijkstra et al. [72]. They found that suspension of titanium(IV) oxide was four times more active than TiO_2 deposited on a solid support. Also, intermediate products of the photocatalysis reaction might settle on the immobilized photocatalyst's surface, which could significantly reduce its activity [73]. In addition, it has often been reported in the literature that the deposited photocatalyst layer is not stable and is susceptible to abrasion during the photocatalytic reaction [42, 74].

Therefore, other separation methods should be developed, focusing primarily on a magnetic separation using an external magnetic field. Attempts to combine photoactive semiconductors with magnetic compounds have been first described in the 1990s. Since then, researches are still underway to obtain the optimal structure of such a composite. Many solutions are proposed, ranging from disordered mixtures of both phases [75, 76], through more precise connections, such as a core-shell [77, 78], and ending with even multi-stage syntheses that allow obtaining multilayer structures [79]. The various proposed composite structures are presented schematically in Figure 4.

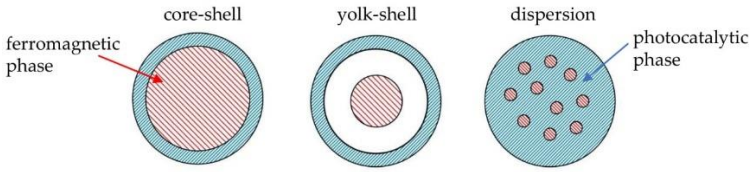

Figure 4. Examples of combined ferromagnet-photocatalyst structures. Author's scheme based on [79].

In recent years a great deal of attention has been directed towards TiO_2 modification with ferromagnetic iron oxides such as Fe_3O_4 [77], [80], $ZnFe_2O_4$ [81], $BaFe_{12}O_{19}$ [82, 83]. The most often used magnetic material is iron(II, III) oxide (Fe_3O_4), which crystal structure is presented in Figure 5. Fe_3O_4 is commonly used as a ferromagnetic material due to its simple synthesis method [84] as well as by excellent magnetic properties with M_s value of about 90 Am^2/kg, enable its efficient separation from the suspension.

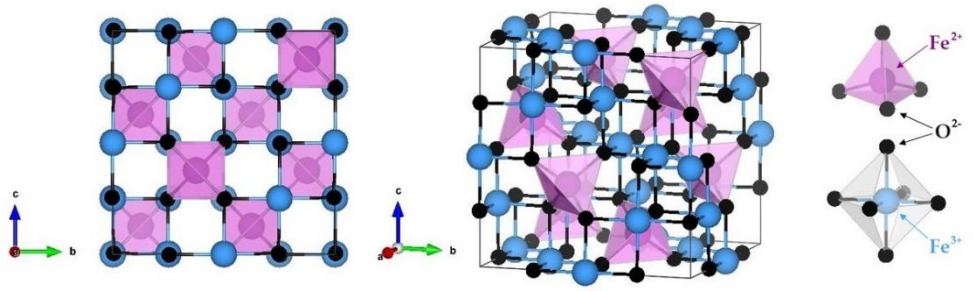

Figure 5. Crystal structure of Fe_3O_4. Octahedrals were not marked for clearer structure visibility.

In the Fe_3O_4 structure are unpaired electrons which, in an external magnetic field, create the partial magnetic moments, due to their ordered orbits movement around individual atoms. The created magnetic moments equal to the macroscopic magnetic properties of magnetic material. Also, the existence of the magnetic domains, i.e. areas in the material structure where partial magnetic moments are

directed in one direction, is characteristic for ferromagnets [85]. In photocatalysis, magnetic separation is efficient for high saturation magnetization (M_s) values. M_s represents the force of interaction between the magnetic particle and the current magnetic field. However, at present, there is no clearly defined value of M_s that would allow for efficient separation of the photocatalyst from the aqueous phase. Some authors indicate that M_s value of 1 Am^2/kg is enough for efficient separation [86]; however, similar claims are not supported by any broader research.

The most crucial requirements for building ferromagnet-photocatalyst structures are the stability of the entire structure and no interference of the magnetic compound on the photocatalytic process. Several reports are indicating that magnetic materials, e.g. Fe_3O_4, are semiconductors themselves and could support the charge carriers separation, generated in the photocatalyst structure [87, 88]. However, the direct contact of those compound could also result in a decrease in photocatalytic activity [89]. It could be caused by both reduction of iron(III) to iron(II) in the Fe_3O_4 structure as well as its further leaching in an acidic environment and its secondary oxidation to iron(III) [90]. The possible reactions of iron oxidation and reduction are presented in equations (4)-(7) [89].

$$Fe^{3+}(s) + e^- \rightarrow Fe^{2+}(s) \quad (4)$$

$$Fe_2O_3 + 6H^+ + 2e^- \rightarrow 2Fe^{2+} + 3H_2O \quad (5)$$

$$Fe_3O_4 + 8H^+ + 3e^- \rightarrow 3Fe^{2+} + 4H_2O \quad (6)$$

$$Fe^{2+}(aq) + h^+ \rightarrow Fe^{3+}(aq) \quad (7)$$

As a result, the generated charge carriers are used for iron oxidation, not on photocatalytic degradation of pollutants. Moreover, iron dissolution could cause poisoning of photocatalyst and, as a consequence, breakdown of the ferromagnet-photocatalyst structure [91], as presented in Figure 6.

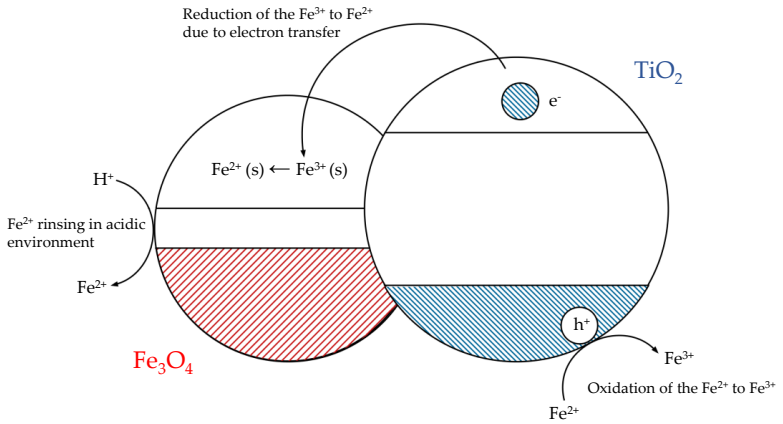

Figure 6. Possible reactions in Fe_3O_4/TiO_2 composite, contributing to Fe_3O_4 degradation and decrease in photoactivity. Author's scheme based on [92].

In this regard, limiting the interaction between a ferromagnet and the environment as well as excluding the possibility of charge carriers migration are highly desirable. This approach was recently presented in the literature, which resulted in proposing the use of the core-shell structures, where the core is magnetic compound and shell is a photocatalyst, using an additional intermediate layer, which is isolation between the two relevant phases of the composite. As an inert interlayer, SiO_2 [93 – 95], as well as polymers, such as poly(methacrylic acid) [96] or polyaniline [97] and carbon [98 – 99], could be used. The presented approaches prevent the charge migration between magnetic and photocatalytic compounds. However, the used polymers could be degraded after long term use as a result of their secondary reactions with generated radicals [100]. Another issue is the thickness of the introduced interlayer. The SiO_2 layer thickness, effectively separating magnetic core and photocatalytic shell, should not be less than 5-10 nm [101 – 102]. However, it should be noted, that presented value is purely theoretical, and for all designed composited, it should be determined individually and experimentally.

Nonetheless, in the literature, since the first reports on magnetic TiO_2 photocatalysts preparation and characterization, there is still a lack of answers for several problems:

- How to obtain stable core-shell structure – lack of universal synthesis method;
- Is there a possibility to combine magnetic stability and photocatalytic activity of composite material in visible light – comparison of different TiO_2 matrices, different methods of increase of visible light activity (surface modification with metal nanoparticles, vacancies formation and their combination);
- Are obtained magnetic photocatalysts equally effective in photooxidation/photoreduction reactions and degradation of various organic compounds.

Chapter 2

Research goals

Based on the literature overview, the white spots were indicated, explanations which I have undertaken in the framework of the doctoral thesis. The main focused of PhD dissertation was to obtain TiO_2-based photocatalyst highly active in UV-Vis light and separable in the magnetic field after the photocatalytic treatment process.

In order to achieve the intended goal, several studies have been taken to explain:

- The effect of titanium vacancies formed in the crystal structure of TiO_2 photocatalysts during the preparation procedure as well as the effect of surface modification of TiO_2-based magnetic photocatalyst with platinum and/or copper nanoparticles on increasing visible light photoactivity;

- The influence of the preparation method on magnetic photocatalyst core-shell structure stability, photocatalytic and magnetic properties. Researches were mainly focused on the selection of a proper methodology (TiO_2 type and TiO_2:SiO_2: ferrite molar ratio) with an emphasis on reaction environment, which allow to self-organize the composite components and create the core-shell structure of the photocatalyst;

- The effect of TiO_2 matrix and its modifications' on magnetic nanocomposites' properties, particularly on photocatalytic activity both in UV-Vis and Vis light in different oxidation and reduction reactions;

- The relationship between the type of deposited metals and their morphology on the efficiency of organic pollutant degradation;

- The significance of superoxide anion radicals and hydroxyl radicals in the mechanism of persistent organic pollutants degradation;

- The relationship between the type of deposited metal on light absorption properties – action spectrum analyses;

- The possibility of using the photocatalytic method to degrade organic compounds that are not susceptible to biological degradation (carbamazepine, organic compounds present in the technological fluids with high salinity). Optimization of the degradation process.

Chapter 3

Research description

The research issues of the PhD dissertation are studied and discussed in detail in a series of six publications and 3 patents listed below:

- Z. Bielan, E. Kowalska, S. Dudziak, K. Wang, B. Ohtani, A. Zielińska-Jurek, Mono- and bimetallic (Pt/Cu) titanium(IV) oxide photocatalysts. Physicochemical and photocatalytic data of magnetic nanocomposites' shell, Data in Brief. 31 (2020) 105814 (Q1, IF 0.93), henceforth referred to as **P1**;

- Z. Bielan, S. Dudziak, A. Sulowska, D. Pelczarski, J. Ryl, A. Zielińska-Jurek, Preparation and Characterization of Defective TiO_2. The Effect of the Reaction Environment on Titanium Vacancies Formation, Materials. 13 (2020) 2763 (Q2, IF 2.972), henceforth referred to as **P2**;

- Z. Bielan, A. Sulowska, S. Dudziak, K. Siuzdak, J. Ryl, A. Zielińska-Jurek, Defective TiO_2 Core-Shell Magnetic Photocatalyst Modified with Plasmonic Nanoparticles for Visible Light-Induced Photocatalytic Activity, Catalysts. 10 (2020) 672 (Q2, IF 3.444), henceforth referred to as **P3**;

- A. Zielińska-Jurek, Z. Bielan, I. Wysocka, J. Strychalska, M. Janczarek, T. Klimczuk, Magnetic semiconductor photocatalysts for the degradation of recalcitrant chemicals from flow back water, Journal of Environmental Management. 195 part 2 (2017) 157-165 (Q1, IF 4.005), henceforth referred to as **P4**;

- A. Zielińska-Jurek, Z. Bielan, S. Dudziak, I. Wolak, Z. Sobczak, T. Klimczuk, G. Nowaczyk, J. Hupka, Design and Application of Magnetic Photocatalysts for Water Treatment. The Effect of Particle Charge on Surface Functionality, Catalysts. 7 (2017) 360-379 (Q2, IF 3.465), henceforth referred to as **P5**;

- A. Zielińska-Jurek, Z. Bielan, Sposób otrzymywania fotokatalizatora magnetycznego wielowarstwowego (Method of preparation of a multilayer magnetic photocatalyst), Patent PL. 233343 (2019); Patent PL. 233344 (2019); PL. 233345 (2019), henceforth referred to as **P6**;

- Z. Bielan, E. Kowalska, S. Dudziak, K. Wang, B. Ohtani, A. Zielińska-Jurek, Mono- and bimetallic (Pt/Cu) titanium(IV) oxide core-shell photocatalysts with UV/Vis light activity and magnetic separability, Catalysis Today. (2020) (Q1, IF 4.888) journal pre-proof henceforth referred to as **P7**;

The canon of PhD thesis [**P1**–**P7**] includes the studies conducted to gain a better understanding of the effects of precursor type and a reaction environment on physicochemical properties of magnetic composites. Moreover, the light absorption properties of the synthesized photocatalysts were the second important issue studied in detail within this work.

As illustrated in Figure 7, the first step towards fulfilling the intended goal was an extensive literature review in terms of titanium(IV) oxide advantages as well as its limitations and proposed methods for their overcoming. It allowed designing the complete, five-step plan of PhD dissertation. All stages in the flowchart as main aspects of presented work are briefly discussed in the following subsections as well as described in detail in publications enclosed in full, with formatting, in Chapter 5.

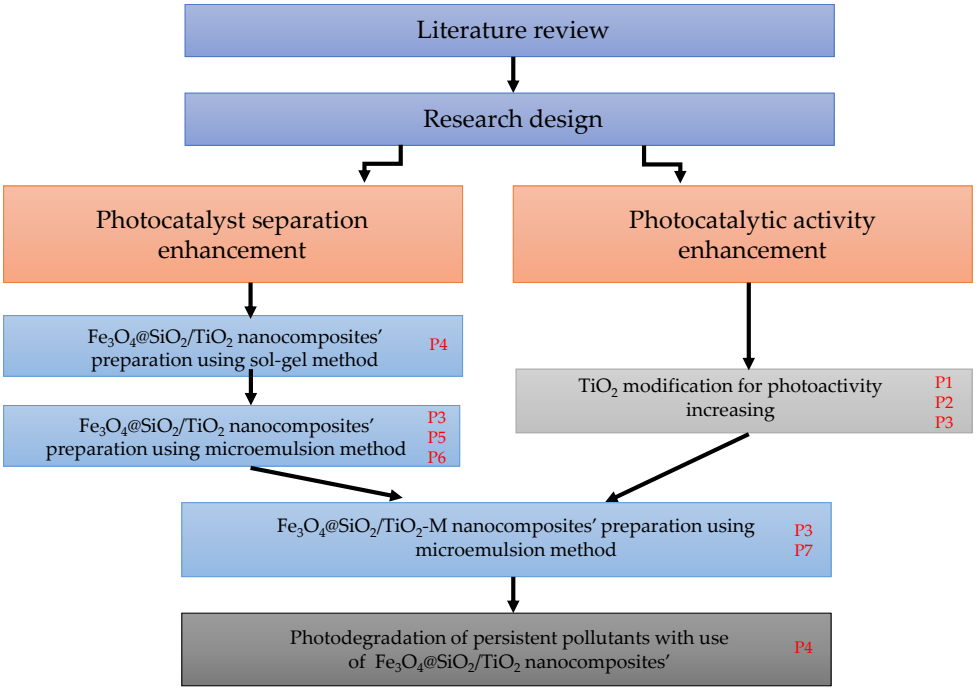

Figure 7. Thematic correlation between the papers that constitute the scientific achievement in the PhD dissertation.

3.1 Enhanced photocatalytic activity in UV-Vis light of TiO_2-based photocatalysts

The first focus was on increasing the visible light activity of titanium(IV) oxide. From all the methods, surface modification with noble and semi-noble metal nanoparticles as well as the introduction of intrinsic defects into TiO_2 crystal structure were selected to improve the activity in Vis light and improvement charge carriers separation [**P1**, **P2**].

Although such great amount of publications regarding TiO_2 surface modification with noble and semi-noble metals have been reported, there is still a lack of

complementary comparison between a wide range of metal-modified TiO_2 matrices, differing in photocatalyst particle sizes and phase composition. Such an attempt was partly made by Endo et al. [31]. In their work, Au and Ag were photodeposited on six different commercial TiO_2, used further for fungi and bacteria photodecomposition. However, there is no information about the photocatalytic activity of the obtained samples. Kowalska et al. [103, 104] studied the effect of Ag, Au and Cu modification of eight TiO_2 matrices on photocatalytic activity. Nonetheless, only monometallic modifications of TiO_2 were obtained. In this regard, the present study [**P1**] focused on correlation the morphological properties of titanium(IV) oxide phases, the concentration of modifying metal and its type with photocatalytic activity in reactions of H_2 generation, nitrophenol reduction, as well as phenol and acetic acid oxidation.

Three commercially available titanium(IV) oxide photocatalysts: ST01, ST41 (Ishihara Sangyo, Japan) and FP6 (Showa Denko K.K., Japan), as well as self-prepared TiO_2 from titanium n-butoxide hydrolysis (sample TBT), were used as a base for further modification. Physicochemical characteristic of selected non-modifiedTiO_2 samples is presented in Table 1.

Table 1. Phase percentage, crystallite size and BET surface area of non-modified TiO_2 photocatalysts [**P1**].

		Anatase [nm]	Anatase [%]	Rutile [nm]	Rutile [%]	Brookite [nm]	Brookite [%]	BET surface area [m^2/g]
TiO_2	TBT	8.2 ± 0.1	63 ± 6	-	-	7.7 ± 0.2	37 ± 4	118
	ST01	7.7 ± 0.1	100.0 ± 0.4	-	-	-	-	181
	FP6	11.3 ± 0.1	78.6 ± 0.3	4.9 ± 0.2	21.4 ± 0.9	-	-	104
	ST41	45.8 ± 0.2	100.0 ± 0.2	-	-	-	-	10

The selected TiO_2 matrices differed in particles size, phase composition and surface area, which further influenced on their photocatalytic activity. Nevertheless, all non-modified titanium(IV) oxide samples absorb UV light with an absorption edge at 400 nm and therefore had negligible photoactivity in visible light range. In order to increase the photoactivity, platinum and copper were used as surface modifiers of TiO_2. Photodeposition method allowed for successful modification of the titanium(IV) oxide surface. The highest photocatalytic activity both in oxidation and reduction reactions revealed Pt-modified TiO_2 samples almost regardless of the

Pt species amount (0.05 – 0.1 mol%) deposited on the semiconductor surface. The TiO_2 template also influenced the efficiency of the photocatalytic reactions. The metal-modified ST01 samples (small anatase NPs) exhibited the highest activity towards hydrogen generation, whereas, for acetic acid oxidation, M-modified ST41 samples (large anatase particles) revealed higher photocatalytic activity than Pt-ST01. Previously, Prieto-Mahaney et al. [105] studied the morphological and photocatalytic properties of 35 commercial TiO_2 samples. It was found that ST01 with a high BET surface area is more suitable for adsorption of methanol in hydrogen evolution reaction, while ST41 photocatalyst with a low BET surface area is more efficient in the reaction of acetic acid decomposition to CO_2. Moreover, deposition of platinum and copper on different titanium(IV) oxide matrix, thereby creating bimetallic structures on TiO_2 resulted in similar dependence as for monometallic TiO_2 photocatalysts. Furthermore, the effect of platinum and copper amount on ST41 support on photocatalytic activity in reduction and oxidation reactions was studied. It was found that deposition of 0.1 mol % of Cu and 0.1 mol % of Pt had a positive impact on phenol degradation and acetic acid decomposition measured as CO_2 evolution. However, the presence of Cu at the surface of TiO_2 decreased the H_2 amount generated in photocatalytic reaction in the presence of Pt-Cu/TiO_2 nanoparticles.

A different approach is presented in the work [**P2**]. By simple hydrothermal method in the presence of three selected oxidizing agents: HIO_3, H_2O_2 and HNO_3, yellow defected TiO_2 was obtained. Similarly to titanium(IV) oxide modification with noble and semi-noble metals, TiO_2 with titanium vacancies (V_{Ti}) allowed for increasing the TiO_2 photoactivity in both UV-Vis and visible light range. Introduction of intrinsic defects into titanium(IV) oxide crystal structure led to shifting the absorption spectra towards longer wavelengths, thus narrowing its bandgap to approximately 2.7-2.9 eV. The electron paramagnetic resonance (EPR) spectroscopy measurements were conducted in order to direct confirmation of intrinsic defects presence. The designated Lande factor (g) of value in range 1.998-2.003 indicated the V_{Ti} formation after TiO_2 synthesis in the oxidative environment (Figure 8). It is also worth to mention that based on XPS analyses, the presence of oxygen defects as well as the possibility of iodine doping were excluded.

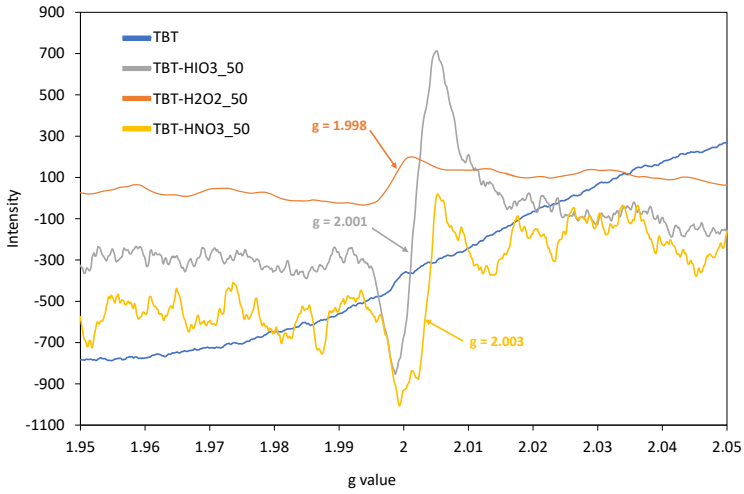

Figure 8. The EPR spectra for defective TiO_2 photocatalysts obtained in different oxidative environments in comparison with pure TiO_2-TBT sample [**P2**].

Photocatalytic activity of the obtained samples was evaluated in reaction of phenol degradation under UV-Vis and Vis light irradiation. The highest efficiency of phenol decomposition in UV-Vis light was observed for TBT-HNO_3_50, whereas under Vis light irradiation for TBT-HIO_3_50. Further studies in the field of defective TiO_2 with V_{Ti} concerned on the most relevant oxidant concentration that will allow reaching the highest photocatalytic activity in the investigated system. Additionally, a thermal stability test of the obtained photocatalysts was performed. It was found that in the investigated range of iodic acid concentrations (from 0.5 mol % to 100 mol %), the most optimal for creating the photocatalytic material with high photoactivity was the addition of 20 mol% to 50 mol% of HIO_3 to the reaction environment. Higher oxidant concentrations resulted in a high amount of created crystalline defects and, in consequence, decreasing the efficiency of organic pollutants degradation. The photocatalytic activity for the obtained samples correlates well with photoluminescence (PL) spectra, UV-Vis spectra, and EPR spectra analyses, see in Figure 9.

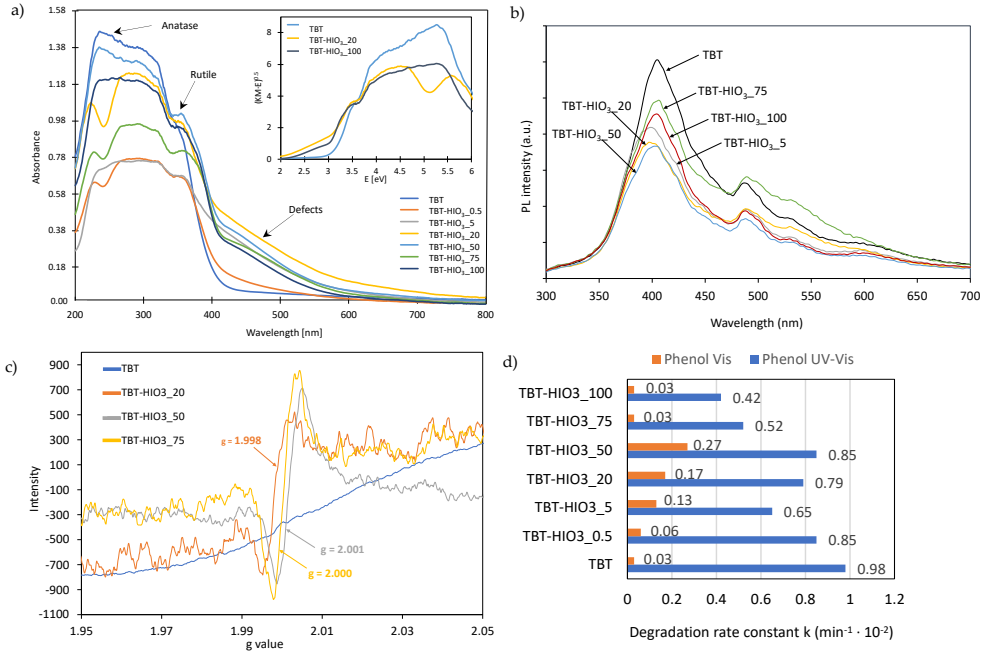

Figure 9. Correlation of the diffuse reflectance (DR)/UV-Vis spectra for pure TiO_2 and defective TiO_2-HIO_3 photocatalysts (a); Photoluminescence (PL) spectra for defective TiO_2-HIO_3 samples (b); with EPR analyses (c) and photodegradation of phenol in UV-Vis and Vis light analyses (d) [**P2**].

The most intense EPR signal was assigned to defective TBT-HIO_3_75, where the highest concentration of oxidant (75 mol%) was used. From the PL spectra analysis, the TBT-HIO_3_75 sample showed the highest intensity among analyzed photocatalysts, which indicated the highest electron-hole recombination as well as the lowest phenol degradation efficiency. It could suggest that too high concentration of defects in the TiO_2 structure could significantly decrease the photocatalytic activity of the semiconductor.

Furthermore, in thermal stability tests, increasing of calcination temperature from 300 to 1000 °C resulted in significant crystal dimensions growth with simultaneous BET specific surface area reduction. Higher calcination temperature was also associated with anatase to rutile transition, while the presence of defects

promoted this transformation at lower temperatures [**P2**]. However, despite the durability of the yellow colour of the samples, which indicated the titanium defects thermal stability, the visible light photoactivity was markedly lower for samples calcined above 450 °C. In order to determine the photocatalytic reaction mechanism in the presence of defective TiO_2 photocatalyst (see in Figure 10), the photocatalytic processes in the presence of scavengers were performed. In this regard, 1,4-benzoquinone (BQ), silver nitrate (SN), ammonium oxalate (AO) and tert-butanol (t-BuOH) were used as superoxide radical anions ($\cdot O_2^-$), electrons (e^-), holes (h^+) and hydroxyl radicals (·OH) scavengers, respectively.

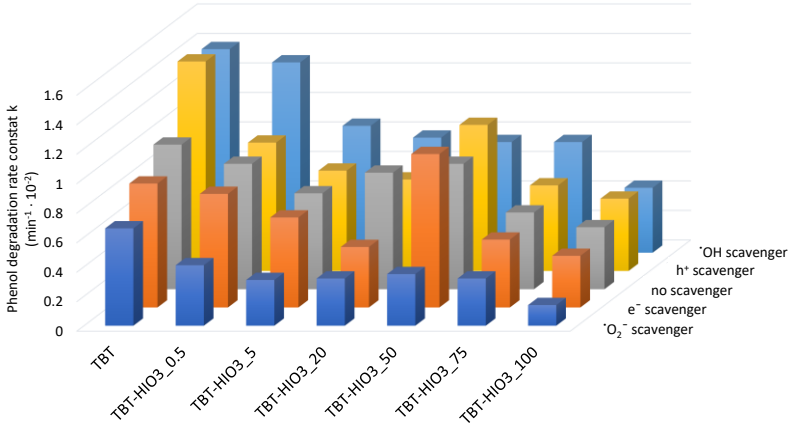

Figure 10. Photocatalytic degradation of phenol for defective TiO_2 photocatalysts in the presence of e^-, h^+, $\bullet O_2^-$, and $\bullet$OH scavengers [**P2**].

Addition of BQ as superoxide radical anions scavenger caused a significant reduction of photocatalytic activity for all obtained TBT-HIO_3 photocatalysts. Therefore, it can be assumed that $\bullet O_2^-$ are crucial reactive oxygen species participating in the photocatalytic reaction in the presence of defective TBT-HIO_3 samples. Finally, the stability tests performed in three 3-hours-long subsequent cycles of phenol degradation under UV-Vis light confirmed the reusability and no loss in phenol degradation.

Furthermore, the characterized defective d-TiO_2 samples were for the first time modified with Pt and Cu nanoparticles to increase the photocatalytic activity in Vis light [**P3**] and then deposited on the magnetite core [**P3**, **P7**] to effectively separate photocatalyst nanoparticles after the photodegradation process.

The physicochemical characteristic containing BET surface area, crystallite size, phase composition, as well as bandgap values of the obtained d-TiO_2-Pt/Cu photocatalysts are presented in Table 2 [**P3**].

Table 2. The physicochemical characteristic of d-TiO_2-Pt/Cu samples.

Sample	Crystalline Size and Phase Content					
	Anatase		Rutile		Brookite	
	Size (nm)	Phase Content (wt.%)	Size (nm)	Phase Content (wt.%)	Size (nm)	Phase Content (wt.%)
TiO_2	5.97 ± 0.04	95.5 ± 1	-	-	6.1 ± 0.3	4.5 ± 1
d-TiO_2_20	5.14 ± 0.03	96 ± 1.0	-	-	4.0 ± 0.6	3.5 ± 0.5
d-TiO_2_75	5.67 ± 0.05	21 ± 3.5	6.6 ± 0.1	80 ± 2	-	-
TiO_2-Pt0.05	5.71 ± 0.06	91 ± 0.5	-	-	5.7 ± 0.6	9 ± 1
d-TiO_2_20-Pt0.05	5.66 ± 0.03	85 ± 8	9.8 ± 0.7	9 ± 1.0	4.9 ± 0.3	6 ± 0.5
d-TiO_2_75-Pt0.05	5.49 ± 0.04	48 ± 2	7.53 ± 0.12	52 ± 2	-	-
d-TiO_2_20-Pt0.1	5.58 ± 0.03	81 ± 8	7.6 ± 0.8	6 ± 1	4.8 ± 0.3	13 ± 1
d-TiO_2_20-Cu0.1	6.62 ± 0.04	72 ± 11	11.7 ± 0.4	9 ± 2	1.52 ± 0.08	8.5 ± 1
d-TiO_2_20-Pt0.1/Cu0.1	5.52 ± 0.03	83 ± 12	9.5 ± 0.6	8 ± 2	5.1 ± 0.3	8.5 ± 1

The obtained results indicated that not so much the surface area but rather the presence of Ti defects and modification with metal nanoparticles caused the enhanced photoactivity of the obtained photocatalysts. Based on DR/UV-Vis analysis, it was found that the modification of defective d-TiO_2 with Pt and Cu increased Vis light absorbance. The samples of defective TiO_2 exhibited narrower bandgap of 2.7–2.9 eV compared to TiO_2 and TiO_2-Pt0.05 photocatalysts. Moreover, the deposition of Pt caused a more significant absorbance increment than the same modification with Cu species. The almost inactive in Vis light d-TiO_2_75 sample, obtained by the hydrothermal process, after surface modification with 0.05 mol% of Pt, exhibited three-times higher photocatalytic activity. It could result from better charge carriers' separation and decreasing the electron-hole recombination rate,

caused by both titanium defects and plasmon resonance properties of Pt. From the analysis of Mott–Schottky plot, the location of flat band energy (E_{fb}) for bare TiO_2 and Pt modified d-TiO_2 was determined. Modification of TiO_2 resulted in the shift of the valence band and conduction band, as shown in Figure 11. The work function of Pt affects the location of the flat band potential of modified TiO_2. The efficient charge carriers separation for defective TiO_2-Pt photocatalyst in comparison with pure TiO_2 enhance the ability of TiO_2 to oxidize adsorbed species [**P3**].

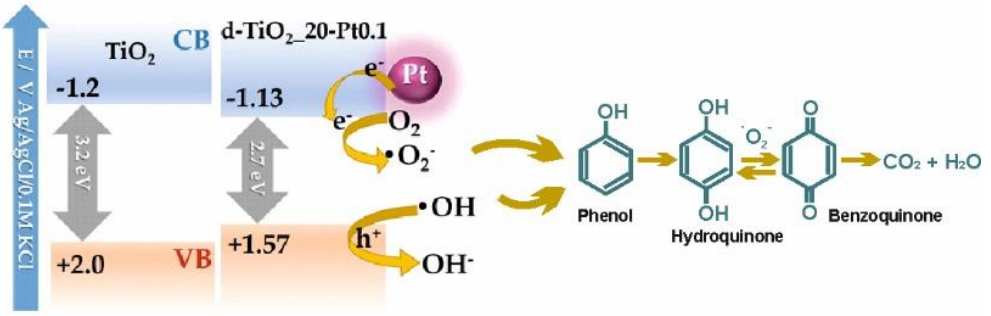

Figure 11. The position of VB and CB of defective TiO_2-Pt photocatalyst in comparison with pure TiO_2 together with the indication of charge transfer within the Schottky junction and schematic mechanism of phenol degradation in the visible light range [**P3**].

3.2. Design, synthesis and characterization of magnetic photocatalysts with core-shell structure.

The reusability of the nanosemiconductor photocatalysts is still a major problem hindering practical application in industrial processes [106]. Compared to other methods, described in Chapter 2, magnetic core and the photocatalytic shell structure is the most promising for maintaining high photocatalytic activity resulting from the nanometric size of the particles and at the same time able to separate after the final purification process effectively. However, the stable structure is one of the most crucial issues regarding magnetic photocatalysts preparation. Two

different methods, ultrasonic-assisted sol-gel, as well as the microemulsion method, were used, in this study [**P4**, **P5**]. In the first one, described in [**P4**], each layer was precipitated separately in an ethanol solution. The homogeneity and the expected structure formation facilitation were provided by ultrasonication process. As a magnetic core, commercially available Fe_3O_4, with nominate particles diameter of about 50 nm (Sigma Aldrich) with a high saturation magnetization (90 Am^2/kg) were used. Self-prepared TBT and TIP – from titanium n-butoxide and titanium isopropoxide hydrolysis, respectively, were used as TiO_2 shell. Between magnetic and photocatalytic phases, an inert silica layer was introduced to avoid iron photoleaching. The effect of TiO_2 matrix and molar ratio of TiO_2 to Fe_3O_4 on photocatalytic activity and magnetic properties in the degradation of organic compounds was studied in detail [**P4**], and the obtained results are presented in Table 3. Simultaneously, magnetic Fe_3O_4/TiO_2 photocatalysts, without silica interlayer were obtained for physicochemical and photocatalytic properties comparison.

Table 3. Physicochemical and photocatalytic characteristic of Fe_3O_4/TiO_2 and $Fe_3O_4@SiO_2/TiO_2$ obtained by the ultrasonic-assisted sol-gel method [**P4**].

Sample	Fe_3O_4 /TiO_2	Fe_3O_4/ TEOS	BET surface area [m^2/g]	M_s [Am^2/kg]	Degradation rate constant k [$min^{-1}\cdot10^{-2}$]			Eg [eV]
					Phenol	Pyridine	4-Heptanone	
Fe_3O_4/TiO_2_1	1:1	-	16	18.2	1.01	0.18	1.36	1.8
Fe_3O_4/TiO_2_2	1:2	-	37	14.8	1.34	0.64	1.21	1.8
Fe_3O_4/TiO_2_3	1:4	-	79	7.5	3.02	0.26	2.10	1.9
Fe_3O_4/TiO_2_4	2:1	-	15	42.5	0.85	0.15	0.46	1.7
$Fe_3O_4@SiO_2/TiO_2$_5	1:2	1:2	210	20.2	0.68	0.04	0.69	1.8
$Fe_3O_4@SiO_2/TiO_2$_6	1:2	1:8	297	15.3	0.77	0.18	0.72	1.8
$Fe_3O_4@SiO_2/TiO_2$_7	1:2	1:16	269	10.0	0.43	0.03	0.83	1.7

The specific surface area of magnetic photocatalysts was mainly affected by TiO_2 particles and SiO_2 introduced into the structure of the nanocomposites. The magnetic properties resulted from the magnetic phase content in the nanocomposite structure. The highest value of saturation magnetization (~42.5 emu/g) was observed for Fe_3O_4/TiO_2_4 with the mass ratio of Fe_3O_4 to TiO_2 equal 2:1. The introduction of the SiO_2 layer between Fe_3O_4 and TiO_2 resulted in the reduction of saturation magnetization (M_s) from about 20 emu/g to 10 emu/g. At the same time, the best

photocatalytic activity in reaction of phenol and 4-heptanone degradation revealed samples with the highest proportion of TiO_2 to Fe_3O_4. Furthermore, based on the obtained physicochemical characteristics and photocatalytic activity results, the most suitable parameters corresponding to the amount of Fe_3O_4 to TiO_2 and molar ratio of TEOS to Fe_3O_4 were selected. As presented in Table 4, the highest efficiency of organic pollutants degradation was noticed for magnetic photocatalysts obtained by deposition of TiO_2 P25 on a magnetic core, which was applied in the further study [**P7**].

Table 4. Characteristic of Fe_3O_4@SiO_2/TiO_2 nanocomposites. The effect of TiO_2 matrix [**P4**].

Sample label	Fe_3O_4/ TiO_2	TEOS/ Fe_3O_4	BET surface area [m^2/g]	Degradation constant rate [min^{-1}]·10^{-2}			Eg [eV]
				Phenol	Pyridine	4-Heptanone	
P25	-	-	55	4.78	0.87	0.77	3.15
Fe_3O_4	-	-	8	0.90	0.22	0.49	0.1
Fe_3O_4@SiO_2/TiO_2_ST01	1:2	8:1	191	2.81	0.60	1.26	2.8
Fe_3O_4@SiO_2/TiO_2_P25	1:2	8:1	124	4.60	0.85	1.98	3.15
Fe_3O_4@SiO_2/TiO_2_TIP	1:2	8:1	163	1.00	0.44	0.78	1.9
Fe_3O_4@SiO_2/TiO_2_TBT	1:2	8:1	297	0.77	0.18	0.72	1.8

The sol-gel ultrasonic-assisted method of synthesis allowed for obtaining the series of magnetic photocatalysts with good photoactivity and determine the most favourable magnetite/silica/titanium(IV) oxide molar ratios. It also provides the core-shell structure formation. However, due to lack of possibility for controlling the preparation process, obtained nanocomposite was not entirely monodisperse, with thinner or thicker layers of SiO_2 and TiO_2 deposited on the magnetic core.

In order to overcome the mentioned problem, in the next attempt, w/o microemulsion method was applied [**P5**]. In this system, the nanodroplets of aqueous phase are dispersed in a continuous oil phase, stabilized by the surfactant and co-surfactant at the w/o interface. Firstly, before starting synthesis, a series of zeta potential analysis for Fe_3O_4, SiO_2 and TiO_2 were performed, and the results are presented in Figure 12. After careful analysis, the formation of two compartments - below and above pH 7 could be noticed. In the alkaline environment, all of the tested materials were characterized by a negative zeta potential, which may indicate

their negatively surface charged. In the acidic environment, only SiO_2 remains negatively charged, while for other components below the isoelectric point (IEP) around pH 6.5-7.5 the surface was positively charged. Therefore, it could be concluded, that the formation of stable core-shell structure between SiO_2 and iron oxides or TiO_2 could take place without additional stabilizing substances, such as surfactants, when the surface charge of two compounds is opposite [**P6**]. In such a system, particles attract to each other creating successive layers. However, at alkaline conditions, the stabilizing agent should be introduced to self-assembly of anionic silicates and cationic surfactant molecules, e.g. cetyltrimethylammonium bromide (CTAB) to form silica shell on a ferrite core. The cationic surfactant also effectively interacts with negatively charged titanium(IV) oxide species in alkaline media, resulting in the core-interlayer-shell structure of nanocomposite [**P5**, **P6**].

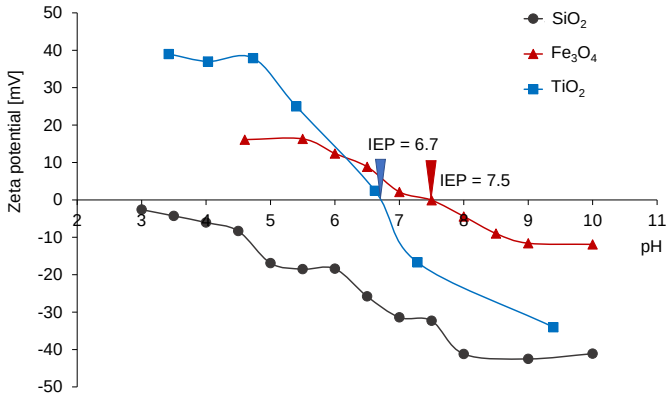

Figure 12. Zeta potential as a function of pH for Fe_3O_4, SiO_2 and TiO_2 nanoparticles [**P5**].

As a confirmation of the presented thesis, two Fe_3O_4@SiO_2/TiO_2 magnetic photocatalysts were synthesized in water/cyclohexane/surfactant microemulsion system, in two pH ranges: at acidic (pH = 5) and alkaline (pH = 10) conditions. As photocatalyst, the commercial P25 (Evonik, a mixture of anatase (73-85 %), rutile (14-17 %) and amorphous phase (0-13 %), with BET surface area 50 m^2/g [107]) was used. Cationic cetyltrimethylammonium bromide (CTAB) and t-

octylphenoxypolyethoxyethanol (TX-100) were used as surfactants in pH = 10 and 5, respectively. Schematic illustration of used synthesis method is presented in Figure 13, while the general characteristic of obtained nanocomposites is given in Table 5.

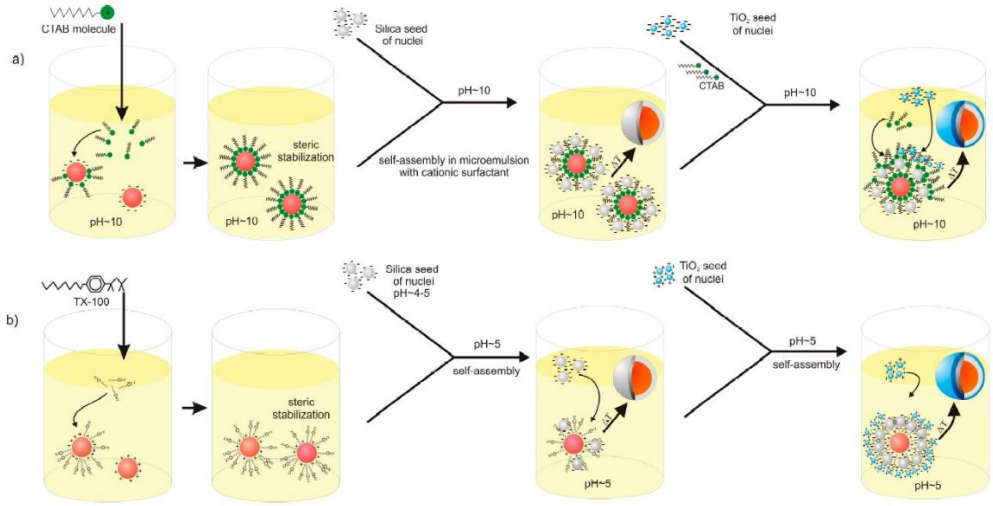

Figure 13. Magnetic photocatalysts preparation procedure scheme at pH 10 (a) and pH 5 (b) in w/o microemulsion [**P5**].

Table 5. General characteristic of obtained $Fe_3O_4@SiO_2/TiO_2$ samples [**P5**].

Sample	Preparation conditions		BET surface area [m^2/g]	M_s [Am^2/kg]	Crystalline Size [nm]			Phenol degradation [%]
	pH	Surfactant			Anatase	Rutile	Magnetite	
$Fe_3O_4@SiO_2/TiO_2$_1	5	TX-100	101	8	19	26	47	86
$Fe_3O_4@SiO_2/TiO_2$_2	10	CTAB	95	7	19	24	45	82

Both prepared magnetic photocatalysts revealed almost identical physicochemical and photocatalytic properties, which proves the effectiveness of the w/o microemulsion method with pH correction. The formation of the desired core-shell structure was also confirmed with the use of the scanning transmission electron microscope (STEM) (see in Figure 14).

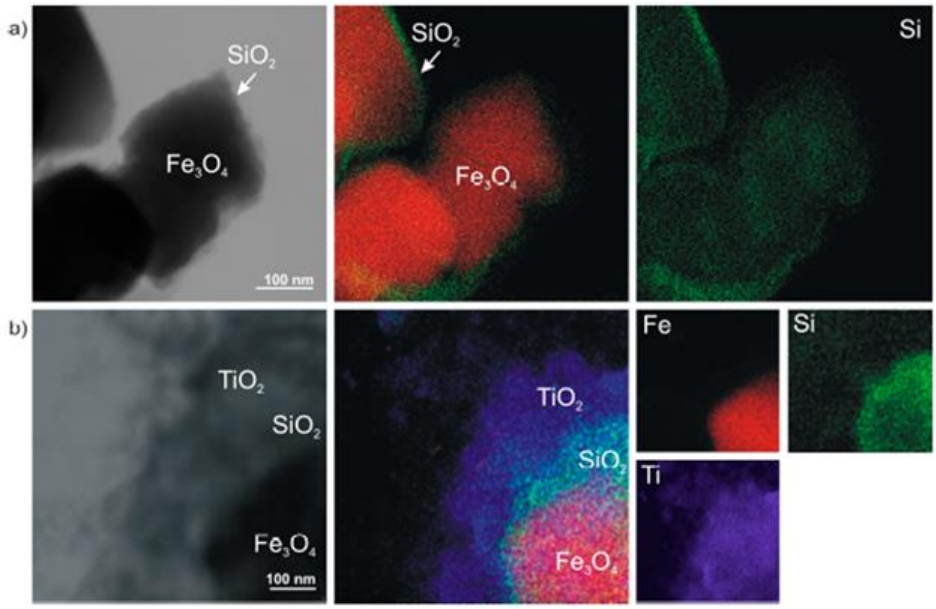

Figure 14. STEM images of Fe_3O_4@SiO_2 (a) and Fe_3O_4@SiO_2/TiO_2 (b) combined with mappings of Ti, Fe and Si elements [**P5**].

The efficiency of phenol degradation of Fe3O_4@SiO_2/TiO_2 was comparable to the commercial nanosized TiO_2 P25 (Evonik, Essen, Germany), which proves effective deposition of TiO_2 P25 onto the magnetic core with the ability to easily separation of photocatalyst from the reaction system. Total organic carbon (TOC) analysis also revealed high mineralization. For Fe_3O_4@SiO_2/TiO_2_1 after 30 min. of irradiation, more than 90% of phenol was decomposed, and mineralization equaled 86%. Due to the undoubted advantage of the w/o microemulsion method over the ultrasonic-assisted sol-gel method, the further synthesis of TiO_2-based magnetic photocatalysts were carried out in w/o microemulsion system. Moreover, the presented methods of synthesis are protected by three Polish patents [**P6**].

3.3 TiO_2-based magnetic photocatalysts active in Vis light range

All TiO_2-based magnetic photocatalysts consist of TiO_2 photoactive shell. In order to increase the utilization of lower-energy light (Vis) provided by the Sun, the proposed in the works [**P1**-**P3**] modified titanium(IV) oxide photocatalysts were deposited on magnetite core resulting in the preparation of TiO_2-based magnetic photocatalysts with core-shell structure, which are characterized by both Vis light activity and magnetic separability.

For the first time, mono- and bimetal- modified titanium(IV) oxide photocatalysts of different polymorphic compositions loaded on magnetic core were obtained and studied in the photooxidation of phenol, acetic acid, and methanol dehydrogenation [**P7**]. The obtained by photodeposition method mono- and bimetallic TiO_2 particles, described in detail in [**P1**] were deposited on Fe_3O_4@SiO_2 nanocomposite using microemulsion method at pH 10. Two different types of Fe_3O_4@SiO_2 magnetic matrices were studied, marked as z2 and z3, differing by the adding order of TEOS and NH_4OH. It was found that both z2 (sample obtained by adding NH_4OH to TEOS), and z3 (sample obtained by addition of TEOS to NH_4OH) are suitable for further modification, with almost the same efficiency towards acetic acid degradation and H_2 generation.

The photoabsorption properties of the prepared magnetic materials were compared with the previously obtained for metal-modified TiO_2 samples. The light absorption edge in the ultraviolet region for nanocomposites was close to that of the pure TiO_2 particles. After surface modification with Pt and Pt/Cu of TiO_2, the light absorption of magnetic composites were extended in the range above 400 nm.

The microscopy analysis confirmed the core-shell structure as well as the presence of platinum on the TiO_2 surface. Magnetite particles with a size of about 50 nm tended to agglomerate, which led to creating about 20 nm SiO_2/TiO_2 shell on the entire agglomerated surface. Pt nanoparticles of the average diameter smaller than 10 nm were uniformly distributed on the TiO_2 surface. Although the same content of platinum was used for modification, the surface content of platinum was almost three times higher in the magnetic bimetallic nanocomposite, which might suggest

that co-deposition of copper could result in the formation of larger nanoparticles compared to Pt-modified TiO_2 nanoparticles.

The photocatalytic activity of magnetic photocatalysts was compared with the photoactivity of TiO_2 matrices. Higher efficiency of acetic acid decomposition was noticed for Fe_3O_4@SiO_2 surface coated with TiO_2 particles, which suggests that the obtained magnetic photocatalysts are more suitable for oxidation processes rather than reduction due to the development of the specific surface area of TiO_2-SiO_2 photocatalytic layer compared to pure TiO_2 particles. The obtained results were further confirmed in the reduction of 4-nitrophenol to 4-aminophenol as well as phenol oxidation reaction. Significantly higher photocatalytic activity in reaction of phenol degradation was observed for magnetic photocatalysts. However, the highest activity in 4-nitrophenol reduction to 4-aminophenol was noticed for TiO_2 FP6 nanoparticles.

Furthermore, in work [**P7**] for the first time for metal-modified TiO_2 matrices embedded on a magnetic core, quantum efficiency was determined in the phenol oxidation reaction under monochromatic irradiation in the range of 320-620 nm. Photocatalyst suspension in phenol solution at a concentration of 20 ppm was placed in a quartz cuvette and irradiated with monochromatic light at seven irradiation wavelengths: 320, 380, 440, 450, 500, 560 and 620 nm. The generation of BQ, as a phenol intermediate, was analyzed using the HPLC system and then calculated to quantum efficiency. The dependence of measured phenol degradation quantum efficiency on the irradiation wavelength is presented in Figure 15.

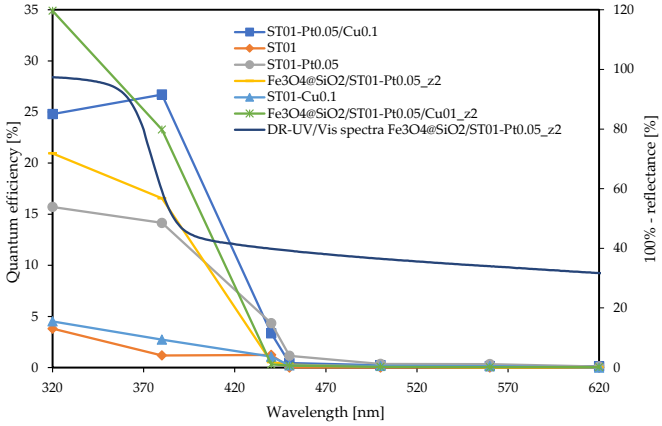

Figure 15. Action spectra of phenol degradation for obtained TiO_2-based photocatalysts in comparison with its DR-UV/Vis spectra [**P7**].

High quantum efficiency in UV light range for magnetic photocatalysts was expected, because of previous research in [**P4**] and [**P5**]. Furthermore, its almost negligible value above 440 nm was also expected. However, in the range of 400-440 nm, designated Fe_3O_4@SiO_2/TiO_2-M nanocomposites revealed higher photocatalytic activity, which confirms the possibility of their use in sunlight-driven photocatalytic processes.

3.4 Application of Fe_3O_4@SiO_2/TiO_2 nanocomposites for degradation of persistent organic pollutants

Persistent organic pollutants (POPs) are organic compounds that are resistant to environmental degradation through chemical, biological, and photolytic processes. Bio-accumulative potential, long-term residuality, high toxicity and not susceptibility to biodegradation are the main factors for classification of organic compounds to POPs [108]. This group primarily includes i.a. pesticides and herbicides, phenols, antibiotics and other pharmaceuticals.

3.4.1. Photodegradation of organic compounds present in flowback water

Flowback water, produced in hydraulic fracturing, due to its high salinity, containing some of the fracking constituents which are toxic, resistant to degradation and cancerogenic (presented in Table 6) could also be included in the group of persistent organic pollutants.

For a complete treatment of flowback water, a combination of chemical, biological and physical method is necessary. Photodegradation process in the presence of Fe_3O_4@SiO_2/TiO_2 nanocomposite was performed to remove the POPs, and in detail described in [**P4**]. Firstly, three model pollutants: phenol, pyridine and 4-heptanone, presented in flowback water, were photodegraded separately, to determine the composition characterized by magnetic separation ability and high photocatalytic activity. Obtained results are presented in Figure 16.

Table 6. Organic contaminants in flowback water, determined with the use of gas chromatography with mass spectrometry (GC-MS) analysis [**P4**].

Organic compound	Quantity in flowback water [%]
1,3,5-trimethylbenzene	1
Toluene	0.3
Butyl glycol	0.2
Decahydronaphthalene	4
1-bromo-3-methylcyclohexane	3
Ethyl *tert*-butyl ether	1
Pyridine	44
2,3-dimethyl-decahydronaphthalene	2.5
Benzaldehyde	0.3
4-heptanone	4
Phenol	1.1
1,2-diisopropenyl-cyclobutane	6.9
1,2-dimethyldiazene-1-oxide	28.7
Oxalic acid, 6-ethyloct-3-yl isobutyl ester	3

Model pollutants photodegradation confirmed susceptibility of flowback water individual components to photocatalytic decomposition. As a next attempt, a real sample of flowback water photodegradation in the presence of Fe_3O_4@SiO_2/TiO_2, where Fe_3O_4/TiO_2 molar ratio was 1:2 and TEOS/Fe_3O_4 molar ratio: 8:1 was

performed. The sample was preliminarily coagulated and centrifuged in order to eliminate the suspended solid particles. Obtained results, presented as TOC removal, together with major physicochemical characteristic of flowback water is given in Figure 17.

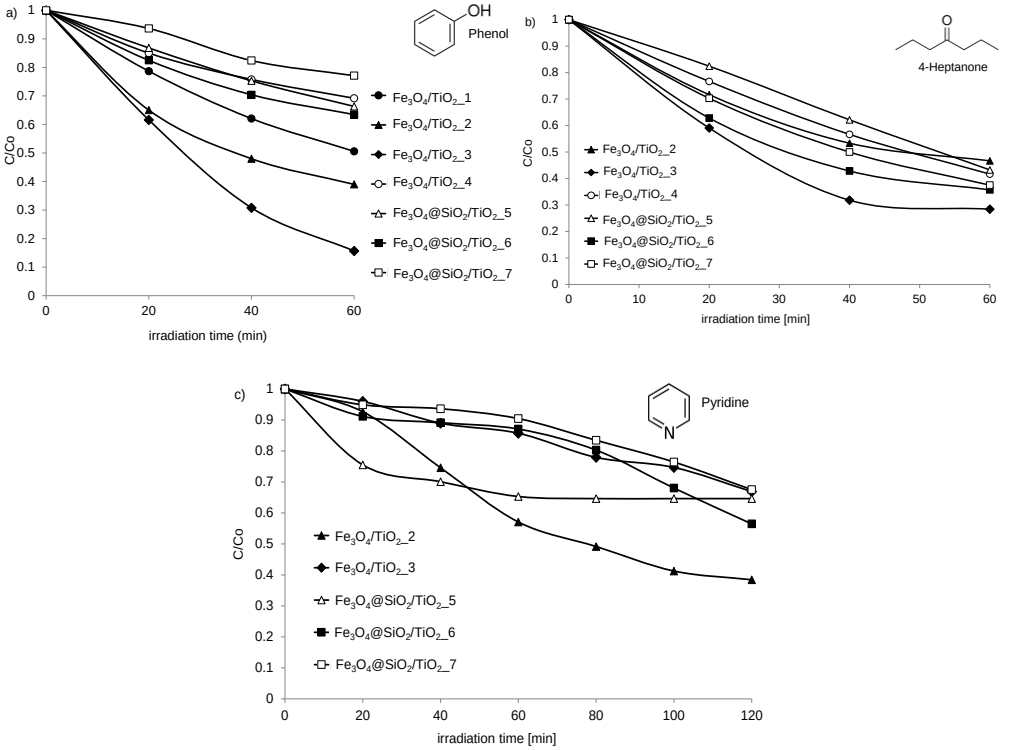

Figure 16. Degradation of phenol (a), 4-heptanone (b) and pyridine (c) with magnetic TiO_2-based photocatalysts under UV-Vis irradiation [**P4**].

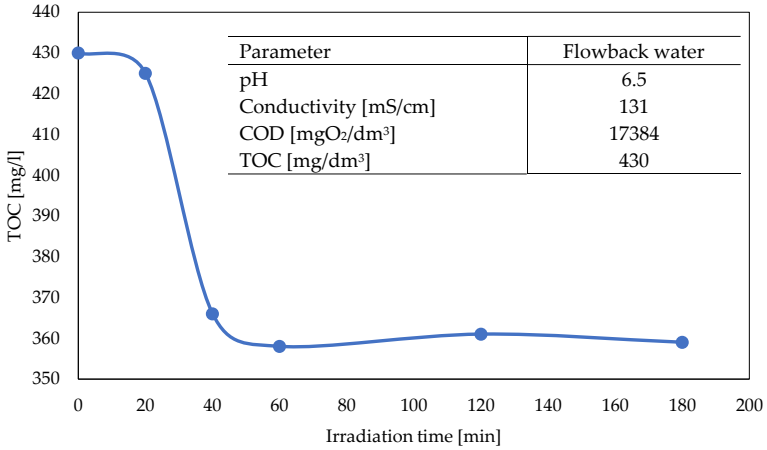

Figure 17. Flowback water photodegradation under UV-Vis irradiation in the presence of Fe_3O_4@SiO_2/TiO_2 nanocomposite, together with flowback water physicochemical parameters [**P4**].

After 180 min of irradiation in UV-Vis light, the reduction of TOC in the flowback real sample was about 15%. Therefore, for degradation efficiency increasing, the photocatalytic process should be combined with the biological treatment method.

3.4.2. Photodegradation of carbamazepine

As the final stage of the presented study, the photocatalytic degradation of selected pharmaceutical – carbamazepine – was investigated. In literature, the combination of phrases "photocatalysis & pharmaceuticals" from one year to another is increasing, as it could be seen in Figure 18. About 20 % of those works apply to photodegradation of carbamazepine (CBZ), antiepileptic and psychotropic drug, the most often pharmaceutical detected in wastewaters and, for this reason, chosen as possible anthropogenic water system marker [109 – 111]. CBZ is also insusceptible to biological degradation, which makes photocatalysis one of few suitable methods for its removal from wastewaters.

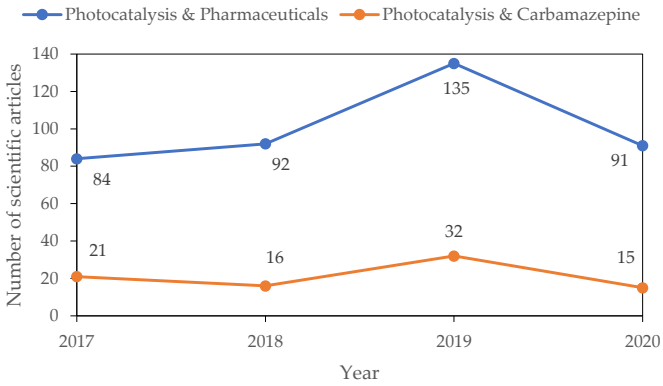

Figure 18. The number of scientific articles in the Scopus database for the keywords "photocatalysis & pharmaceuticals" and "photocatalysis & carbamazepine". Stats for the year 2020 were up to July.

Extensive research is devoted mainly to TiO_2 photocatalytic oxidation. However, there are still no complementary works on CBZ degradation showing the influence of simultaneous use of various parameters (e.g., photocatalyst loading, irradiation flux, and pH) on contamination deterioration.

The first attempt of carbamazepine photodegradation in the presence of TiO_2-based magnetic photocatalysts was described in **P5**. It was found that Fe_3O_4@SiO_2/TiO_2 core-shell photocatalyst, where TiO_2 was commercially available P25, as well as other core-shell composites with different magnetic iron oxides as cores, i.e. $CoFe_2O_4$ and $BaFe_{12}O_{19}$, are suitable for almost complete CBZ mineralization. In the last part of PhD dissertation as the photocatalyst, Fe_3O_4@SiO_2/d-TiO_2-Pt was used, with Ti vacancies in TiO_2 structure, which physicochemical and photocatalytic properties were in detail discussed in [**P2**] and [**P3**].

In order to determine the optimum environment for the most effective CBZ photodegradation, six different parameters: photocatalyst loading, pH, aeration, temperature, irradiation intensity (flux) and addition of auxiliary oxidant (30% H_2O_2 solution) were studied, which were varied on 4 or 5 different levels, based on the

central composite design (CCD). Detailed information about factors and their levels are presented in Table 7. Series of 79 measurements of carbamazepine photodegradation were performed with 3 different processes in factor 0 point, for estimating the experimental error. Additionally, a series of dark and photolysis reactions in order to verify CBZ stability and adsorption possibility.

Table 7. Investigated factors and their levels.

Factor	Coded levels and their values				
	-a	-1	0	1	a
photocatalyst loading [g/dm^3]	0.25	0.5	1	1.5	2
temperature [°C]	10	20	25	30	40
flux [mW/cm^2]	30	35	45	60	70
pH	3	5	7	9	11
aeration [dm^3/h]	0	0	3	4	7
H_2O_2 addition [mg/dm^3]	0	0	26.5	46.6	63.6

Commonly in the literature, the effect of various parameters on carbamazepine degradation efficiency is considered separately for each parameter [112, 113]. In the present study, all six factors were tested at the same time, allowing not only to determine the CBZ photodegradation efficiency, but also interactions between factors itself. The most significant impact on both CBZ removal as well as total organic carbon (TOC) mineralization was revealed by the combination of pH together with H_2O_2 addition, as presented in Pareto charts (Figure 18 a-b).

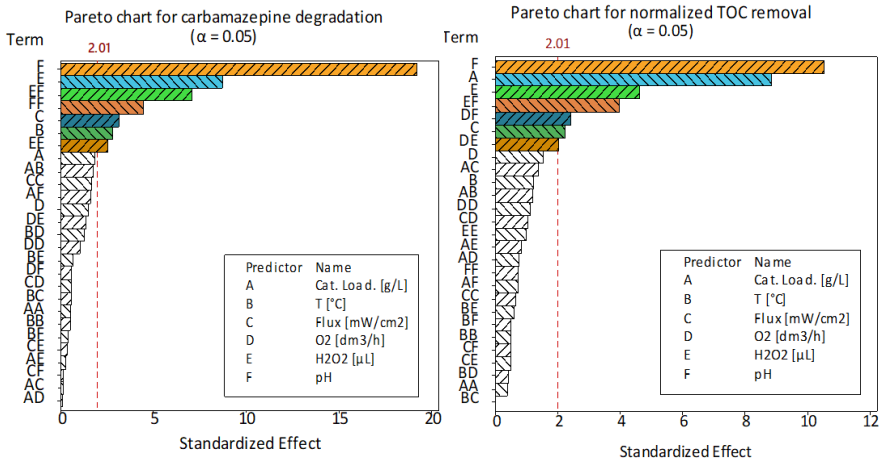

Figure 18. Calculated effect of included terms on carbamazepine removal (a) and TOC mineralization (b).

Since it was expected that pH should affect TiO_2 reactivity and its interactions with the organic species [114 – 116], further analyses were performed inside different pH regions. The summary of the obtained models is presented in Table 8. The terms included higher in the table are more significant and sign next to them indicate their effect on the response when shifted toward higher levels ((+) means a positive impact on CBZ and TOC removal, (-) – negative).

Decreasing pH from 7 resulted in more factors affecting both CBZ degradation and mineralization. Also, H_2O_2 addition became more significant than in neutral or alkaline conditions. Interestingly, the constant trend to inhibit TOC removal when increasing photocatalyst content in the system was observed, which was present throughout the whole pH range, while the negligible effect was noticed for removal of CBZ itself. It is also noticeable that flux intensity or its interactions became more significant in the alkaline conditions, while they are not present or relatively less important in pH ≤ 7.

The intermediate compounds identified during the photodegradation process are acridine, acridone, hydroxy-carbamazepine, 10,11-dihydro-dihydroxy-carbamazepine and acridone-hydroxide using HPLC/DAD and LC-TOFMS systems.

The hydroxy-carbamazepine (OH-CBZ) and acridine (AC) were detected in most of the analysed samples. Meanwhile, an acridone (ACD) was found as a by-product of the photocatalytic reaction proceeded at alkaline conditions.

Table 8. The comparison of terms' significance obtained in different pH regions for CBZ and TOC removal.

Response	Effect	Whole pH range	pH < 7	pH = 7	pH > 7
CBZ removal	Significant	pH (-) H_2O_2 (+) pH·H_2O_2 (-) pH^2 (+) Flux (+) Temp. (+) $H_2O_2^2$ (+)	H_2O_2 (+) Cat.load (-) Flux (+) Temp (+) Flux·O_2 (-) Cat.load·Temp (+)	Temp (+) $H_2O_2^2$ (+)	Flux (+) O_2·H_2O_2 (+)
	Possible	Cat.load (-) Cat.load·Temp (+)	Cat.load·O_2 (-)	-	Temp·O_2 (-)
TOC removal	Significant	pH (-) Cat.load (-) H_2O_2 (+) pH·H_2O_2 (-) O_2·pH (-) Flux (+) O_2·H_2O_2 (-)	H_2O_2 (+) Cat.load (-) O_2 (+) O_2·H_2O_2 (-)	Cat.load (-) H_2O_2 (+)	Cat.load (-) Cat.load·Temp (+) Flux·H_2O_2 (-)
	Possible	-	Temp·H_2O_2 (+) Flux (+)	Temp. (+)	-

Furthermore, to better understand the mechanism of carbamazepine photodegradation, the photocatalytic activity analyses were performed in the presence of scavengers. The holes (h^+), hydroxyl radicals ($^{\cdot}OH$), superoxide radical anion ($^{\cdot}O_2^-$) are the probable reactive oxygen species taking part in the photodegradation of carbamazepine. Results of the photocatalytic degradation in the presence of e–, h+, $^{\cdot}O_2^-$ and $^{\cdot}OH$ scavengers showed that both e^- and $^{\cdot}O_2^-$ play an important role in the photodegradation process. However, the efficiency of carbamazepine degradation was not influenced by the presence of oxalic acid used as h+ scavenger. Therefore, it can be assumed that h^+ had little effect on photodegradation, as a result of their trapping inside the defective structure of TiO_2.

It is in agreement with the study made by Morgan and Watson, who have predicted hole trapping on the O sites surrounding the V_{Ti} defect [117].

The proposed photodegradation pathway is presented in Figure 19. The transformation of carbamazepine is initiated by reactive oxygen species attack (mainly $^{\bullet}O_2^-$) leading to epoxide and hydroxy-carbamazepine intermediates. Acridine formation was the limiting step of photodegradation of carbamazepine process in a wide spectrum of pH. Likewise, acridone formation was observed in alkaline conditions. Further decomposition of acridone and acridine leads to forming of simple aromatic and chain compounds and, finally, to carbon(IV) oxide and water.

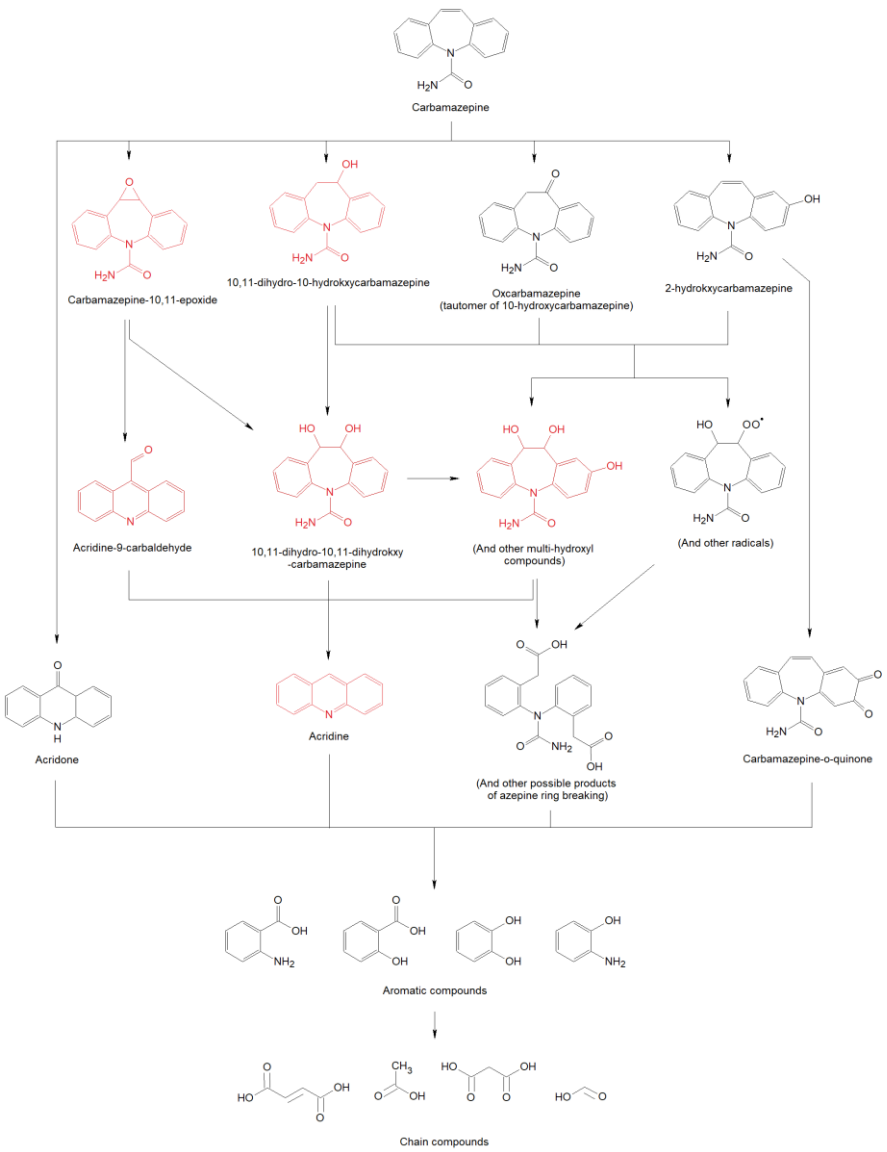

Figure 19. Scheme of possible carbamazepine degradation pathways through photooxidation process'. Confirmed intermediates are marked in red.

Chapter 4

Conclusions

The results obtained during the research included in the scope of the PhD thesis refer to the preparation of novel photocatalytic materials that are active in UV and visible light and possess an important property of separation in the magnetic field that can be used for oxidizing persistent organic pollutants.

The novelty of the presented dissertation could be summarized in the following statements:

a. Regarding the preparation of TiO_2 photocatalysts with titanium defects by a simple hydrothermal reaction in the oxidative environment:
   - Demonstrating the effect of oxidant type (HNO_3, HIO_3, H_2O_2) and its concentration in the reaction environment on titanium defects formation, physicochemical properties and photocatalytic activity in Vis light.
   - Demonstrating the effect of calcination temperature on photocatalytic activity and anatase to rutile temperature transition.

b. Regarding the preparation of TiO_2 modified with mono- and bimetal Pt/Cu nanoparticles:
   - Determining the effects of the type and size of the TiO_2 particles on the physicochemical properties and activity of photocatalysts modified with mono- and bimetallic particles in oxidation and reduction reactions.
   - Demonstrating the effect of metal type and amount on the physicochemical properties and photocatalytic activity.
   - Demonstrating the significance of superoxide anion radicals and electrons in the mechanism of phenol degradation.

c. Regarding the synthesis of TiO_2-based magnetic photocatalysts with core-shell structure:
   - Design of universal w/o microemulsion method for core-shell photocatalysts' synthesis based on zeta potential measurements and surface charge functionalization.

- Demonstrating the effects of the TiO_2 type and TiO_2: SiO_2: Fe_3O_4 molar ratio on the photocatalytic and magnetic properties of the resulting photocatalysts.

d. Regarding the preparation of TiO_2-based magnetic photocatalysts with the general formula Fe_3O_4@SiO_2/TiO_2-M, where M is Pt, Cu or Pt/Cu nanoparticles:
   - Obtained nanocomposites are characterized by both magnetic separability and visible light activity.
   - The obtained magnetic photocatalysts did not negatively influence the photocatalytic performance, as reported for immobilized photocatalysts.
   - Demonstrating the significance of superoxide anion radicals and electrons in the mechanism of phenol degradation.
   - Demonstrating the effect of irradiation wavelength on the efficiency of phenol degradation – action spectrum analysis.
   - Demonstrating the stability of magnetic photocatalysts and their reusability.

e. Regarding the degradation of persistent organic pollutants:
   - Demonstrating the possibility of using the photocatalytic method to degrade organic compounds present in flowback water, that are not susceptible to biological degradation.
   - Demonstrating that the obtained magnetic photocatalysts did not negatively influence the photocatalytic performance, as reported for immobilized photocatalysts.
   - Optimization of carbamazepine photodegradation in the presence of magnetic Fe_3O_4@SiO_2/TiO_2-Pt nanocomposite with a simultaneous designation of a quadratic model with 2-factor interactions of 6 parameters (pH, temperature, flux intensity, catalyst loading, aeration and H_2O_2 addition) varied on 4-5 levels.

The proposed w/o microemulsion synthesis method, based on the difference in the surface charges of individual substrates, leads to the formation of the core-shell structure, with magnetic core, photocatalytic shell and inert interlayer. Creation of assumed structure has been confirmed by several studies, including STEM, EDX, XPS analysis and the study of magnetic properties. Stability of obtained structures was tested during a series of successive cycles of phenol photodegradation. Fe_3O_4@SiO_2/TiO_2 magnetic nanocomposites were characterized by an almost

invariable photocatalytic activity, which may indicate the possibility of their use after separation in the magnetic field.

By applying the photodeposition method for the surface modification of TiO_2, and afterwards the w/o microemulsion method, it was possible to successfully obtain the magnetic nanocomposites Fe_3O_4@SiO_2/TiO_2-M, where M is Pt, Cu or a bimetallic Pt/Cu system. Their application has a positive effect on photocatalytic activity increasing in both oxidation (methanol dehydrogenation, phenol degradation) and reduction (acetic acid to CO_2 conversion, nitrophenol/aminophenol conversion) reactions. Furthermore, the quantum efficiency analysis showed a higher photocatalytic potential of bimetallic nanocomposites comparing to monometallic at wavelengths $\lambda < 450$ nm, which proves the positive correlation between platinum and copper on the TiO_2 surface.

All presented results were published in JCR-listed journals from the chemistry discipline. Three patents on the preparation method of a multilayer magnetic could provide a basis for future commercialization of the results.

Chapter 5

Publications

1. Mono- and bimetallic (Pt/Cu) titanium(IV) oxide photocatalysts. Physicochemical and photocatalytic data of magnetic nanocomposites' shell

Zuzanna Bielan, Ewa Kowalska, Szymon Dudziak, Kunlei Wang, Bunsho Ohtani, Anna Zielińska-Jurek

Data in Brief 31 (2020) 105814

DOI: 10.1016/j.dib.2020.105814

P1

Data in Brief 31 (2020) 105814

Contents lists available at ScienceDirect

Data in Brief

journal homepage: www.elsevier.com/locate/dib

Data Article

Mono- and bimetallic (Pt/Cu) titanium(IV) oxide photocatalysts. Physicochemical and photocatalytic data of magnetic nanocomposites' shell

Zuzanna Bielan[1,2,*], Ewa Kowalska[2], Szymon Dudziak[1], Kunlei Wang[2], Bunsho Ohtani[2], Anna Zielińska-Jurek[1]

[1] Department of Process Engineering and Chemical Technology, Chemical Faculty, Gdansk University of Technology, 80-233 Gdansk, Poland
[2] Institute for Catalysis (ICAT), Hokkaido University, N21, W10, 001-0021 Sapporo, Japan

ARTICLE INFO

Article history:
Received 17 May 2020
Accepted 28 May 2020
Available online 4 June 2020

Keywords:
bimetallic nanoparticles
copper
core-shell structure
magnetic photocatalysts
platinum
surface modification
titania

ABSTRACT

Surface modification of titania with noble and semi-noble metals resulted in significant enhancement of photocatalytic activity. Presented data, showing the photocatalytic properties of TiO_2-M (where M is Pt and/or Cu) photocatalysts were further used as Fe_3O_4@SiO_2/TiO_2-M magnetic nanocomposites shells in "Mono- and bimetallic (Pt/Cu) titanium(IV) oxide core-shell photocatalysts with Vis light activity and magnetic separability" [1]. Platinum and copper were photodeposited on four different titania matrices (commercial and self-obtained ones). The prepared photocatalysts were characterized by X-ray diffraction (XRD) analysis, specific surface area measurements using the Brunauer-Emmet-Teller (BET) isotherm, diffuse reflectance spectroscopy (DR-UV/Vis) analysis as well as scanning transmission electron microscopy (STEM) analysis. Photocatalytic properties were investigated in three different reactions: H_2 generation, acetic acid oxidation to CO_2, and phenol degradation.

* Corresponding author(s):
E-mail addresses: bielan_chan@onet.eu, zuzbiela@student.pg.edu.pl (Z. Bielan).

https://doi.org/10.1016/j.dib.2020.105814

Specifications table

Subject	Catalysis
Specific subject area	Photocatalytic pollutants degradation
Type of data	Tables Figures
How data were acquired	X-ray diffractometer (Rigaku Intelligent X-ray diffraction system SmartLab); specific surface analyser with BET method (Micromeritics Gemini V); diffuse reflectance spectrometer (JASCO V-670) equipped with a PIN-757 integrating sphere; high-performance liquid chromatograph (Shimadzu LC-20AD); gas chromatograph (Shimadzu GC-8A); total organic carbon analyser (Shimadzu TOC-L)
Data format	Raw Analyzed
Parameters for data collection	XRD: 2θ range of 5-80°, scan speed $1°\cdot min^{-1}$, scan step 0.01° DR-UV/Vis: 200-800 nm scan BET: temperature of 77 K (liquid nitrogen temperature) Photocatalytic tests parameters are presented in detail in Experimental Design, Materials, and Methods section.
Description of data collection	TiO_2-M photocatalysts samples where obtained using photodeposition method from metal precursors in methanol: water (vol% 50:50) mixture. Irradiation was carried out for 1 hour using mercury lamp. Obtained TiO_2-M precipitate was dried at 80°C and calcined at 400°C for 2 hours. Detailed description of conducted researches is presented in Experimental Design, Materials, and Methods section.
Data source location	Department of Process Engineering and Chemical Technology, Chemical Faculty, Gdansk University of Technology, Gdansk, Poland Institute for Catalysis (ICAT), Hokkaido University, Sapporo, Japan
Data accessibility	With the article
Related research article	Z. Bielan, E. Kowalska, S. Dudziak, K. Wang, B. Ohtani, A. Zielińska-Jurek; Mono- and bimetallic (Pt/Cu) titanium(IV) oxide core-shell photocatalysts with UV/Vis light activity and magnetic separability; Catalysis Today; In Press [1]

Value of the data

- Physicochemical and photocatalytic characterization of mono- and bimetallic TiO_2 matrices complement the analysis of magnetic Fe_3O_4@SiO_2/TiO_2-M nanocomposites.
- Data presents new information in the field of titania modification with noble and semi-noble metals.
- A multitude of obtained samples allows the designation of an overall trend of photocatalytic activity for different TiO_2 matrices.

1. Data Description

1.1. XRD analysis (Fig. 1 a-b; Tables 1-3)

Exemplary XRD patterns for TiO_2-M samples are presented in Fig. 1 a-b with detailed phase composition and crystallite sizes for all samples being listed in Tables 1-3.

All obtained TiO_2-based photocatalysts consisted of mainly anatase polymorph, and two of them were composed of only this phase (ST01 and ST41), whereas FP6 and TBT samples also contained rutile (21.4%) and brookite (37.0%), respectively. The crystallite sizes of anatase and brookite in TBT samples, based on the main peaks, reached approximately 8 nm (brookite) and 8.5 nm (anatase). In the case of commercial samples, the sizes of the crystallites vary from 5 nm to 55 nm. It was found that the crystallite size of titania increased slightly after modification with metals. For example, from 7.7 nm to 16.6 nm for ST01 modified with 0.05 mol% of Pt, which

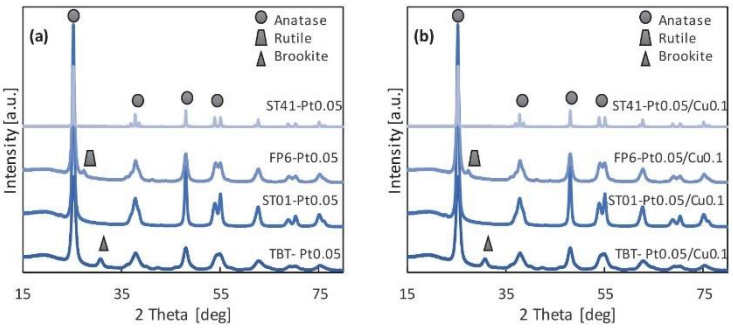

Fig. 1. XRD patterns for monometal (a) and bimetal (b) TiO_2-M

Table 1
Phase percentage and crystallite size for no-metal TiO_2 photocatalysts

		Anatase [nm]	Anatase [%]	Rutile [nm]	Rutile [%]	Brookite [nm]	Brookite [%]
TiO_2	TBT	8.17 ± 0.04	63 ± 6	-	-	7.69 ± 0.19	37 ± 4
	ST01	7.66 ± 0.05	100.0 ± 0.4	-	-	-	-
	FP6	11.32 ± 0.07	78.6 ± 0.3	4.87 ± 0.19	21.4 ± 0.9	-	-
	ST41	45.8 ± 0.2	100.0 ± 0.2	-	-	-	-

Table 2
Phase percentage and crystallite size for monometallic TiO_2-M photocatalysts

		Anatase [nm]	Anatase [%]	Rutile [nm]	Rutile [%]	Brookite [nm]	Brookite [%]
TBT	Pt0.05	9.0 ± 1.3	64.50 ± 0.19	-	-	8.11 ± 0.06	35.5 ± 0.4
	Pt0.1	8.681 ± 0.015	67 ± 5	-	-	8.01 ± 0.05	33 ± 2
	Cu0.1	8.523 ± 0.013	62 ± 18	-	-	8.00 ± 0.06	38 ± 28
	Cu0.5	8.481 ± 0.012	68.2 ± 0.3	-	-	7.81 ± 0.06	31.8 ± 0.4
ST01	Pt0.05	16.58 ± 0.04	100 ± 5	-	-	-	-
	Pt0.1	16.44 ± 0.09	100 ± 1	-	-	-	-
	Cu0.1	16.01 ± 0.05	100 ± 2	-	-	-	-
	Cu0.5	15.25 ± 0.04	100 ± 8	-	-	-	-
FP6	Pt0.05	12.55 ± 0.02	96.2 ± 0.4	6.76 ± 0.12	3.8 ± 0.3	-	-
	Pt0.1	12.58 ± 0.02	92.5 ± 0.6	4.33 ± 0.07	7.5 ± 1.3	-	-
	Cu0.1	12.37 ± 0.02	97.1 ± 1.9	14.4 ± 0.3	2.9 ± 0.6	-	-
	Cu0.5	12.12 ± 0.02	96.8 ± 0.6	13.9 ± 0.4	3.2 ± 0.6	-	-
ST41	Pt0.05	54.0 ± 0.8	100.0 ± 0.2	-	-	-	-
	Pt0.1	41.42 ± 0.19	100.0 ± 0.2	-	-	-	-
	Cu0.1	45.5 ± 0.2	100.0 ± 0.2	-	-	-	-
	Cu0.5	40.2 ± 0.2	100.0 ± 0.2	-	-	-	-

was caused by post-calcination. For FP6-M samples, anatase, as the dominant polymorphic form, ranges from 93 to 97% of the TiO_2 crystalline phase. However, the pattern also showed peaks from rutile, mainly at 27.3 degree (110) (ICDD card No. 9004142). The size of rutile crystallites ranges from ca. 5 nm for pure FP6 to 14 nm for FP6-Cu0.1, whereas the anatase crystallites for all samples had a similar size of ca. 12 nm (11 nm for pure and 12.5 nm for FP6-Cu0.1). Compared to other TiO_2 matrices, ST41 photocatalysts are characterized by the largest crystallites of ca. 45 nm. In the case of bimetallic TiO_2 photocatalysts, similar crystalline properties to monometallic photocatalysts were obtained, as shown in Tables 2 and 3. It should be pointed out that the position of the peaks did not shift after titania modification with metals [2]. The presence of

Table 3
Phase percentage and crystallite size for bimetallic TiO_2-M photocatalysts.

		Anatase [nm]	Anatase [%]	Rutile [nm]	Rutile [%]	Brookite [nm]	Brookite [%]
TBT	Pt0.05/Cu0.1	10.48 ± 0.05	65 ± 5	-	-	8.0 ± 0.2	35 ± 2
	Pt0.1/Cu0.1	8.81 ± 0.04	68 ± 7	-	-	8.01 ± 0.17	32 ± 4
	Pt0.05/Cu0.5	10.29 ± 0.05	68 ± 2	-	-	8.0 ± 0.2	32 ± 3
ST01	Pt0.05/Cu0.1	14.38 ± 0.06	100.0 ± 0.3	-	-	-	-
	Pt0.1/Cu0.1	14.69 ± 0.06	100.0 ± 0.3	-	-	-	-
	Pt0.05/Cu0.5	13.97 ± 0.03	100.0 ± 0.3	-	-	-	-
FP6	Pt0.05/Cu0.1	11.35 ± 0.06	94.8 ± 0.3	10.0 ± 0.4	5.20 ± 0.19	-	-
	Pt0.1/Cu0.1	11.45 ± 0.06	89.1 ± 0.3	6.5 ± 0.4	10.9 ± 0.5	-	-
	Pt0.05/Cu0.5	11.41 ± 0.06	82.2 ± 0.4	4.4 ± 0.1	17.8 ± 1.2	-	-
ST41	Pt0.05/Cu0.1	46.6 ± 0.2	100.0 ± 0.2	-	-	-	-
	Pt0.1/Cu0.1	47.0 ± 0.2	100.0 ± 0.2	-	-	-	-
	Pt0.05/Cu0.5	47.5 ± 0.2	100.0 ± 0.2	-	-	-	-

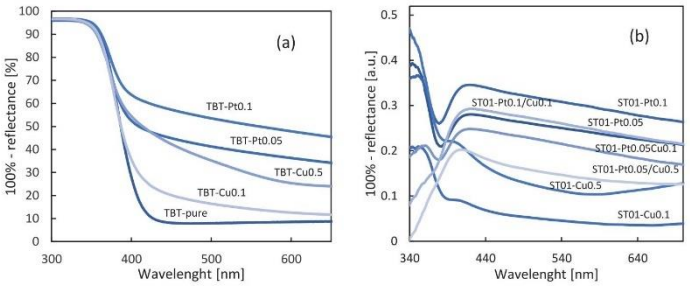

Fig. 2. Exemplary DR-UV/Vis spectra of nanocomposites taken with $BaSO_4$ (a) and pure ST01 (b) as reference.

platinum and copper was not confirmed by XRD analysis (no peaks for platinum or copper) due to their low content (0.05-0.5 mol%) and nanometric size.

1.2. DR-UV/Vis spectroscopy (Fig. 2 a-b)

Photoabsorption properties of no- and metal-modified TiO_2 samples were studied by diffuse reflectance spectroscopy, and exemplary data are shown in Fig. 2 a-b.

All samples absorb UV light due to titania presence with an absorption edge at ca. 400 nm, with no difference among each polymorphic phase. The presence of noble metals resulted in the appearance of Vis absorption, as clearly shown for TBT samples in Fig. 2 a. An increase in absorption associated with the surface modification with metals is proportional to the amount of the specific type of metal used, with platinum modification resulting in a more significant increase in absorption than modification with an analogous amount of copper. Besides, for TiO_2-Cu photocatalysts, especially when 0.5 mol% of copper was used, the spectra rises above 600 nm what is characteristic for the presence of Cu^{2+} [3]. DR-UV/Vis plots for bimetallic TiO_2 photocatalysts are analogous to the spectra for monometallic TiO_2.

The presence of LSPR peaks for Pt and Cu was confirmed based on DR-UV/Vis spectra measured for ST01 mono- and bimetallic photocatalysts with pure ST01 as a reference as presented in Fig. 2 b. Surface plasmon resonance of platinum is visible through an increase of the absorption in the range of about 420-440 nm [4]. Increased absorption intensity from 400 to 450 nm corresponds to an electron transfer between Cu(II) and valence band of titanium(IV) oxide or

Table 4
BET surface area for no- and monometallic TiO_2 photocalysts

TiO_2 matrix	BET surface area [$m^2 \cdot g^{-1}$]				
	No-metal	Pt0.05	Pt0.1	Cu0.1	Cu0.5
TBT	118	113	112	118	100
ST01	181	113	106	113	116
FP6	104	86	81	86	88
ST41	10	10	10	10	10

Table 5
BET surface area measurements for bimetallic TiO_2 photocalysts

TiO_2 matrix	BET surface area [$m^2 \cdot g^{-1}$]		
	Pt0.05/Cu0.1	Pt0.1/Cu0.1	Pt0.05/Cu0.5
TBT	107	112	108
ST01	116	107	117
FP6	86	86	90
ST41	10	11	11

due to the presence of Cu(I). The lack of evident peak at 500-580 absorption region (typical for LSPR of Cu) indicated that zero-valent copper (photodeposited on titania surface) was easily oxidized to other forms of copper [5], which is typical for Cu-modified titania kept under ambient conditions [6].

For all obtained TiO_2-M photocatalysts, bandgap, calculated from Kubelka-Munk transformation, was similar to the unmodified TiO_2 (ca. 3.2 eV).

1.3. BET surface area analysis (Tables 4-5)

The specific surface area (BET) for the obtained no-, mono- and bimetallic TiO_2 photocatalysts are presented in Tables 4 and 5. The specific surface areas of bare (10 $m^2 \cdot g^{-1}$ for ST41, 104 $m^2 \cdot g^{-1}$ for FP6, 118 $m^2 \cdot g^{-1}$ for TBT and 181 $m^2 \cdot g^{-1}$ for ST01) and metal-modified titania samples correlate well with crystallite sizes of anatase (approximately 46, 11, 8 and 7.5 nm, respectively). It was found that the metal presence caused a slight decrease in BET (Table 4) for ST01 and FP6 samples.

1.4. STEM analysis (Fig. 3)

For confirmation of metal presence, STEM analysis was performed. As exemplary photocatalyst, ST01-Pt0.05 was selected. The obtained images made in the dark mode are presented in Fig. 3. Platinum nanoparticles, which diameter is up to 20 nm, are marked with red squares.

1.5. Photocatalytic activity of mono- and bimetallic TiO_2 (Fig. 4-8)

Before evaluation of the photocatalytic activity of obtained nanocomposites [1], series of pure TiO_2 matrices and mono- and bimetallic TiO_2-M photocatalysts were tested as to their reference. Obtained results, presented as H_2 and CO_2 evolution, are shown in Fig. 4 a-d with respect on the TiO_2 matrix as well as the amount of deposited platinum and copped.

Platinum nanoparticles significantly increase photocatalytic activity for both reaction systems, with the highest difference observed between unmodified and 0.05% Pt addition, due to the formation of Schottky barriers hindering the charge carriers' recombination. The ST01 samples

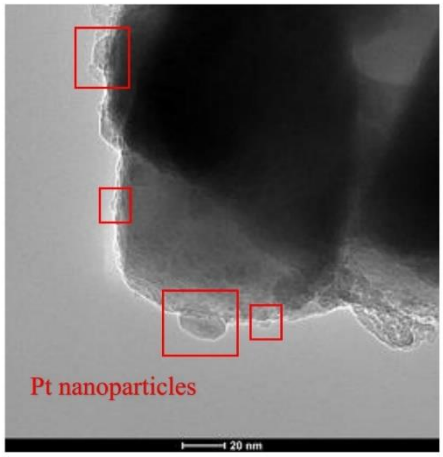

Fig. 3. STEM images of ST01-Pt0.05 sample

exhibited the highest activity towards hydrogen generation and the worst one for acetic acid oxidation, whereas ST41 samples behaved oppositely in both cases. It has already been reported (for comparison of 35 commercial titania photocatalysts) that for methanol dehydrogenation, a high specific surface area (ST01) for efficient adsorption of methanol is required, whereas low BET favoured acetic acid decomposition (ST41) [7]. Photocatalysts obtained from TBT and FP6 generally achieved similar results towards both H_2 generation and CH_3OOH oxidation. However, a little difference is still present, especially for the effect of Pt modification (Fig. 4 b). An interesting observation was also made for photocatalytic activity dependence for both platinum and copper amounts used for TiO_2 surface modification. There was hardly any difference in H_2 and CO_2 generation quantity between 0.05 and 0.1% for Pt- and 0.1 and 0.5% for Cu-modified titania. Similar results were presented by Ahmed et al. [8]. The optimum platinum amount for titania modification was 0.5 wt.%, which was confirmed by methanol dehydrogenation reaction.

The similar analysis was performed for bimetallic TiO_2-Pt/Cu photocatalysts. Obtained results for H_2 and CO_2 liberation are presented in Fig. 5 a-b.

Analogical dependence between used titania matrix as for monometallic TiO_2 was observed after the photodeposition of platinum and copper on the titania surface, thereby creating bimetallic structures. In reduction reaction, the ST01 matrix (containing only small anatase particles) was the most active, while in oxidation reaction – ST41 (only big anatase particles). The described dependence occurred regardless of the amount of modifying metals. For further analysis, the relationship between the platinum and copper content on ST41 matrix on photocatalytic activity in reduction and oxidation reactions is shown in Fig. 6 a-b.

As it was presented in Fig. 6 b, a combination of Pt and Cu nanoparticles on ST41 photocatalyst has hardly any influence on acetic acid oxidation. It follows that in the presented system, CH_3OOH decomposition to carbon(IV) oxide mainly depends on the TiO_2 matrix, to a lesser extent, from the type and concentration of metals. In reduction reaction, as it is presented in Fig. 6 a, simultaneous modification of titania surface with both Pt and Cu nanoparticles resulted in a significant decrease of H_2 evolution, mainly because of copper introduction. The higher the mol percentage of copper used, the lower the photocatalytic activity of bimetallic TiO_2-M.

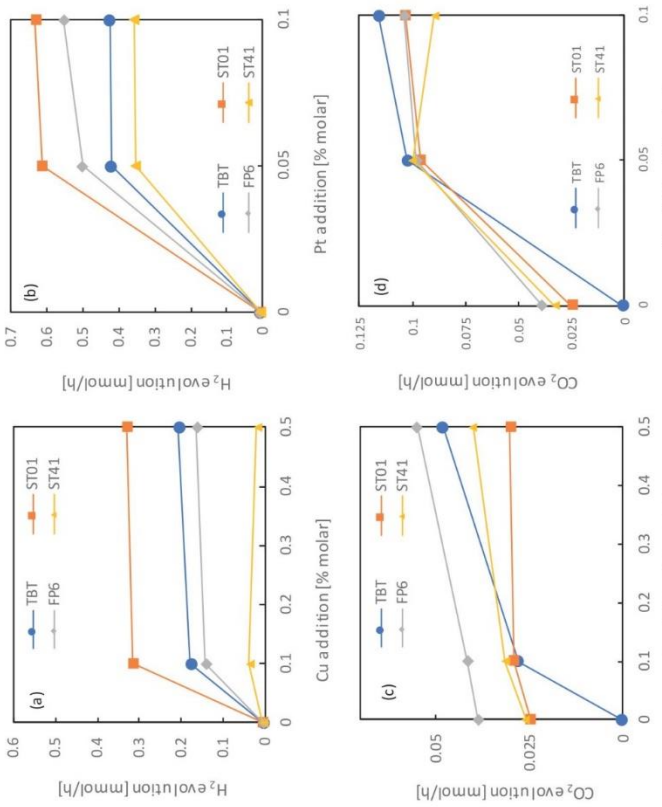

Fig. 4. The effect of metal content on the photocatalytic activity for: (a-b) methanol dehydrogenation (H_2 evolution), and (c-d) acetic acid decomposition (CO_2 evolution) for different monometallic titania samples

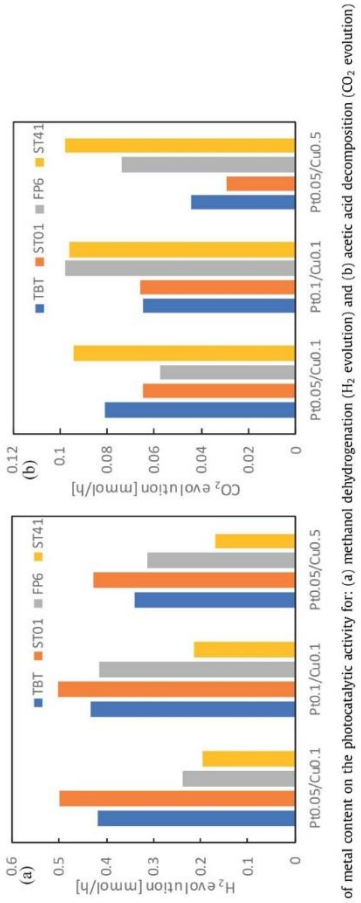

Fig. 5. The effect of metal content on the photocatalytic activity for: (a) methanol dehydrogenation (H_2 evolution) and (b) acetic acid decomposition (CO_2 evolution)

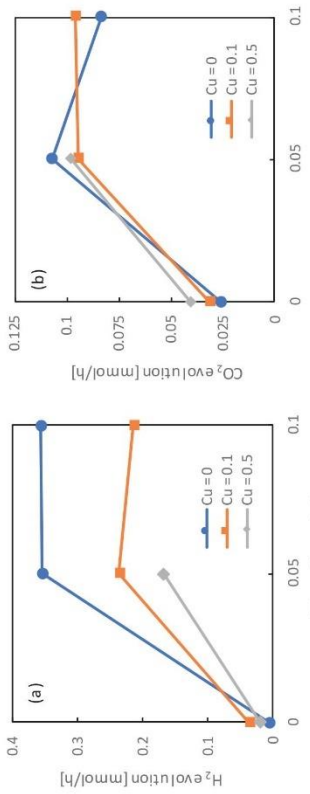

Fig. 6. The relationship between Pt and Cu in (a) methanol dehydrogenation (H_2 evolution) and (b) acetic acid decomposition (CO_2 evolution) for bimetallic-modified ST41 titania samples

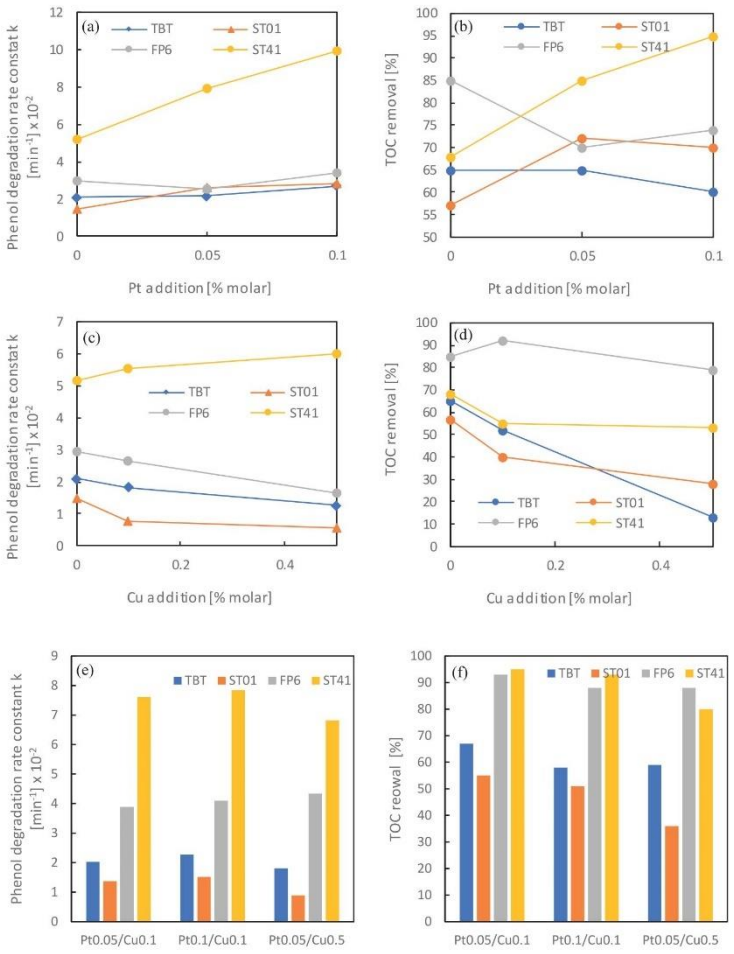

Fig. 7. Phenol degradation, presented as a rate constant k and TOC removal for different monometallic (a-d) and bimetallic (e-f) TiO_2-based photocatalysts

For further analysis of the photocatalytic activity of mono- and bimetallic TiO_2 samples, phenol degradation reaction was studied. Obtained results presented as rate constant k and TOC removal are shown in Fig. 7 a-d.

In all tested systems, ST41 matrices were the most active ones, allowing for both – the highest phenol degradation as well as the highest organic carbon mineralization. The increase of

the platinum content caused an increase in photocatalytic activity, while the opposite trend was observed for copper nanoparticles.

2. Experimental Design, Materials, and Methods

2.1. Materials

Commercial titania samples: ST01 (ST-01, Ishihara Sangyo, Osaka, Japan), ST41 (ST-41, Ishihara Sangyo) and FP6 (Showa Denko K.K., Tokyo, Japan) were supplied as photocatalysts matrix. Other chemicals, including titanium n-butoxide (TBT, 96.0%), chloroplatinic acid hexahydrate (99%), copper(II) sulfate (99.9%), methanol, acetic acid, acetonitrile (HPLC grade), phosphoric acid (HPLC grade, 85%) and phenol (99.5%) were purchased by Wako Pure Chemicals (Osaka, Japan). All materials were used as received without further purification.

2.2. Preparation of TiO_2-M photocatalysts

Four different types of titania (commercial: ST01, ST41, and FP6, and self-prepared TBT - from titanium n-butoxide hydrolysis) were modified with platinum and/or copper nanoparticles using photodeposition method. TiO_2 was dispersed in methanol-water solution (volume ratio 50:50) and the corresponding amount of Pt/Cu precursors' solutions (0.05 and 0.1 mol% of Pt and 0.1 and 0.5 mol% of Cu in respect to TiO2) were added. The obtained suspension was bubbled with argon for oxygen removal. The reaction tube was sealed with a rubber septum and then irradiated for 1 h using a mercury lamp. Repeatable conditions were provided by continuous stirring (500 rpm) and temperature control using a thermostated water bath. The efficiency of photodeposition was controlled via hydrogen generation measurements taken every 15 min of irradiation. The obtained TiO2-M photocatalysts, where M corresponds to Pt, Cu, or Pt/Cu nanoparticles, were washed with deionized water, centrifugally separated, and dried at 80°C for 24 h. Finally, samples were calcinated at 400°C for 2 h.

2.3. Characterization of obtained photocatalysts

XRD analyses were performed using the Rigaku Intelligent X-ray diffraction system SmartLab (Tokyo, Japan) equipped with a sealed tube X-ray generator (a copper target; operated at 40 kV and 30 mA). Data were collected in the 2θ range of 5-80°. Scan speed and scan step were fixed at $1^{o}{\cdot}min^{-1}$ and 0.01°, respectively. The analysis was based on the International Centre for Diffraction Data (ICDD) database. The crystallite size of the photocatalysts in the vertical direction to the corresponding lattice plane was determined using Scherrer's equation, with Scherrer's constant equals 0.891. Quantitative analysis, including phase composition with standard deviation, was calculated using the Reference Intensity Ratio (RIR) method from the most intensive independent peak of each phase.

Nitrogen adsorption-desorption isotherms (BET method for the specific surface area) were recorded using the Micromeritics Gemini V (model 2365) (Norcross, GA, USA) instrument at 77 K (liquid nitrogen temperature).

Diffuse reflectance (DR) spectra were measured, and the data were converted to obtain absorption spectra. The bandgap energy of photocatalysts was calculated from the corresponding Kubelka-Munk function, $F(R)^{0.5}E_{ph}^{0.5}$ against E_{ph}, where E_{ph} is photon energy. The measurements were carried out on JASCO V-670 (Tokyo, Japan), equipped with a PIN-757 integrating sphere. $BaSO_4$ or respective bare titania were used as references.

Noble metal nanoparticles presence was determined by scanning transmission electron microscopy (STEM) equipped with energy-dispersive X-ray spectroscopy (EDS; HITACHI, HD-2000, Tokyo, Japan).

2.4. Photocatalytic activity analysis

Photocatalytic activity of obtained samples was evaluated in three reaction systems: (1) phenol degradation reaction under UV-Vis irradiation, (2) decomposition of acetic acid under UV-Vis irradiation, and (3) dehydrogenation of methanol under UV-Vis irradiation. For phenol degradation reaction, a 300-W xenon lamp (LOT Oriel, Darmstadt, Germany) was used. A 0.05 g (1 g•dm^{-3}) of a photocatalyst, together with a 20 mg•dm^{-3} phenol solution, was added to a 50 cm^3 quartz photoreactor with an exposure layer thickness of 3 cm, and obtained suspension was stirred in darkness for 30 min to provide adsorption-desorption stabilization. After equilibrium was established, photocatalyst suspension was irradiated (60 mW•cm^{-3}) for 60 min under continuously stirring. The constant temperature of the aqueous phase was kept at 20°C using a thermostated water bath. Every 10 min of irradiation, 1.0 cm^3 of suspension was collected and filtered through a syringe filter (pore size: 0.2 μm) for the removal of photocatalysts particles. The concentration of phenol and formed intermediates was estimated using a reversed-phase high-performance liquid chromatography (HPLC) system, equipped with a C18 chromatography column with bound residual silane groups (Phenomenex, model 00F-4435-E0) and a UV-Vis detector with a DAD photodiodes array (model SPD-M20A, Shimadzu). The tests were carried out at 45°C and under isocratic flow conditions of 0.3 cm^3•min^{-1} and volume composition of the mobile phase of 70% acetonitrile, 29.5% water, and 0.5% orthophosphoric acid. Qualitative and quantitative analysis was performed based on measurements of relevant substance standards and using the method of an external calibration curve. Total organic carbon (TOC) was measured using the TOC-L analyzer (Shimadzu, Kyoto, Japan).

For acetic acid decomposition, 0.05 g of the photocatalyst was suspended in 5 cm^3 of 5 vol% aqueous acetic acid solution. The 30 cm^3 testing tube with as prepared suspension was sealed with a rubber septum and irradiated for 60 min using 400 W mercury lamp (Hamamatsu Photonics, Hamamatsu, Japan) under continuous stirring and temperature control. Every 20 min, liberated CO_2 in a gas phase was estimated chromatographically using a Shimadzu GC-8A Chromatograph (Shimadzu Corporation, Kyoto, Japan) equipped with thermal conductivity detector (TCD) and Porapak Q column (Agilent Technologies, Santa Clara, CA, USA).

For methanol dehydrogenation, 0.05 g of the photocatalyst was suspended in 5 cm^3 in methanol-water solution (volume ratio 50:50). The obtained suspension was first purged with argon for oxygen removal. The testing tube was sealed with a rubber septum, and irradiated for 60 min using mercury lamp (same reaction system as that used for acetic acid decomposition). Generated hydrogen was determined every 15 min using a Shimadzu GC-8A Chromatograph with TCD detector and MS-5A column (Agilent Technologies).

Declaration of Competing Interest

The authors declare that they have no known competing financial interests or personal relationships which have, or could be perceived to have, influenced the work reported in this article.

Acknowledgments

This work was supported by the Polish National Science Centre (Grant No. NCN 2016/23/D/ST5/01021) and Gdansk University of Technology by InterPhD II (POWER) project (No. POWR.03.02.00-IP.08-00-DOK/16)

Z.B. would like to highly acknowledge Dr. Maya Endo-Kimura from the Institute for Catalysis, Hokkaido University, Japan, for the inestimable help during conducting research.

Supplementary materials

Supplementary material associated with this article can be found, in the online version, at doi:10.1016/j.dib.2020.105814.

References

[1] Z. Bielan, E. Kowalska, S. Dudziak, K. Wang, B. Ohtani, A. Zielińska-Jurek, Mono- and bimetallic (Pt/Cu) titanium(IV) oxide core-shell photocatalysts with Vis light activity and magnetic separability, Catalysis Today, In Press.
[2] K. Wang, M. Janczarek, Z. Wei, T. Raja-Mogan, M. Endo-Kimura, T.M. Khedr, B. Ohtani, E. Kowalska, Morphology- and Crystalline Composition-Governed Activity of Titania-Based Photocatalysts: Overview and Perspective, Catalysts 9 (2019) 1–30.
[3] M. Janczarek, Z. Wei, M. Endo, B. Ohtani, E. Kowalska, Silver- and copper-modified decahedral anatase titania particles as visible light-responsive plasmonic photocatalyst, Journal of Photonics for Energy 7 (2016) 1–16.
[4] S. Kunwar, M. Sui, P. Pandey, Z. Gu, S. Pandit, J. Lee, Improved Configuration and LSPR Response of Platinum Nanoparticles via Enhanced Solid State Dewetting of In-Pt Bilayers, Scientific Reports 9 (2019) 1–14.
[5] G.H. Chan, J. Zhao, E.M. Hicks, G.C. Schatz, R.P. Van Duyne, Plasmonic Properties of Copper Nanoparticles Fabricated by Nanosphere Lithography, Nano Letters 7 (2007) 1947–1952.
[6] Z. Wei, M. Endo, K. Wang, E. Charbit, A. Markowska-szczupak, B. Ohtani, E. Kowalska, Noble metal-modified octahedral anatase titania particles with enhanced activity for decomposition of chemical and microbiological pollutants, Chemical Engineering Journal 318 (2017) 121–134.
[7] O.O. Prieto-Mahaney, N. Murakami, R. Abe, B. Ohtani, Correlation between Photocatalytic Activities and Structural and Physical Properties of Titanium(IV) Oxide Powders, Chemistry Letters 38 (2009) 238–239.
[8] L.M. Ahmed, I. Ivanova, F.H. Hussein, D.W. Bahnemann, Role of Platinum Deposited on TiO_2 in Photocatalytic Methanol Oxidation and Dehydrogenation Reactions, International Journal of Photoenergy 2014 (2014) 1–9.

2. Preparation and Characterization of Defective TiO_2. The Effect of the Reaction Environment on Titanium Vacancies Formation

Zuzanna Bielan, Szymon Dudziak, Agnieszka Sulowska, Daniel Pelczarski, Jacek Ryl, Anna Zielińska-Jurek

Materials 13 (2020) 2763

DOI: 10.3390/ma13122763

P2

materials

MDPI

Article

Preparation and Characterization of Defective TiO_2. The Effect of the Reaction Environment on Titanium Vacancies Formation

Zuzanna Bielan [1,*], Szymon Dudziak [1], Agnieszka Sulowska [1], Daniel Pelczarski [2], Jacek Ryl [3] and Anna Zielińska-Jurek [1,*]

[1] Department of Process Engineering and Chemical Technology, Faculty of Chemistry, Gdansk University of Technology (GUT), G. Narutowicza 11/12, 80-233 Gdansk, Poland; dudziakszy@gmail.com (S.D.); sulowska.as@gmail.com (A.S.)
[2] Department of Physics of Electronic Phenomena, Faculty of Applied Physics and Mathematics, Gdansk University of Technology (GUT), G. Narutowicza 11/12, 80-233 Gdansk, Poland; daniel.pelczarski@pg.edu.pl
[3] Department of Electrochemistry, Corrosion and Materials Engineering, Faculty of Chemistry, Gdansk University of Technology (GUT), G. Narutowicza 11/12, 80-233 Gdansk, Poland; jacryl@pg.edu.pl
* Correspondence: zuzanna.bielan@gmail.com (Z.B.); annjurek@pg.edu.pl (A.Z.-J.)

Received: 13 May 2020; Accepted: 16 June 2020; Published: 18 June 2020

Abstract: Among various methods of improving visible light activity of titanium(IV) oxide, the formation of defects and vacancies (both oxygen and titanium) in the crystal structure of TiO_2 is an easy and relatively cheap alternative to improve the photocatalytic activity. In the presented work, visible light active defective TiO_2 was obtained by the hydrothermal reaction in the presence of three different oxidizing agents: HIO_3, H_2O_2, and HNO_3. Further study on the effect of used oxidant and calcination temperature on the physicochemical and photocatalytic properties of defective TiO_2 was performed. Obtained nanostructures were characterized by X-ray diffractometry (XRD), specific surface area (BET) measurements, UV-Vis diffuse reflectance spectroscopy (DR-UV/Vis), photoluminescence spectroscopy (PL), X-ray photoelectron spectroscopy (XPS), and electron paramagnetic resonance (EPR) spectroscopy. Degradation of phenol as a model pollutant was measured in the range of UV-Vis and Vis irradiation, demonstrating a significant increase of photocatalytic activity of defective TiO_2 samples above 420 nm, comparing to non-defected TiO_2. Correlation of EPR, UV-Vis, PL, and photodegradation results revealed that the optimum concentration of HIO_3 to achieve high photocatalytic activity was in the range of 20–50 mol%. Above that dosage, titanium vacancies amount is too high, and the obtained materials' photoactivity was significantly decreased. Studies on the photocatalytic mechanism using defective TiO_2 have also shown that $^{\bullet}O_2^-$ radical is mainly responsible for pollutant degradation.

Keywords: titanium vacancies; HIO_3; phenol degradation; scavengers; photocatalysis

1. Introduction

One of the main challenges of the 21st century is the pollution of the water environment. Compounds such as pharmaceuticals, hormones, or personal care products are detected in surface waters, which negatively affect human health and entire ecosystems [1]. In this regard, advanced oxidation processes (AOPs) allow for the effective removal of impurities from water. Heterogeneous photocatalysis, as one of the AOPs, has gained considerable attention due to effective removal in the presence of light and semiconductor of xenobiotics not susceptible to biological degradation.

In the photocatalytic process, semiconductor absorbs electromagnetic radiation with an energy greater or equal to energy bandgap. The generated charge carriers take part at the surface in redox reactions with the water, oxygen, and hydroxyl ion molecules leading to the formation of reactive oxygen species, capable of non-selective and sufficient oxidation of pollutants. Titanium(IV) oxide is one of the most frequently used semiconductors for photocatalysis due to its good photocatalytic activity, cost-effectiveness, non-toxicity, and high stability [2]. However, the use of TiO_2 in heterogeneous photocatalysis is limited due to charge carriers' recombination and almost no activity in the visible light.

Several different strategies have been proposed to obtain TiO_2 active in the range of visible light. Advanced modification of semiconductor materials with metals (Ag [3], Au [4], Mo [5], Fe [6], Pt [7], and Pd [8]), as well as doping with non-metals (N [9], C [10], F [11], Cl [12], and S [13]) and dyes sensitization [14–16] enable to obtain heterogeneous photocatalysts active in the visible light. Nonetheless, all the presented methods have several drawbacks. Non-metal-doped semiconductors usually are unstable in long-term processes because of dopant liberation from surface layers [17,18]. Introducing non-metals into the TiO_2 lattice could also result in the formation of oxygen vacancies, which could act as additional electron-hole pairs recombination centers [19,20]. In turn, doping with metal ions, as well as a surface modification with its nanoparticles, is more expensive and is not cost-effective in photocatalysis scaling-up [21]. Moreover, such nanomaterials often suffer from thermal and optical instability [22]. As for the matter of dye-sensitized semiconductors, widely used sensitizers such as alizarin red S [23], bipyridine complexes [24,25], phthalocyanine [16,26] absorbed on the surface of TiO_2 could be desorbed during the photocatalytic process and greatly depress the photoactivity [27,28].

Another possibility of increasing the photoactivity of TiO_2 is an introduction to its crystal structure intrinsic defects. To the category of this self-structural modification belong titanium/oxygen vacancy self-doping and a surface disorder as well as the formation of Ti-OH bonds on the surface layer [29,30]. Great attention to blue (Ti^{3+} defected) and black TiO_2 is related mostly to extending the light absorption to the visible region [31,32]. As presented by Lettieri et al. [33], blue TiO_2 could be obtained from commercially available P25 and anatase powders in simple solvent reflux thermal treatment. It allowed to surface and sub-surface oxygen vacancies formation. Consequently, TiO_2 bandgap has been narrowed to about 2.3 eV and visible light activity was significantly increased. Among all studied titania defects, the most rarely investigated are titanium vacancies and titanium interstitials despite their excellent quadrupole donor and acceptor properties. Revolutionary work in the field of TiO_2 vacancies was reported by Wu et al. [34]. The yellow, ultra-small defective TiO_2 was obtained by a simple sol–gel method within 8 h of UV irradiation, without introducing any external dopants. The formed titanium vacancies and titanium interstitials played a crucial role in visible-light-driven H_2 production from formaldehyde solution, not only initiating but also promoting photocatalytic activity in visible light. Furthermore, cycling tests indicated the stability of yellow defective TiO_2, compared with normal TiO_2 assisted with co-catalysts [34].

Phenol is one of the commonly used model organic compounds in photocatalytic wastewater treatment. Its degradation pathway is intensively studied for a thorough understanding of the photocatalytic reaction with the application of various photocatalysts [35–37]. Kang et al. studied degradation under visible light using F-doped TiO_2 hollow nanocubes with oxygen vacancies [38]. After 60 min of irradiation, about 60% of organic contamination was degraded. A different approach was presented by Colón et al. [39]. The titanium(IV) ox0ide photocatalysts obtained from titanium isopropoxide precursor were treated with different inorganic acids and then calcined in temperature range from 400 to 800 °C. It was reported that such treatment was responsible for the generation of oxygen vacancies on the surface of the photocatalysts. The highest photocatalytic activity was noticed for pre-sulfated TiO_2 calcined in 600 °C [39]. Nevertheless, in the literature there is lack of information concerning the photocatalytic activity of defective TiO_2 with titanium vacancies under visible or UV-visible light in reaction of phenol degradation.

Therefore, in this study, we propose a simple method of preparation visible light active TiO_2 with titanium vacancies obtained by a hydrothermal reaction in a suitable oxidizing environment

(HIO_3, H_2O_2, and HNO_3). The most appropriate amount of used oxidant, as well as the durability of generated titanium vacancies were investigated. The effect of introduced defects on physicochemical and photocatalytic properties was studied. The obtained samples were characterized by X-ray diffractometry (XRD), specific surface area (BET) measurements, UV-Vis diffuse reflectance spectroscopy (DR-UV/Vis), photoluminescence spectroscopy (PL), X-ray photoelectron spectroscopy (XPS), and electron paramagnetic resonance (EPR) spectroscopy. The photodegradation of phenol as a model organic pollutant using the obtained photocatalysts was subsequently investigated in the range of UV-Vis and Vis irradiation. Furthermore, the mechanism of phenol degradation and the role of four oxidative species (h^+, e^-, $^{\bullet}OH$, and $^{\bullet}O_2^-$) in the studied photocatalytic process were investigated.

2. Materials and Methods

Titania organic precursor: titanium(IV) butoxide (99+%) was provided by Alfa Aesar (Haverhill, MA, USA). Iodic acid (99.5%), nitric acid (68%), and hydrogen peroxide (30%) were purchased from Sigma (Poznan, Poland) and were used for TiO_2 structure modification. Acetonitrile and orthophosphoric acid (85%) for HPLC mobile phase preparation were provided by Merck (Darmstadt, Germany) and VWR (Gdansk, Poland), respectively. Phenol, used as a model organic recalcitrant pollutant in photocatalytic activity measurements, was purchased from VWR. All reagents were used without further purification.

2.1. Preparation of Defective TiO_2 in the Presence of Different Oxidizing Agents

The preparation of defective TiO_2 was performed by a hydrothermal method and annealing process. Titanium(IV) butoxide (TBT) was used as a TiO_2 precursor, and iodic acid (HIO_3), nitric acid (HNO_3), or hydrogen peroxide (H_2O_2) was used as an oxidizing environment. First, an appropriate amount of HIO_3, HNO_3, or H_2O_2 (as mentioned in Table 1) was dissolved in 80 cm^3 of distilled water. After that, 10 cm^3 of TBT was added dropwise, and the obtained suspension was stirred for 1 h at room temperature. In the next step, the suspension was transferred into a Teflon-lined autoclave for thermal treatment at 110 °C for 24 h. The resultant precipitate was centrifuged, dried at 70 °C, and then calcined at 300 °C. Calcination was carried out in two steps: with a heating rate of 3 °C·min^{-1} to the temperature of 180° for 45 min, then with a heating rate of 2 °C·min^{-1} to the temperature of 300° for 3 h. A series of defective TiO_2 photocatalysts with different content of used oxidants, calculated as amount relative to TiO_2, are presented in Table 1. For easier recognition of samples, TBT-HIO_3, TBT-HNO_3, and TBT-H_2O_2 names are assigned to defective photocatalysts obtained in the assistance of HIO_3, HNO_3, and H_2O_2 oxidants, respectively.

Table 1. The oxidant concentration used for preparation of the defective TiO_2 photocatalyst.

Sample	Oxidant Concentration (mol%)	Mass of Added Oxidant (g)
TiO_2-TBT	0	0
TBT-HIO_3_0.5	0.5	0.026
TBT-HIO_3_5	5	0.258
TBT-HIO_3_20	20	1.032
TBT-HIO_3_50	50	2.579
TBT-HIO_3_75	75	3.869
TBT-HIO_3_100	100	5.159
TBT-HNO_3_50	50	0.948
TBT-H_2O_2_50	50	1.65

In order to obtain the defective photocatalysts' series for their thermal stability test, TBT-HIO_3_20 was synthesized hydrothermally, as was reported in the previous paragraph. Further, the

dry product was calcined in five different temperatures: 300 °C, 400 °C, 450 °C, 650 °C, and 1000 °C. Calcination was carried out in two steps: with a heating rate of 3 °C·min^{-1} to the temperature of 180° for 45 min, then with a heating rate of 2 °C·min^{-1} to the set temperature for 3 h.

2.2. Characterization of Obtained Defective Photocatalysts

The XRD analyses were performed using the Rigaku Intelligent X-ray diffraction system SmartLab (Rigaku Corporation, Tokyo, Japan) equipped with a sealed tube X-ray generator (a copper target; operated at 40 kV and 30 mA). Data was collected in 2θ range of 5–80° with a scan speed and scan step of 1°·min^{-1} and 0.01°, respectively. The analyses were based on the International Centre for Diffraction Data (ICDD) database. The crystallite size of the photocatalysts in the vertical direction to the corresponding lattice plane was determined using the Scherrer's equation with the Scherrer's constant equal to 0.891. Quantitative analysis, including phase composition with standard deviation, was calculated using the reference intensity ratio (RIR) method from the most intensive independent peak of each phase.

Nitrogen adsorption–desorption isotherms (BET method for the specific surface area) were recorded using the Micromeritics Gemini V (model 2365; Norcross, GA, USA) instrument at 77 K (liquid nitrogen temperature).

Light absorption properties were measured using diffuse reflectance (DR) spectroscopy in the range of 200–800 nm. The bandgap energy of obtained samples was calculated from $(F(R)\cdot E)^{0.5}$ against E graph, where E is the photon energy, and F(R) is the Kubelka–Munk function, proportional to the radiation's absorption. The measurements were carried out using ThermoScientific Evolution 220 Spectrophotometer (Waltham, MA, USA) equipped with a PIN-757 integrating sphere. As a reference, $BaSO_4$ was used.

X-ray photoelectron spectroscopy (XPS) measurements were conducted using Escalab 250Xi multi-spectrometer (Thermofisher Scientific, Walthman, MA, USA) using Mg K X-rays. Photoluminescence (PL) spectra were recorded on a Perkin-Elmer LS 55 fluorescence spectrometer (Waltham, MA, USA) employing Xenon discharge lamp equivalent to 20 kW as the excitation source. The samples were excited at 250 nm in the air at room temperature. A 290 nm cut off filter was used during measurements at range 300–700 nm.

Electron paramagnetic resonance (EPR) spectroscopy was used for intrinsic defects formation confirmation. Measurements were conducted using RADIOPAN SE/X-2547 spectrometer (Poznań, Poland), operating at room temperature, with frequency in range 8.910984–8.917817 GHz.

Defective TiO_2 photocatalysts morphology was determined by scanning electron microscopy (SEM) equipped with energy-dispersive X-ray spectroscopy (EDS; HITACHI, S-3400N, Tokyo, Japan).

2.3. Measurements of Photocatalytic Activity

Photocatalytic activity of the obtained samples was evaluated in phenol degradation reaction, both in UV-Vis and Vis light irradiation, using 300 W Xenon lamp (LOT Oriel, Darmstadt, Germany). For the visible light measurements, a cut-off 420 nm filter (Optel, Opole, Poland) was used to obtain a settled irradiation interval. A 0.05 g (2 g·dm^{-3}) of a photocatalyst, together with a 20 mg·dm^{-3} phenol solution, was added to a 25 cm^3 quartz photoreactor with an exposure layer thickness of 3 cm and obtained suspension was stirred in darkness for 30 min to provide adsorption–desorption equilibrium. After that, photocatalyst suspension was irradiated under continuous stirring and a power flux of 30 mW·cm^{-2} for 60 min. The constant temperature of the aqueous phase was kept at 20 °C using a water bath. Every 20 min of irradiation, 1.0 cm^3 of suspension was collected and filtered through syringe filters (pore size = 0.2 μm) for the removal of photocatalysts particles. Phenol concentration, as well as a formation of degradation intermediates, were analyzed using reversed-phase high-performance liquid chromatography (HPLC) system 9 (Shimadzu, Kyoto, Japan), equipped with C18 chromatography column with bound residual silane groups (Phenomenex, model 00F-4435-E0) and a UV-Vis detector with a DAD photodiodes array (model SPD-M20A, Shimadzu).

The tests were carried out at 45 °C and under isocratic flow conditions of 0.3 mL·min^{-1} and volume composition of the mobile phase of 70% acetonitrile, 29.5% water, and 0.5% orthophosphoric acid. Qualitative and quantitative analysis was performed based on previously made measurements of relevant substance standards [40] and using the method of an external calibration curve.

Phenol removal percentage was calculated from the equation:

$$D\% = \frac{C_o - C_n}{C_o} \cdot 100\% \quad (1)$$

where: C_o—phenol initial concentration (mg·dm^{-3}) and C_n—phenol concentration during photodegradation (mg·dm^{-3}).

Rate constant k was determined from $\ln(C_o/C_n)$ against t plot where C_o and C_n are phenol concentrations (mg·dm^{-3}) and t is degradation time (min). Rate constant k is equal to the directional coefficient "a" of the plot.

In order to evaluate the stability of obtained photocatalysts, three 3-hours-long subsequent cycles of phenol under UV-Vis light with use of the most active defective TBT-HIO3_50 sample were performed. After each cycle, photocatalyst was separated from the suspension with use of a syringe filter and use in next cycle without additional treatment.

The effect of charge carrier scavengers was examined by addition into phenol solution 1 cm^3 of 500 mg·dm^{-3} of tert-butyl alcohol (t-BuOH), benzoquinone (BQ) ammonium oxalate (AO), and silver nitrate (SN).

3. Results and Discussion

3.1. The Influence of Oxidizing Conditions on Defective TiO_2 Properties

As the first step, a series of three defective TiO_2 photocatalysts were obtained by the hydrothermal method. The physicochemical characteristic of the obtained samples, including BET surface area with pore volume, bandgap (Eg) and their images, compared with TiO_2–TBT photocatalyst, are presented in Table 2.

Table 2. Physicochemical characteristic of the obtained defective TiO_2 samples.

Sample	BET ($m^2 \cdot g^{-1}$)	V Pores ($cm^3 \cdot g^{-1}$)	Eg (eV)	Photo
TiO_2-TBT	169	0.0836	3.2	
TBT-HIO_3_50	166	0.0818	2.9	
TBT-HNO_3_50	198	0.0966	3.05	
TBT-H_2O_2_50	174	0.0858	3.1	

The XRD patterns for the as-obtained photocatalyst series are presented in Figure 1, while detailed crystalline phases characteristic is given in Table 3. For pure TiO_2–TBT sample, 95.5% of the crystalline phase of anatase, with the most intense peak at 25° 2θ was observed ([101], ICDD's card No. 7206075). After introducing to hydrothermal synthesis the oxidizing agent, the percentage of

anatase decreased in favor of other titania polymorphs: brookite ([211], with the main peak at 31° 2θ, ICDD's card No. 9004138), and rutile ([110], with the main peak at 27° 2θ, ICDD's card No. 9004141). According to the previous study of Gamboa and Pasquevich [41], the presence of halogen ions (chlorine, iodine, and bromine) affects rutile formation even below the anatase to rutile transition (ART) temperature [42].

Nonetheless, the anatase crystallite size was about 5–6 nm. Changes in the crystalline phases did not affect the BET surface area, which remained in the range of 166–198 $m^2 \cdot g^{-1}$ for TBT-HIO_3_50 and TBT-HNO_3_50, respectively.

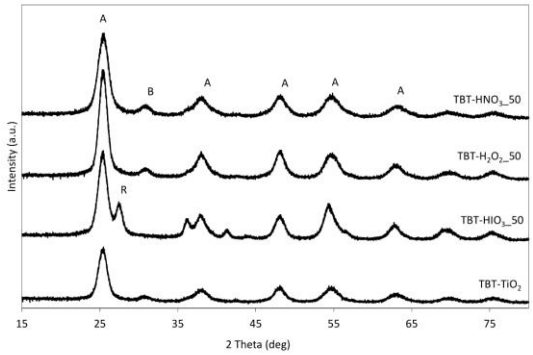

Figure 1. XRD patterns for defective TiO_2 photocatalysts (A—anatase, B—brookite, and R—rutile).

Table 3. Crystalline phases characteristic for obtained defective TiO_2.

Sample	Crystalline Size and Phase Content					
	Anatase		Rutile		Brookite	
	Size (nm)	Phase Content (wt %)	Size (nm)	Phase Content (wt %)	Size (nm)	Phase Content (wt %)
TBT	5.97 ± 0.04	95.5 ± 1	-	-	6.1 ± 0.5	4.5 ± 0.9
TBT-HIO_3_50	5.70 ± 0.04	68 ± 3	9.08 ± 0.17	32 ± 17	-	-
TBT-HNO_3_50	5.07 ± 0.03	83 ± 10	-	-	4.6 ± 0.3	17 ± 2
TBT-H_2O_2_50	5.69 ± 0.04	75.5 ± 5	-	-	5.7 ± 0.3	24.5 ± 1.5

For optical absorption properties studies of the obtained defective TiO_2, DR/UV-Vis spectroscopy analyses were performed, and the results are presented in Figure 2. Comparing to pure TBT-TiO_2, the samples obtained in the oxidative environment had absorption spectra shifted towards the visible light due to the creation of crystalline defects. After recalculation of spectra into the Kubelka–Munk function, the Tauc transformation was used for bandgap energy determination, and its values are presented in Table 2. For TBT-HNO_3_50 and TBT-H_2O_2_50, the bandgap energies were comparable to pure TBT-TiO_2 bandgap energy and equaled 3.05 and 3.1 eV, respectively. The slightly smaller value of 2.9 eV was reported for TBT-HIO_3_50 photocatalyst. It could also be caused by a 30% rutile content in the crystal structure of the photocatalyst [43].

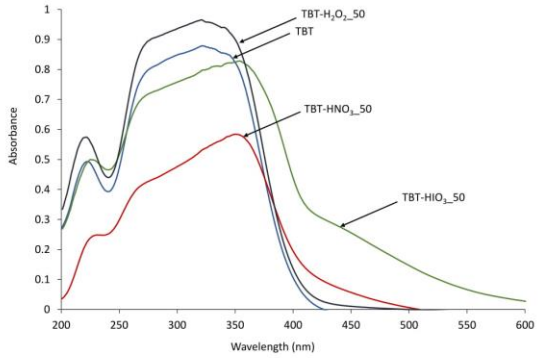

Figure 2. UV-Vis diffuse spectra for pure and defective TiO_2 obtained using different oxidants.

For the direct confirmation of intrinsic defects formation in obtained titanium(IV) oxide photocatalysts, EPR analyses were performed, and the results are presented as the signal intensity against the g value graph (Figure 3). The Lande factor (g) was calculated from the equation:

$$g = \frac{h \cdot f}{m_B \cdot B} \quad (2)$$

where: g–Lande factor (a.u.); h–Planck's constant (6.62·10−34; J·s); f–frequency (Hz); mB–Bohr magneton (9.2740154·10−24; J·T−1); and B–magnetic field induction (T).

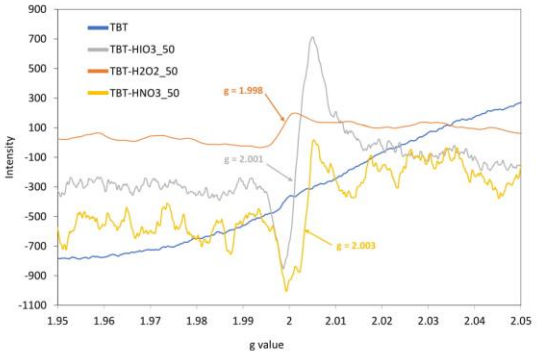

Figure 3. The EPR spectra recorded in the room temperature for defective TiO_2 photocatalysts obtained in different oxidative environments, compared with pure TBT-TiO_2 sample (blue line).

For defective TiO_2 samples, an intense signal was noticed in the range of g from 1.998 to 2.003 for TBT-H_2O_2_50 and TBT-HIO_3_50 samples, respectively. According to the literature, it could be

attributed to titanium vacancies (V_{Ti}) in titanium(IV) oxide structure [34,44,45]. This signal was not observed for TBT-TiO_2 sample. Moreover, there were no signals in the range of g = 1.960–1.990 and above 2.020, suggesting the absence of Ti^{3+} defects as well as oxygen vacancies [45,46].

The photocatalytic activity, together with physicochemical properties, are the most important parameters for assessing the semiconductor utility in organic recalcitrant chemicals' degradation. In this regard, the series of UV-Vis and Vis light degradation reactions of phenol as a model pollutant were performed in the presence of the obtained defective TiO_2 photocatalysts. The obtained results, presented as the percentage of phenol degradation and degradation rate constant k, are shown in Figure 4a,b.

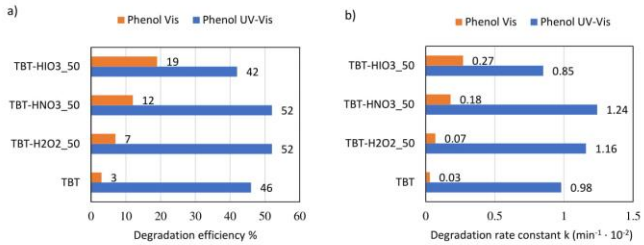

Figure 4. Efficiency of phenol degradation in UV-Vis and Vis light for TBT-TiO_2 and defective TiO_2 photocatalysts, presented as % of degradation (**a**) and rate constant k (**b**).

Comparing to pure TiO_2 (TBT sample), two defective TiO_2 photocatalysts, TBT-H_2O_2_50 and TBT-HNO_3_50, showed higher photocatalytic activity in UV-Vis light (52% after 1 hour of irradiation). In turn, defective TBT-HIO_3_50 obtained in the presence of iodic acid revealed in UV-Vis light decrease of photoactivity, compared with reference TBT-TiO_2 (42% of phenol degradation). Nonetheless, a different trend was observed under visible light range. TBT-HIO_3_50, for which photoactivity in UV-Vis light was the lowest when irradiated with the wavelength >420 nm, revealed the highest phenol degradation efficiency, equaled to 19%. It results from the synergic effect of anatase and rutile [47], and it is in agreement with the previously described shifting of the absorbance spectrum maximum towards higher wavelengths (see in Figure 2). The TBT-TiO_2 sample (anatase with a minority of brookite) showed negligible photocatalytic activity in the visible light range [48–50].

For determining the mechanism of photocatalytic degradation with the use of defective TiO_2, series of UV-Vis light photoactivity analyses, in the presence of scavengers, were performed. Benzoquinone (BQ), silver nitrate (SN), ammonium oxalate (AO), and tert-butanol (t-BuOH) were used as superoxide radical anions ($^{\bullet}O_2^-$), electrons (e^-), holes (h^+), and hydroxyl radicals ($^{\bullet}OH$) scavengers, respectively. Obtained results, presented as phenol degradation rate constant k, in comparison to the photodegradation process without scavengers, are presented in Figure 5.

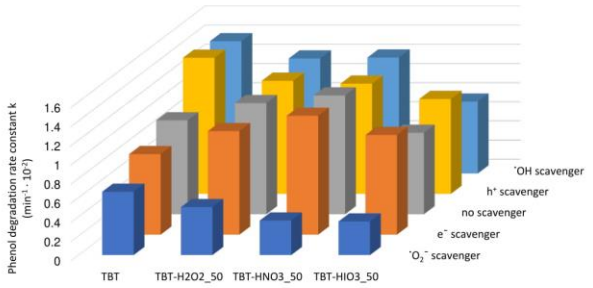

Figure 5. UV-Vis photocatalytic degradation of phenol for defective TiO_2 photocatalysts in the presence of e^-, h^+, $^{\bullet}O_2^-$, and $^{\bullet}OH$ scavengers.

The most significant impact on phenol degradation reaction, with the use of defected TiO_2, revealed superoxide radicals. After introducing to the photocatalyst suspension of BQ, the phenol degradation efficiency decreased significantly. A slight decrease was also observed when SN as an electron trapping agent was used. On the other hand, the addition of AO and t-BuOH did not cause diminishing of phenol degradation rate. Furthermore, for the TBT-TiO_2 sample, a slight increase in photoactivity was noted after adding to the system scavenger of holes or hydroxyl radicals. It could result from the additional in-situ formation of the reactive species on the photocatalysts' surface [36]. Based on the study, a schematic mechanism of phenol degradation in the presence of defective TiO_2 (sample TBT-HIO_3) was proposed and illustrated in Figure 6.

For pure TiO_2 the valence band (VB) and conduction band (CB) are located at +2.5 eV and −0.7 eV, respectively (in respect to normal hydrogen electrode NHE) [51]. After hydrothermal treatment in oxidative conditions, titanium defects were created, which led to the narrowing of the bandgap to the value of 2.9 eV. Irradiation of the TBT-HIO_3 surface with UV-Vis or Vis light caused exciting the electron and, as a result, creating superoxide radicals. Subsequently, their reaction with phenol promotes creating intermediate products, such as hydroquinone (HQ) and benzoquinone (BQ), whose presence was confirmed using HPLC analysis. Benzoquinone and hydroquinone concentration in irradiated solution reached equilibrium due to electron and proton transfer and reversible oxidation/reduction process between these two intermediates. Hydroquinone could also be accumulated during the process due to sequential charge transfer [52].

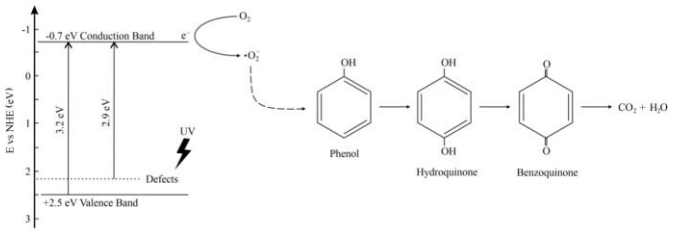

Figure 6. Schematic illustration of phenol degradation mechanism in the presence of defective TBT-HIO_3 photocatalyst.

However, after approximately 40 min of continuous irradiation, intermediates concentration started to decrease to more simple and more-quickly oxidizable compounds, consequently leading to complete mineralization. The presented mechanism is in good agreement with the literature [40,53].

3.2. The Effect of HIO_3 Content on Defective TiO_2 Physicochemical and Photocatalytic Properties

The selected in the previous step HIO_3 as an oxidant for preparation of defective TiO_2 was further used in six different quantities (from 0.5 to 100 mol % to TiO_2) for study the effect of oxidant amount on titanium vacancies formation. General physicochemical characteristics of the obtained defective TiO_2-HIO_3 samples, i.e., BET surface area, pore volume, calculated bandgap (Eg), and their images are shown in Table 4.

Table 4. Physicochemical characteristic of the obtained defective TiO_2-HIO_3 samples.

Sample	BET ($m^2 \cdot g^{-1}$)	V Pores ($cm^3 \cdot g^{-1}$)	Eg (ev)	Photo
TBT	169	0.0836	3.2	
TBT-HIO_3_0.5	155	0.0764	3.0	
TBT-HIO_3_5	153	0.0754	2.8	
TBT-HIO_3_20	172	0.0847	2.7	
TBT-HIO_3_50	166	0.0818	2.9	
TBT-HIO_3_75	167	0.0826	2.9	
TBT-HIO_3_100	146	0.0726	3.0	

Based on the obtained results, it was found that changing of the HIO_3 concentration does not significantly affect the BET surface area of defective TiO_2-HIO_3 photocatalysts. Among the obtained samples, TBT-HIO_3_20 showed the highest specific surface area of 172 $m^2 \cdot g^{-1}$ and the highest total pore volume of 0.0847 $cm^3 \cdot g^{-1}$.

The XRD patterns of TBT-TiO_2 and defective TiO_2-HIO_3 obtained with a different dosage of iodic acid are presented in Figure 7. The percentage of phases and the size of crystallites are given in Table 5. All photocatalysts contain anatase in their structure, with the most intense peak at 25° 2θ ([101], ICDD's card No. 7206075). Among the defective TiO_2-HIO_3 photocatalyst series, TBT-HIO_3_20 exhibited the smallest size of anatase crystallites (5.1 nm based on the Scherrer's formula) and was characterized by the highest anatase phase content of 96.4%. The most stable titanium(IV) oxide polymorphic phase, rutile, occurs when the mol.% of iodic acid taken as an oxidant reached 50 mol%.

Simultaneously, the intensity of the primary rutile signal at 27° 2θ ([110], ICDD's card No. 9004141), increased significantly with the increase of iodic acid dosage for samples TBT-HIO_3_50, TBT-HIO_3_75, and TBT-HIO_3_100. It is known that for an unmodified sample, anatase to rutile transition takes place at temperatures above 600 °C [54]. Obtained TBT-HIO_3 samples calcination was carried out at 300 °C. On this basis, it could be assumed that the high content of HIO_3 may disturb the TiO_2 anatase crystalline structure, therefore promoting the low-temperature formation of rutile. It is in agreement with the study of Hanaor and Sorrell [55], which reported that impurities, dopants, and defects influence anatase to rutile transition (ART) kinetics.

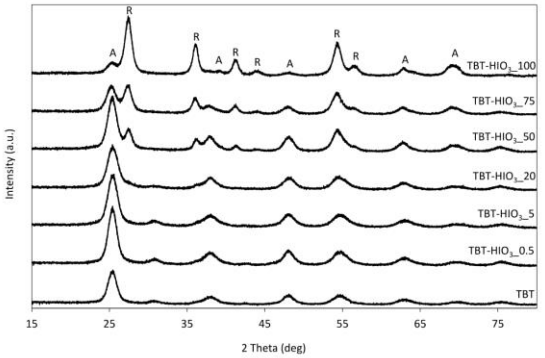

Figure 7. XRD patterns for defective TiO_2-HIO_3 photocatalysts (A–anatase, B–brookite, and R–rutile).

Table 5. Crystalline phases characteristic for the obtained defective TiO_2-HIO_3 samples.

Sample	Crystalline Size and Phase Content					
	Anatase		Rutile		Brookite	
	Size (nm)	Phase Content (wt%)	Size (nm)	Phase Content (wt%)	Size (nm)	Phase Content (wt%)
TBT	5.97 ± 0.04	95.5 ± 1	-	-	6.1 ± 0.3	4.5 ± 0.9
TBT-HIO_3_0.5	6.09 ± 0.03	86 ± 1	-	-	5.50 ± 0.19	14 ± 1.5
TBT-HIO_3_5	5.43 ± 0.03	89 ± 0.5	-	-	5.2 ± 0.2	11 ± 1
TBT-HIO_3_20	5.14 ± 0.03	96 ± 1	-	-	4.0 ± 0.6	3.5 ± 0.5
TBT-HIO_3_50	5.70 ± 0.04	68 ± 3.5	9.08 ± 0.17	32 ± 17	-	-
TBT-HIO_3_75	5.67 ± 0.05	20.5 ± 3.5	6.57 ± 0.09	7± 1.8	-	-
TBT-HIO_3_100	6.3 ± 0.2	15 ± 3.5	7.45 ± 0.06	85 ± 1	-	-

The UV/Vis diffusion reflectance spectra of pure TiO_2 and defective TiO_2-HIO_3 obtained with a different dosage of iodic acid are presented in Figure 8a. The pure TiO_2 absorbs radiation up to 400 nm. For titanium(IV) oxide samples obtained in the presence of HIO_3 as an oxidant, the absorption edge shifted to the visible region. It corresponds to the yellow colour of these samples and indicates the bandgap narrowing due to changes in electronic structure in TiO_2. The most significant shift of absorbance maximum was noticed for TBT-HIO_3_50, TBT-HIO_3_75, and TBT-HIO_3_100 photocatalysts. It corresponds well with previously analysed XRD spectra. For iodic acid content of

50 mol% and higher, rutile phase is starting to dominate as a titanium(IV) oxide most stable polymorph, which could also affect absorbance spectra shifting [56]. The energy bandgaps of all samples were calculated from the plot of (Kubelka–Munk·E)$^{0.5}$ versus E, where E is energy equal to hv, as shown in Figure 8b and summarized in Table 4. The sample TBT-HIO_3_20 exhibited the narrowest bandgap of 2.70 eV among the defective TiO_2_HIO_3 photocatalysts.

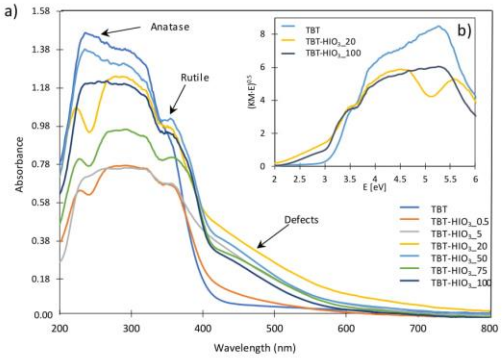

Figure 8. The diffuse reflectance (DR)/UV-Vis spectra for pure TiO_2 and defective TiO_2-HIO_3 photocatalysts (**a**) together with exemplary Tauc transformation (**b**).

For further confirmation of creating titanium vacancies, EPR analyses for the selected samples (TBT-HIO_3_20, TBT-HIO_3_50, and TBT-HIO_3_75) were performed. The obtained results, compared with spectra for TBT-TiO_2 are presented in Figure 9.

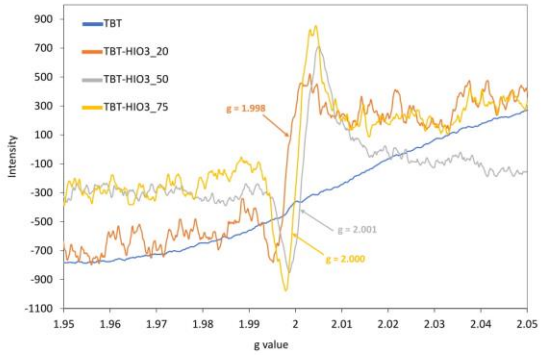

Figure 9. The EPR spectra recorded in the room temperature for selected defective TiO_2-HIO_3 photocatalysts, compared with the pure TiO_2–TBT sample (blue line).

As it was reported in the previous subsection, for defective TiO_2 photocatalysts obtained in a different oxidative environment, the intense signal attributed to titanium vacancies (V_{Ti}) appeared in the range of g from 1.998 to 2.001 for TBT-HIO_3_20 and TBT-HIO_3_50 samples, respectively. No additional signals were detected. It is also worth noting that the V_{Ti} signal increased with the increase of the iodic acid mol% used for the synthesis of defective TiO_2. It could suggest that more intrinsic defects are formed after oxidant concentration increase. Moreover, the presented trend was inversely proportional to the observed light absorbance spectra in the range of 400–500 nm (see in Figure 8). For the TBT-HIO_3_20 photocatalyst, visible light absorption was the highest, while for TBT-HIO_3_75, the lowest, which indicated that too high concentration of defects could also have a negative impact on TiO_2 photocatalytic activity. Titanium vacancies formation was also analyzed by Li et al. [57] and Ma et al. [58]. Obtained hydroxyfluorinated and lithium intercalated defected TiO_2-based photocatalysts were characterized by cationic vacancies, which successfully could work in the electrochemical applications.

The photoluminescence spectra of irradiated semiconductor materials give information on electron-hole recombination properties. Figure 10 shows normalized PL spectra of the pure TBT-TiO_2 as well as defective TBT-HIO_3_5, TBT-HIO_3_20, TBT-HIO_3_50, TBT-HIO_3_75, and TBT-HIO_3_100 photocatalyst samples. The excitation was carried out at 250 nm at a room temperature. The PL emission of maximum intensity in the high-energy region was observed at 400 nm for all samples, which was equal to 3.10 eV. It corresponds to indirect band-to-band recombination across the bandgap [59]. Other emission peaks in the visible light region were detected at 485 nm (2.56 eV) and 530 nm (2.24 eV). The emission in the 380–700 nm range could be assigned to the transition of electrons from the defect states to the valence band of titanium(IV) oxide [60] as well as trapped holes [59]. The emission in the blue region at 480 nm is related to indirect recombination via defects [60].

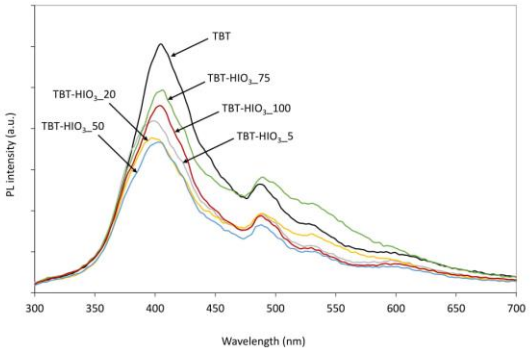

Figure 10. Photoluminescence (PL) spectra for defective TiO_2-HIO_3 samples.

In order to evaluate the surface properties and the state of elements, the XPS analyses were performed. The obtained results for the selected samples are presented in Figure 11a–d and in Table 6.

Table 6. Fraction of oxidation states of Ti as well as surface composition of the selected defected TBT-HIO_3 photocatalysts determined by X-ray photoelectron spectroscopy analysis.

Photocatalyst	Ti 2p3/2 (%)		O 1s (%)
	Ti^{4+}	Ti^{3+}	

TBT-HIO_3_20	27.56	0.9	71.54
TBT-HIO_3_100	27.47	0	72.54

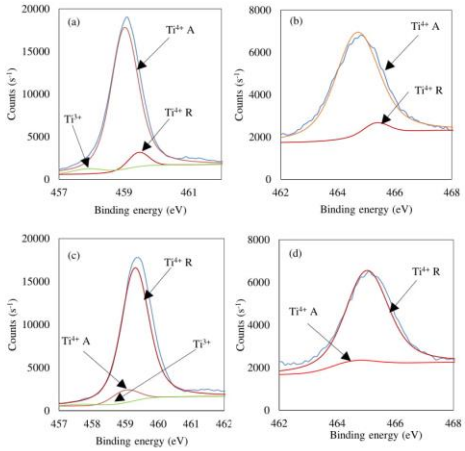

Figure 11. Deconvolution of X-ray photoelectron spectroscopy (XPS) spectra for Ti $2p_{3/2}$ and $2p_{1/2}$ for TBT-HIO_3_20 (**a**,**b**) and TBT-HIO_3_100 (**c**,**d**).

The Ti 2p spectrum could be deconvoluted into two components at 459 eV and 465 eV binding energies that refer to Ti $2p_{3/2}$ and $2p_{1/2}$, respectively. Ti $2p_{3/2}$ after deconvolution could be divided into 459.0 eV and 459.5 eV peaks and identified as Ti^{4+}, resulting from the presence of anatase and rutile, respectively. For sample TBT-HIO_3_20 a trace quantity (0.9 at.%) of Ti^{3+} was observed, which could be assigned to oxygen vacancies [61]. However, apart from this sample, there was no Ti^{3+} signal observed, suggesting the lack of reduced form of titanium as well as oxygen vacancies. The presented XPS titanium peaks corresponding to both anatase and rutile correlate with XRD analysis. Together with the increase of HIO_3 oxidant amount used for the synthesis, the rutile content increase, which is also clearly visible in the presented spectra. The Ti/O ratio for all analyzed photocatalysts was equaled to 0.38. It suggests no surface and state of elements change between TBT-HIO_3 samples.

For final evaluation, since the synthesized photocatalysts do not have admixtures but their color as well as physicochemical and photocatalytic properties arise from created intrinsic defects the region I 3d was analyzed to check the presence of iodine species in the obtained samples. The results are presented in Figure 12.

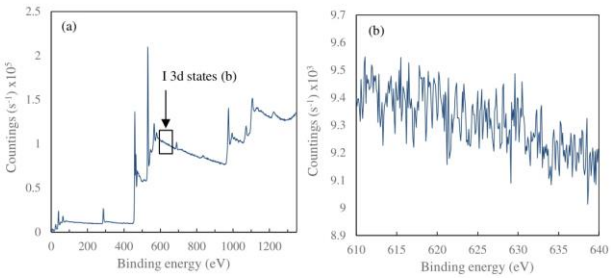

Figure 12. XPS analyses spectra for TBT-HIO$_3$_20 sample (**a**) with the I 3d states binding energy enlargement (**b**).

As mentioned in the literature [62–64] I 3d states are in the range of 620–635 eV. However, as it could be seen in Figure 12b, there is no peak, which could be assigned to I 3d states. In this regard, for TBT-HIO$_3$ samples changes in physicochemical and, what is the most important, photochemical properties are caused by intrinsic defects, not titania doping with impurities.

In order to evaluate morphological differences among the obtained defective TiO_2 photocatalysts, the SEM analysis for selected samples was conducted, and the results are presented in Figure S1 in the Supplementary Materials. It was found that both samples are formed from aggregated particles. However, it is noticeable that aggregates of TBT-HIO$_3$_50 had a much smaller size, comparing to the TiO_2-TBT photocatalyst, although no differences were determined in crystalline sizes or the BET specific surface area.

The photocatalytic activity of defective TiO_2-HIO$_3$ samples was evaluated in the phenol degradation reaction, both in UV-Vis and Vis ($\lambda > 420$ nm) light. Simultaneously, the effect of e^-, h^+, $^\bullet O_2^-$, and $^\bullet$OH scavengers' presence on photoactivity was studied. The results, presented as the efficiency of phenol removal (%) as well as phenol degradation rate constant k are presented in Figure 13a,b and Figure 14.

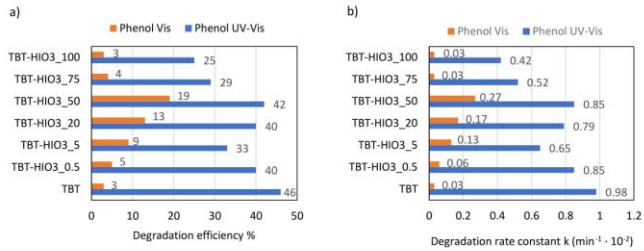

Figure 13. Efficiency of phenol degradation in UV-Vis and Vis light for defective TiO_2-HIO$_3$ photocatalysts, presented as % of degradation (**a**) and rate constant k (**b**).

The best photocatalytic activity was obtained for the defective TBT-HIO$_3$_50 sample. After 60 min of irradiation, about 42% of phenol was degraded in UV-Vis and 19% in Vis light. It may also be noticed a characteristic normal distribution of the obtained results, where maximum falls on 50 mol%

of iodic acid. Both smaller and higher concentrations of oxidant used in hydrothermal synthesis process caused a decrease in obtained TBT-HIO_3 photoactivity.

The obtained photodegradation efficiency results correlate well with photoluminescence (PL) spectra, UV-Vis spectra, and EPR spectra analyses. From the three analyzed samples (TBT-HIO_3_20, TBT-HIO_3_50, and TBT-HIO_3_75), the most intense EPR signal was assigned to defective TBT-HIO_3_75, where the highest concentration of oxidant (75 mol%) was used. From the PL spectra analysis, the TBT-HIO_3_75 sample showed the highest intensity among analyzed photocatalysts, which indicated the highest electron-hole recombination as well as the lowest phenol degradation efficiency. It could suggest that too high of a concentration of defects in the TiO_2 structure could significantly decrease the photocatalytic activity of the defective material. The presented results also correlate with the crystalline structure of the obtained materials. With the increase of the HIO_3 concentration, the rutile content was increased (up to 80% for the TBT-HIO_3_75 photocatalyst). According to the literature, too high rutile concentration could also be responsible for decreasing of the TiO_2 photocatalytic activity [65].

The addition of BQ as an $^{\bullet}O_2^-$ scavenger caused a significant reduction of photoactivity of all obtained TBT-HIO_3 photocatalysts, regardless of the used HIO_3 concentration for their synthesis. It indicated that superoxide radical anions are the most crucial reactive oxygen species in the photocatalytic reaction with the use of defective TBT-HIO_3 samples. After introducing to the photoreactive SN, AO, and t-BuOH, the changes of the phenol degradation rate constant k, comparing to the process without scavenger, were negligible.

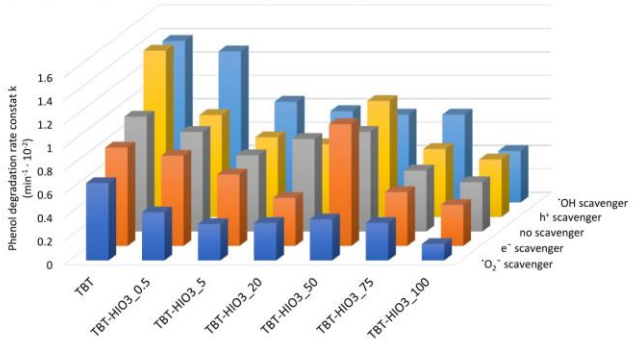

Figure 14. UV-Vis photocatalytic degradation of phenol for TiO_2-HIO_3 photocatalyst in the presence of e^-, h^+, $^{\bullet}O_2^-$, and $^{\bullet}OH$ scavengers.

The physicochemical and surface properties of the most active defective TiO_2 photocatalyst (TBT-HIO_3_50) was analyzed before and after 1 hour of phenol degradation process in the presence of UV-Vis irradiation to confirm the photocatalyst stability. The obtained results are presented in Figures S2–S4 and in Table S1 in the Supplementary Materials. The additional XPS as well as XRD analysis showed, that after 1 hour of degradation process the physicochemical properties, e.g., crystalline size and surface composition did not change. Moreover, both TBT-HiO_3_50 samples showed also a similar FTiR spectra (see in Figure S3) with a broad band at 3450–3050 cm^{-1} attributed to the stretching mode of the hydroxyl group on the TiO_2 surface. The Ti-O bending mode and deformative vibration of the Ti-OH stretching mode may be observed at 498-463 cm^{-1} and 1629 cm^{-1} respectively. The band at 1629 cm^{-1} may be attributed to water adsorbed on the TiO_2 surface.

Final stability and reusability test of defective TBT-HIO_3_50 photocatalyst was performed in three 3-hours-long subsequent cycles of phenol degradation under UV-Vis light. The obtained results are presented in Figure 15.

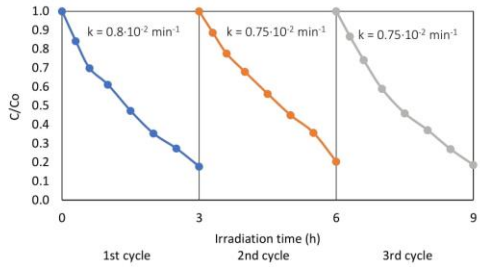

Figure 15. Efficiency of UV-Vis phenol degradation in the presence of a defective TBT-HIO_3_50 photocatalyst measured in the three subsequent cycles.

After 9 h of irradiation, the percentage of degraded phenol was 80%, which is almost equal to photodegradation efficiency after 3 h (82%). A slight drop in the rate constant k could be seen (from k = 0.8·× 10^{-2} min^{-1} after first cycle to k = 0.75·× 10^{-2} min^{-1} after the second and the third cycle). However, the analysed photocatalyst still revealed good stability and reusability.

3.3. The Effect of Thermal Treatment on Defective TiO_2-HIO_3 Physicochemical and Photocatalytic Properties

Further, the investigation on defective photocatalysts concerned with the thermal stability of TiO_2-HIO_3 samples was undertaken. A series of five TiO_2-HIO_3 photocatalysts, calcined in different temperatures from 300 to 1000 °C was obtained. As a reference, as characterized earlier, the TBT-HIO_3_20 photocatalyst was used, named as TBT-HIO_3_20_300, as it was calcined at 300 °C. General physicochemical characteristics of the obtained defective TiO_2-HIO_3_T samples, i.e., BET surface area, pore volume, calculated bandgap (Eg), and their images are shown in Table 7.

Table 7. Physicochemical characteristic of the obtained defective TiO_2-HIO_3_T samples.

Sample	BET ($m^2 \cdot g^{-1}$)	V Pores ($cm^3 \cdot g^{-1}$)	Eg (ev)	Photo
TBT	169	0.0836	3.2	
TBT-HIO_3_20_300	172	0.0847	2.7	
TBT-HIO_3_20_400	88	0.0432	2.85	
TBT-HIO_3_20_450	48	0.0236	2.9	

TBT-HIO_3_20_650	0.7	0.0003	2.9	
TBT-HIO_3_20_1000	0.4	0.0002	2.8	

The addition of HIO_3 to the reaction environment had a negligible effect on changing the BET surface area as well as particles and crystallites sizes. Nonetheless, increasing the calcination temperature by 100 °C led to a 50% surface area decreasing (from 172 to 88 $m^2 \cdot g^{-1}$ for TBT-HIO_3_20_300 and TBT-HIO_3_20_400, respectively). Further increasing of the thermal treatment up to 1000 °C caused the decrease of the BET surface area to 0.4 $m^2 \cdot g^{-1}$.

Changes in the BET surface area correlate well with differences noted on the XRD patterns for TBT-HIO_3_T samples, presented in Figure 16. The higher the calcination temperature, the more intense the XRD diffraction peaks, which resulted from the increase in photocatalysts crystallinity [66]. Other changes concern crystallites growth (for anatase: from 5 to 12 nm TBT-HIO_3_20_300 and TBT-HIO_3_20_450, respectively and for rutile: from 17 to 53.5 nm for TBT-HIO_3_20_400 and TBT-HIO_3_20_1000, respectively) as well as the anatase to rutile phase transition. No rutile phase was present in TBT-HIO_3_20_300 photocatalyst, while its content increased rapidly as the calcination temperature increased until it reached 100% at T = 650 °C. As mentioned before, the anatase to rutile transition takes place in about 600 °C. However, the introduction to crystal structure various types of defects promotes this transformation at lower temperatures [67].

The detailed information about crystallite sizes and phase contents presented with standard deviation are given in Table 8.

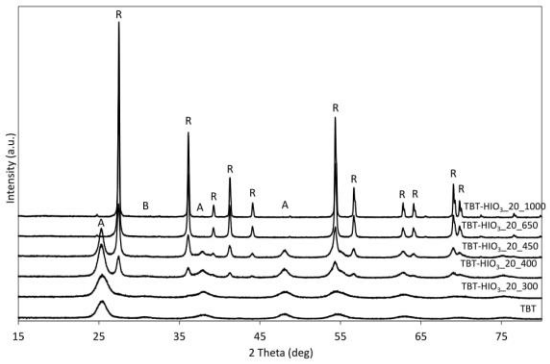

Figure 16. XRD patterns for defective TiO_2-HIO_3_T photocatalysts (A–anatase, B–brookite, and R–rutile).

Table 8. Crystalline phases characteristic for the obtained defective TiO_2-HIO_3_T samples.

Sample	Crystalline Size and Phase Content					
	Anatase		Rutile		Brookite	
	Size (nm)	Phase Content (wt%)	Size (nm)	Phase Content (wt%)	Size (nm)	Phase Content (wt%)
TBT	5.97 ± 0.04	95.5 ± 1	-	-	6.1 ± 0.3	4.5 ± 1
TBT-HIO_3_20_300	5.14 ± 0.03	96 ± 1	-	-	4.0 ± 0.6	4 ± 0.5
TBT-HIO_3_20_400	8.34 ± 0.05	70.5 ± 0.5	17.4 ± 0.2	29.5 ± 0.5	-	-
TBT-HIO_3_20_450	12.13 ± 0.09	40 ± 0.5	22.51 ± 0.19	60.5 ± 0.5	-	-
TBT-HIO_3_20_650	-	-	40.3 ± 0.3	100 ± 0.5	-	-
TBT-HIO_3_20_1000	-	-	53.5 ± 0.3	100 ± 0.5	-	-

Shifting of the absorption maximum on DR/UV-Vis spectra for defective TiO_2-HIO_3_T samples (Figure 17) was mostly related to the anatase to rutile phase transition. It was mentioned by Valencia et al. [68] that anatase bandgap is equal to 3.23 eV, while rutile from 3.06 to 3.10 eV. From Tauc transformation, bandgap values forr TiO_2-HIO_3_T photocatalysts were calculated and are in the range from 2.7 to 2.9 eV. Despite the changes in photocatalysts phase contents a slight decrease in bandgap value, in response to TiO_2, could be caused by defects formation in the crystal structure [69].

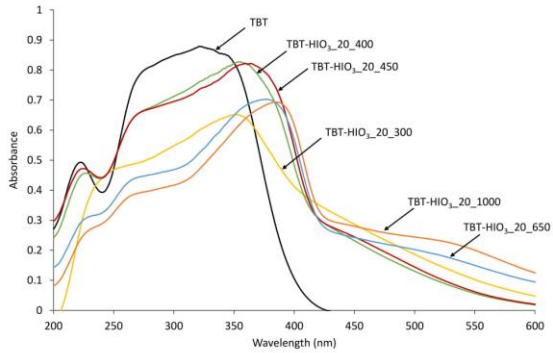

Figure 17. UV-Vis diffuse spectra for pure TiO_2 and defective TiO_2-HIO_3_20_T photocatalysts calcined in different temperatures.

Similarly to TBT-HIO_3 photocatalysts, TBT-HIO_3_20_T samples' surface properties, as well as the state of elements, were analyzed using XPS analysis. The obtained results are presented in Figure 18a–f and Table 9.

Table 9. Fraction of oxidation states of Ti as well as surface composition of selected defected TBT-HIO_3_20_T photocatalysts determined by X-ray photoelectron spectroscopy (XPS).

Photocatalyst	Ti $2p_{3/2}$ (%)		O 1s (%)
	Ti^{4+}	Ti^{3+}	
TBT-HIO_3_20_300	27.56	0.9	71.54
TBT-HIO_3_20_400	27.99	0	72.01
TBT-HIO_3_20_450	28.43	0	71.58

States of elements for thermally treated TBT-HIO_3_20_T are identical as for previously described TBT-HIO_3 samples. Oxygen vacancies are not detected, except TBT-HIO_3_20_300 photocatalyst with 0.9 at.% of Ti^{3+} form. Observed deconvoluted spectra for Ti $2p_{3/2}$ and $2p_{1/2}$ corresponded well with XRD analysis and showed the anatase–rutile transition.

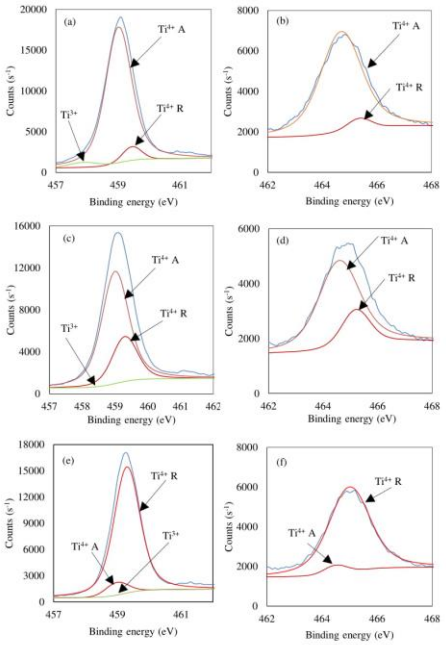

Figure 18. Deconvolution of X-ray photoelectron spectroscopy (XPS) spectra for Ti $2p_{3/2}$ and $2p_{1/2}$ for TBT-HIO_3_20_300 (**a**,**b**), TBT-HIO_3_20_400 (**c**,**d**) and TBT-HIO_3_20_450 (**e**,**f**).

For the final evaluation, photocatalytic activity tests for TiO_2-HIO_3_20_T samples in the phenol degradation reaction, both in UV-Vis and Vis ($\lambda > 420$ nm) light, were performed. Simultaneously, the effect of e^-, h^+, $^\bullet O_2^-$, and $^\bullet OH$ scavengers' presence on photoactivity was studied. Results,

presented as phenol removal in % as well as phenol degradation rate constant k, are presented in Figure 19a,b and Figure 20.

According to the literature, the optimum calcination temperature for iodine-doped photocatalysts is between 300 and 400 °C, with the temperature of 300 °C preferred when potassium iodide is used as an iodine precursor, while 400 °C when iodic acid is applied as a precursor [70,71]. Above these temperatures, the photoactivity of prepared materials decreased significantly. Nonetheless, for TBT-HIO_3 defective photocatalysts, where iodic acid was used as an oxidative environment for titanium vacancies generation, the highest efficiency in phenol degradation reaction was noticed for sample calcined in 450 °C (57% of phenol removal after 1 h of UV-Vis light irradiation). Moreover, the yellow color of the sample was maintained even after calcination at 1000 °C (see in Table 7). It suggests that the obtained intrinsic defects in the crystal structure of TiO_2 were stable even in higher calcination temperatures. A slightly different situation was observed when photoactivity tests were carried out in the visible light. Apart from TBT-HIO_3_20_300 photocatalyst, all samples showed negligible efficiency in phenol degradation reaction. However, this could be caused by increasing rutile phase content in the photocatalyst structure [72].

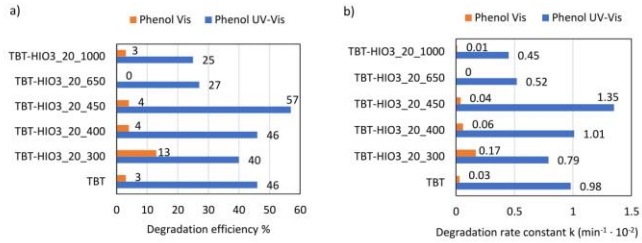

Figure 19. Efficiency of phenol degradation in UV-Vis and Vis light for defective TiO_2-HIO_3_20_T photocatalysts, presented as % of degradation (a) and rate constant k (b).

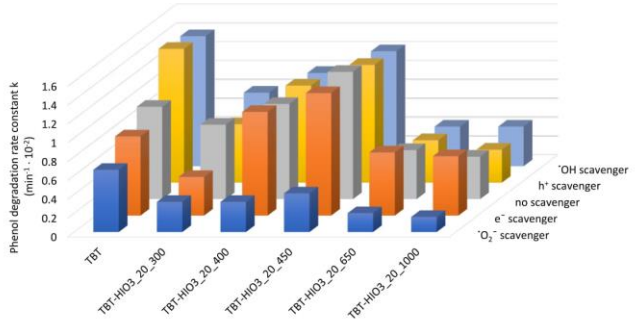

Figure 20. UV-Vis photocatalytic degradation of phenol for TiO_2-HIO_3_20_T photocatalysts in the presence of e^-, h^+, $^{\bullet}O_2^-$, and $^{\bullet}OH$ scavengers.

For TiO_2-HIO_3_20_T photocatalysts, there was no difference in mechanistic studies as compared to the previously discussed defected TiO_2 series. The superoxide radical anions remained the most crucial for the phenol degradation reaction, while the addition of ammonium oxalate, tert-butyl alcohol, and silver nitrate as scavengers did not affect the photoactivity.

4. Conclusions

Hydrothermal treatment in the presence of an oxidative environment led to titanium vacancies generation in the structure of TiO_2. Created intrinsic defects caused yellow coloration of titania, while at the same time, absorption of semiconductor was shifted to visible light as well as bandgap was reduced to 2.9 eV. Among studied oxidants, defective TiO_2 samples obtained in the presence of iodic acid were characterized by the highest phenol degradation efficiency in visible light. In-depth analysis, including EPR and XPS measurements, confirmed that increasing in photoactivity, compared to pure material, is directly caused by defects, not by doping. Further analysis regarding the optimum amount of HIO_3 as well as the thermal stability of synthesized defected TiO_2-HIO_3 photocatalysts, showed that from 20 to 50 mol% of oxidant added to hydrothermal reaction is capable of creating material with a great photoactivity and no loss in photoactivity up to 450 °C.

Supplementary Materials: The following are available online at www.mdpi.com/1996-1944/13/12/2763/s1, Figure S1: SEM analysis of pure TiO2-TBT (a,b) and defective TBT-HIO3_50 (c,d) photocatalysts, Figure S2: Deconvolution of X-ray photoelectron spectroscopy (XPS) for Ti 2p3/2 and O 1s for TBT-HIO3_50 before (a,b) and after phenol photodegradation (c,d). Figure S3: XRD patterns for defective TBT-HIO3_50 photocatalyst before and after a photocatalytic phenol degradation (A–anatase, R–rutile). Figure S4: Fast-Fourier transformation spectroscopy (FTIR) spectra of defective TBT-HIO3_50 before and after phenol photodegradation. Table S1: Fraction of oxidation states of Ti as well as surface composition of defective TBT-HIO3_50 photocatalyst before and after phenol degradation.

Author Contributions: Conceptualization, A.Z.-J.; methodology, A.Z.-J. and S.D.; formal analysis, Z.B., A.S. and S.D.; investigation, Z.B., A.S., D.P. and J.R.; resources, A.Z.-J.; writing—original draft preparation, Z.B.; writing—review and editing, A.Z.-J.; supervision, A.Z.-J.; funding acquisition, A.Z.-J. All authors have read and agreed to the published version of the manuscript.

Funding: This research was funded by Polish National Science Centre (Grant No. NCN 2018/30/E/ST5/00845).

Acknowledgments: This research was supported by Polish National Science Centre, grant no. NCN 2018/30/E/ST5/00845) and Polish Ministry of Science and Higher Education grant no. 0525/E-359/STYP/13/2018-Scholarships for outstanding young scientists.

Conflicts of Interest: The authors declare no conflict of interest.

References

1. Awfa, D.; Ateia, M.; Fujii, M.; Johnson, M.S.; Yoshimura, C. Photodegradation of pharmaceuticals and personal care products in water treatment using carbonaceous-TiO_2 composites: A critical review of recent literature. *Water Res.* **2018**, *142*, 26–45.
2. Naeem, K.; Ouyang, F. Preparation of Fe^{3+} -doped TiO_2 nanoparticles and its photocatalytic activity under UV light. *Phys. B Phys. Condens. Matter* **2010**, *405*, 221–226.
3. Ashkarran, A.A.; Aghigh, S.M.; Kavianipour, M.; Farahani, N.J. Visible light photo-and bioactivity of Ag/TiO_2 nanocomposite with various silver contents. *Curr. Appl. Phys.* **2011**, *11*, 1048–1055.
4. Zielińska-Jurek, A.; Kowalska, E.; Sobczak, J.; Lisowski, W.; Ohtani, B.; Zaleska-Medynska, A. Preparation and characterization of monometallic (Au) and bimetallic (Ag/Au) modified-titania photocatalysts activated by visible light. *Appl. Catal. B: Environ.* **2010**, *101*, 504–514.
5. Huang, J.G.; Guo, X.T.; Wang, B.; Li, L.Y.; Zhao, M.X.; Dong, L.L.; Liu, X.J.; Huang, Y.T. Synthesis and photocatalytic activity of Mo-doped TiO2 nanoparticles. *J. Spectrosc.* **2015**, 681850 .
6. Yamashita, H.; Harada, M.; Misaka, J.; Takeuchi, M.; Neppolian, B.; Anpo, M. Photocatalytic degradation of organic compounds diluted in water using visible light-responsive metal ion-implanted TiO_2 catalysts: Fe ion-implanted TiO2. *Catal. Today* **2003**, *84*, 191–196.

7. A. Zielińska-Jurek, Z.; Wei, M.; Janczarek, I.; Wysocka, E.; Kowalska, Size-controlled synthesis of Pt particles on TiO_2 surface: Physicochemical characteristic and photocatalytic activity. *Catalysts* **2019**, *9*, 940, doi:10.3390/catal9110940.
8. Zielińska-Jurek, A.; Wei, Z.; Janczarek, M.; Wysocka, I.; Kowalska, E.; Jurek, Z. The effect of calcination temperature on structure and photocatalytic properties of Au/Pd nanoparticles supported on TiO_2. *Appl. Catal. B Environ.* **2014**, *152–153*, 202–211.
9. Suwannaruang, T.; Kamonsuangkasem, K.; Kidkhunthod, P.; Chirawatkul, P.; Saiyasombat, C.; Chanlek, N.; Wantala, K. Influence of nitrogen content levels on structural properties and photocatalytic activities of nanorice-like N-doped TiO2 with various calcination temperatures. *Mater. Res. Bull.* **2018**, *105*, 265–276.
10. Irie, H.; Watanabe, Y.; Hashimoto, K. Carbon-doped Anatase TiO2 Powders as a Visible-light Sensitive Photocatalyst. *Chem. Lett.* **2003**, *32*, 772–773.
11. Trapalis, C.; Todorova, N.; Giannakopoulou, T.; Romanos, G.; Vaimakis, T.; Yu, J. Preparation of fluorine-doped TiO2 photocatalysts with controlled crystalline structure. *Int. J. Photoenergy* **2008**, doi:10.1155/2008/534038.
12. Wang, X.K.; Wang, C.; Jiang, W.Q.; Guo, W.L.; Wang, J.G. Sonochemical synthesis and characterization of Cl-doped TiO_2 and its application in the photodegradation of phthalate ester under visible light irradiation. *Chem. Eng. J.* **2012**, *189–190*, 288–294.
13. Rockafellow, E.M.; Stewart, L.K.; Jenks, W.S. Is sulfur-doped TiO2 an effective visible light photocatalyst for remediation? *Appl. Catal. B Environ.* **2009**, *91*, 554–562.
14. Chowdhury, P.; Moreira, J.; Gomaa, H.; Ray, A.K. Visible-solar-light-driven photocatalytic degradation of phenol with dye-sensitized TiO_2: Parametric and kinetic study. *Ind. Eng. Chem. Res.* **2012**, *51*, 4523–4532.
15. Diaz-Angulo, J.; Gomez-Bonilla, I.; Jimenez-Tohapanta, C.; Mueses, M.; Pinzon, M.; Machuca-Martinez, F. Visible-light activation of TiO_2 by dye-sensitization for degradation of pharmaceutical compounds. *Photochem. Photobiol. Sci.* **2019**, *18*, 897–904.
16. Shang, J.; Zhao, F.; Zhu, T.; Li, J. Photocatalytic degradation of rhodamine B by dye-sensitized TiO_2 under visible-light irradiation. *Sci. China Chem.* **2011**, *54*, 167–172.
17. Nosaka, Y.; Matsushita, M.; Nishino, J.; Nosaka, A. Nitrogen-doped titanium dioxide photocatalysts for visible response prepared by using organic compounds. *Sci. Technol. Adv. Mater.* **2005**, *6*, 143–148.
18. Kitano, M.; Funatsu, K.; Matsuoka, M.; Ueshima, M.; Anpo, M. Preparation of Nitrogen-Substituted TiO2 Thin Film Photocatalysts by the Radio Frequency Magnetron Sputtering Deposition Method and Their Photocatalytic Reactivity under Visible Light Irradiation. *J. Phys. Chem. B* **2006**, *110*, 25266–25272.
19. Dong, F.; Guo, S.; Wang, H.; Li, X.; Wu, Z. Enhancement of the Visible Light Photocatalytic Activity of C-Doped TiO2 Nanomaterials Prepared by a Green Synthetic Approach. *J. Phys. Chem. C* **2011**, *115*, 13285–13292.
20. Dong, H.; Zeng, G.; Tang, L.; Fan, C.; Zhang, C.; He, X.; He, Y. An overview on limitations of TiO_2-based particles for photocatalytic degradation of organic pollutants and the corresponding countermeasures. *Water Res.* **2015**, *79*, 128–146.
21. Zhang, J.; Wu, Y.; Xing, M.; Leghari, S.A.K.; Sajjad, S. Development of modified N doped TiO2 photocatalyst with metals, nonmetals and metal oxides. *Energy Environ. Sci.* **2010**, *3*, 715–726.
22. Di Paola, A.; Ikeda, S.; Marcì, G.; Ohtani, B.; Palmisano, L. Transition metal doped TiO_2: Physical properties and photocatalytic behaviour. *Int. J. Photoenergy* **2001**, *3*, 171–176.
23. Wang, Z.; Lang, X. Visible Light Photocatalysis of Dye-Sensitized TiO2: The Selective Aerobic Oxidation of Amines to Imines. *Appl. Catal. B Environ.* **2018**, *224*, 404–409.
24. Ferrere, S.; Gregg, B.A. Photosensitization of TiO2 by [FeII(2,2′-bipyridine-4,4′-dicarboxylic acid)2(CN)2]: Band Selective Electron Injection from Ultra-Short-Lived Excited States. *J. Am. Chem. Soc.* **1998**, *120*, 843–844.
25. Mongal, B.N.; Tiwari, A.; Malapaka, C.; Pal, U. Ruthenium(III)-bis(phenolato)bipyridine/TiO2 hybrids: Unprecedented photocatalytic hydrogen evolution. *Dalt. Trans.* **2019**, *48*, 10070–10077.
26. Priyanka, K.P.; Sankararaman, S.; Balakrishna, K.M.; Varghese, T. Enhanced Visible Light Photocatalysis using TiO2/Phthalocyanine Nanocomposites for the Degradation of Selected Industrial Dyes. *J. Alloys Compd.* **2017**, *720*, 541–549.
27. Zhao, J.; Wu, T.; Wu, K.; Oikawa, K.; Hidaka, H.; Serpone, N. Photoassisted Degradation of Dye Pollutants. 3. Degradation of the Cationic Dye Rhodamine B in Aqueous Anionic Surfactant/TiO_2 Dispersions under Visible Light Irradiation: Evidence for the Need of Substrate Adsorption on TiO_2 Particles. *Environ. Sci. Technol.* **1998**, *32*, 2394–2400.

28. Zhao, J.; Chen, C.; Ma, W. Photocatalytic degradation of organic pollutants under visible light irradiation. *Top. Catal.* **2005**, *35*, 269–278.
29. Kang, X.; Liu, S.; Dai, Z.; He, Y.; Song, X.; Tan, Z. Titanium Dioxide: From Engineering to Applications. *Catalysts* **2019**, *9*, 1–32.
30. Lin, L.; Huang, J.; Li, X.; Abass, M.A.; Zhang, S. Effective Surface Disorder Engineering of Metal Oxide Nanocrystals for Improved Photocatalysis. *App. Catal. B Environ.* **2017**, *203*, 615–624.
31. Zuo, F.; Bozhilov, K.; Dillon, R.J.; Wang, L.; Smith, P.; Zhao, X.; Bardeen, C.; Feng, P. Active Facets on Titanium(III)-Doped TiO2: An Effective Strategy to Improve the Visible-Light Photocatalytic Activity. *Angew. Chem.* **2012**, *51*, 6223–6226.
32. Ullattil, S.G.; Narendranath, S.B.; Pillai, S.C.; Periyat, P. Black TiO2 Nanomaterials: A Review of Recent Advances. *Chem. Eng. J.* **2018**, *343*, 708–736.
33. Lettieri, S.; Gargiulo, V.; Alfe, M.; Amati, M.; Zeller, P.; Maraloiu, V.-A.; Borbone, F.; Muñoz-García, A.B.; Pavone, M.; Maddalena, P. A Simple Ethanol Refluxing Method for Production of Blue Colored Titanium Dioxide with Oxygen Vacancies and Visible Light-Driven Photocatalytic Properties. *J. Phys. Chem. C* **2020**, *124*, 3564–3576.
34. Wu, Q.; Huang, F.; Zhao, M.; Xu, J.; Zhou, J.; Wang, Y. Ultra-small yellow defective TiO_2 nanoparticles for co-catalyst free photocatalytic hydrogen production. *Nano Energy* **2016**, *24*, 63–71.
35. Guo, Z.; Ma, R.; Li, G. Degradation of phenol by nanomaterial TiO_2 in wastewater. *Chem. Eng. J.* **2006**, *119*, 55–59.
36. Sulowska, A.; Wysocka, I.; Pelczarski, D.; Karczewski, J.; Zielińska-Jurek, A. Hybrid TiO2 – Polyaniline Photocatalysts and their Application in Building Gypsum Plasters. *Materials* **2020**, *13*, 1–22.
37. Shet, A.; Vidya, S.K. Solar light mediated photocatalytic degradation of phenol using Ag core-TiO2shell (Ag@TiO2) nanoparticles in batch and fluidized bed reactor. *Sol. Energy* **2016**, *127*, 67–78.
38. Kang, X.; Song, X.-Z.; Han, Y.; Cao, J.; Tan, Z. Defect-engineered TiO2 Hollow Spiny Nanocubes for Phenol Degradation under Visible Light Irradiation. *Sci. Rep.* **2018**, *8*, 5904.
39. Colon, G.; Sanchez-Espana, J.M.; Hidalgo, M.C.; Navio, J.A. Effect of TiO2 acidic pre-treatment on the photocatalytic properties for phenol degradation. *J. Photochem. Photobiol. A Chem.* **2006**, *179*, 20–27.
40. Wysocka, I.; Kowalska, E.; Trzciński, K.; Łapiński, M.; Nowaczyk, G.; Zielińska-Jurek, A. UV-Vis-Induced Degradation of Phenol over Magnetic Photocatalysts Modified with Pt, Pd, Cu and Au Nanoparticles. *Nanomaterials* **2018**, *8*, 1–20.
41. Gamboa, J.A.; Pasquevich, D.M. Effect of Chlorine Atmosphere on the Anatase-Rutile Transformation. *J. Am. Chem. Soc.* **1992**, *75*, 2934–2938.
42. Byrne, C.; Fagan, R.; Hinder, S.; McCormack, D.E.; Pillai, S.C. New Approach of Modifying the Anatase to Rutile Transition Temperature in TiO2 Photocatalysts. *RSC Adv.* **2016**, *6*, 95232–95238.
43. Janczarek, M.; Kowalska, E. On the Origin of Enhanced Photocatalytic Activity of Copper-Modified Titania in the Oxidative Reaction Systems. *Catalysts* **2017**, *7*, 1–26.
44. Fittipaldi, M.; Gatteschi, D.; Fornasiero, P. The power of EPR techniques in revealing active sites in heterogeneous photocatalysis: The case of anion doped TiO_2. *Catal. Today* **2013**, *206*, 2–11.
45. Kumar, C.P.; Gopal, N.O.; Wang, T.C. EPR Investigation of TiO_2 Nanoparticles with Temperature-Dependent Properties. *J. Phys. Chem. B* **2006**, *110*, 5223–5229.
46. Wang, S.; Pan, L.; Song, J.-J.; Mi, W.; Zou, J.-J.; Wang, L.; Zhang, X. Titanium-Defected Undoped Anatase TiO2 with p-Type Conductivity, Room-Temperature Ferromagnetism, and Remarkable Photocatalytic Performance. *J. Am. Chem. Soc.* **2015**, *137*, 2975–2983.
47. Su, R.; Bechstein, R.; Sø, L.; Vang, R.T.; Sillassen, M.; Esjornsson, B.; Palmqvist, A.; Besenbacher, F. How the Anatase-to-Rutile Ratio Influences the Photoreactivity of TiO_2. *J. Phys. Chem. C* **2011**, *115*, 24287–24292.
48. Kubiak, A.; Siwińska-Ciesielczyk, K.; Jesionowski, T. Titania-Based Hybrid Materials with ZnO, ZrO_2 and MoS$_2$: A Review. *Materials* **2018**, *11*, 1–56.
49. Zalas, M. Synthesis of N-doped template-free mesoporous titania for visible light photocatalytic applications. *Catal. Today* **2014**, *230*, 91–96.
50. Wang, K.; Janczarek, M.; Wei, Z.; Raja-Mogan, T.; Endo-Kimura, M.; Khedr, T.M.; Ohtani, B.; Kowalska, E. Morphology- and Crystalline Composition-Governed Activity of Titania-Based Photocatalysts: Overview and Perspective. *Catalysts* **2019**, *9*, 1054.
51. Shimura, K.; Yoshida, H. Heterogeneous photocatalytic hydrogen production from water and biomass. *Energy Environ. Sci.* **2011**, *4*, 2467–2481.

52. Palmer, A.G.; Gao, R.; Maresh, J.; Erbil, W.K.; Lynn, D.G. Chemical Biology of Multi-Host/Pathogen Interactions: Chemical Perception and Metabolic Complementation. *Annu. Rev. Phytopathol.* **2014**, *42*, 439–464.
53. Lv, K.; Guo, X.; Wu, X.; Li, Q.; Ho, W.; Li, M.; Ye, H.; Du, D. Photocatalytic selective oxidation of phenol to produce dihydroxybenzenes in a TiO2/UV system: Hydroxyl radical versus hole. *Appl. Catal. B Environ.* **2016**, *199*, 405–411.
54. Wetchakun, N.; Incessungvorn, B.; Wetchakun, K.; Phanichphant, S. Influence of calcination temperature on anatase to rutile phase transformation in TiO_2 nanoparticles synthesized by the modified sol-gel method. *Mater. Lett.* **2012**, *82*, 195–198.
55. Hanaor, D.A.H.; Sorrell, C.C. Review of the anatase to rutile phase transformation. *J. Mater. Sci.* **2011**, *46*, 855–874.
56. Powell, M.J.; Quesada-Cabrera, R.; Travis, W.L.; Parkin, I.P. High-throughput synthesis of core–shell and multi-shelled materials by fluidised bed chemical vapour deposition. Case study: Double-shell rutile–anatase particles. *J. Mater. Chem. A* **2015**, *3*, 17241–17247.
57. Li, W.; Body, M.; Legein, C.; Borkiewicz, O.J.; Dambournet, D. Atomic Insights into Nanoparticle Formation of Hydroxyfluorinated Anatase Featuring Titanium Vacancies. *Inorg. Chem.* **2016**, *55*, 7182–7187.
58. Ma, J.; Li, W.; Morgan, B.J.; Światowska, J.; Baddour-Hadjean, R.; Body, M.; Legein, C.; Borkiewicz, O.J.; Leclerc, S.; Groult, H.; et al. Lithium Intercalation in Anatase Titanium Vacancies and the Role of Local Anionic Environment. *Chem. Mater.* **2018**, *30*, 3078–3089.
59. Saha, A.; Moya, A.; Kahnt, A.; Iglesias, D.; Marchesan, S.; Wannemacher, R.; Prato, M.; Vilatela, J.J.; Guldi, D.M. Interfacial Charge Transfer in Functionalized Multi-walled Carbon Nanotube@TiO_2 nanofibres. *Nanoscale* **2017**, *9*, 7911–7921.
60. Liu, B.; Zhao, X.; Zhao, Q.; He, X.; Feng, J. Effect of heat treatment on the UV-vis-NIR and PL spectra of TiO2 films. *J. Electron Spectros. Relat. Phenomena* **2005**, *148*, 158–163.
61. Bielan, Z.; Kowalska, E.; Dudziak, S.; Wang, K.; Ohtani, B.; Zielińska-Jurek, A. Mono- and bimetallic (Pt/Cu) titanium(IV) oxide core-shell photocatalysts with UV/Vis light activity and magnetic separability. *Catal. Today* **2020**, doi:10.1016/j.cattod.2020.05.034.
62. Zielińska-Jurek, A.; Klein, M.; Hupka, J. Enhanced visible light photocatalytic activity of Pt/I-TiO_2 in a slurry system and supported on glass packing. *Sep. Purif. Technol.* **2017**, *189*, 246–252.
63. Tojo, S.; Tachikawa, T.; Fujitsuka, M.; Majima, T. Iodine-Doped TiO_2 Photocatalysts: Correlation between Band Structure and Mechanism. *J. Phys. Chem. C* **2008**, *112*, 14948–14954.
64. Jayashree, S.; Ashokkumar, M. Switchable Intrinsic Defect Chemistry of Titania for Catalytic Applications. *Catalysts* **2018**, *8*, 1–26.
65. Gautam, A.; Kshirsagar, A.; Biswas, R.; Banerjee, S.; Khanna, P.K. Photodegradation of Organic Dyes Based on Anatase and Rutile TiO2 Nano-Particles. *RSC Adv.* **2016**, *6*, 2746–2759.
66. Mrotek, E.; Dudziak, S.; Malinowska, I.; Pelczarski, D.; Ryżyńska, Z.; Zielińska-Jurek, A. Improved degradation of etodolac in the presence of core-shell $ZnFe_2O_4$/SiO_2/TiO_2 magnetic photocatalyst. *Sci. Total Environ.* **2020**, *724*, 1–12.
67. Ricci, P.C.; Carbonaro, C.M.; Stagi, L.; Salis, M.; Casu, A.; Enzo, S.; Delogu, F. Anatase-To-Rutile Phase Transition In Nanoparticles Irradiated By Visible Light. *J. Phys. Chem. C* **2013**, *117*, 785–7857.
68. Valencia, S.; Marín, J.M.; Restrepo, G. Study of the Bandgap of Synthesized Titanium Dioxide Nanoparticules Using the Sol-Gel Method and a Hydrothermal Treatment. *Open Mater. Sci. J.* **2010**, *4*, 9–14.
69. Khan, M.E.; Khan, M.M.; Min, B.-K.; Cho, M.H. Microbial fuel cell assisted band gap narrowed TiO2 for visible light- induced photocatalytic activities and power generation. *Sci. Rep.* **2018**, *8*, 1–12.
70. Wang, W.A.; Shi, Q.; Wang, Y.P.; Cao, J.L.; Liu, G.Q.; Peng, P.Y. Preparation and characterization of iodine-doped mesoporous TiO2 by hydrothermal method. *Appl. Surf. Sci.* **2011**, *257*, 3688–3696.
71. Wang, Y.; Ren, J.; Liu, G.; Peng, P. Synthesis and characterization of iodine ion doped mesoporous TiO_2. by sol-gel method. *Mater. Chem. Phys.* **2011**, *130*, 493–499.
72. Luttrell, T.; Halpegamage, S.; Tao, J.; Kramer, A.; Sutter, E.; Batzill, M. Why is anatase a better photocatalyst than rutile?-Model studies on epitaxial TiO2 films. *Sci. Rep.* **2014**, *4*, 1–8.

3. Defective TiO_2 Core-Shell Magnetic Photocatalyst Modified with Plasmonic Nanoparticles for Visible Light-Induced Photocatalytic Activity

Zuzanna Bielan, Agnieszka Sulowska, Szymon Dudziak, Katarzyna Siuzdak, Jacek Ryl, Anna Zielińska-Jurek

Catalysts 10 (2020) 672

DOI: 10.3390/catal10060672

P3

catalysts

MDPI

Article

Defective TiO_2 Core-Shell Magnetic Photocatalyst Modified with Plasmonic Nanoparticles for Visible Light-Induced Photocatalytic Activity

Zuzanna Bielan [1,*], Agnieszka Sulowska [1], Szymon Dudziak [1], Katarzyna Siuzdak [2], Jacek Ryl [3] and Anna Zielińska-Jurek [1,*]

1 Department of Process Engineering and Chemical Technology, Faculty of Chemistry, Gdansk University of Technology (GUT), G. Narutowicza 11/12, 80-233 Gdansk, Poland; Sulowska.as@gmail.com (A.S.); dudziakszy@gmail.com (S.D.)
2 Physical Aspects of Ecoenergy Department, The Szewalski Institute of Fluid-Flow Machinery Polish Academy of Science, Fiszera 14, 80-231 Gdansk, Poland; katarzyna.siuzdak@imp.gda.pl
3 Department of Electrochemistry, Corrosion and Materials Engineering, Faculty of Chemistry, Gdansk University of Technology (GUT), G. Narutowicza 11/12, 80-233 Gdansk, Poland; jacek.ryl@pg.edu.pl
* Correspondence: zuzanna.bielan@gmail.com (Z.B.); annjurek@pg.edu.pl (A.Z.-J.)

Received: 19 May 2020; Accepted: 11 June 2020; Published: 15 June 2020

check for updates

Abstract: In the presented work, for the first time, the metal-modified defective titanium(IV) oxide nanoparticles with well-defined titanium vacancies, was successfully obtained. Introducing platinum and copper nanoparticles (NPs) as surface modifiers of defective d-TiO_2 significantly increased the photocatalytic activity in both UV-Vis and Vis light ranges. Moreover, metal NPs deposition on the magnetic core allowed for the effective separation and reuse of the nanometer-sized photocatalyst from the suspension after the treatment process. The obtained Fe_3O_4@SiO_2/d-TiO_2-Pt/Cu photocatalysts were characterized by X-ray diffractometry (XRD) and specific surface area (BET) measurements, UV-Vis diffuse reflectance spectroscopy (DR-UV/Vis), X-ray photoelectron spectroscopy (XPS) and transmission electron microscopy (TEM). Further, the mechanism of phenol degradation and the role of four oxidative species (h^+, e^-, $^\bullet OH$, and $^\bullet O_2^-$) in the studied photocatalytic process were investigated.

Keywords: titanium vacancies; phenol degradation; scavengers; magnetic photocatalysts; platinum-modified defective TiO_2

1. Introduction

In recent years, among wastewater treatment and environmental remediation technologies, photocatalysis has gained attention as a promising technique for the degradation of persistent organic pollutants at ambient temperature and pressure [1–4]. Pilot scale-installations for water treatment using photocatalysis are more and more popular among the world [5,6]. The structural and surface properties of photocatalysts significantly influence their physicochemical and photocatalytic properties. In this regard, one of the most important issues in the photocatalytic process is the preparation of well-characterized and highly active photocatalytic material.

Titanium(IV) oxide (TiO_2), the most widely used semiconductor in photocatalysis, is extensively exploited to obtain highly photoactive in UV-Vis range semiconductor material. The TiO_2 nanoparticles differing in size and surface area. Nonetheless, despite different morphology and polymorphic composition, all pristine titanium(IV) oxide particles own wide bandgap energy (Eg), which differs in the range of 3.0–3.2 eV, for rutile and anatase, respectively [7]. In this regard, TiO_2 photoexcitation is possible only with UV irradiation ($\lambda < 388$ nm), and therefore the application of solar radiation is highly limited.

Much effort has been done to shift TiO_2 excitation energy to longer wavelengths, especially in visible light range (400–750 nm). Among various methods [8–10], surface modification with noble and semi-noble metals is the most widely used and effective method. Wysocka et al. [11] obtained mono- (Pt, Ag, and Cu) and bimetal- (Cu/Ag, Ag/Pt, and Cu/Pt) modified TiO_2 photocatalysts, where TiO_2 matrix was commercially available ST01 (fine anatase particles). Metal ions were reduced using the chemical ($NaBH_4$ solution) as well as thermal treatment methods. Klein et al. [12] prepared TiO_2-P25 modified with Pt, Pd, Ag, and Au using radiolysis reduction. Obtained photocatalysts were further immobilized on the glass plate and used for toluene removal from the gas phase. Moreover, Janczarek et al. [13] proposed a method of obtaining Ag- and Cu-modified decahedral anatase particles (DAP) by photodeposition. Wei et al. [14] reported that selective deposition of nanometals (Au/Ag nanoarticles) on (001) facets of decahedral anatase particles (DAP), together with octahedral anatase particles (OAP) result in significant photocatalytic process improvement under visible light irradiation.

Another possibility of titania visible light activation is the introduction of intrinsic defects to its crystal structure. Titanium or oxygen vacancies and surface disorders led to changes in electronic and crystal changes, resulting in better electrons and holes separation and even bandgap narrowing [15]. Defected TiO_2 is often evidenced by their color: pale blue for oxygen vacancies (due to d–d transitions of bandgap states) and yellow for titanium vacancies (consumption of free electrons and holes), which also suggest shifting its light absorption to the visible light range [15].

Nevertheless, TiO_2 particle size and shape determine not only the number of active sites but also separation and reusability properties. Commercially available titanium(IV) oxide—P25 forms a stable suspension due to its nanometric sizes, which cause the detached process to be highly expensive and energy-consuming [16,17]. The immobilization of nanoparticles on solid substrates [18] could, in turn, result in a decrease in photocatalytic activity due to significantly reducing specific surface area [19,20]. Alternative way of photocatalyst separation is its deposition on magnetic compound, such as Fe_3O_4 [21,22], $CoFe_2O_4$ [23], $ZnFe_2O_4$ [24], and $BaFe_{12}O_{19}$ [25]. Along with using magnetic materials, the percentage of photocatalyst recovery and the possibility of its reuse significantly increase [26–29]. However, the direct contact of ferrite particles with photocatalyst (e.g., TiO_2) may result in unfavorable electron transfer from TiO_2 into the magnetic compound, causing its transformation and photocorrosion [26]. Thus, their separation with an inert interlayer of silica [26–31] or carbon [32] could effectively prevent the charge carriers recombination. In this regard, the magnetic Fe_3O_4@SiO_2/TiO_2 nanocomposites with a core-shell structure, where the core was Fe_3O_4, the photoactive shell was TiO_2, and silica was used as an inert interlayer, are a relatively new and promising group of composite materials.

The previous studies focused on the preparation and characterization of noble metal NPs modified with different titania matrices [33,34], as well as TiO_2 nanoparticles deposited on various magnetic cores (Fe_3O_4, $CoFe_2O_3$, and $ZnFe_2O_4$) [26–29]. However, in the literature, there is a lack of complex researches on the correlation between structural defects and TiO_2 modification with different materials (metal nanoparticles or other oxides).

In this regard, deeply characterized defective d-TiO_2 with stable titanium vacancies, obtained by a simple hydrothermal method was further modified with Pt and Cu nanoparticles as well as deposited on the magnetite core. The obtained samples were characterized by X-ray diffractometry (XRD), specific surface area (BET) measurements, UV-Vis diffuse reflectance spectroscopy (DR-UV/Vis), X-ray photoelectron spectroscopy (XPS), and transmission electron microscopy (TEM). The photodegradation of phenol as a model organic pollutant in the presence of the obtained photocatalysts was subsequently investigated in the range of UV-Vis and Vis irradiation. Further, the mechanism of phenol degradation and the role of four oxidative species (h^+, e^-, $^\bullet OH$, and $^\bullet O_2^-$) in the studied photocatalytic process were investigated.

2. Results

2.1. Physicochemical Characterization of d-TiO_2-Pt/Cu and Magnetic Fe_3O_4@SiO_2/d-TiO_2-Pt/Cu Photocatalysts

The preparation of d-TiO_2 photocatalysts was based on the hydrothermal method in the oxidative environment (addition of 20–75 mol% of HIO_3). The electron paramagnetic resonance (EPR) analysis confirmed the presence of titanium vacancies with g value of 1.995 after calcination. The signal at EPR spectra for bulk Ti^{3+} was not observed for pure TiO_2 sample, see in Figure 1.

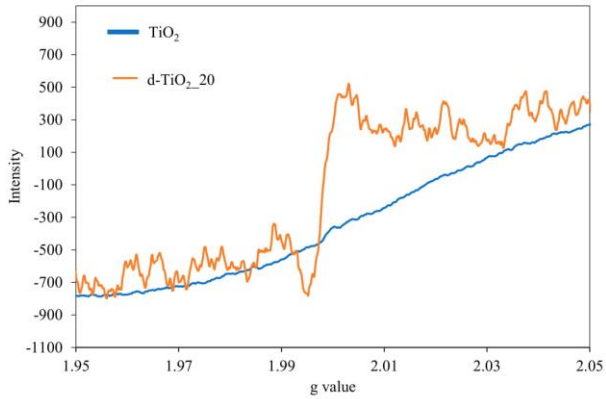

Figure 1. The electron paramagnetic resonance (EPR) spectra in the room temperature for TiO_2 (blue line) and TiO_2 with titania vacancies (orange line).

The general physicochemical and photocatalytic characteristics of the obtained defective d-TiO_2-Pt/Cu and Fe_3O_4@SiO_2/d-TiO_2-Pt/Cu samples, i.e., BET surface area, pore volume, calculated bandgap (Eg) and phenol degradation efficiency in UV-Vis and Vis light are presented in Tables 1 and 2.

Table 1. Physicochemical and photocatalytic characteristics of the obtained defective d-TiO_2-Pt/Cu samples.

Sample	BET ($m^2 \cdot g^{-1}$)	V Pores ($cm^3 \cdot g^{-1}$)	Eg (eV)	Rate Constant k ($min^{-1} \cdot 10^{-2}$ UV-Vis	Phenol Removal (%) UV-Vis	Rate Constant k ($min^{-1} \cdot 10^{-2}$ Vis	Phenol Removal (%) Vis
TiO_2	169	0.0836	3.2	0.98	46	0.03	3
d-TiO_2_20	172	0.0847	2.7	0.79	40	0.17	13
d-TiO_2_75	167	0.0826	2.9	0.52	29	0.03	4
TiO_2-Pt0.05	166	0.0819	3.2	2.30	76	0.22	14
d-TiO_2_20-Pt0.05	148	0.0727	2.85	1.10	48	0.33	20
d-TiO_2_75-Pt0.05	164	0.0808	2.9	1.02	46	0.26	15
d-TiO_2_20-Pt0.1	152	0.0747	2.7	1.42	57	0.41	22
d-TiO_2_20-Cu0.1	101	0.0499	2.9	0.51	30	0.12	7
d-TiO_2_20-Pt0.1/Cu0.1	152	0.0744	2.75	1.47	59	0.27	17

Table 2. Physicochemical and photocatalytic characteristics of the obtained magnetic Fe_3O_4@SiO_2/d-TiO_2-Pt/Cu samples.

Sample	BET ($m^2 \cdot g^{-1}$)	V Pores ($cm^3 \cdot g^{-1}$)	Rate Constant k ($min^{-1} \cdot 10^{-2}$ UV-Vis	Phenol Removal (%) UV-Vis	Rate Constant k ($min^{-1} \cdot 10^{-2}$ Vis	Phenol Removal (%) Vis
Fe_3O_4@SiO_2/d-TiO_2_20	117	0.0578	0.41	20	0.13	8
Fe_3O_4@SiO_2/d-TiO_2_20-Pt0.05	115	0.0568	0.15	11	0.08	4
Fe_3O_4@SiO_2/d-TiO_2_20-Pt0.1	122	0.0602	0.41	19	0.19	11
Fe_3O_4@SiO_2/d-TiO_2_20-Cu0.1	117	0.0579	0.22	15	0.05	2
Fe_3O_4@SiO_2/d-TiO_2_20-Pt0.1/Cu0.1	117	0.0580	0.36	22	0.26	11

The BET surface area of pure TiO_2 obtained from Titanium(IV) butoxide (TBT) hydrolysis in water and defective TiO_2 samples was similar and ranged from 167 to 172 $m^2 \cdot g^{-1}$. The specific surface area of the metal-modified d-TiO_2 samples fluctuated from 166 to 101 $m^2 \cdot g^{-1}$ and depended on the type and amount of metallic species deposited on d-TiO_2 surface. The samples modified with Pt NPs revealed a higher BET surface area of about 148 $m^2 \cdot g^{-1}$ compared to d-TiO_2 modified with copper oxide (101 $m^2 \cdot g^{-1}$), and bimetallic Pt/Cu NPs (152 $m^2 \cdot g^{-1}$). The relations between photoactivity in UV-Vis and Vis light range versus BET surface area are also shown in Tables 1 and 2. The obtained results indicated that not so much the surface area but rather the presence of Ti defects and modification with metal nanoparticles caused the enhanced photoactivity of the obtained photocatalysts. Moreover, as shown in Table 2, the addition of surface-modifying metal nanoparticles, as well as further deposition of d-TiO_2-Pt/Cu on magnetic matrice, did not affect the magnitude order of the BET surface area, which remained in the range of 101 to 172 $m^2 \cdot g^{-1}$ for d-TiO_2_20-Cu0.1 and d-TiO_2_20, respectively.

The energy bandgaps for all samples were calculated from the plot of $(Kubelka–Munk \cdot E)^{0.5}$ versus E, where E is energy equal to hv, and summarized in Table 1. The samples consist of defective TiO_2 exhibited narrower bandgap of 2.7–2.9 eV compared to TiO_2 and TiO_2-Pt0.05 photocatalysts. Moreover, for all metal-modified defective photocatalysts, the bandgap value, calculated from Kubelka–Munk, transformation did not change, compared to d-TiO_2 matrice, indicating surface modification than doping [11].

The XRD patterns for selected d-TiO_2-Pt/Cu and Fe_3O_4@SiO_2/d-TiO_2-Pt/Cu samples are presented in Figures 1 and 2, with a detailed phase composition and crystalline sizes for all photocatalysts being listed in Tables 3 and 4. Peaks marked "A", "R", and "B" corresponds to anatase, rutile, and brookite phases, respectively. Both crystalline structures (anatase and brookite) appeared for pure TiO_2 prepared by the sol–gel method. For Pt-modified TiO_2 anatase was the major phase, whereas brookite existed as the minor phase. The average crystallite size of anatase was 5–6 nm. The preparation of d-TiO_2 photocatalysts proceeded in the oxidative environment. The introduction into the crystal structure of various types of defects promotes the transformation of anatase to rutile at lower temperatures. Therefore, for the samples obtained in the presence of HIO_3 as the oxidizing agent, after the annealing process the percentage of anatase (the most intense peak at 25° 2θ, with the (101) plane diffraction, ICDD's card No. 7206075) was decreased in favor of (110) rutile, with the peak at 31° 2θ (ICDD's card No. 9004141), even below the anatase to rutile phase transformation temperature [35–37]. For the samples d-TiO_2_75 and d-TiO_2_75-Pt0.05, the dominant phase was rutile with a crystallite size of about 6 nm. Further, the surface modification with plasmonic platinum and semi-noble copper did not cause changes in anatase crystallite size, remaining about 5–6 nm size. The percentage of the brookite phase increased to 8.5% and 13% for d-TiO_2 _20-Pt0.1/Cu0.1, and d-TiO_2_20-Pt0.1 samples, respectively. It resulted from the additional thermal treatment after metal nanoparticles deposition on the photocatalyst surface. Moreover, Pt and Cu modification of TiO_2 did not cause the shift of the peaks in the XRD pattern. The presence of platinum and copper deposited on TiO_2 was not approved (no peaks for platinum or copper) due to low content (0.05–0.1 mol%) and nanometric size.

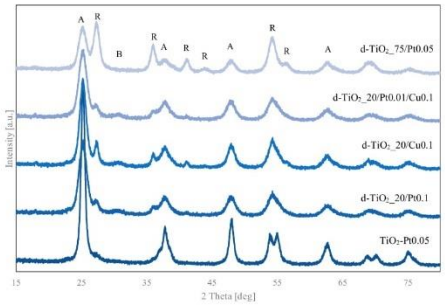

Figure 2. X-ray diffractometry (XRD) patterns for selected defective d-TiO_2-Pt/Cu photocatalysts (A—anatase, B—brookite, and R—rutile).

Table 3. Crystalline phases characteristic for obtained defective d-TiO_2-Pt/Cu samples.

Sample	Crystalline Size and Phase Content					
	Anatase		Rutile		Brookite	
	Size (nm)	Phase Content (wt.%)	Size (nm)	Phase Content (wt.%)	Size (nm)	Phase Content (wt.%)
TiO_2	5.97 ± 0.04	95.5 ± 1	-	-	6.1 ± 0.3	4.5 ± 1
d-TiO_2_20	5.14 ± 0.03	96 ± 1.0	-	-	4.0 ± 0.6	3.5 ± 0.5
d-TiO_2_75	5.67 ± 0.05	21 ± 3.5	6.57 ± 0.09	80 ± 2	-	-
TiO_2-Pt0.05	5.71 ± 0.06	91 ± 0.5	-	-	5.7 ± 0.6	9 ± 1
d-TiO_2_20-Pt0.05	5.66 ± 0.03	85 ± 8	9.8 ± 0.7	9 ± 1.0	4.9 ± 0.3	6 ± 0.5
d-TiO_2_75-Pt0.05	5.49 ± 0.04	48 ± 2	7.53 ± 0.12	52 ± 2	-	-
d-TiO_2_20-Pt0.1	5.58 ± 0.03	81 ± 8	7.6 ± 0.8	6 ± 1	4.8 ± 0.3	13 ± 1
d-TiO_2_20-Cu0.1	6.62 ± 0.04	72 ± 11	11.7 ± 0.4	9 ± 2	1.52 ± 0.08	8.5 ± 1
d-TiO_2_20-Pt0.1/Cu0.1	5.52 ± 0.03	83 ± 12	9.5 ± 0.6	8 ± 2	5.1 ± 0.3	8.5 ± 1

Table 4. Crystalline phases characteristic for the obtained magnetic Fe_3O_4@SiO_2/d-TiO_2_20-Pt/Cu samples.

Sample	Crystalline Size and Phase Content					
	Anatase		Rutile		Magnetite	
	Size (nm)	Phase Content (wt.%)	Size (nm)	Phase Content (wt.%)	Size (nm)	Phase Content (wt.%)
Fe_3O_4@SiO_2/d-TiO_2_20	5.19 ± 0.05	71 ± 1.5	8.6 ± 0.5	8 ± 0.5	46.1 ± 1.1	21 ± 0.5
Fe_3O_4@SiO_2/d-TiO_2_20-Pt0.05	5.60 ± 0.05	71 ± 1.5	8.9 ± 0.5	7 ± 0.5	45.7 ± 1.4	21 ± 0.5
Fe_3O_4@SiO_2/d-TiO_2_20-Pt0.1	5.49 ± 0.05	68 ± 2	9.1 ± 0.6	7 ± 1	47.2 ± 4.0	24 ± 0.5
Fe_3O_4@SiO_2/d-TiO_2_20-Cu0.1	7.81 ± 0.17	57 ± 2	13.3 ± 1.4	5 ± 1	37.1 ± 1.8	28 ± 1.5
Fe_3O_4@SiO_2/d-TiO_2_20-Pt0.1/Cu0.1	5.48 ± 0.05	69 ± 1	7.9 ± 0.4	8 ± 0.5	42.6 ± 3.3	22 ± 1

The XRD analysis of Fe_3O_4@SiO_2/d-TiO_2-Pt/Cu confirmed the formation of a magnetic composite, and, as observed in Figure 3 and Table 4, there was no significant difference between the diffraction patterns of the obtained magnetic photocatalysts modified with Pt/Cu NPs. The presence of pure magnetite, with diffraction peaks at 30.2°, 35.6°, 43.3°, 57.3°, and 62.9° 2θ corresponding to (220), (311), (400), (511), and (440) cubic inverse spinel planes (ICDD's card No. 9005813) was confirmed for all Fe_3O_4@SiO_2/d-TiO_2-Pt/Cu magnetic photocatalysts. The decrease in Fe_3O_4 peaks intensity was caused by the formation of tight non-magnetic shell on the core surface, which was previously described by Zielińska-Jurek et al. [26]. The broad peak at 15–25° 2θ corresponds to amorphous silica [38,39]. The content of the magnetite crystalline phase varied from 21% to 28% for Fe_3O_4@SiO_2/d-TiO_2_20-Pt0.05 and Fe_3O_4@SiO_2/d-TiO_2_20-Cu0.1, respectively. At the same time, TiO_2 crystallite size and anatase to rutile phase content ratio remained unchanged for Fe_3O_4@SiO_2/d-TiO_2_20 and Fe_3O_4@SiO_2/d-TiO_2_20-Pt/Cu samples. No other crystalline phases were identified in the XRD patterns, which indicated the crystal purity of the obtained composites.

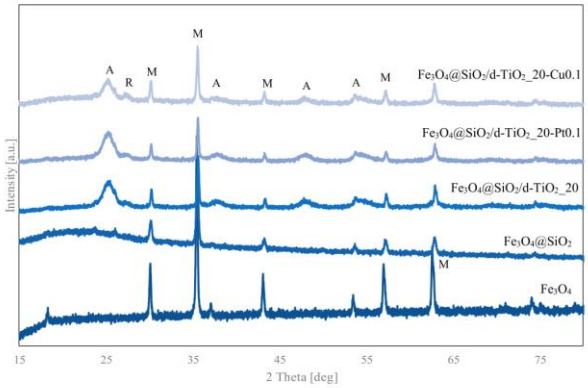

Figure 3. XRD patterns of magnetic photocatalysts, compared with Fe_3O_4 and Fe_3O_4@SiO_2 (A—anatase, R—rutile, and M—magnetite).

The photoabsorption properties of metal-modified defective d-TiO_2 samples were studied by diffuse reflectance spectroscopy, and exemplary data are shown in Figure 4. Comparing to pure TiO_2 photocatalyst, introducing platinum as a surface modifier caused an increase of absorption in the visible light region, however, without shifting a maximum, as presented for sample TiO_2–Pt0.05. Modification of defective d-TiO_2 with Pt and Cu was associated with a further increase of Vis light absorbance and proportional to the amount of the deposited metal. Moreover, the deposition of Pt caused a more significant absorbance increment than the same modification with Cu species.

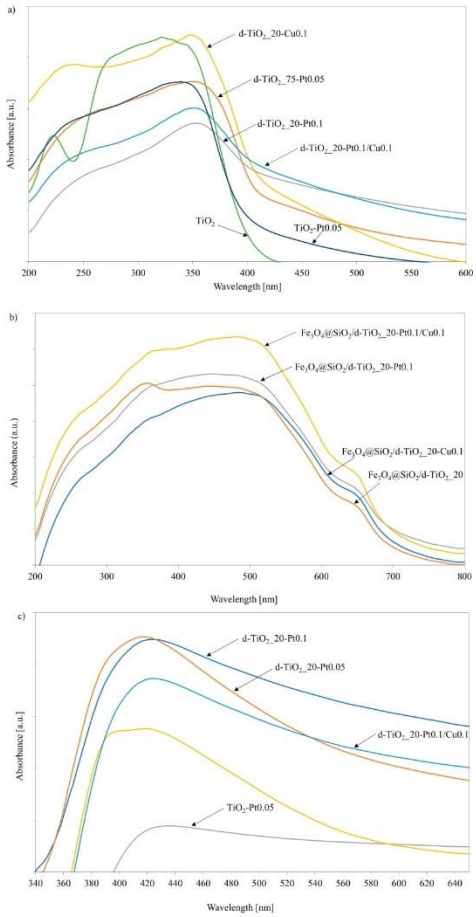

Figure 4. DR/UV-Vis spectra for selected d-TiO_2-Pt/Cu (**a**) and Fe_3O_4@SiO_2/d-TiO2-Pt/Cu (**b**) photocatalysts together with Pt and Cu plasmon determination with bare TiO_2 as a reference (**c**).

Defective d-TiO_2-Pt/Cu deposited on Fe_3O_4@SiO_2 core were characterized by extended light absorption ranged to 700 nm. It could be observed that the described absorption properties in the Vis light for metal-modified TiO_2 and absorption properties of final composites have been preserved.

The presence of Localized Surface Plasmon Resonance (LSPR) peaks for Pt and Cu were confirmed based on DR-UV/Vis spectra measurements with pure TiO_2 as a reference (see in Figure 4c). Platinum surface plasmon resonance was observed at the wavelength of about 410–420 nm [33,40]. Electron transfer between Cu(II) and valence band of titanium(IV) oxide could be confirmed by absorption increment from 400 to 450 nm. The typical LSPR signal for zero valent copper at 500–580 nm was not observed, suggesting that Cu is mainly present in its oxidized forms [41,42].

To confirm the presence of noble metal and semi-noble metal NPs on defective TiO_2 surface, the XPS analyses for the selected photocatalysts and deconvolution of Pt 4f and Cu 2p were performed, and the results are presented in Figure 5. Platinum species deposited on the titania surface were designated by deconvolution of Pt 4f peak into two components: Pt $4f_{7/2}$ and Pt $4f_{5/2}$. According to the literature, Pt $4f_{7/2}$ peak, with binding energies in the range of 74.2 to 75.0 eV, refers to the Pt^0, while Pt $4f_{5/2}$ peak, appearing at 77.5–77.9 eV is assigned to Pt^{4+} [11]. The main peaks for Cu 2p appeared as Cu $2p_{3/2}$ and Cu $2p_{1/2}$ at 934 eV and 952 eV. Both of those peaks are commonly attributed to Cu^+ and Cu^{2+} ions [13,43,44]. Obtained data indicated that both Pt and Cu species were successfully deposited on the titania surface.

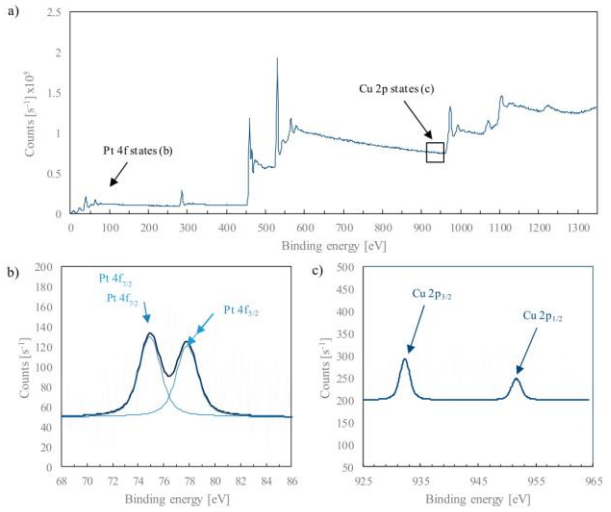

Figure 5. XPS spectra for d-TiO_2_20-Pt0.1/Cu0.1 sample (**a**) with the deconvolution for Pt 4f (**b**) and Cu 2p (**c**).

Moreover, the presence of Pt NPs at the surface of the magnetic nanocomposites was also confirmed by microscopy analysis. As presented in Figure 6, the formation of SiO_2/TiO_2 shell, with a thickness of about 20 nm, tightly covering magnetite nanoparticles was observed. Platinum nanoparticles with a diameter of about 10–20 nm were evenly distributed on the d-TiO_2 layer.

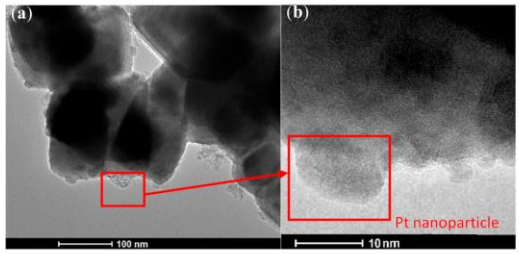

Figure 6. Transmission electron microscopy (TEM) analysis for Fe_3O_4@SiO_2/d-TiO_2_20/Pt0.1 sample (**a**) magnification on Pt nanoparticle (**b**).

2.2. Photocatalytic Activity of d-TiO_2-Pt/Cu and Fe_3O_4@SiO_2/d-TiO_2-Pt/Cu Photocatalysts

The effect of Pt and Cu presence on the properties of defective d-TiO_2 photocatalysts was evaluated in reaction of phenol degradation under UV-Vis and Vis light irradiation. The results, presented as the efficiency of phenol degradation as well as phenol degradation rate constant k, are given in Figures 7 and 8. Additionally, the effect of the electron (e^-), hole (h^+), hydroxyl radical ($^\bullet OH$), and superoxide radical ($^\bullet O_2^-$) scavengers were investigated and presented in Figure 9.

Among analyzed metal-modified photocatalysts, TiO_2–Pt0.05 revealed the highest phenol degradation in UV-Vis light. After 60 min of irradiation, about 76% of phenol was degraded. After introducing plasmonic platinum and semi-noble copper species as a surface modifiers, UV-Vis photoactivity of defective d-TiO_2 samples increased to 59%. The degradation rate constant k increased to 1.47×10^{-2} min^{-1} compared to d-TiO_2_20 (0.79×10^{-2} min^{-1}), and d-TiO_2_75 (0.52×10^{-2} min^{-1}) photocatalysts. Nonetheless, the most significant changes were observed during the photocatalytic process in visible light ($\lambda > 420$ nm). Modifying with 0.05 mol% of Pt, the surface of almost inactive in Vis light d-TiO_2_75 resulted in three-times higher photocatalytic activity under visible light. Therefore, a highly positive effect of metal surface modification of defective d-TiO_2 photocatalyst surface was noticed. It resulted from better charge carriers' separation and decreasing the electron-hole recombination rate. Moreover, the narrower bandgap of the defective d-TiO_2 (in comparison with pure TiO_2) and modification with Pt possessing surface plasmon resonance properties, could also enhance visible light absorption and consequently led to photocatalytic activity increase.

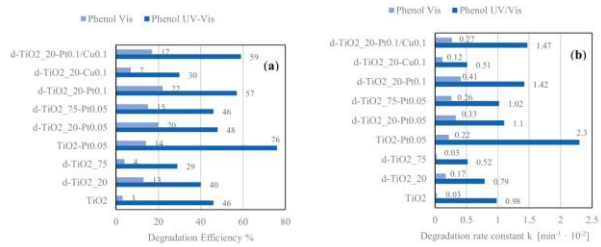

Figure 7. Efficiency of phenol degradation in UV-Vis and Vis light for d-TiO_2-Pt/Cu photocatalysts, presented as % of degradation (**a**) and rate constant k (**b**).

Pure magnetite, coated with inert silica, did not affect the photocatalytic process. Furthermore, the Fe_3O_4@SiO_2/d-TiO_2 composite modified with Pt NPs, and bimetallic Pt/Cu NPs revealed the highest photocatalytic activity in Vis light range. The phenol degradation rate constant in Vis light was 2-times higher for Fe_3O_4@SiO_2/d-TiO_2-Pt/Cu compared to Fe_3O_4@SiO_2/d-TiO_2 sample. However, the obtained magnetic photocatalysts had similar photocatalytic activity in UV-Vis light, almost regardless of the surface modification of d-TiO_2 with noble metals. It probably resulted from larger Pt particles (~20 nm) deposition at the surface of Fe_3O_4@SiO_2/d-TiO_2 composite than for TiO_2–Pt0.05 with particles size of about 2–3 nm. Previously, we have reported that the size of noble metal nanoparticles, especially platinum, deposited on the TiO_2 surface strictly depends on the semiconductor surface area, as well as its crystal lattice defects [33,45]. Fine metal particles are produced on the TiO_2 surface with a developed specific surface area with a high density of oxygen traps and nucleation sites, and the highest photocatalytic activity is noticed for Pt-modified photocatalyst, where the size of Pt is below 3 nm [33]. In the present study, Pt nanoparticles' average diameter was about 20 nm as a result of the deposition of Pt ions and their reduction on formed particles' defects. Therefore, the lower metal/semiconductor interface resulted in a decrease in photocatalytic activity under UV-Vis light irradiation.

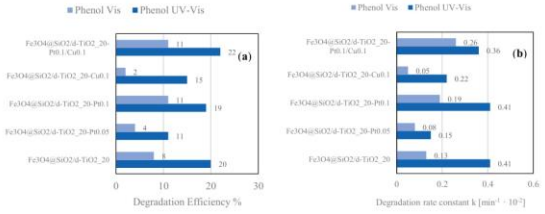

Figure 8. Efficiency of phenol degradation in UV-Vis and Vis light for magnetic Fe_3O_4@SiO_2/d-TiO_2-Pt/Cu photocatalysts, presented as % of degradation (**a**) and rate constant k (**b**).

For the final stability and reusability test, the most active defective photocatalyst was selected. For sample d-TiO_2_20/Pt0.1/Cu0.1, three 1-h-long subsequent cycles of phenol degradation under UV-Vis light were performed. The obtained results are presented in Figure 9.

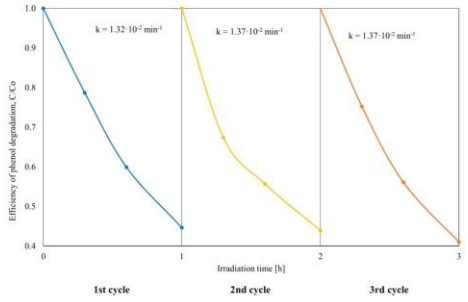

Figure 9. Efficiency of UV-Vis phenol degradation in the presence of defective d-TiO_2_20/Pt0.1/Cu0.1 photocatalyst measured in the three subsequent cycles.

There was no significant change in phenol degradation rate constant after the second and third cycles. Thus, the analyzed photocatalyst revealed good stability and reusability.

Furthermore, the reactive species were investigated to understand the photocatalytic reaction mechanism. Benzoquinone (BQ), silver nitrate (SN), ammonium oxalate (AO), and tert-butanol (t-BuOH) were used as superoxide radical anions ($\cdot O_2^-$), electrons (e^-), holes (h^+), and hydroxyl radicals ($\cdot$OH) scavengers, respectively. Obtained results, presented as phenol degradation rate constant k, in comparison to the photodegradation process without scavengers, are presented in Figure 10. The most significant impact on phenol degradation reaction in the presence of metal-modified d-TiO_2 was observed for superoxide radicals. After introducing to the photocatalyst suspension BQ solution, the phenol degradation efficiency was significantly inhibited. A slight decrease was also observed in the presence of SN as an electron trap. On the other hand, the addition of AO and t-BuOH did not decrease the phenol degradation rate.

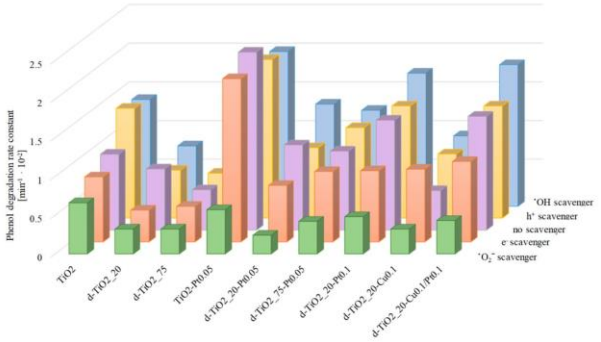

Figure 10. Photocatalytic degradation of phenol for defective Fe_3O_4@SiO_2/d-TiO_2-Pt/Cu photocatalysts in the presence of e^-, h^+, $^\bullet O_2^-$, and $^\bullet$OH scavengers.

Modification of TiO_2 resulted in the shift of the valence band as was revealed from the analysis of Mott–Schottky plot, where the relation between applied potential vs. Csc^{-2} is presented (see in Figure 11). According to the intersection with E axis the flat band potential was estimated. In the case of pure titania it equals to −1.2 V, whereas for d-TiO_2_20-Pt0 the value of −1.13 was reached. In order to prepare energy diagram of both materials given in Figure 12, the values of bandgap energy was taken into account. As could be seen, for the modified material the position both the conduction and valence band are shifted. According to Monga et al. [46] the Schottky barrier formed at the metal-TiO_2 interface affecting the efficiency of e- transfer. The lowering of the CB band edge is in accordance with the literature indicating that the work function of the metal prone decrease of the CB location. Then, the Schotky barrier is decreased at the metal/semiconductor heterojunction. As a result, the transfer of the photoexcited electron from metal NPs to titania is facilitated and plays important role in photocatalytic activity improvement. The introduction of titanium defects to the TiO_2 crystal structure also resulted in narrowing the bandgap from 3.2 to 2.7 eV.

Based on the presented results, a schematic mechanism of UV-Vis phenol degradation in the presence of metal-modified defective Fe_3O_4@SiO_2/d-TiO_2-Pt/Cu photocatalyst was proposed and shown in Figure 12. After irradiation of the photocatalyst surface with UV-Vis light, electrons from the Pt are injected to the conduction band of titania and then utilized in oxygen reduction to form

reactive oxygen radicals. The path of phenol degradation led through several intermediates, such as benzoquinone, hydroquinone, catechol, resorcinol, oxalic acid, and finally, to complete mineralization to CO_2 and H_2O [47–49]. An analysis of possible charge carriers' impact revealed that for photoactivity of d-TiO_2-Pt/Cu, they are responsible for mainly generated superoxide radicals. The phenol degradation mechanism proceeded by the generation of reactive oxygen species, e.g., $^{\bullet}O_2^-$, which attacked the phenol ring, resulting in benzoquinone and hydroquinone formation confirmed by high-performance liquid chromatography (HPLC) analyses. Moreover, during the photoreaction, the concentration of formed intermediates decreased, which suggests mineralization of recalcitrant chemicals to simple organic compounds.

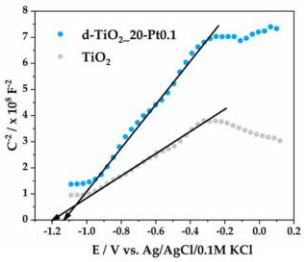

Figure 11. The Mott–Schottky plot for the bare and Pt modified d-TiO_2.

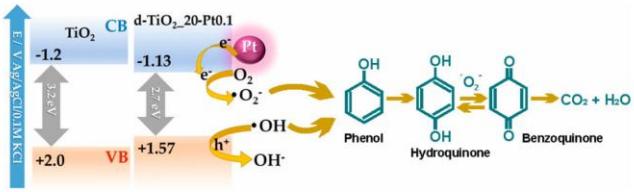

Figure 12. Energy diagram depicting the position of valence and conduction bands of bare and modified titania including the indication of charge transfer within the Schottky junction, and schematic illustration of phenol degradation mechanism over defective Fe_3O_4@SiO_2/d-TiO_2-Pt/Cu photocatalysts.

3. Materials and Methods

Titanium(IV) oxide organic precursor: titanium(IV) butoxide (>99%) was provided by Alfa Aesar (Haverhill, MA, USA). Iodic acid (99.5%), sodium borohydride (99%), chloroplatinate acid hydrate ($H_2PtCl_4 \cdot xH_2O$) (99.9%) and copper nitrate trihydrate ($Cu(NO_3)_2 \cdot 3H_2O$) (99–104%), used for TiO_2 structure and surface modification, were purchased from Sigma (Poznan, Poland). Ferrous ferric oxide (Fe_3O_4, 97%) with a declared particles size of 50 nm was purchased from Aldrich (Poznan, Poland). Tetraethyl orthosilicate (TEOS) was provided by Aldrich and was used as a precursor for the inert interlayer of magnetic nanoparticles. Ammonium hydroxide solution (25%) was purchased from Avantor (Gliwice, Poland). Chemicals for w/o microemulsions preparation, such as cyclohexane and 2-propanol, were purchased from Avantor. Cationic surfactant, hexadecyltrimethylammonium bromide (CTAB), was provided by Sigma Aldrich (Poznan, Poland). Acetonitrile and orthophosphoric acid (85%) for HPLC mobile phase preparation were provided by Merck (Darmstadt, Germany)

and VWR (Gdansk, Poland), respectively. Phenol, used as a model organic recalcitrant pollutant in photocatalytic activity measurements, was purchased from VWR. For the titania paste formation polyethylene glycol (PEG) from Sigma Aldrich (Poznan, Poland) was used, while Na_2SO_4 used for electrolyte preparation was purchase from VWR. All reagents were used without further purification.

3.1. Preparation of Defective TiO_2-Pt/Cu Photocatalysts

Defective TiO_2 (marked as d-TiO_2) was obtained by the hydrothermal method assisted with the annealing process. Titanium(IV) butoxide (TBT) and iodic acid (HIO_3) were used as a TiO_2 precursor and oxidizing environment for titanium vacancies formation, respectively. Briefly, the appropriate amount of HIO_3 (presented in Table 5) was dissolved in 80 cm^3 of distilled water. After that, 10 cm^3 of TBT was added dropwise, and the obtained suspension was stirred for 1 h with magnetic stirring at room temperature. In the next step, the suspension was transferred into a Teflon-lined autoclave for thermal treatment at 110 °C for 24 h. The resultant precipitate was centrifuged, dried at 70 °C and then calcined at 300 °C for 3 h.

Table 5. HIO_3 concentrations used for the synthesis of each d-TiO_2 photocatalyst.

Sample	Oxidant Concentration [mol%]	Mass of Added Oxidant [g]
TBT	0	0
d-TiO_2_20	20	1.032
d-TiO_2_75	75	3.869

The obtained defective d-TiO_2 photocatalysts were modified using platinum and copper nanoparticles by the co-precipitation method. In this regard, d-TiO_2 was dispersed in 50 cm^3 of deionized water, and Pt/Cu precursor solutions (0.05 and 0.1 mol% of Pt and 0.1 mol% of Cu with respect to TiO_2) were added. After that, $NaBH_4$ solution was introduced to reduce the metals ions followed by their deposition on the titania surface. The mole ratio of metal ions to $NaBH_4$ was 1:3. After the reduction process, the photocatalyst suspension was mixed for 2 h, and the d-TiO_2-Pt/Cu nanoparticles were separated, washed with deionized water, and dried at 80 °C to dry mass. The final step was calcination at 300 °C for 3 h.

3.2. Preparation of Magnetic Fe_3O_4@SiO_2/d-TiO_2-Pt/Cu Nanocomposites

Previously obtained d-TiO_2-Pt/Cu nanoparticles were deposited on a magnetic substrate as a thin photocatalytic active shell. Magnetite (Fe_3O_4) was selected as a core of the designed composite due to its excellent magnetic properties (high Ms value and low Hc), which enable us to separate obtained photocatalyst in the external magnetic field. Silica was used as an interlayer to isolate Fe_3O_4 from TiO_2 and suppress possible electron transfer between them. The magnetic photocatalysts were obtained in the w/o microemulsion system based on changes in the particles surface charge as a function of pH, described in the previous study [26].

Firstly, commercially available Fe_3O_4 nanoparticles with nominate particles diameter of 50 nm were dispersed in water at pH 10. The prepared suspension was then introduced to cyclohexane/isopropanol (100:6 volume ratio) mixture in the presence of cationic surfactant and cetyltrimethylammonium bromide (CTAB) creating stable w/o microemulsion system with water nanodroplets dispersed in the continuous oil phase. The molar ratio of water to surfactant was set at 30. After the microemulsion stabilization, the corresponding amount of tetraethyl orthosilicate (TEOS) was added, resulting in the formation of SiO_2 interlayer on Fe_3O_4 core, after ammonia solution introduced into the microemulsion system. The molar ratio of TEOS to Fe_3O_4 was 8:1, and NH_4OH to TEOS was 16:1. The microemulsion was destabilized using acetone and obtained nanocomposite Fe_3O_4@SiO_2 was separated, washed with ethanol and water, dried at 70 °C to dry mass, and calcined at 400 °C for 2 h.

In the second step, previously obtained Fe_3O_4@SiO_2 particles were combined with d-TiO_2-Pt/Cu in order to create photocatalytic active nanomaterial. The reversed-phased microemulsion system at

pH 10 was used, and Fe_3O_4 to the TiO_2 molar ratio was equaled to 1:4 [27]. The junction between magnetic/SiO_2 and photocatalytic layers was promoted by their opposite surface charges, provided by the presence of CTAB at the basic conditions. The as-obtained Fe_3O_4@SiO_2/d-TiO_2-Pt/Cu samples, after their separation and purification using water and ethanol, were dried at 70 °C to dry mass and calcined at 300 °C for 2 h.

3.3. Characterization of the Obtained Magnetic Photocatalysts

The XRD analyses were performed using the Rigaku Intelligent X-ray diffraction system SmartLab equipped with a sealed tube X-ray generator (a copper target; operated at 40 kV and 30 mA). Data was collected in the 2θ range of 5–80° with a scan speed and scan step of 1°·min^{-1} and 0.01°, respectively. The analyses were based on the International Centre for Diffraction Data (ICDD) databased. The crystallite size of the photocatalysts in the vertical direction to the corresponding lattice plane was determined using Scherrer's equation with Scherrer's constant equal to 0.891. Quantitative analysis, including phase composition with standard deviation, was calculated using the Reference Intensity Ratio (RIR) method from the most intensive independent peak of each phase.

Nitrogen adsorption-desorption isotherms (BET method for the specific surface area) were recorded using the Micromeritics Gemini V (model 2365) (Norcross, GA, USA) instrument at 77 K (liquid nitrogen temperature).

Light absorption properties were measured using diffuse reflectance (DR) spectroscopy in the range of 200–800 nm. The bandgap energy of obtained samples was calculated from $(F(R)\cdot E)^{0.5}$ against E graph, where E is photon energy, and F(R) is Kubelka–Munk function, proportional to the radiation's absorption. The measurements were carried out using ThermoScientific Evolution 220 Spectrophotometer (Waltham, MA, USA) equipped with a PIN-757 integrating sphere. As a reference, $BaSO_4$ was used.

X-ray photoelectron spectroscopy (XPS) measurements were conducted using Escalab 250Xi multi-spectrometer (Thermofisher Scientific) using Mg K X-rays.

The morphology and distribution size for Fe_3O_4@SiO_2/d-TiO_2-Pt as a reference magnetic nanocomposite sample was further analyzed using HR-TEM imagining (Tecnai F20 X-Twin, FEI Europe) together with elements identification in nanometric scale by EDS mapping.

Electron paramagnetic resonance (EPR) spectroscopy was used for intrinsic defects formation confirmation. Measurements were conducted using RADIOPAN SE/X-2547 spectrometer (Poznań, Poland), operating at room temperature, with frequency in range 8.910984–8.917817 GHz.

3.4. Photocatalytic Activity Analysis

Photocatalytic activity of the obtained samples was evaluated in phenol degradation reaction, both in UV-Vis and Vis light irradiation, using 300 W Xenon lamp (LOT Oriel, Darmstadt, Germany). For the visible light measurements, a cut-off 420 nm filter (Optel, Opole, Poland) was used to obtain a settled irradiation interval. A 0.05 g (2 g·dm^{-3}) of a photocatalyst, together with a 20 mg·dm^{-3} phenol solution, was added to a 25 cm^3 quartz photoreactor with an exposure layer thickness of 3 cm and obtained suspension was stirred in darkness for 30 min to provide adsorption-desorption equilibrium. After that, photocatalyst suspension was irradiated under continuous stirring and a power flux (irradiation intensity) of 30 mW·cm^{-2} for 60 min. The constant temperature of the aqueous phase was kept at 20 °C using a water bath. Every 20 min of irradiation, 1.0 cm^3 of suspension was collected and filtered through syringe filters (pore size = 0.2 µm) for the removal of photocatalysts particles. Phenol concentration, as well as a formation of degradation intermediates, were analyzed using reversed-phase high-performance liquid chromatography (HPLC) system, equipped with C18 chromatography column with bound residual silane groups (Phenomenex, model 00F-4435-E0) and a UV-Vis detector with a DAD photodiodes array (model SPD-M20A, Shimadzu). The tests were carried out at 45 °C and under isocratic flow conditions of 0.3 mL·min^{-1} and volume composition of the mobile phase of 70% acetonitrile, 29.5% water and 0.5% orthophosphoric acid. Qualitative and

quantitative analysis was performed based on previously made measurements of relevant substance standards and using the method of an external calibration curve.

Phenol removal percentage was calculated from the equation:

$$D\% = \frac{C_o - C_n}{C_o} \cdot 100 \quad (1)$$

where: C_o—phenol initial concentration [mg·dm^{-3}], C_n—phenol concentration during photodegradation [mg·dm^{-3}].

Rate constant k was determined from $\ln(C_o/C_n)$ against t plot where C_o and C_n are phenol concentrations [mg·dm^{-3}] and t is degradation time [min]. Rate constant k is equal to directional coefficient "a" of the plot.

In order to evaluate the stability of the obtained photocatalysts, three 1-h-long subsequent cycles of phenol degradation under UV-Vis light using the most active defective d-TiO_2_20/Pt0.1/Cu0.1 sample were performed. After each cycle, photocatalyst was separated from the suspension and use in the next cycle without additional treatment.

The effect of charge carrier scavengers was examined by addition into phenol solution 1 cm^3 of 500 mg·dm^{-3} of tert-butyl alcohol (t-BuOH), benzoquinone (BQ), ammonium oxalate (AO), and silver nitrate (SN), respectively.

3.5. Electrochemical Measurements

In order to prepare Mott–Schottky plot the fabricated titania powders were used to form the paste, deposited using doctor-blade technique onto the Pt support. The paste consist of 0.2 g of photocatalyst in 0.1 g of polyethylene glycol (PEG) and 1 cm^3 of deionized water. Finally the calcination was carried out at 400 °C for 5 h with a heating rate 1 °C·min^{-1} ensuring removal of the organic binder. The fabricated electrode material stayed as working electrode tested in three electrode arrangement where Ag/AgCl/0.1M KCl and Pt mesh were used as reference and counter electrode, respectively. The deaerated 0.5 M Na_2SO_4 was applied as electrolyte. The electrochemical spectroscopy (EIS) impedance data was recorded from the anodic towards cathodic direction. Prior the tests, the investigated samples were not subjected to any preliminary treatment or measurement and their potential was held to reach a steady-state conditions. EIS data were recorded for the single frequency of 1000 Hz in the potential range from +0.1 to −1.2 V vs. Ag/AgCl/0.1 M KCl using a 10 mV amplitude of the AC signal. The capacitance of space charge layer was further calculated from the imaginary part of the measured impedance following the equation [50]:

$$C_{SC} = \frac{-1}{2\pi f Z_{im}} \quad (2)$$

where f stands for the frequency of the AC signal and Z_{im} for the imaginary part of impedance.

4. Conclusions

Surface modification of defective d-TiO_2 photocatalyst with platinum and copper nanoparticles resulted in a significant increase in its photocatalytic activity, both in UV-Vis and Vis range. The EPR analysis confirmed the presence of Ti defects in the structure of TiO_2 samples. The highest activity in Vis light was noticed for d-TiO_2 modified with Pt NPs. It resulted from surface plasmon resonance properties of Pt and narrowing the bandgap of the defective d-TiO_2. Among magnetic photocatalysts, the highest activity in Vis light was observed for Pt-modified and Pt/Cu-modified defective d-TiO_2 deposited on Fe_3O_4@SiO_2 magnetic core. Analysis of phenol degradation mechanism revealed that superoxide radicals are mainly responsible for phenol oxidation and mineralization. However, the photocatalytic activity in reaction of phenol degradation in UV-Vis light in the presence of Pt-modified Fe_3O_4@SiO_2/d-TiO_2 with the Pt particle size of about 20 nm was comparable with

the activity of Fe_3O_4@SiO_2/d-TiO_2. It resulted from the deposition of Pt NPs in the place of titanium vacancies, and as a consequence formation of larger metal particles due to the seed-mediated growth mechanism on the TiO_2. In this regard, a lower metal/semiconductor interface resulted in a decrease in photocatalytic activity in the UV-Vis spectrum range. Furthermore, the creation of a core-shell magnetic Fe_3O_4@SiO_2/d-TiO_2-Pt/Cu nanostructures allowed an effective separation of the obtained magnetic photocatalysts.

Author Contributions: Conceptualization, A.Z.-J.; Formal analysis, Z.B., S.D., J.R., K.S., and A.S.; Funding acquisition, A.Z.-J.; Investigation, Z.B.; Methodology, A.Z.-J. and Z.B.; Project administration, A.Z.-J.; Writing—original draft, A.Z.-J. and Z.B.; Writing—review and editing, A.Z.-J. and Z.B. All authors have read and agreed to the published version of the manuscript.

Funding: This research was funded by Polish National Science Centre (Grant No. NCN 2016/23/D/ST5/01021).

Acknowledgments: This research was supported by Polish National Science Centre, grant no. NCN 2016/23/D/ST5/01021.

Conflicts of Interest: The authors declare no conflict of interest.

References

1. Al-Mamun, M.R.; Kader, S.; Islam, M.S.; Khan, M.Z.H. Photocatalytic activity improvement and application of UV-TiO_2 photocatalysis in textile wastewater treatment: A review. *J. Environ. Chem. Eng.* **2019**, *7*, 103248. [CrossRef]
2. Zhu, D.; Zhou, Q. Action and mechanism of semiconductor photocatalysis on degradation of organic pollutants in water treatment: A review. *Environ. Nanotechnol. Monit. Manag.* **2019**, *12*, 100255. [CrossRef]
3. Ahmad, K.; Ghatak, H.R.; Ahuja, S.M. Photocatalytic Technology: A review of environmental protection and renewable energy application for sustainable development. *Environ. Technol. Innov.* **2020**, *19*, 100893. [CrossRef]
4. Wang, K.; Janczarek, M.; Wei, Z.; Raja-Mogan, T.; Endo-Kimura, M.; Khedr, T.M.; Ohtani, B.; Kowalska, E. Morphology- and Crystalline Composition-Governed Activity of Titania-Based Photocatalysts: Overview and Perspective. *Catalysts* **2019**, *9*, 1054. [CrossRef]
5. Koe, W.S.; Lee, J.W.; Chong, W.C.; Pang, Y.L.; Sim, L.C. An overview of photocatalytic degradation: Photocatalysts, mechanisms, and development of photocatalytic membrane. *Environ. Sci. Pollut. Res.* **2020**, *27*, 2522–2565. [CrossRef] [PubMed]
6. Loeb, S.K.; Alvarez, P.J.J.; Brame, J.A.; Cates, E.L.; Choi, W.; Crittenden, J.; Dionysiou, D.D.; Li, Q.; Li-Puma, G.; Quan, X.; et al. The Technology Horizon for Photocatalytic Water Treatment: Sunrise or Sunset? *Environ. Sci. Technol.* **2019**, *53*, 2937–2947. [CrossRef] [PubMed]
7. Serpone, N. Is the Band Gap of Pristine TiO_2 Narrowed by Anion- and Cation-Doping of Titanium Dioxide in Second-Generation Photocatalysts? *J. Phys. Chem. B* **2006**, *110*, 24287–24293. [CrossRef] [PubMed]
8. Dozzi, M.V.; Selli, E. Doping TiO_2 with p-block elements: Effects on photocatalytic activity. *J. Photochem. Photobiol. C Photochem. Rev.* **2013**, *14*, 13–28. [CrossRef]
9. Diaz-Angulo, J.; Gomez-Bonilla, I.; Jimenez-Tohapanta, C.; Mueses, M.; Pinzon, M.; Machuca-Martinez, F. Visible-light activation of TiO_2 by dye-sensitization for degradation of pharmaceutical compounds. *Photochem. Photobiol. Sci.* **2019**, *18*, 897–904. [CrossRef]
10. Endo-Kimura, M.; Janczarek, M.; Bielan, Z.; Zhang, D.; Wang, K.; Markowska-Szczupak, A.; Kowalska, E. Photocatalytic and Antimicrobial Properties of Ag2O/TiO2 Heterojunction. *ChemEngineering* **2019**, *3*, 3. [CrossRef]
11. Wysocka, I.; Kowalska, E.; Ryl, J.; Nowaczyk, G.; Zielińska-Jurek, A. Morphology, Photocatalytic and Antimicrobial Properties of TiO_2 Modified with Mono- and Bimetallic Copper, Platinum and Silver Nanoparticles. *Nanomaterials* **2019**, *9*, 1129. [CrossRef]
12. Klein, M.; Grabowska, E.; Zaleska, A. Noble metal modified TiO_2 for photocatalytic air purification. *Physicochem. Probl. Miner. Process.* **2015**, *51*, 49–57.
13. Janczarek, M.; Wei, Z.; Endo, M.; Ohtani, B.; Kowalska, E. Silver- and copper-modified decahedral anatase titania particles as visible light-responsive plasmonic photocatalyst. *J. Photonics Energy* **2016**, *7*, 12008. [CrossRef]

14. Wei, Z.; Janczarek, M.; Endo, M.; Wang, K.; Balcytis, A.; Nitta, A.; Mendez-Medrano, M.G.; Colbeau-Justin, C.; Juodkazis, S.; Ohtani, B.; et al. Noble Metal-Modified Faceted Anatase Titania Photocatalysts: Octahedron versus Decahedron. *Appl. Catal. B Environ.* **2018**, *237*, 574–587. [CrossRef] [PubMed]
15. Wu, Q.; Huang, F.; Zhao, M.; Xu, J.; Zhou, J.; Wang, Y. Ultra-small yellow defective TiO_2 nanoparticles for co-catalyst free photocatalytic hydrogen production. *Nano Energy* **2016**, *24*, 63–71. [CrossRef]
16. Liriano-Jorge, C.F.; Sohmen, U.; Özkan, A.; Gulyas, H.; Otterpohl, R. TiO_2 Photocatalyst Nanoparticle Separation: Flocculation in Different Matrices and Use of Powdered Activated Carbon as a Precoat in Low-Cost Fabric Filtration. *Adv. Mater. Sci. Eng.* **2014**, *2014*, 1–12. [CrossRef]
17. Lee, S.-A.; Choo, K.-H.; Lee, C.-H.; Lee, H.-I.; Hyeon, T.; Choi, W.; Kwon, H.-H. Use of Ultrafiltration Membranes for the Separation of TiO_2 Photocatalysts in Drinking Water Treatment. *Ind. Eng. Chem. Res.* **2001**, *40*, 1712–1719. [CrossRef]
18. Ray, S.; Lalman, J.A. Fabrication and characterization of an immobilized titanium dioxide (TiO_2) nanofiber photocatalyst. *Mater. Today Proc.* **2016**, *3*, 1582–1591. [CrossRef]
19. Zielińska-Jurek, A.; Klein, M.; Hupka, J. Enhanced visible light photocatalytic activity of Pt/I-TiO2in a slurry system and supported on glass packing. *Sep. Purif. Technol.* **2017**, *189*, 246–252. [CrossRef]
20. Wei, J.H.; Leng, C.J.; Zhang, X.Z.; Li, W.H.; Liu, Z.Y.; Shi, J. Synthesis and magnetorheological effect of Fe_3O_4-TiO_2 nanocomposite. *J. Phys. Conf. Ser.* **2009**, *149*, 25–29. [CrossRef]
21. Zhang, L.; Wu, Z.; Chen, L.; Zhang, L.; Li, X.; Xu, H.; Wang, H.; Zhu, G. Preparation of magnetic Fe_3O_4/TiO_2/Ag composite microspheres with enhanced photocatalytic activity. *Solid State Sci.* **2016**, *52*, 42–48. [CrossRef]
22. Abbas, M.; Rao, B.P.; Reddy, V.; Kim, C. Fe_3O_4/TiO_2 core/shell nanocubes: Single-batch surfactantless synthesis, characterization and efficient catalysts for methylene blue degradation. *Ceram. Int.* **2014**, *40*, 11177–11186. [CrossRef]
23. Sathishkumar, P.; Viswanathan, R.V.; Anandan, S.; Ashokkumar, M. $CoFe_2O_4/TiO_2$ nanocatalysts for the photocatalytic degradation of Reactive Red 120 in aqueous solutions in the presence and absence of electron acceptors. *Chem. Eng. J.* **2013**, *220*, 302–310. [CrossRef]
24. Jia, Y.; Liu, J.; Cha, S.; Choi, S.; Chang, Y.C.; Liu, C. Magnetically separable Au-TiO_2/nanocube $ZnFe_2O_4$ composite for chlortetracycline removal in wastewater under visible light. *J. Ind. Eng. Chem.* **2017**, *47*, 303–314. [CrossRef]
25. Fu, W.; Yang, H.; Li, M.; Chang, L.; Yu, Q.; Xu, J.; Zou, G. Preparation and photocatalytic characteristics of core-shell structure $TiO_2/BaFe_{12}O_{19}$ nanoparticles. *Mater. Lett.* **2006**, *60*, 2723–2727. [CrossRef]
26. Zielińska-Jurek, A.; Bielan, Z.; Dudziak, S.; Wolak, I.; Sobczak, Z.; Klimczuk, T.; Nowaczyk, G.; Hupka, J. Design and Application of Magnetic Photocatalysts for Water Treatment. The Effect of Particle Charge on Surface Functionality. *Catalysts* **2017**, *7*, 360. [CrossRef]
27. Zielińska-Jurek, A.; Bielan, Z.; Wysocka, I.; Strychalska, J.; Janczarek, M.; Klimczuk, T. Magnetic semiconductor photocatalysts for the degradation of recalcitrant chemicals from flow back water. *J. Environ. Manage.* **2017**, *195*, 157–165. [CrossRef]
28. Wysocka, I.; Kowalska, E.; Trzciński, K.; Łapiński, M.; Nowaczyk, G.; Zielińska-Jurek, A. UV-Vis-Induced Degradation of Phenol over Magnetic Photocatalysts Modified with Pt, Pd, Cu and Au Nanoparticles. *Nanomaterials* **2018**, *8*, 28. [CrossRef]
29. Mrotek, E.; Dudziak, S.; Malinowska, I.; Pelczarski, D.; Ryżyńska, Z.; Zielińska-Jurek, A. Improved degradation of etodolac in the presence of core-shell $ZnFe_2O_4/SiO_2/TiO_2$ magnetic photocatalyst. *Sci. Total Environ.* **2020**, *724*, 138167. [CrossRef]
30. Gad-Allah, T.A.; Fujimura, K.; Kato, S.; Satokawa, S.; Kojima, T. Preparation and characterization of magnetically separable photocatalyst ($TiO_2/SiO_2/Fe_3O_4$): Effect of carbon coating and calcination temperature. *J. Hazard. Mater.* **2008**, *154*, 572–577. [CrossRef]
31. Fan, Y.; Ma, C.; Li, W.; Yin, Y. Synthesis and properties of $Fe_3O_4/SiO_2/TiO_2$ nanocomposites by hydrothermal synthetic method. *Mater. Sci. Semicond. Process.* **2012**, *15*, 582–585. [CrossRef]
32. Shi, F.; Li, Y.; Zhang, Q.; Wang, H. Synthesis of $Fe_3O_4/C/TiO_2$ magnetic photocatalyst via vapor phase hydrolysis. *Int. J. Photoenergy* **2012**, *2012*, 1–8. [CrossRef]
33. Zielińska-Jurek, A.; Wei, Z.; Janczarek, M.; Wysocka, I.; Kowalska, E. Size-Controlled Synthesis of Pt Particles on TiO_2 Surface: Physicochemical Characteristic and Photocatalytic Activity. *Catalysts* **2019**, *9*, 940. [CrossRef]

34. Bielan, Z.; Kowalska, E.; Dudziak, S.; Wang, K.; Ohtani, B.; Zielińska-Jurek, A. Mono- and bimetallic (Pt/Cu) titanium(IV) oxide core-shell photocatalysts with UV/Vis light activity and magnetic separability. *Catal. Today* **2020**, in press. [CrossRef]
35. Gamboa, J.A.; Pasquevich, D.M. Effect of Chlorine Atmosphere on the Anatase-Rutile Transformation. *J. Am. Chem. Soc.* **1992**, *75*, 2934–2938. [CrossRef]
36. Byrne, C.; Fagan, R.; Hinder, S.; McCormack, D.E.; Pillai, S.C. New Approach of Modifying the Anatase to Rutile Transition Temperature in TiO_2 Photocatalysts. *RSC Adv.* **2016**, *6*, 95232–95238. [CrossRef]
37. Ricci, P.C.; Carbonaro, C.M.; Stagi, L.; Salis, M.; Casu, A.; Enzo, S.; Delogu, F. Anatase-To-Rutile Phase Transition In Nanoparticles Irradiated By Visible Light. *J. Phys. Chem. C* **2013**, *117*, 785–7857. [CrossRef]
38. Liu, H.; Jia, Z.; Ji, S.; Zheng, Y.; Li, M.; Yang, H. Synthesis of TiO_2/SiO_2@Fe_3O_4 magnetic microspheres and their properties of photocatalytic degradation dyestuff. *Catal. Today* **2011**, *175*, 293–298. [CrossRef]
39. Chi, Y.; Yuan, Q.; Li, Y.; Zhao, L.; Li, N.; Li, X.; Yan, W. Magnetically separable Fe_3O_4@SiO_2@TiO_2-Ag microspheres with well-designed nanostructure and enhanced photocatalytic activity. *J. Hazard. Mater.* **2013**, *262*, 404–411. [CrossRef] [PubMed]
40. Zielińska-Jurek, A.; Hupka, J. Preparation and characterization of Pt/Pd-modified titanium dioxide nanoparticles for visible light irradiation. *Catal. Today* **2013**, *230*, 181–187. [CrossRef]
41. Bielan, Z.; Kowalska, E.; Dudziak, S.; Wang, K.; Ohtani, B.; Zielinska-Jurek, A. Mono- and bimetallic (Pt/Cu) titanium(IV) oxide photocatalysts. Physicochemical and photocatalytic data for magnetic nanocomposites' shell. *Data Brief* **2020**, *31*, 105814. [CrossRef]
42. Chan, G.H.; Zhao, J.; Hicks, E.M.; Schatz, G.C.; Van Duyne, R.P. Plasmonic Properties of Copper Nanoparticles Fabricated by Nanosphere Lithography. *Nano Lett.* **2007**, *7*, 1947–1952. [CrossRef]
43. Ghodselahi, T.; Vesaghi, M.A.; Shafiekhani, A.; Baghizadeh, A.; Lameii, M. XPS study of the Cu@Cu_2O core-shell nanoparticles. *Appl. Surf. Sci.* **2008**, *225*, 2730–2734. [CrossRef]
44. Li, B.; Luo, X.; Zhu, Y.; Wang, X. Immobilization of Cu(II) in KIT-6 Supported Co3O4 and Catalytic Performance for Epoxidation of Styrene. *Appl. Surf. Sci.* **2015**, *359*, 609–620. [CrossRef]
45. Zielińska-Jurek, A.; Wei, Z.; Wysocka, I.; Szweda, P.; Kowalska, E. The effect of nanoparticles size on photocatalytic and antimicrobial properties of Ag-Pt/TiO_2 photocatalysts. *Appl. Surf. Sci.* **2015**, *353*, 317–325. [CrossRef]
46. Monga, A.; Rather, R.A.; Pal, B. Enhanced co-catalytic effect of Cu-Ag bimetallic core-shell nanocomposites imparted to TiO2 under visible light illumination. *Sol. Energy Mater Sol. Cells* **2017**, *172*, 285–292. [CrossRef]
47. Devi, L.G.; Kavitha, R. A review on plasmonic metal—TiO_2 composite for generation, trapping, storing and dynamic vectorial transfer of photogenerated electrons across the Schottky junction in a photocatalytic system. *Appl. Surf. Sci.* **2016**, *360*, 601–622. [CrossRef]
48. Dang, T.T.T.; Le, S.T.T.; Channei, D.; Khanitchaidecha, W.; Nakaruk, A. Photodegradation mechanisms of phenol in the photocatalytic process. *Res. Chem. Intermed.* **2016**, *42*, 5961–5974. [CrossRef]
49. Esplugas, S.; Gimenez, J.; Contreras, S.; Pascual, E.; Rodriguez, M. Comparison of different advanced oxidation processes for phenol degradation. *Water Res.* **2002**, *36*, 1034–1042. [CrossRef]
50. Beranek, R. (Photo)electrochemical methods for the determination of the band edge positions of TiO_2-based nanomaterials. *Adv. Phys. Chem.* **2011**, *2011*, 80–83. [CrossRef]

4. Magnetic semiconductor photocatalysts for the degradation of recalcitrant chemicals from flow back water

Anna Zielińska-Jurek, Zuzanna Bielan, Izabela Wysocka, Judyta Strychalska, Marcin Janczarek, Tomasz Klimczuk

Journal of Environmental Management 195 part 2 (2017) 157-165

DOI: 10.1016/j.jenvman.2016.06.056

P4

Journal of Environmental Management 195 (2017) 157–165

Contents lists available at ScienceDirect

Journal of Environmental Management

journal homepage: www.elsevier.com/locate/jenvman

Research article

Magnetic semiconductor photocatalysts for the degradation of recalcitrant chemicals from flow back water

Anna Zielińska-Jurek [a, *], Zuzanna Bielan [a], Izabela Wysocka [a], Judyta Strychalska [b], Marcin Janczarek [a], Tomasz Klimczuk [b]

[a] Department of Chemical Technology, Chemical Faculty, Gdansk University of Technology (GUT), Narutowicza 11/12, 80-233 Gdansk, Poland
[b] Department of Solid State Physics, Faculty of Applied Physics and Mathematics, (GUT), Poland

ARTICLE INFO

Article history:
Received 16 February 2016
Received in revised form
8 June 2016
Accepted 26 June 2016
Available online 6 July 2016

Keywords:
Heterogenous photocatalysis
Magnetic nanoparticles
Fe_3O_4/TiO_2 nanocomposites
Titanium (IV) oxide
Flow back water

ABSTRACT

In the present study treatability of persistent organic compounds from the flow back water after hydrauling fracturing was investigated. The combination of TiO_2 photocatalyst and magnetic oxide nanoparticles enhance the separation and recoverable property of nanosized TiO_2 photocatalyst. Fe_3O_4/TiO_2 and $Fe_3O_4@SiO_2/TiO_2$ nanocomposites were prepared by heteroagglomeration. The photocatalysts' characteristics by X-ray diffractometry (XRD), scanning electron microscopy (SEM), diffuse reflectance spectroscopy (DRS) showed that sample with the mass ratio of Fe_3O_4 to TiO_2 equal 1:4 and molar ratio of TEOS:Fe_3O_4 = 8:1 and NH_4OH:TEOS = 16:1 obtained by deposition TiO_2 P25 (Evonik) on magnetite core had about 124 $m^2\ g^{-1}$ specific surface area and superparamagnetic properties. The prepared composites contained TiO_2 and Fe_3O_4 crystal phases. The photocatalytic activity was estimated by measuring the decomposition rate of three model pollutants identified in the flow back water from one of the Baltic Shale Basin. Regarding flow back water treatment after shale gas exploration, the progress of photocatalytic degradation of organic compounds was measured by chemical oxygen demand (COD) concentration. The $Fe_3O_4@SiO_2/TiO_2$_P25 composite nanoparticles were recovered and re-used without significant reduction of efficiency.

1. Introduction

Water is a strategic resource for shale gas extraction, as it is used for hydraulic fracturing, the main method for fracturing rock during natural gas production (Chen and Carter, 2016). Fracturing technologies for shale gas production were developed mainly in the USA (Ray, 1976) and are currently being adapted to geological conditions and environmental requirements in China (Li et al., 2016), Germany, Poland (Baranzelli et al., 2015), Australia, New Zealand and other countries (Blythe et al., 2016). Hydraulic fracturing stimulate the flow of natural gas or oil, increasing the volumes that can be recovered. It is based on pumping fracturing fluid at very high pressure into the well, in order to prevent the fracture closing after reducing the pressure (Li et al., 2015). As shown in Fig. 1 the fracturing fluid, consists mainly of water and proppant (99.5%) and chemical additives (0.5%) (Gregory et al., 2011). Proppant is a material which prevents fractures from closing. Usually it is sand, sometimes ceramic material or resin coated sand (Mader, 1989). Chemicals are used to stimulate a reservoir and have various tasks in the fracturing fluids (see Table S1 in supporting materials), they are: friction reducers, acids, corrosion inhibitors, biocides, iron control agent, gelling agent, cross-linker, breaker, KCl, NaCl (Brannon and Tjon-Joe-Pin, 1996).

Hydraulic fracturing consumes 8000–20,000 m^3 of water per 1000 m horizontal well segment. After the hydraulic fracturing process is completed and pressure is released, between 20 and 30% of the original volume of the fracturing fluid will return to the surface as a flow back water (Stringfellow et al., 2014). The treatment and recycling of flowback water for reuse in hydraulic fracturing can enhance economic viability of gas production. It also minimizes potential environmental impacts, reduces demands on local water supplies, and meets regulatory requirements (Chen and Carter, 2016).

However, the flow back water managment is one of the major challenges for shale gas exploration and development. It is especially difficult since the flowback contain high concentration of

* Corresponding author. ul. Narutowicza 11/12, 80-233 Gdansk, Poland.
E-mail address: annjurek@pg.gda.pl (A. Zielińska-Jurek).

http://dx.doi.org/10.1016/j.jenvman.2016.06.056
0301-4797/

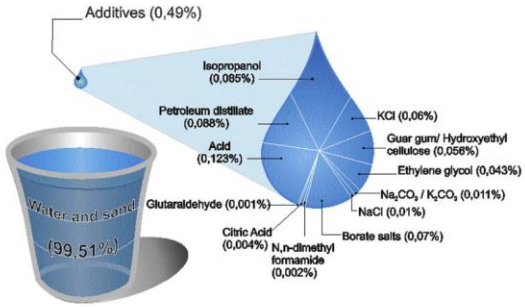

Fig. 1. Composition of fracturing fluid.

total dissolved solids (TDS). Depending on the well location, the TDS concentration in wastewater ranges from a few thousand mg/l to over 200,000 mg/l (Gregory et al., 2011). The concentration of salt in flow back water increases with time of residence down-hole. The main compound contributing to TDS value is NaCl; however, other soluble salts also affect this parameter (Gregory et al., 2011). Moreover, flow back fluid contains various combinations of heterocyclic organic compounds such as ethers, azines, ketones (acetone, MIBK, MEK), trihalomethanes, benzhydryl compounds (n-butylbenzene), aromatic hydrocarbons (trimethylbenzene, BTEX), tertiary alcohols (t-butyl alcohol), polycyclic aromatic hydrocarbons (naphthalene), alkylbenzenes (p-Cymene), organochlorides (Kargbo et al., 2010). Highly saline wastewater stream and some hydraulic fracturing chemical additives are difficult to treat with conventional processes. Therefore, there is a great demand for a more efficient and environmentally benign technology which can be applied for treating low concentration persistent organic pollutants from flow back water.

Chemical, biological, and physical methods have been implemented for treatment of flow back water. Pre-treatment techniques remove the suspended solids in the process of filtration. The nanofiltration and reverse osmosis processes are commonly used to desalinate water. However, the conventional processes are effective for TDS removal from flow back as the serial MF/UF membrane treatment and does not allow for the mineralization of organic impurities. The biggest problem is encountered in the removal of recalcitrant organic compounds.

Heterogeneous photocatalytic oxidation of organic pollutants occurred to be a promising process for water purification since many recalcitrant organic compounds at low concentration can be oxidized at a room temperature in the presence of a semiconductor photocatalyst (e.g. TiO_2) (Zielińska-Jurek et al., 2015). Photocatalysis has been used for the degradation of organic compounds such as alcohols, carboxylic acids, phenolic derivatives, or chlorinated aromatics, into harmless products e. g, carbon dioxide, water, and simple mineral acids (Lee et al., 2003; Sirtori et al., 2006; Chan et al., 2003). Water contaminated by oil can be treated efficiently by photocatalytic reaction (Jing et al., 2015). Herbicides and pesticides that may contaminate water such as 2,4,5 trichlorophenoxyacetic acid, 2,4,5 trichlorophenol, s-triazine herbicides and DDT can be also mineralized (Barbeni et al., 1987; Jang et al., 2005). Photocatalytic decomposition of ethylene glycol and propylene glycol by using UV-illuminated TiO_2 and platinum or palladium loaded TiO_2 photocatalyst led to carbon dioxide and water (Kim and Hoffmann, 2008).

However, the application of photocatalysts for wastewater treatment still needs to tackle a variety of technical problems (Zhang et al., 2014). The recovery and cyclic utilization of the nano-semiconductor photocatalysts is still a major problem hindering practical application in industrial processes (Fan et al., 2012). The combination of TiO_2 photocatalyst and magnetic oxide nanoparticles may enhance the separation and recoverable property of nanosized TiO_2 photocatalyst (Liu et al., 2011).

In this regard the aim of present study was preparation and characterization of Fe_3O_4/TiO_2 and $Fe_3O_4/SiO_2/TiO_2$ photocatalysts easier separable after water treatment process. The effect of TiO_2 matrix and molar ratio of TiO_2 to Fe_3O_4 on photocatalytic activity and magnetic properties in degradation of organic compounds present in flow back water were investigated.

2. Experimental

Detailed descriptions of materials, methods and instruments are available in the Supporting materials (S 2.1).

2.1. Preparation of Fe_3O_4/TiO_2 and Fe_3O_4@SiO_2/TiO_2 photocatalysts

The Fe_3O_4/TiO_2 nanocomposites of four different magnetite to titanium (IV) oxide molar ratios were prepared by an ultrasonic-assisted sol-gel method. Firstly, commercial Fe_3O_4 magnetic nanoparticles were dispersed in ethanol and ultrasonicated for 15 min. Then, TiO_2 was coated directly onto Fe_3O_4 nanoparticles by hydrolysis and condensation of titanium butoxide (TBT) in ethanol solution. The suspension was stirred for 2 h and ultrasonicated for another 1 h at temperature below 35 °C. The resulting Fe_3O_4/TiO_2 nanoparticles were separated, dried at 60 °C to dry mass and then calcinated at 400 °C for 2 h.

An inertial layer of silica between TiO_2 shell and magnetic core was proposed in order to avoid leaching of iron. In this regard, the magnetite particles (~50 nm) were dispersed in ethanol and homogenized by ultrasonication for 15 min. Then alcoholic solution of ammonia was added dropwise into magnetite dispersion and sonicated for another 15 min. Tetraethyl orthosilicate (TEOS), preliminarily diluted in ethanol was added to the magnetite particle suspension and the suspension was ultrasonicated for the next 15 min. The molar ratio of TEOS to Fe_3O_4 and NH_4OH to TEOS was

equal 8:1 and 16:1, respectively. After aging of silica gel ethanolic solution of TiO_2 precursor (TIP, TBT) or suspension of commercial TiO_2 (P25, ST-01) in ethanol was added into Fe_3O_4/SiO_2 dispersion. Mixing was carried out for 2 h and then the obtained suspension of the photocatalyst was centrifuged, dried at 70 °C to dry mass and calcinated at 400 °C for 2 h. The calcination temperature was attained at a heating rate of 2 °C min^{-1}.

3. Results and discussion

3.1. Characterization of nanocomposites

The morphological properties determine the photocatalytic activity of TiO_2-based nanocomposites. Sample labeling, the amount of Fe_3O_4 to TiO_2, molar ratio of TEOS to Fe_3O_4 used during the preparation procedure, as well as the magnetic properties of obtained photocatalysts and their BET surface area are given in Tables 1 and 2. The surface area for pure TiO_2_TBT was 91 $m^2 g^{-1}$. The surface area of the Fe_3O_4/TiO_2 samples obtained by hydrolysis of TBT in Fe_3O_4 dispersion, fluctuated from 15 $m^2 g^{-1}$ to 79 $m^2 g^{-1}$ and was dependent on the mass ratio of Fe_3O_4 to TiO_2. Introduction of silica layer between Fe_3O_4 and TiO_2 results in increase of BET surface area. The surface area of the samples $Fe_3O_4@SiO_2/TiO_2$_5–7 obtained by TBT hydrolysis fluctuated from 210 to 297 $m^2 g^{-1}$ and were dependent on silica content (molar ratio of TEOS to Fe_3O_4) in the sample.

Relations between photoactivity in reaction of phenol, pyridine and 4-heptanone degradation versus BET surface area are also shown in Table 1.

The surface area of $Fe_3O_4@SiO_2/TiO_2$ samples prepared using different TiO_2 source (see in Table 2) was mainly affected by surface area of TiO_2 particles and SiO_2 introduced into structure of obtained nanocomposites. For $Fe_3O_4@SiO_2/TiO_2$ nanocomposites, obtained with the same preparation conditions (Fe_3O_4:TiO_2 = 1:2; TEOS:Fe_3O_4 = 8:1), but by introducing different TiO_2 source during preparation procedure, the BET surface area fluctuated from 124 to 297 $m^2 g^{-1}$. The obtained results indicate that not so much the surface area but rather the amount and source of TiO_2 deposited on $Fe_3O_4@SiO_2$ nanocomposite influences the photocatalytic activity.

The X-ray diffraction pattern of the obtained Fe_3O_4/TiO_2 and $Fe_3O_4@SiO_2/TiO_2$ are presented in Fig. 2a,b. For Fe_3O_4/TiO_2 nanocomposites obtained using TBT as a titania NPs precursor pure phase anatase was obtained. The average size of the TiO_2 crystallites calculated using the Scherrer equation to the main peak of anatase (101) was about 9 nm. The diffraction peaks at 30°, 35.6°, 43.2°, 57.2°, 62.8° refer to [220], [311], [400], [511] and [440] planes of cubic inverse spinel Fe_3O_4, respectively. The results are in good agreement with XRD patterns of magnetite nanoparticles previously reported in the literature (Hui et al., 2010; Wu et al., 2015). Additionally, the reflection peaks related to the maghemite [220], [440] or hematite [104], [113] at 33° and 41° can be also detected. Kazeminezhad et al. reported that heat treatment of inverse cubic spinel structure of magnetite nanoparticles at a temperature above 200 °C resulted in conversion to the cubic structure of maghemite (γ-Fe_2O_3). Further, the increasing of temperature up to 650 °C caused the phase transformation of cubic γ-Fe_2O_3 to tetragonal structure of γ-Fe_2O_3 and finally to the phase of rhombohedral hematite (α-Fe_2O_3) at 800 °C (Kazeminezhad and Mosivand, 2014). Guivar et al. observed that the diffraction peaks at 2θ value of around 30°, 32°, 35°, 42°, 53°, 57°, 63° and 75° correspond to [221], [310], [311], [400], [511], [440] and [533] planes of maghemite (Guivar et al., 2014). On the other hand, hematite is the most stable iron oxide under ambient conditions (Kazeminezhad and Mosivand, 2014). Bora et al. reported that in the case of magnetite nanoparticles with diameter below 20 nm, the maghemite phase is the most stable phase due to the dominant factor of surface free energy which is lower than for hematite. Transformation of small Fe^{3+} nanoparticles to hematite requires therefore higher temperatures for nanocomposites than for bulk material. However, larger iron oxide particles transform to α-Fe_2O_3 (Bora et al., 2012). Therefore, it should be noted that in the case of existence or coexistence of magnetite, maghemite and/or hematite it is difficult to identify the crystalline phase formed from the techniques of X-ray diffraction. As shown in Fig. 2-b magnetic photocatalysts containing a core of Fe_3O_4 and a SiO_2 layer in order to avoid photodissolution of iron and to prevent phase transformation of Fe_3O_4 to Fe_2O_3 have shown no diffraction peaks at 33° and 41°. This means that at the calcination step no oxidation of the magnetite core to hematite or maghemite was occured.

The DR/UV-Vis absorption spectra for the Fe_3O_4/TiO_2 and final $Fe_3O_4@SiO_2/TiO_2$ nanostructures are presented in Fig. 3a,b. The obtained Fe_3O_4/TiO_2 magnetic photocatalysts showed two absorption bands at the wavelength of about 300–350 nm attributed to titanium (IV) oxide nanoparticles and at around 450 nm attributed to magnetite nanoparticles absorption response. The pristine TiO_2 only absorbs UV light with wavelength shorter than 380 nm because of its wide band gap (3.0–3.2 eV). The absorption of visible light for obtained nanocomposites results from introducing of iron ions into the lattice structure of TiO_2. On the other hand, Stefan at el. stated that the absorption band observed at about 485 nm appears due to the fact that iron oxide nanoparticles can increase the energy spacing between the TiO_2 conduction band states finally leading to the energy quantization of levels (Stefan et al., 2014). The absorption properties under Vis light were depended on the ratio of TiO_2 (obtained from TBT) to Fe_3O_4. The sample Fe_3O_4/TiO_2_4 with mass ratio of Fe_3O_4 to TiO_2 equal 2:1 showed 2-times stronger absorption of visible light compared to Fe_3O_4/TiO_2_3 nanocomposite with proportion of Fe_3O_4 to TiO_2 at 1:4 (see in Fig. 3-a).

The energy band gap of the semiconductor samples was calculated by the Kubelka-Munk theory. As shown in Table 2, for magnetic photocatalysts with TiO_2 obtained via precursor hydrolysis (TBT or TIP) the band gap values decrease and the absorption edge generates red shift. Introduction of SiO_2 layer, which is characterized by a low absorption in the analyzed wavelength range reduces

Table 1
Characteristic of Fe_3O_4/TiO_2 and $Fe_3O_4@SiO_2/TiO_2$ photocatalysts obtained by hydrolysis of TBT in Fe_3O_4 dispersion.

Sample label[a]	Fe_3O_4/TiO_2	TEOS/Fe_3O_4	BET surface area [m^2/g]	Magnetic properties [emu/g]	Degradation constant rate [min^{-1}]·10^{-2}			Energy band gap [eV]
					Phenol	Pyridine	4-Heptanone	
Fe_3O_4/TiO_2_1	1:1	–	16	18.2	1.01	0.18	1.36	1.8
Fe_3O_4/TiO_2_2	1:2	–	37	14.8	1.34	0.64	1.21	1.8
Fe_3O_4/TiO_2_3	1:4	–	79	7.5	3.02	0.26	2.10	1.9
Fe_3O_4/TiO_2_4	2:1	–	15	42.5	0.85	0.15	0.46	1.7
$Fe_3O_4@SiO_2/TiO_2$_5	1:2	2:1	210	20.2	0.68	0.04	0.69	1.8
$Fe_3O_4@SiO_2/TiO_2$_6	1:2	8:1	297	15.3	0.77	0.18	0.72	1.8
$Fe_3O_4@SiO_2/TiO_2$_7	1:2	16:1	269	10.0	0.43	0.03	0.83	1.7

[a] All the samples were obtained using TBT as a TiO_2 precursor during preparation procedure.

Table 2
Characteristic of Fe_3O_4@SiO_2/TiO_2 nanocomposites – the effect of TiO_2 matrix.

Sample label	Fe_3O_4/TiO_2	TEOS/Fe_3O_4	BET surface area [m^2/g]	Degradation constant rate [min^{-1}]·10^{-2}			Energy band gap [eV]
				Phenol	Pyridine	4-Heptanone	
P25	–	–	55	4.78	0.87	0.77	3.15
Fe_3O_4	–	–	8	0.90	0.22	0.49	0.1
Fe_3O_4@SiO_2/TiO_2_ST01	1:2	8:1	191	2.81	0.60	1.26	2.8
Fe_3O_4@SiO_2/TiO_2_P25	1:2	8:1	124	4.60	0.85	1.98	3.15
Fe_3O_4@SiO_2/TiO_2_TIP	1:2	8:1	163	1.00	0.44	0.78	1.9
Fe_3O_4@SiO_2/TiO_2_TBT	1:2	8:1	297	0.77	0.18	0.72	1.8

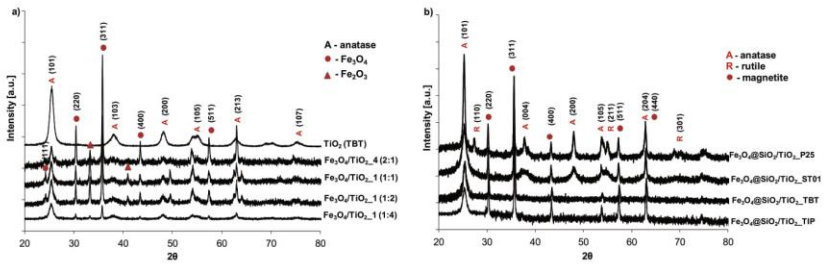

Fig. 2. XRD patterns of Fe_3O_4/TiO_2 nanoparticles (a); Fe_3O_4@SiO_2/TiO_2 nanocomposites varying the source of TiO_2 NPs (b).

the absorption properties in the range from 300 nm to 700 nm (as shown in Fig. 3-a for samples Fe_3O_4@SiO_2/TiO_2_5–7).

The inset in Fig. 3-b showed the optical absorption edge (in eV) for magnetic photocatalyst based on commercial form of TiO_2 (P25) and the sample with TiO_2 obtained from TBT hydrolysis. It was found that the band gap energy for Fe_3O_4@SiO_2/TiO_2_P25 photocatalyst was about 3.15, which indicates that silica and magnetite particles were not introduce into structure of TiO_2. For Fe_3O_4@SiO_2/TiO_2_TBT the band gap energy equaled 1.8 eV, indicating doping of TiO_2 lattice with iron oxide during preparation procedure. Our results are in good agreement with the literature. Niu et al. (2014) obtained Fe_3O_4@TiO_2 nanocomposites by solvothermal crystallization of titanium precursor (TBT) on preformed Fe_3O_4 nanoparticles. The energy bandgap for obtained Fe_3O_4@TiO_2 nanoparticles calculated by the Kulbeka-Munk theory was about 2.10 eV Banisharif et al. (2013) reported that the band-gap of TiO_2/Fe_3O_4 photocatalysts prepared by an ultrasonic-assisted deposition-precipitation method using $TiCl_4$ as a titania precursor is narrower than that of TiO_2 (from 2.0 to 2.4 eV) and increases with increasing the molar ratio of TiO_2/Fe_3O_4. The Fe^{3+} replaces Ti^{4+} disassociated from TiO_2 and then generates an interband trap that shifts TiO_2 absorption spectrum to the visible range (Banisharif et al., 2013). The DR/UV-Vis analysis are also in good agreement with SEM results.

SEM/EDS composition maps in a selected areas of Fe_3O_4@SiO_2/TiO_2_TBT sample shown in Fig. 4-a indicated that Fe and Ti coexist in the structure of nanocomposite. Aggregates of nanoparticles of TiO_2 did not completely cover the Fe_3O_4 particles surface. Moreover, morphological comparison between samples Fe_3O_4@SiO_2/TiO_2_TBT and Fe_3O_4@SiO_2/TiO_2_P25 revealed differences in the

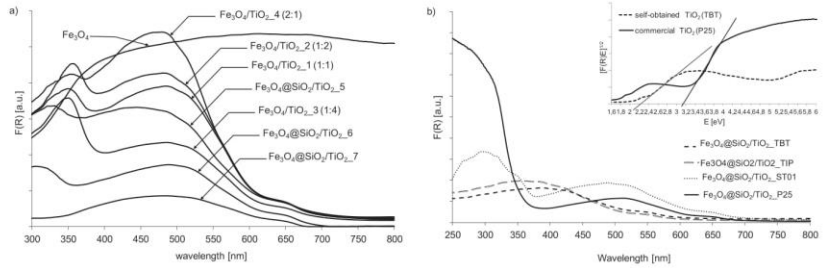

Fig. 3. DR/UV-Vis spectra of Fe_3O_4/TiO_2 nanoparticles (a); Fe_3O_4@SiO_2/TiO_2 nanocomposites varying the source of TiO_2 (b).

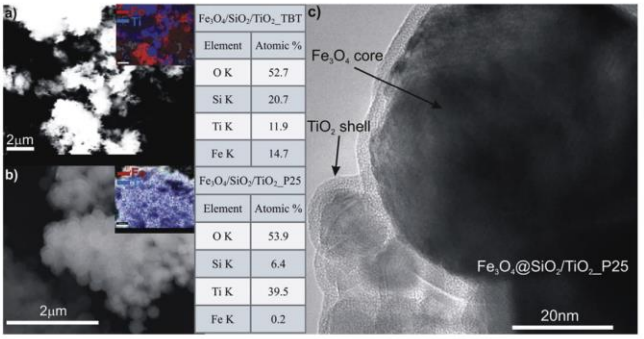

$Fe_3O_4/SiO_2/TiO_2$_TBT	
Element	Atomic %
O K	52.7
Si K	20.7
Ti K	11.9
Fe K	14.7

$Fe_3O_4/SiO_2/TiO_2$_P25	
Element	Atomic %
O K	53.9
Si K	6.4
Ti K	39.5
Fe K	0.2

Fig. 4. SEM microscopy images for sample $Fe_3O_4@SiO_2/TiO_2$_TBT (a) for sample $Fe_3O_4@SiO_2/TiO_2$_P25 (b) TEM analysis for $Fe_3O_4@SiO_2/TiO_2$_P25 (c).

textural features and composition of the surface layer of the $Fe_3O_4@SiO_2/TiO_2$ nanocomposites. As shown in Fig. 4-b for sample $Fe_3O_4@SiO_2/TiO_2$_P25 a greater amount of Ti to Fe was detected based on EDS analysis, which could be related to the formation of TiO_2 layer coated on Fe_3O_4 core particles (Hasanpour et al., 2012).

Morphology of $Fe_3O_4@SiO_2/TiO_2$_P25 core-shell nanoparticles were further determined using transmission electron microscopy. Based on Fig. 4-c it can be seen that $Fe_3O_4@SiO_2/TiO_2$_P25 nanoparticles show a roughly spherical morphology with aggregates of magnetite particles surrounded by SiO_2 and thin TiO_2 layer.

The magnetic properties of as-prepared Fe_3O_4/TiO_2 composites were measured at room temperature (273 K) and the results are presented in Fig. 5-a. Magnetic properties depend on the amount of magnetic phase fraction in the nanocomposites. The highest observed value of saturation magnetization (~42.2 emu/g) was found for Fe_3O_4/TiO_2_4 (ratio 2:1). The introduction of silica layer between Fe_3O_4 and TiO_2 resulted in a reduction of the saturation magnetization (M_s) from 20.2 emu/g for sample $Fe_3O_4@SiO_2/TiO_2$_5 (TEOS:Fe_3O_4 = 2:1) to 10 emu/g for sample $Fe_3O_4@SiO_2/TiO_2$_7 with molar ratio TEOS/Fe_3O_4 = 16:1.

Taking into account the morphological, magnetic and photocatalytic properties of the obtained nanocomposites (as shown in Table 1 and Fig. 5-b), we selected parameters corresponding to the amount of Fe_3O_4 to TiO_2 and molar ratio of TEOS to Fe_3O_4 in order to investigate the effect of TiO_2 matrix on photocatalytic activity of magnetically separable photocatalysts. The most active sample $Fe_3O_4@SiO_2/TiO_2$_P25 presented in Fig. 5-c showed the saturation magnetization value of 12.1 emu/g. However, the remanent magnetization (M_r) of this sample was close to zero, indicating that photocatalyst revealed superparamagnetic properties at room temperature.

3.2. Characterization of flow back water

In our study flow back water from Baltic Shale Basin was analyzed. The water samples were collected on days 1, 5, 10 and 15 following the fracturing process. The turbidity on the first day after hydrofracturing was 420 NTU. Therefore, the study of physicochemical parameters of flowback water was performed after the pre-treatment step of coagulation using iron (II) sulphate. The amount of the coagulant was calculated based on the measured turbidity of the samples. The pH value of flow back water remains near neutrality (see in Table S2 in supporting materials). The concentration of salt in flow back increases with time of residence down-hole. The organic compounds measured as TOC were removed in the pre-treatment process with the very little efficiency (below 5%), which indicates that they were mainly in the dissolved phase. Exemplary results of GC/MS analysis for the flowback water after 5 day of fracturing is presented in Fig. S1. Most of the organic matter was organic aromatic hydrocarbons, which are also the dominant constituent in extracts of organic shale that have not been hydrofracked. Analysis by GC/MS showed that the waters contained low amounts of organics that were added to the hydrofracking solution (see Table 3). These results indicate that flow back waters contain some of the fracking constituents which are toxic, resistant to degradation and cancerogenic. For future photocatalytic properties studies we selected three model pollutants present in investigated flow back water, which are: pyridine, phenol and 4-heptanone. Pyridine was chosen as model, since this compound is one of the most toxic and cancerogenic organic compounds present in flow back water. 4-heptanone is a volatile organic compound and phenol is a non-volatile, common contaminant frequently present in industrial wastewaters. Moreover, the US Environmental Protection Agency (EPA) and The European Union (EU) have classified phenolic compounds as priority pollutants since they are harmful to organisms at low concentrations and to human health.

3.3. Photocatalytic degradation of model pollutants present in flow back water

The kinetics of phenol photodegradation in aqueous solution under UV-Vis light in the presence of Fe_3O_4/TiO_2 and $Fe_3O_4@SiO_2/TiO_2$ obtained using TBT as a TiO_2 precursor during preparation procedure are shown in Fig. 6-a and the observed rate constants are also included in Table 1. Among Fe_3O_4/TiO_2 nanocomposites the best photocatalytic activity in reaction of phenol and 4-heptanone degradation revealed samples with the highest proportion of TiO_2 to Fe_3O_4. The apparent rate constants of the first-order kinetic of phenol photodegradation increased from $0.85 \cdot 10^{-2}$ min^{-1} to $1.34 \cdot 10^{-2}$ min^{-1} and $3.02 \cdot 10^{-2}$ min^{-1} for Fe_3O_4/TiO_2_4 (Fe_3O_4:TiO_2 = 2:1); Fe_3O_4/TiO_2_2 (Fe_3O_4:TiO_2 = 1:2) and Fe_3O_4/

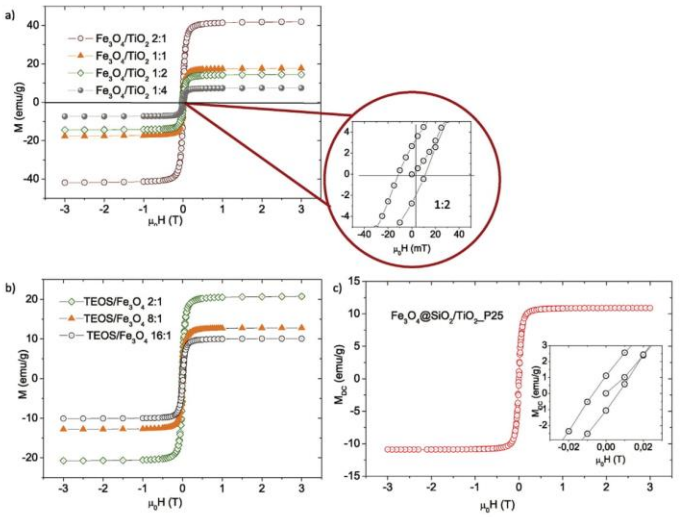

Fig. 5. Magnetic hysteresis for obtained Fe_3O_4/TiO_2 (a), $Fe_3O_4@SiO_2/TiO_2$ nanocomposites (b) and the most photoactive sample $Fe_3O_4@SiO_2/TiO_2$_P25 (c).

Table 3
Organic contaminants in flow back water, median day 10th.

Description	Percentage	Hazards from MSDS
1,3,5-Trimethylbenzene	1	Harmful if inhaled or swallowed
Toluene	0.3	Irritant
Butyl glycol	0.2	Harmful if inhaled or swallowed
Decahydronaphthalene	4	Harmful if inhaled or swallowed
1-Bromo-3-methylcyclohexane	3	Harmful if swallowed.
Ethyl *tert*-butyl ether	1	Irritant, Harmful if swallowed
Pyridine	44	Harmful by ingestion, inhalation and if absorbed through skin.
2,3-Dimethyl-decahydronaphthalene	2.5	Not found
Benzaldehyde	0.3	Harmful if swallowed or inhaled
4-Heptanone	4	Harmful if inhaled
Phenol	1.1	Harmful if inhaled or swallowed.
1,2-Diisopropenyl-cyclobutane	6.9	Harmful by ingestion, inhalation and if absorbed through skin.
1,2-Dimethyldiazene 1-oxide	28.7	May cause cancer. May cause heritable genetic damage.
Oxalic acid, 6-ethyloct-3-yl isobutyl ester	3	Not found

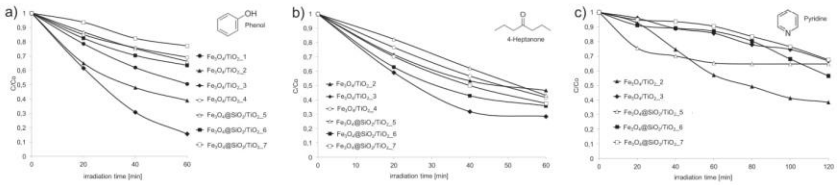

Fig. 6. Degradation of phenol (a), pyridine (b) and 4-heptanone (c) with magnetic TiO_2-based photocatalysts under UV-vis irradiation.

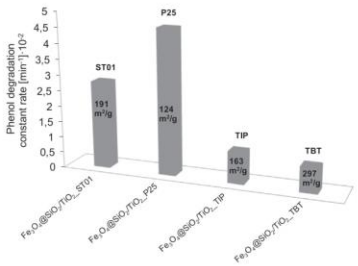

Fig. 7. Degradation constant rates of Fe_3O_4@SiO_2/TiO_2 nanoparticles prepared using different TiO_2 matrix.

TiO_2_3 (Fe_3O_4:TiO_2 = 1:4), respectively. The 4-heptanone degradation constant rate increased from $0.46 \cdot 10^{-2}$ min^{-1} to $2.10 \cdot 10^{-2}$ min^{-1} for Fe_3O_4/TiO_2_4 and Fe_3O_4/TiO_2_3, respectively. The photocatalytic activity in reaction of pyridine degradation of Fe_3O_4/TiO_2 nanocomposites increased with increasing Fe_3O_4:TiO_2 mass ratio from 2:1 up to 1:2 and then decreased for sample Fe_3O_4:TiO_2_3 for which the mass ratio of Fe_3O_4:TiO_2 equal 1:4 (see in Fig. 6-c). Sample Fe_3O_4/TiO_2_3 with Fe_3O_4:TiO_2 mass ratio of 1:4 had the highest photocatalytic activity in reaction of phenol and 4-heptanone degradation but 2 times lower value of saturation magnetization compared to samples Fe_3O_4/TiO_2_1 and Fe_3O_4/TiO_2_2.

In Fe_3O_4/TiO_2 nanocomposites the photogenerated charge carriers in the excite TiO_2 can be transferred into Fe_3O_4 phase because of its lower lying conduction band and upper lying valence. In order to prevent phase transformation of Fe_3O_4 to Fe_2O_3 and photodissolution of iron, coating of silica nanoparticles was performed. The silica content was controlled by varying the experimental parameters eg. molar ratio of TEOS to Fe_3O_4 and NH_4OH to TEOS. Among Fe_3O_4@SiO_2/TiO_2 nanocomposites obtained by hydrolysis of TBT in Fe_3O_4 dispersion the best photocatalytic activity revealed sample with molar ratio TEOS:Fe_3O_4 equal 8:1. The 60 min irradiation resulted in 37% of phenol, 13% of pyridine and 64% of 4-heptanone degradation. Considering the effect of mass ratio Fe_3O_4:TiO_2, molar ratios of TEOS to Fe_3O_4 and NH_4OH to TEOS on magnetic and photocatalytic properties of obtained nanocomposites, for further investigation sample Fe_3O_4@SiO_2/TiO_2_6 was selected due to its much higher photocatalytic activity and magnetic properties compared to samples Fe_3O_4@SiO_2/TiO_2_5 and Fe_3O_4@SiO_2/TiO_2_7.

Simply dissolution test using ASA spectrophotometer was carried out to check a silica coating insulation function. The results, reported in Table S3 clearly indicate that no dissolution of magnetite was ensured by presence of the silica shell.

The phenol photodegradation efficiency in the presence of Fe_3O_4@SiO_2/TiO_2 nanoparticles prepared using different TiO2 types is presented in Fig. 7. It could be clearly observed that photocatalytic activity of the obtained nanocomposites strongly depends on the physical properties of TiO_2 (e.g., crystal structure and particle size) and operating conditions during preparation procedure. Deposition of commercial TiO_2 photocatalyst on the core of magnetite nanoaprticles resulted in enhancement of photoactivity. The best photocatalytic activity revealed sample Fe_3O_4@SiO_2/TiO_2_P25. After 60 min of irradiation about 95% of phenol was degraded. This sample was selected for further reusability studies of magnetic photocatalyst. In order to evaluate the effectiveness of Fe_3O_4@SiO_2/TiO_2_P25 photocatalyst after its recovery, the four subsequent cycles of pyridine degradation were proceed. The photocatalyst was not removed from the reactor during the whole experiment. Therefore, before the 2nd, 3rd and 4th cycles, the working solution was additionally irradiated until a complete pyridine degradation was achieved. After that a defined amount of pyridine was added to the reactor to attain the initial concentration of 200 mg/dm^3 and the next photodegradation cycle was started. The obtained results are presented in Fig. 8-a. In the first cycle the average degradation constant rate was 0.85 ± 0.03 min^{-1}. In the second run the average degradation constant rate slightly decreases to 0.78 ± 0.02 min^{-1} and then achieved the highest loss of photocatalyst effectiveness of 0.67 ± 0.02 min^{-1} due to adsorption of organic compounds over the nanoparticles surface. In the fourth cycle the average degradation rate increased to the initial value measured in the second cycle of irradiation. The results proven a high photocatalytic activity of the obtained Fe_3O_4@SiO_2/TiO_2_P25 nanocomposite and the possibility of its re-use.

Afterwards, the efficiency of a model flow back water degradation containing all three selected contaminants and salinity at the value of 30 g dm^{-3} was performed. It was found that during 30 min of dark reaction (without irradiation) no adsorption of the model pollutants on the surface of photocatalyst occured. The decomposition of pyridine, 4-heptanone and phenol was studied by GC/MS analysis. As shown in Fig. 8-b, after 180 min of irradiation about 44% of pyridine was decomposed followed by degradation of 65% of 4-heptanon and 78% of phenol. Photocatalytic degradation of phenol and 4-heptanon in the mixture was only slightly lower compared to their decomposition separately as individual organic pollutants. However, the efficiency of pyridine degradation decreased by about 30%. Elsayed (2015) have also observed that increasing the initial concentration of the solution would decrease

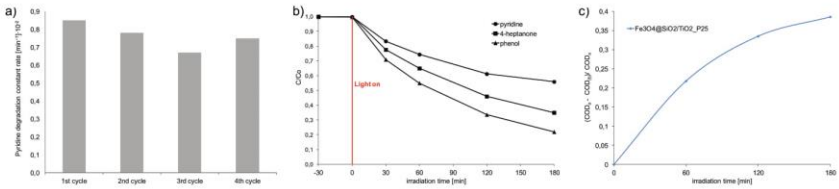

Fig. 8. Pyridine degradation constant rate in the presence of Fe_3O_4@SiO_2/TiO_2_P25 measured in the fourth subsequent cycles (a), Photocatalytic decomposition of aqueous solution of three model pollutants using Fe_3O_4@SiO_2/TiO_2_P25 nanocomposite (b) Degradation of organic compounds from flow back water. The COD removal as a function of time for Fe_3O_4@SiO_2/TiO_2_P25 photocatalyst (c).

the removal rates of pyridine. Moreover in the model solution, chloride or sodium ions can compete with the organic pollutant for the active sites, thus inhibiting the TiO_2 nanoparticles towards organic molecules degradation [Zielińska-Jurek et al., 2015].

Regarding real sample of flow back fluid treatment, the efficiency of organic compounds degradation is presented in Fig. 8-c and described as the COD removal fraction using parameter R as:

$$\left(COD_o - COD_{(t)}\right)/COD_o$$

where COD_0 and $COD_{(t)}$ are the initial and at any irradiation time COD values. The experiments were carried out under the natural flow back water pH of 6.2 and temperature of 293 K. The flow back water sample used for the photocatalytic degradation was preliminarily submitted to coagulation and centrifugation to eliminate the suspended solid. The results, reported in Fig. 8-c shows a COD reduction of about 40% after 180 min of irradiation.

4. Conclusions

The efficiency of degradation of organic compounds present in flow back water using Fe_3O_4/TiO_2 and $Fe_3O_4@SiO_2/TiO_2$ nanocomposites is reported in this article. Magnetic photocatalysts were prepared by heteroagglomeration method and their photocatalytic efficiency as well as the ability of separation by the external magnetic field were investigated. For Fe_3O_4/TiO_2 nanocomposites the photocatalytic activity increase gradually with increasing proportion of TiO_2 to Fe_3O_4 but the saturation magnetization decrease since the content of Fe_3O_4 magnetic particles decrease. In order to keep the composite particles with both photocatalytic efficiency and magnetism at an appropriate level the optimum proportion of Fe_3O_4 to TiO_2 was determined to 1:2. Magnetic cores were coated with silica layer to prevent photodissolution of iron and phase transformation of Fe_3O_4. Metal leaching was not detected in the products, demonstrating the efficiency of magnetic separation and stability of magnetite core during irradiation and under acidic conditions ($3 < pH < 5$).

The results reported herein show for the first time that the TiO_2 source (commercial TiO_2 or obtained from precursor hydrolysis) influences the structural, photocatalytic and magnetic properties of $Fe_3O_4@SiO_2/TiO_2$ nanocomposites. Among all the obtained $Fe_3O_4@SiO_2/TiO_2$ nanocomposites the best photocatalytic activity was observed for the sample $Fe_3O_4@SiO_2/TiO_2$_P25, which was almost as effective as TiO_2 (P25, Evonik) but easier separable due to their superparamagnetic properties. Photocatalytic activity measured in the fourth subsequent cycles showed good reusability as no loss of efficiency of pyridine degradation was observed. The efficiency of the model organic compounds degradation in their mixture was 40%, 50% and 60% for pyridine, phenol and 4-heptanone, respectively. Regarding flow back water treatment for real sample, the photoactivity under UV-Vis light irradiation after 180 min of irradiation measured by chemical oxygen demand (COD) removal was about 40%. The complete degradation of the organic substances present in flow back water could be reached within 8 h of illumination.

Acknowledgments

This research was financially supported by Norway Grants in the Polish-Norwegian Research Programme (Small Grant Scheme) operated by the National Center for Research and Development, Grant No. POL-NOR/207659/23/2013 and The Center for Advanced Studies – The development of interdisciplinary doctoral studies at the Gdansk University of Technology in the key areas of the Europe 2020 Strategy.

Appendix A. Supplementary data

Supplementary data related to this article can be found at http://dx.doi.org/10.1016/j.jenvman.2016.06.056.

References

Banisharif, A., Hakim Ellahi, S., Anaraki Firooz, A., Khodadadi, A.A., Mortazavi, Y., 2013. TiO_2/Fe_3O_4 nanocomposite photocatalysts for enhanced photodecolorization of Congo red dye. Int. J. Nanosci. Nanotechnol. 9 (4), 193–202.
Baranzelli, C., Vandecasteele, I., Barranco, R.R., Rivero, I.M.i, Pelletier, N., Batelaan, O., Lavalle, C., 2015. Scenarios for shale gas development and their related land use impacts in the Baltic Basin, Northern Poland. Energy Policy 84, 80–95.
Barbeni, M., Morello, M., Pramauro, E., Pelizzetti, E., Vincenti, M., Borgarello, E., Serpone, N., 1987. Sunlight photodegradation of 2,4,5-trichlorophenoxy-acetic acid and 2,4,5-trichlorophenol on TiO_2. Identification of intermediates and degradation pathway. Chemosphere 16 (6), 1165–1179.
Blythe, K., Jeffries, R., Travers, M., 2016. Chapter 13 – an international perspective of challenges and constraints in shale gas extraction. In: Environmental and Health Issues in Unconventional Oil and Gas Development, pp. 225–248.
Bora, D.K., Braun, A., Erat, S., Safonova, O., Graule, T., Constable, E.C., 2012. Evolution of structural properties of iron oxide nano particles during temperature treatment from 250 °C-900 °C: X-ray diffraction and Fe K-shell pre-edge X-ray absorption study. Curr. Appl. Phys. 12 (3), 817–825.
Brannon, H.D., Tjon-Joe-Pin, R.M., 1996. Fracturing Fluid Treatment Design to Optimize Fluid Rheology and Proppant Pack Conductivity. US 5562160 A.
Chan, A.H.C., Chan, C.K.C., Barford, C.J.P., Porter, J.F., 2003. Water Res. 37, 1125–1135.
Chen, H., Carter, K.E., 2016. Water usage for natural gas production through hydraulic fracturing in the United States from 2008 to 2014. J. Environ. Manag. 170, 152–159.
Elsayed, M.A., 2015. Ultrasonic removal of pyridine from wastewater: optimization of the operating conditions. Appl. Water Sci. 5, 221–227.
Fan, Y., Ma, C., Li, W., Yin, Y., 2012. Synthesis and properties of $Fe_3O_4/SiO_2/TiO_2$ nanocomposites by hydrothermal synthetic method. Mater. Sci. Semicond. Process. 15, 582–585.
Gregory, K.B., Vidic, R.D., Dzombak, D.A., 2011. Water management challenges associated with the production of shale gas by hydraulic fracturing. Elements 7, 181–186.
Guivar, J.A.R., Martínez, A.I., Anaya, A.O., Valladares, L.D.L.S., Félix, L.L., Dominguez, A.B., 2014. Structural and magnetic properties of monophasic maghemite (γ-Fe_2O_3) nanocrystalline powder. Adv. Nanoparticles 3, 114–121.
Hasanpour, A., Niyaifar, M., Mohammadpour, H., Amighian, J., 2012. A novel non-thermal process of TiO_2-shell coating on Fe_3O_4-core nanoparticles. J. Phys. Chem. Solids 73, 1066–1070.
Hui, C., Shen, C., Tian, J., Bao, L., Ding, H., Li, C., Tian, Y., Shi, X., Gao, H.-J., 2010. Core-shell $Fe_3O_4@SiO_2$ nanoparticles synthesized with well-dispersed hydrophilic Fe_3O_4 seeds. Nanoscale 3, 701–705.
Jang, S.-J., Kim, M.-S., Kim, B.-W., 2005. Photodegradation od DDT with the photodeposited ferric ion on the TiO_2 film. Water Res. 39 (10), 2178–2188.
Jing, L., Chen, B., Zhang, B., Li, P., 2015. Process simulation and dynamic control for marine oily wastewater treatment using UV irradiation. Water Res. 81, 101–112.
Kargbo, W.D.M., Ron, G., Campbell, D.J., 2010. Natural gas plays in the marcellus shale: challenges and potential opportunities. Environ. Sci. Technol. 44, 5679–5684.
Kazeminezhad, I., Mosivand, S., 2014. Phase transition of electrooxidized Fe_3O_4 to γ and α-Fe_2O_3 nanoparticles using sintering treatment. Acta Phys. Pol. A 125, 1210–1214.
Kim, K.N., Hoffmann, M.R., 2008. Heterogeneous photocatalytic degradation of ethylene glycol and propylene glycol. Korean J. Chem. Eng. 25 (1), 89–94.
Lee, H.-J., Kang, D.-W., Chi, J., Lee, D.-H., 2003. Degradation kinetics of recalcitrant organic compounds in a decontamination process with UV/H_2O_2 and UV/H_2O_2/TiO_2 processes. Korean J. Chem. Eng. 20 (3), 503–508.
Li, M.B., Liu, G.H., Li, J., Zhang, T., He, M., 2015. Thermal performance analysis of drilling horizontal wells in high temperature formations. Appl. Therm. Eng. 78, 217–227.
Li, Y., Li, Y., Wang, B., Chen, Z., Nie, D., 2016. The status quo review and suggested policies for shale gas development in China. Renew. Sustain. Energy Rev. 59, 420–428.
Liu, H., Jia, Z., Ji, S., Zheng, Y., Yang, H., 2011. Synthesis of $TiO_2/SiO_2@Fe_3O_4$ magnetic microspheres and their properties on photocatalytic degradation dyestuff. Catal. Today 175, 293–298.
Mader, D., 1989. Hydraulic Proppant Fracturing and Gravel Packing. Developments in Petroleum Science, 26. Elsevier Science Publishers B.V.
Niu, H., Wang, Q., Liang, H., Chen, M., Mao, C., Song, J., Zhang, S., Gao, Y., Chen, C., 2014. Visible-light active and magnetically recyclable nanocomposites for the degradation of organic dye. Materials 7, 4034–4044.
Ray, E.O., 1976. Shale Development in Eastern Kentucky. US Energy Research and Development Administration, Washington, D.C.
Sirtori, C., Altvater, P.K., Freitas, A., Peralta-Zamora, P.G., 2006. Degradation of aqueous solutions of camphor by heterogeneous photocatalysis. J. Hazard.

Mater. 129, 110–115.
Stefan, M., Pana, O., Leostrean, C., Bele, C., Silipas, D., Senila, M., Gautron, E., 2014. Synthesis and characterization of Fe_3O_4-TiO_2 core-shell nanoparticles. J. od Appl. Phys. 116, 114312.
Stringfellow, W.T., Domen, J.K., Camarillo, M.K., Sandelin, W.L., Borglin, S., 2014. Physical, chemical, and biological characteristics of compounds used in hydraulic fracturing. J. Hazard. Mater 275, 37–54.
Wu, W., Wu, Z., Yu, T., Jiang, C., Kim, W.-S., 2015. Recent progress on magnetic iron oxide nanoparticles: synthesis, surface functional strategies and biomedical applications. Sci. Technol. Adv. Mater. 16 (023501), 43.
Zhang, L., Siu, T.M., Kiang, T.O., 2014. Facile in situ synthesis of visible light-active Pt/C-TiO_2 nanoparticles for environmental remediation. J. Environ. Chem. Eng. 2, 1214–1220.
Zielińska-Jurek, A., Wysocka, I., Janczarek, M., Stampor, W., Hupka, J., 2015. Sep. Purif. Technol. 156, 369–378.

GDAŃSK UNIVERSITY OF TECHNOLOGY
FACULTY OF CHEMISTRY

5. Design and Application of Magnetic Photocatalysts for Water Treatment. The Effect of Particle Charge on Surface Functionality

Anna Zielińska-Jurek, Zuzanna Bielan, Szymon Dudziak, Izabela Wolak, Zuzanna Sobczak, Tomasz Klimczuk, Grzegorz Nowaczyk, Jan Hupka

Catalysts 7 (2017) 360-379

DOI: 10.3390/catal7120360

P5

catalysts

MDPI

Article

Design and Application of Magnetic Photocatalysts for Water Treatment. The Effect of Particle Charge on Surface Functionality

Anna Zielińska-Jurek [1,*], Zuzanna Bielan [1], Szymon Dudziak [1], Izabela Wolak [1], Zuzanna Sobczak [2], Tomasz Klimczuk [2], Grzegorz Nowaczyk [3] and Jan Hupka [1]

[1] Department of Chemical Technology, Faculty of Chemistry, Gdansk University of Technology (GUT), G. Narutowicza 11/12, 80-233 Gdansk, Poland; bielan_chan@onet.eu (Z.B.); dudziakszy@gmail.com (S.D.); izawolak@wp.pl (I.W.); jhupka@pg.gda.pl (J.H.)

[2] Department of Solid State Physics, Faculty of Applied Physics and Mathematics, Gdansk University of Technology (GUT), 80-233 Gdansk, Poland; zuzsobcz@gmail.com (Z.S.); tomklimc@pg.edu.pl (T.K.)

[3] NanoBioMedical Center, Adam Mickiewicz University, Umultowska 85, 61-614 Poznan, Poland; grzegorznowaczyk76@gmail.com

* Correspondence: annjurek@pg.gda.pl

Received: 6 October 2017; Accepted: 21 November 2017; Published: 27 November 2017

Abstract: Core-interlayer-shell $Fe_3O_4/SiO_2/TiO_2$, $CoFe_2O_4/SiO_2/TiO_2$ and $BaFe_{12}O_{19}/SiO_2/TiO_2$ magnetic photocatalysts were obtained. A water-in-oil microemulsion system with suitable surfactants was used for functionalization of the magnetic core with silica interlayer and TiO_2-based photocatalyst. Uncoated and coated particles were characterized by electrophoretic measurements, X-ray diffractometry (XRD), scanning electron microscopy (SEM), transmission electron microscopy (TEM), specific surface area (BET) measurements, diffuse reflectance spectroscopy (DRS) and vibrating sample magnetometer (VSM) analysis. The pH of the solution and corresponding zeta potential was found to be essential for appropriate formation of ferrite core/silica interlayer/TiO_2 shell nanocomposite, since the electrical charge controls interactions during functionalization of the magnetic core particles. Thus, the development of multilayer structure in the isoelectric point (IEP) region enhanced adhesion of ferrite, silica and titania particles. The obtained $Fe_3O_4/SiO_2/TiO_2$, $CoFe_2O_4/SiO_2/TiO_2$ and $BaFe_{12}O_{19}/SiO_2/TiO_2$ nanocomposites revealed superparamagnetic behavior. The decomposition rate of phenol and carbamazepine allowed to estimate their photocatalytic activity. Progress of photocatalytic mineralization of organic compounds was evaluated by total organic carbon (TOC) measurements. Photocatalytic activity measured in four subsequent cycles showed good reusability as no loss of efficiency of phenol degradation was observed.

Keywords: heterogeneous photocatalysis; magnetic photocatalysts; $Fe_3O_4/SiO_2/TiO_2$; $CoFe_2O_4/SiO_2/TiO_2$; $BaFe_{12}O_{19}/SiO_2/TiO_2$; core-shell structure; reusability; zeta potential

1. Introduction

UV–vis light driven photooxidation of persistant organic pollutants [1–3], removal of odors from enclosed space [4], destruction of bacteria with low intensity radiation [5] and self-cleaning surfaces [6] are examples of the potential of nanostructure-based photocatalysts. One of major challenges in photocatalysis application is separation and recovery of nanosized TiO_2 particles from the treated water, since sedimentation is usually insufficient, while filtration is costly [7]. Even if coagulation, flocculation or centrifugation is used, the supernatant may not be clear. In the past decade, much effort was devoted to photocatalyst immobilization on Raschig rings, glass tubes, glass beads, glass fiber, zeolites and activated carbon [8–10]. However, immobilized TiO_2 was less active due to lower specific surface area in such systems.

In this regard, preparation of well performing and readily separable photocatalysts is a priority in heterogeneous photocatalysis. Mesoporous titania micro- and sub-micro spheres, hierarchical TiO_2 micro-sized particles were proposed for photodegradation of organic contaminants facilitating its reuse [11–13]. Furthermore, to ease separation, composites consisting of a magnetic core and photoactive shell have been also developed. Already in 1994 Hiroshi and coworkers patented a preparation of Fe_3O_4/TiO_2 nanocomposites by deposition of titanium(IV) oxide onto a magnetic core. $TiOSO_4$ was hydrolyzed and precipitated [14]. Another early patented (1997) magnetic photocatalyst was obtained by dispersion of ferromagnetic metal particles in TiO_2 suspension [15]. After 1998, others followed depositing photocatalyst onto magnetic core particles [16–19].

Beydoun et al. [20] have shown that contact between crystalline photoactive titanium(IV) oxide and magnetic iron oxide resulted in lower photocatalytic performance with respect to titanium(IV) oxide only for degradation of organic compounds. Interactions between the iron oxide core and the titanium(IV) oxide shell may result in charge carrier recombination of Fe_3O_4 during illumination, see Figure 1. Photogenerated electrons elevate to the conduction band (CB) of titanium(IV) oxide, and reduce iron being transferred into the lower conduction band of Fe_3O_4 core. The photogenerated holes at the valence band (VB) of TiO_2 prefer a more elevated conduction band of the iron oxide core, leading to iron oxidation and subsequent leaching of iron ions into the solution.

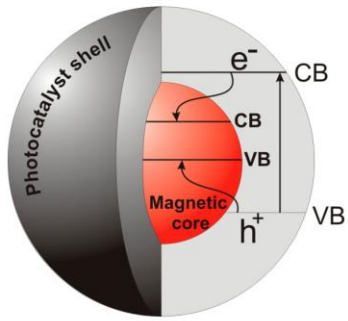

Figure 1. Recombination of charge carriers and photodissolution of Fe_3O_4 during irradiation of magnetic core and TiO_2 shell photocatalyst.

To overcome photodissolution and protect the magnetic core addition of silica [21,22] or carbon [23], inert layer between the magnetic core and the TiO_2 shell was proposed. The structure of the three-component photocatalyst comprises (1) a magnetic core for separation in magnetic field; (2) an interlayer preventing photodissolution and charge carrier recombination; and (3) photocatalytic shell layer for degradation of persistent organic pollutants. Introduction of magnetic nanoparticles into the core/interlayer/shell structure including magnetite [24], maghemite [25], ferrites [26], bimetallic nanoparticles of Fe-Ni, Co-Fe, Fe-Pt [27], has recently been examined.

In order to provide satisfactory magnetic response and efficient photocatalytic activity for environmental purposes, further research is needed on preparation procedures that will ensure uniform shape and size of magnetic particles as well as their core-interlayer-shell structure.

The aim of this investigation is to better understand the effect of the preparation procedure on adhesion, magnetic properties and photocatalytic activity of $Fe_3O_4/SiO_2/TiO_2$, $CoFe_2O_4/SiO_2/TiO_2$ and $BaFe_{12}O_{19}/SiO_2/TiO_2$ composites in order to ease the separation of the photocatalysts. A novel preparation procedure based on zeta potential analysis in a function of pH was used. The photocatalytic

activity was examined through degradation of phenol and carbamazepine as model organic pollutants. The effect of the magnetic core, photocatalytic shellstructure, reaction matrix on the preparation of the three-component magnetic photocatalyst in microemulsion system was investigated.

2. Results and Discussion

2.1. Preparation of Magnetic Photocatalysts—Measurement of Electrophoretic Mobility in a Function of pH (Zeta Potential Determination)

In water suspension, the surface charge balance is referred to the diffuse layer and it is determined by electrokinetic measurements, such as the zeta potential. It was found that electrostatic forces play important roles in the process of deposition and development of ferrite core, silica interlayer and TiO_2 shell structure of the nanocomposites. The relative charges of the surfaces are the determinant parameters indicating whether the interaction is repulsive or attractive during functionalization of the surface (see Figure 2). Values of the isoelectric point (IEP) of particles and substrates indicate the pH, where the zeta potential is equal to zero and the range, where the adhesion is favored. Thus, development of multilayer structure requires the knowledge of the pH values for ferrite, silica and titania particles.

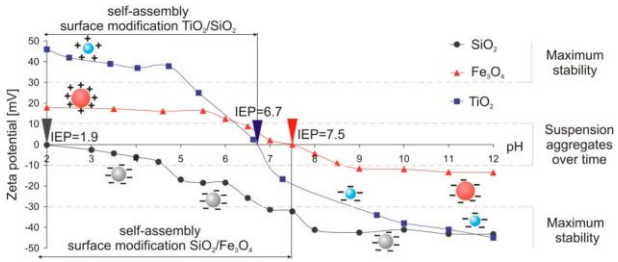

Figure 2. Zeta potential of Fe_3O_4, SiO_2 and TiO_2 nanoparticles as a function of pH.

Metal oxide, ferrites are amphoteric solids, which in contact with water develop surface charge due to protonation and deprotonation reactions. The amphoteric surface reactions can be described as:

$$=FeOH + H^+ \leftrightarrow FeOH_2^+ \rightarrow \text{acidic solution, pH} < \text{IEP} \quad (1)$$

$$\equiv TiOH + H^+ \leftrightarrow TiOH_2^+ \rightarrow \text{acidic solution, pH} < \text{IEP} \quad (2)$$

$$=FeOH \leftrightarrow FeO^- + H^+ \rightarrow \text{basic solution, pH} > \text{IEP} \quad (3)$$

$$\equiv TiOH \leftrightarrow TiO^- + H^+ \rightarrow \text{basic solution, pH} > \text{IEP} \quad (4)$$

From Reactions (1)–(4), the changes of surface charge density as a function of pH are determined. Below pH_{IEC}, protonation reaction leads to the formation of $FeOH_2^+$ and $TiOH_2^+$ groups, while deprotonation occurs above the isoelectric point and gives rise to FeO^- and TiO^- groups. The zeta potential of silica particles remained negative between pH 2 and 12. The zeta potential data (Figures 2 and 3) indicate a positively charged surface of ferrites below pH 6.9 for $CoFe_2O_4$ and 7.5 for Fe_3O_4 and $BaFe_{12}O_{19}$. For TiO_2 particles, the surface was positively charged below pH 6.7 and negatively charged at pH value above the isoelectric point.

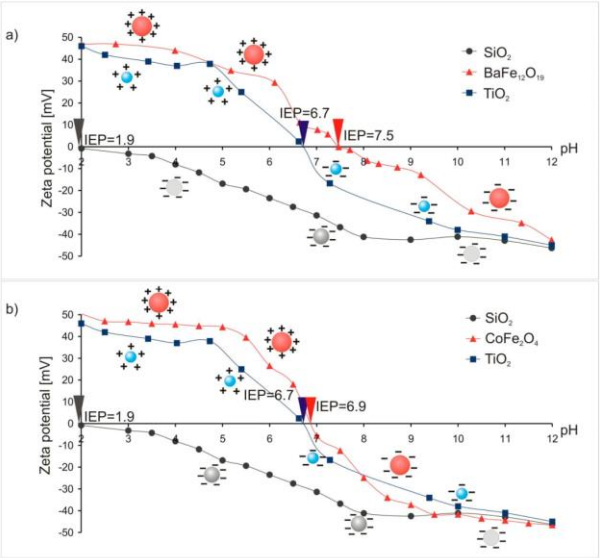

Figure 3. Zeta potential of $CoFe_2O_4$ (**a**) and $BaFe_{12}O_{19}$ (**b**) determined from the electrophoretic mobility in dependence of the pH, I = 1 × 10^{-4} M KCl.

Since, ferrite particles are positively charged at pH 5, interaction with negatively charged silica leads to self-assembly of SiO_2 into the ferrite shell. TiO_2 nanoparticles are positively charged at this pH, and therefore, compete with silica particles deposited on the ferrite core. At pH above 8, such deposition of silica and titania layers at the magnetite core was unsuccessful. Therefore, the magnetic photocatalyst preparation route was carried out in alkaline conditions by self-assembly of anionic silicates and cationic surfactant molecules cetyltrimethylammonium bromide (CTAB) to form silica shell on ferrite core. The cationic surfactant also effectively interacts with negatively charged titania species in alkaline media, resulting in the core-interlayer-shell structure of nanocomposite.

2.2. *Characterization of the Nanoparticles*

The morphology of the prepared ferrite particles and magnetic photocatalyst is determined by SEM (Figure 4) and TEM (Figure 5) analysis. Crystalline $BaFe_{12}O_{19}$ particles hexagonal in shape with random orientation and diameters of the aggregated particles in the range of 40–70 nm were observed. The magnetic $BaFe_{12}O_{19}$ core is surrounded by SiO_2 and TiO_2 layers (Figure 4b). The $CoFe_2O_4$ spherical shape particles coated with SiO_2 and TiO_2 are visible in Figure 4c. Furthermore, TEM images demonstrate $CoFe_2O_4$ particles composed of primary 15 nm diameter (Figure 4d), which corresponds well with the 13 nm crystallite size determined from the XRD pattern using the Scherrer equation.

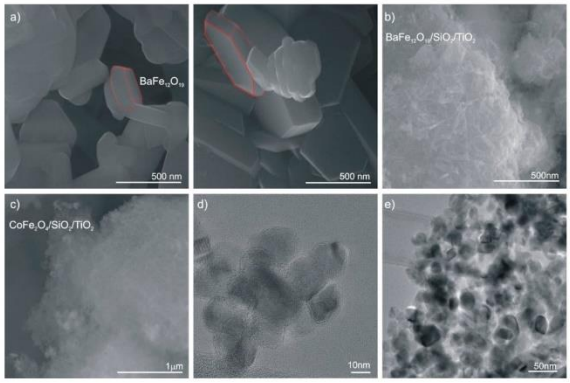

Figure 4. SEM images of barium hexaferrite (**a**); barium hexaferrite coated with SiO_2 and TiO_2 layer (**b**); cobalt ferrite, $CoFe_2O_4$ coated with SiO_2 and TiO_2 layer (**c**); TEM images of $CoFe_2O_4/SiO_2/TiO_2$ (**d**) and $CoFe_2O_4/SiO_2/TiO_2$ (**e**).

The composition of the core-shell and core-interlayer-shell structure of magnetic nanocomposites was studied using Cs corrected Scanning transmision electron microscopy STEM (high angle annular dark field, HAADF) imaging supplemented with Energy-dispersive X-ray spectroscopy (EDXS) mapping, as shown in Figure 5a,b.

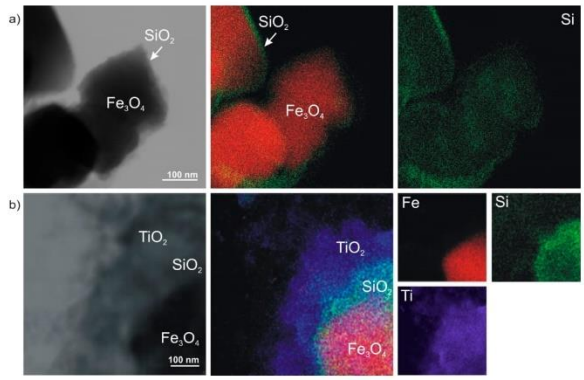

Figure 5. HAADF images of Fe_3O_4/SiO_2 (**a**) and $Fe_3O_4/SiO_2/TiO_2$ (**b**) combined with mappings of Fe_3O_4, SiO_2 and TiO_2 (blue is Ti, red is Fe and green Si).

The single core-shell structure of Fe_3O_4 with uniform SiO_2 nanometer-thick shell is presented in Figure 5a. According to the TEM image of core-interlayer-shell $Fe_3O_4/SiO_2/TiO_2$ nanoparticle the dark and bright regions correspond to the Fe_3O_4 and the shell, respectively. The magnetic core is identified as the darker region compared to the non-magnetic SiO_2 and TiO_2 shell area due to their different electron-absorbing abilities [28]. The core-interlayer-shell structure of Fe_3O_4 coated with SiO_2 and TiO_2 was confirmed by EDXS mapping, presented in Figure 5b.

The physicochemical characteristics of the magnetic particles and magnetic photocatalysts e.g., crystallite sizes, indirect band gap values, BET surface areas are given in Table 1. Cetyltrimethylammonium bromide (CTAB) and *t*-octylphenoxypolyethoxyethanol (Triton X-100) were used as surfactants. Commercial TiO_2 P25 or TiO_2 obtained from titanium butoxide (TBT) hydrolysis were used as starting materials for preparation of photocatalyst layer onto magnetic core. Derived from the plot of the Kubelka-Munk function versus the photon energy gives indirect band gaps of 0.5 eV, 0.7 eV, 1.0 eV and 1.4 eV, 0.9 eV and 1.0 eV for Fe_3O_4, $CoFe_2O_4$, $BaFe_{12}O_{19}$ and Fe_3O_4/SiO_2, $CoFe_2O_4/SiO_2$, $BaFe_{12}O_{19}/SiO_2$ particles, respectively. The energy gap of $Fe_3O_4/SiO_2/TiO_2$, $CoFe_2O_4/SiO_2/TiO_2$, $BaFe_{12}O_{19}/SiO_2/TiO_2$ magnetic photocatalysts were similar to those reported for TiO_2 [29,30], which indicates that silica and magnetite particles were not introduce into structure of TiO_2.

The BET surface area was evaluated from the nitrogen physisorption data using the Brunauer-Emmett-Teller equation [31]. Among ferrite particles, $CoFe_2O_4$ exhibits the smallest crystallite size of 13 nm and the highest specific surface area of 45 $m^2 \cdot g^{-1}$. The BET surface area increased to 124 $m^2 \cdot g^{-1}$ for Fe_3O_4/SiO_2 and 170 $m^2 \cdot g^{-1}$ for $BaFe_{12}O_{19}/SiO_2$ nanocomposites. For magnetic photocatalysts, the BET surface area fluctuated from 60 $m^2 \cdot g^{-1}$ to 154 $m^2 \cdot g^{-1}$ and was dependent mainly on the source of TiO_2 deposited on ferrite/SiO_2 particles (see in Table 1). The BET surface area for $CoFe_2O_4/SiO_2$ coated with commercial TiO_2 P25 (50 $m^2 \cdot g^{-1}$), was more than two times lower compared to $CoFe_2O_4/SiO_2$ coated with self-obtained TiO_2 particles from TBT hydrolysis in water cores of microemulsion with a particle size of 5 nm and BET area of 178 $m^2 \cdot g^{-1}$. This result further confirms the core-shell structure of magnetic photocatalysts. The ferrite core of nanocomposite was encapsulated with titania, and therefore, the BET surface area of magnetic photocatalyst was related to the surface area of pure TiO_2 particles.

Composition of the crystalline phase was examined by XRD analysis with respect to Fe_3O_4, Fe_3O_4/SiO_2, $Fe_3O_4/SiO_2/TiO_2\_2$ (in Figure 7a) and $CoFe_2O_4$, $CoFe_2O_4/SiO_2$, $CoFe_2O_4/SiO_2/TiO_2\_2$ (in Figure 7b), respectively. The Fe_3O_4 nanoparticles exhibit intense peak at $2\theta = 35.2°$, which is the (311) reflection and has highly crystalline cubic spinel structure, in agreement with the standard Fe_3O_4 XRD spectrum (JCPDS card No. 89-3854).

Table 1. Physicochemical characteristics of the ferrite particles and obtained magnetic photocatalysts.

Sample Label	TiO_2 Source	Preparation Conditions		Crystallite Size (nm)			BET Surface Area (m^2/g)	E_g (eV)
		pH	Surfactant	Anatase	Rutile	Ferrite		
Fe_3O_4	-	10	CTAB	-	-	45	9	0.5
$CoFe_2O_4$	-	10	-	-	-	13	45	0.7
$BaFe_{12}O_{19}$	-	10	CTAB	-	-	50	0.6	1.0
Fe_3O_4/SiO_2	-	5	-	-	-	47	169	1.4
$CoFe_2O_4/SiO_2$	-	5	-	-	-	13	124	0.9
$BaFe_{12}O_{19}/SiO_2$	-	10	CTAB	-	-	50	170	1.0
$Fe_3O_4/SiO_2/TiO_2\_1$	P25	5	TX-100	19	26	47	101	3.2
$Fe_3O_4/SiO_2/TiO_2\_2$	P25	10	CTAB	19	24	45	95	3.2
$CoFe_2O_4/SiO_2/TiO_2\_1$	TBT	5	TX-100	5	-	13	154	3.2
$CoFe_2O_4/SiO_2/TiO_2\_2$	P25	5	TX-100	18	27	13	69	3.2
$BaFe_{12}O_{19}/SiO_2/TiO_2\_1$	TBT	10	CTAB	5	-	50	100	3.1
$BaFe_{12}O_{19}/SiO_2/TiO_2\_2$	TBT	5	TX-100	5	-	49	60	3.1

Moreover, for cobalt ferrite particles, the diffraction peak positions attributed to (220), (311), (400) and (440) reflections also confirmed formation of cubic spine phase, which is in accordance with JCPDS card No. 22-1086. The broad diffraction peak at $2\theta = 15–25°$ corresponds to an amorphous silica layer in the nanocomposite structure [32,33]. The diffraction peaks of TiO_2 can be attributed to

(101), (103), (200) and (105) reflections of anatase TiO_2, and (110), (101), (200) reflections of rutile TiO_2 and are in agreement with the standard anatase XRD spectrum (JCPDS card No. 89-4203) and rutile XRD spectrum (JCPDS, No. 76-1940). The most intense diffraction peaks of spinel ferrite particles in the XRD patterns (Figure 7a,b) at 35.3° for Fe_3O_4 and 31.8° for $CoFe_2O_4$ became weaker, due to the formation of the TiO_2 shell on the surface of ferrite particles.

The magnetic properties of uncoated and coated ferrite nanocomposites were investigated using magnetic hysteresis curves from ACMS analysis at room temperature as shown in Figure 6. The magnetic parameters, such as saturation magnetization (M_s), coercivity (H_c) and remanent magnetization (M_r) are given in Table 2. Obtained spinel and hexagonal ferrites posse strong ferromagnetic properties. The saturation magnetization (M_s) of Fe_3O_4, $BaFe_{12}O_{19}$ and $CoFe_2O_4$ were 89 emu/g, 64 emu/g and 39 emu/g, respectively.

Table 2. Magnetic parameters of the uncoated and coated ferrite nanoparticles.

Sample Label	M_s (emu·g^{-1})	H_c (Oe)	M_r (emu·g^{-1})
Fe_3O_4	89	100	9
$CoFe_2O_4$	60	130	2
$BaFe_{12}O_{19}$	64	140	16
Fe_3O_4/SiO_2	17	100	2
$CoFe_2O_4/SiO_2$	15	150	0
$BaFe_{12}O_{19}/SiO_2$	46	80	4
$Fe_3O_4/SiO_2/TiO_2$_1	8	100	1
$Fe_3O_4/SiO_2/TiO_2$_2	7	100	1
$CoFe_2O_4/SiO_2/TiO_2$_1	9	250	1
$CoFe_2O_4/SiO_2/TiO_2$_2	6	150	1
$BaFe_{12}O_{19}/SiO_2/TiO_2$_1	43	80	9
$BaFe_{12}O_{19}/SiO_2/TiO_2$_2	33	80	9

The magnetic properties of materials are influenced by particles size, crystallinity and surface structure. The M_s of the ferrite/SiO_2 and ferrite/SiO_2/TiO_2 nanocomposites decreases after coating with silica and titania layers, while the coercivity of titania-silica-coated Fe_3O_4, $BaFe_{12}O_{19}$ and $CoFe_2O_4$ nanoparticles does not show any change after coating, because coercivity represents the property of magnetic material and is determined by the strength and number of the magnetic dipole in the magnetic domain [34]. Furthermore, saturation magnetization values for Fe_3O_4 nanocomposites were recalculated using emu/mol of Fe_3O_4, see in Figure 6d. The amount of ferrite particles was determined from X-ray fluorescence spectrometer (XRF) analysis and these results were in agreement with theoretical stoichiometric calculations. The hysteresis loops do not change after coating. There is a 14% difference of M_s between uncoated Fe_3O_4 (3372 emu/mol) and Fe_3O_4 coated with SiO_2 or SiO_2/TiO_2 layer (2919 emu/mol).

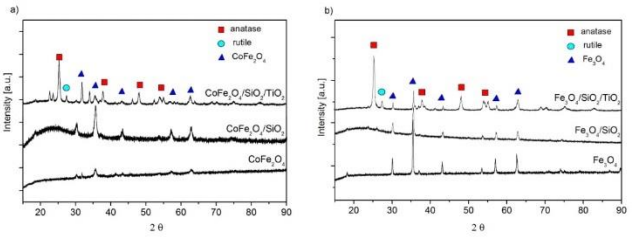

Figure 6. X-ray diffraction patterns of the as-prepared Fe_3O_4, Fe_3O_4/SiO_2, $Fe_3O_4/SiO_2/TiO_2$_2 (**a**) and $CoFe_2O_4$, $CoFe_2O_4/SiO_2$, $CoFe_2O_4/SiO_2/TiO_2$_2 (**b**).

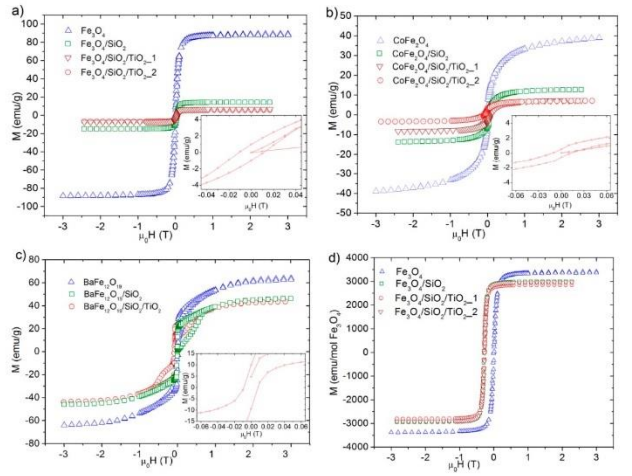

Figure 7. Magnetic hysteresis loops of Fe_3O_4 based nanocomposites (**a**); $CoFe_2O_4$-based nanocomposites (**b**) and $BaFe_{12}O_{19}$-based nanoparticles (**c**); recalculated hysteresis loops for Fe_3O_4 composites (**d**).

The magnetic photocatalysts can exhibit superparamagnetic behavior due to their small H_c and M_r values.

The critical sizes of the magnetic single-domain were calculated using equation:

$$D_{cr} = 5.1\sqrt{\frac{A}{\mu_0 M_s^2}}$$

where A is the exchange stiffness and M_s is the saturation magnetization of the material and the data are given in Table 3. The critical size of a magnetic single-domain calculated for Fe_3O_4 with M_s value

of 89 emu/g, using exchange stiffness A = 0.7 μerg/cm (7 pJ/m) [35] was about 250 nm. This value exceeds the limit of the critical radius for superparamagnetic domain of Fe_3O_4, which is about 49 nm [36]. On the other hand, the single-domain critical sizes (D_{cr}) were 67.5 nm and 24.8 nm for $BaFe_{12}O_{19}$ and $CoFe_2O_4$ and were lower than theoretical values [37,38], suggesting that the obtained $BaFe_{12}O_{19}$ and $CoFe_2O_4$ magnetic nanocomposites can reveal superparamagnetic properties.

Table 3. Critical sizes of single-domain magnetic Fe_3O_4, $BaFe_{12}O_{19}$, $CoFe_2O_4$ nanoparticles.

	M_s (emu/g)	A (pJ/m)	D_{cr} (nm)	Literature D_{cr} (nm)	d (nm)	Refs.
Fe_3O_4	89	7	250	49	>200	[36]
$BaFe_{12}O_{19}$	60	20	67.5	1000	70	[37]
$CoFe_2O_4$	64	3	24.8	30	15	[38]

Furthermore, when the applied intensity of magnetic field is close to zero, the remnant magnetization of samples decreases to zero. It indicates that the samples can be separated from water when an external magnetic field is added, and redispersed in water solution after the external magnetic field is eliminated, as shown in Figure 8, for $CoFe_2O_4/SiO_2/TiO_2$ nanocomposite.

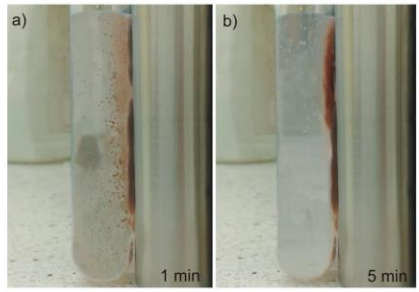

Figure 8. Image of $CoFe_2O_4/SiO_2/TiO_2$ magnetic separation after 1 min (**a**) and 5 min (**b**) after applying magnet rod.

2.3. Photocatalytic Activity of Magnetic Nanocomposites

In the first round of experiments of our study, phenol was selected as a model pollutant. Phenol and its derivatives are commonly encountered organic pollutants in industrial effluents that have caused severe environmental problems. Phenol was not degraded in the absence of illumination, indicating that there was no dark reaction at the surface of self-prepared nanocomposites. The functionalization of the magnetic core with silica interlayer and a layer of commercial TiO_2 P25 results in higher photocatalytic performance, as shown in Figure 9 for $Fe_3O_4/SiO_2/TiO_2$_1, $Fe_3O_4/SiO_2/TiO_2$_2 and $CoFe_2O_4/SiO_2/TiO_2$_2 photocatalysts.

Moreover, phenol degradation for $Fe_3O_4/SiO_2/TiO_2$ and $CoFe_2O_4/SiO_2/TiO_2$_2 nanocomposites was comparable to the commercial nano-sized TiO_2 P25 (Evonik, Essen, Germany), which proves effective deposition of TiO_2 P25 onto the magnetic core with the ability to easily separation of photocatalyst from reaction system. Total organic carbon (TOC) analysis also revealed that high mineralization was achieved for $Fe_3O_4/SiO_2/TiO_2$_1, $CoFe_2O_4/SiO_2/TiO_2$_2 and $Fe_3O_4/SiO_2/TiO_2$_2. After 30 min. of irradiation more than 90% of phenol was decomposed and mineralization was above

80%. The magnetic photocatalysts $CoFe_2O_4/SiO_2/TiO_2$_1 and $BaFe_{12}O_{19}/SiO_2/TiO_2$_2 obtained by deposition of TiO_2 from TBT hydrolysis in water cores of microemulsion revealed lower photocatalytic activity in reactions of phenol degradation. After 30 min. of irradiation about 80% and 27% of phenol was degraded and mineralization was 52% and 15% for $CoFe_2O_4/SiO_2/TiO_2$_1 and $BaFe_{12}O_{19}/SiO_2/TiO_2$_2, respectively. Salamat et al. reported that the variations in the photocatalytic activity of TiO_2/SiO_2 deposited on Fe_3O_4 are probably related to the effect of change in the molar ratio of Ti and Si to Fe_3O_4 [28]. Therefore, it can be assumed that photocatalytic and magnetic properties can be manufactured by appropriately adjusting the reaction condition during formation of the semiconductor shell. That means adjustment of a ratio of the core portion particle diameter and shell thickness depends on appropriately adjusting the formation condition during formation of the shell. Further study on the selection and setting of the specific conditions with respect to individual magnetic particles are presently being conducted.

Another set of experiments were performed using carbamazepine as a model organic compound. Carbamazepine is one of the commonly used pharmaceuticals, which passes through wastewater treatment plants almost completely unaffected and has been found to be highly persistent in the environment. The efficiency of carbamazepine degradation is presented in Figure 10 and described as TOC removal fraction.

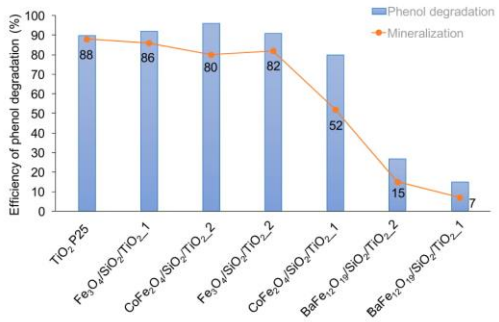

Figure 9. Efficiency of phenol degradation (C/Co) and mineralization (TOC/TOCo) of obtained magnetic photocatalysts.

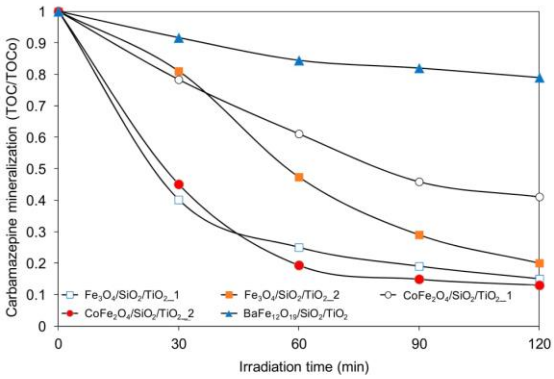

Figure 10. Photomineralization of carbamazepine measured as TOC removal as a function of reaction time. Experimental conditions: phenol initial concentration Co = 6×10^{-5} M, content of photocatalyst 2 g·dm^{-3}, 300 W xenon lamp.

The highest efficiency of carbamazepine mineralization revealed $CoFe_2O_4/SiO_2/TiO_2$_2 and $Fe_3O_4/SiO_2/TiO_2$_1 magnetic photocatalysts, which were also the most active in reaction of phenol degradation. After 120 min. of irradiation, TOC removal was 87% and 85% for $CoFe_2O_4/SiO_2/TiO_2$_2 and $Fe_3O_4/SiO_2/TiO_2$_1, respectively. For $CoFe_2O_4/SiO_2/TiO_2$_1, $Fe_3O_4/SiO_2/TiO_2$_2 and $BaFe_{12}O_{19}/SiO_2/TiO_2$_2 nanocomposites the carbamazepine removal efficiency equaled 54%, 80% and 21%, respectively.

Furthermore, the most active magnetic photocatalyst $CoFe_2O_4/SiO_2/TiO_2$_2 was selected for reusability studies. In order to evaluate the effectiveness of magnetic photocatalyst after its recovery, the four subsequent cycles were carried out, see data in Figure 11. At the end of the first run of phenol degradation, $CoFe_2O_4/SiO_2/TiO_2$_2 nanoparticles were separated from aqueous solution by external magnetic field and then treated wastewater was discharged. The separated photocatalyst was then reused without any treatment. High photocatalytic degradation was maintained after four consecutive cycles, without any loss in degradation.

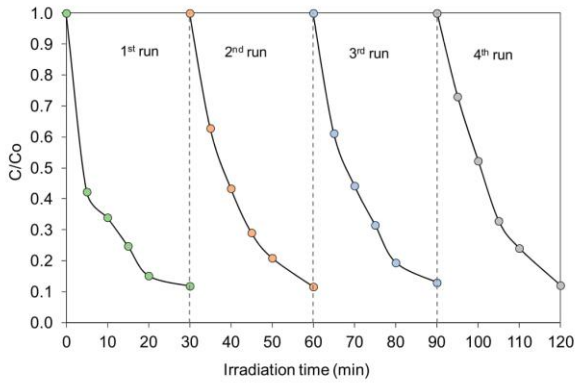

Figure 11. Efficiency of phenol degradation in the presence of $CoFe_2O_4/SiO_2/TiO_2$ magnetic photocatalyst measured in the fourth subsequent cycles.

2.4. Discussion

Core-interlayer-shell structure magnetic photocatalysts were prepared in a w/o microemulsion system based on changes in the zeta potential as a function of pH. Ferrite particles are positively charged in acidic medium (pH < 7), while silica nanoparticles showed negative charge in the pH range of 2–12. Therefore, the functionalization of magnetic core with silica interlayer in acidic medium leads to self-assembly of SiO_2 into the ferrite shell. Electrostatic interactions between negatively charged silica and positively charged titania particles enables the functionalization of magnetic core with silica interlayer and TiO_2 photocatalyst layer in acidic conditions. At pH above 7, such deposition of silica and titania layers at the magnetite core was unsuccessful. Therefore, magnetic photocatalyst preparation route was carried out in alkaline conditions by self-assembly of anionic silicates and cationic surfactant molecules (CTAB) to form a silica shell on a ferrite core. The cationic surfactant also effectively interacts with negatively charged titania species in alkaline media, resulting in the core-interlayer-shell structure of nanocomposites. The energy gap of the core-interlayer-shell magnetic photocatalysts was similar to those reported for TiO_2. Moreover, the ferrite core encapsulated with silica and titania exhibited the BET surface area related to surface area of pure TiO_2 particles, which indicates that the ferrite core was encapsulated with titania shell, and therefore, the BET surface area of magnetic photocatalyst was related to pure TiO_2 particles surface area. Furthermore, the composition of the core-shell and core-interlayer-shell structure of magnetic nanocomposites was confirmed by TEM microscopy with EDXS mapping. The $CoFe_2O_4$ core coated with silica interlayer and TiO_2 P25 layer exhibited long-term photocatalytic activity, in which more than 80% of phenol is decomposed to CO_2 in each 30-min cycle of degradation.

Higher photocatalytic activity was observed for the samples $Fe_3O_4/SiO_2/TiO_2$_1, $CoFe_2O_4/SiO_2/TiO_2$_2 and $Fe_3O_4/SiO_2/TiO_2$_2 obtained by deposition of commercial TiO_2 P25 on the ferrite core and silica shell nanoparticles with respect to the magnetic photocatalysts $CoFe_2O_4/SiO_2/TiO_2$_1 and $BaFe_{12}O_{19}/SiO_2/TiO_2$_2 obtained by deposition of TiO_2 from TBT hydrolysis. The titanium(IV) oxide P25 consisting of mixture of anatase and rutile phases is a well-known and widely investigated photocatalyst used as reference material to evaluate the photocatalytic activity of new materials. The higher photocatalytic activity of TiO_2 P25

compared to anatase is ascribed to synergistic effects of anatase and rutile particles, which enhance the electron-hole separation [39,40]. Recent studies have shown that photoactivity of P25 exceeds that of anatase in several reaction systems [41,42]. Previously, we have also reported that TiO_2 P25, which is a mixture of anatase and rutile phases exhibited higher efficiency of phenol, pyridine and 4-heptanone degradation compared to commercial anatase particles TiO_2 ST-01 and anatase obtained from titanium isopropoxide (TIP) and titanium butoxide (TBT) hydrolysis in aqueous phase [43,44]. Therefore, the lower photocatalytic activity of $BaFe_{12}O_{19}/SiO_2/TiO_2$_2 nanocomposite results from the properties of the photocatalytic layer instead of the magnetic core behavior. Salamat et al. [28] reported that the variations in the photocatalytic activity of TiO_2/SiO_2 deposited on Fe_3O_4 are related to the effect of change in the molar ratio of Ti and Si to Fe_3O_4. Therefore, it can be assumed that the amount of silica and titania deposited on the surface of the ferrite core should be determined depending on the ferrite core particles size and shape. Based on microscopy and XRD analysis, the surface of Fe_3O_4 and $CoFe_2O_4$ spinel ferrites was precisely coated titanium(IV) oxide layer, while titania coating on $BaFe_{12}O_{19}$ hexagonal ferrite obtained under the same preparation conditions (ferrite:TiO_2 = 1:2, TEOS:ferrite = 8:1) was poor and should be further verified by individually adjusting the amount of silica and titania deposited on barium ferrite particles.

Obtained spinel and hexagonal ferrites possess strong ferromagnetic properties. The saturation magnetization (M_s) of Fe_3O_4, $BaFe_{12}O_{19}$ and $CoFe_2O_4$ were 89 emu/g, 64 emu/g and 39 emu/g, respectively. For all magnetic nanocomposites, the saturation magnetization values were calculated into emu/gram of the $Fe_3O_4/SiO_2/TiO_2$, $CoFe_2O_4/SiO_2/TiO_2$ and $BaFe_{12}O_{19}/SiO_2/TiO_2$ photocatalyst including the mass of the non-magnetic silica and titania layer. Therefore, decrease in M_s for magnetic particles coated with non-magnetic silica and titania was observed. Further, the magnetization values were recalculated using emu/mol of Fe_3O_4. The amount of ferrite particles into the structure of the magnetic nanocomposite was determined from XRF analysis and these results were in agreement with the nominal composition of the magnetic photocatalyst which yielded saturation magnetization values only slightly lower (about 14%) with respect to uncoated magnetite particles. The decrease in M_s can be attributed to the non-magnetic iron oxide (Fe_2O_3) content [45] or higher surface spin disorder created by SiO_2 coating [46]. The critical size of a magnetic single-domain calculated for Fe_3O_4 for M_s value of 89 emu/g, using exchange stiffness A = 0.7 μerg/cm (7 pJ/m) [35] was about 250 nm. This value exceeds the limit of a critical radius for superparamagnetic domain of Fe_3O_4, which is about 49 nm, as reported by Petracic [36]. On the other hand, the single-domain critical sizes (D_{cr}) were 67.5 nm and 24.8 nm for $BaFe_{12}O_{19}$ and $CoFe_2O_4$, respectively and were lower than theoretical values [37,38], suggesting that the obtained $BaFe_{12}O_{19}$ and $CoFe_2O_4$ magnetic nanocomposites can reveal superparamagnetic properties. Furthermore, the microscopy TEM/SEM and XRD analyses, as well as M(H) results indicate the superparamagnetic behavior of the $CoFe_2O_4/SiO_2/TiO_2$ and $BaFe_{12}O_{19}/SiO_2/TiO_2$ magnetic photocatalysts.

3. Experimental Part

3.1. Materials

All reagents used were of analytical grade (purchased from Aldrich, Poznan, Poland) and used without further purification.

Commercial TiO_2 P25 (mixture of the crystalline phases: anatase and rutile, S_{BET} = 50 m^2g^{-1}, particle size: 20 nm, supplier: Evonik, Essen, Germany) was used for preparation of magnetic photocatalysts. Ferrous ferric oxide (50 nm; Fe_3O_4, Aldrich, Poznan, Poland) made the magnetic core of nanocomposites. $FeCl_2{\cdot}4H_2O$, $FeCl_3{\cdot}6H_2O$, $FeSO_4{\cdot}7H_2O$, $Fe(NO_3)_3{\cdot}9H_2O$, $ZnCl_2$, $BaNO_3$ were provided by Aldrich (Poznan, Poland), $ZnCl_2$ was provided by Fluka (Bucharest, Romania), and $CoCl_3{\cdot}6H_2O$ was purchased from POCh (Gliwice, Poland) and used as starting materials for preparation of spinel and hexagonal ferrites. Ammonium hydroxide solution (25%) was purchased

from Avantor (Gliwice, Poland Tetraethyl orthosilicate (TEOS) was provided by Aldrich (Poznan, Poland) and used as precursor for preparation of silica-coated magnetic nanoparticles.

Cyclohexane was purchased from Avantor (Gliwice, Poland) and used as the continuous oil phase of w/o microemulsion. Cetyltrimethylammonium bromide (CTAB) and *t*-octylphenoxypolyethoxyethanol (Triton X-100), and n-butanol were purchased from Sigma Aldrich (Poznan, Poland) and were used as surfactants and co-surfactant, respectively. Phenol and carbamazepine were provided by Sigma Aldrich and used as model organic pollutants.

3.2. Preparation of Magnetic Photocatalysts

The magnetic photocatalysts were obtained in w/o microemulsion system using suitable surfactants, allowing adsorption of the individual layers on the surface of the magnetic core. Microemulsion served as a system of nanoreactors for preparation of ultrafine particles with a narrow size distribution. The aqueous phase nanodroplets are dispersed in the continuous oil phase additionally protected and stabilized against agglomeration by the surfactant at the interface of w/o. Each droplet is a nanoreactor, wherein the chemical reaction is carried out. This allows for tight control of the shape and size of the obtained particles.

3.2.1. Preparation of Spinel and Hexagonal Ferrite Particles

Magnetite (Fe_3O_4) and $CoFe_2O_4$ belong to the family of spinels. Magnetite with a valence structure of $(Fe^{3+})[Fe^{2+}Fe^{3+}]O_4^{2-}$, one of the most investigated magnetic compound, was obtained by co-precipitation of ferrous and ferric salts at pH > 8 using cationic surfactant (CTAB). Ferric chloride hexahydrate and ferrous chloride tetrahydrate (2:1) were dissolved in 500 cm^3 de-ionized water. After purging the solution with nitrogen, 0.5 g CTAB in 10 cm^3 of hexane were added followed by addition of 5 M NaOH to the pH value of 10. After 2 h reaction period, particles were separated magnetically, washed with deionized water and dried at 80 °C to dry mass.

Spinel cobalt ferrite, $CoFe_2O_4$, hard magnetic material with cubic magnetocrystalline anisotropy, high coercivity, moderate saturation magnetization and physicochemical stability was obtained by co-precipitation of $FeSO_4 \cdot 7H_2O$ and $CoCl_3 \cdot 6H_2O$ in the mol ratio of Co to Fe equaled to 1:2. The precipitation agent, 5 M NaOH, was added to the solution at room temperature in nitrogen atmosphere to pH value of 10. The mixture was stirred for 30 min, sealed in a Teflon-lined stainless-steel autoclave and maintained at 200 °C for 5 h Obtained particles were separated in external magnetic field, washed with deionized water and dried in 80 °C to dry mass.

Hexagonal ferrite, $BaFe_{12}O_{19}$, magnetic compound, with high resistivity, magneto-crystalline anisotropy and saturation magnetization was prepared by co-precipitation of $Fe(NO_3)_3 \cdot 9H_2O$ and $Ba(NO_3)_2$ with Fe to Ba molar ratio equaled to 10 under nitrogen conditions and in the presence of the cationic surfactant (CTAB). After purging the solution with nitrogen gas, 0.5 g CTAB in 10 cm^3 of hexane were added followed by addition of precipitation agent 5 M NaOH to the pH value of 10. Obtained precipitate was separated, washed with distilled water, dried at 80 °C, and calcined at 1000 °C for 2 h.

3.2.2. Preparation of Spinel and Hexagonal Ferrite Coated with Silica Interlayer and TiO_2 Shell

In this study, the core-shell and core-interlayer-shell magnetic nanocomposites preparation method based on changes in the zeta potential as function of pH was proposed. The functionalization of magnetic core with silica interlayer and TiO_2 photocatalyst layer was carried out in w/o microemulsion system depending on the particles surface charge in aqueous phase in different pH. As shown in Figure 12, magnetic photocatalysts were prepared by two variants of the microemulsion method. In the first variant, presented in Figure 11, magnetic nanoparticles (Fe_3O_4, $CoFe_2O_4$ or $BaFe_{12}O_{19}$) were dispersed in w/o microemulsion of cationic surfactant cethyltrimethylammonium bromide (CTAB), n-hexanol and aqueous phase. Aqueous solution was prepared by dissolving sodium hydroxide in deionized water to pH value of 10. The water content was controlled by fixing the molar ratio

of water to surfactant at 15 and the volume ratio between oil phase and water phase (o/w) was 6. Then, tetraethylorthosilicate (TEOS) dispersed in 20 cm^3 microemulsion containing ammonia in aqueous phase was added into microemulsion containing magnetic nanoparticles. The molar ratios of TEOS to ferrite was 8:1 and NH_4OH to TEOS equaled 16. Obtained Fe_3O_4/SiO_2 particles were covered with commercial TiO_2 (P25, Evonik) or TiO_2 obtained by hydrolysis of TiO_2 precursor (titanium n-butoxide, TBT) in water cores of microemulsio. In this regard, TiO_2 P25 powder or TiO_2 precursor (TBT) was dispersed in a solution of CTAB/n-hexanol in molar ratio 1 to 12.6 and added into microemulsion containing ferrite/SiO_2 particles maintaining aqueous phase (5 M NaOH) pH value at 10. The molar ratio of ferrite to TiO_2 was 1:4 or 1:2. Finally, microemulsion was destabilized with acetone and obtained ferrite/SiO_2/TiO_2 particles were separated, dried at 80 °C to dry mass and calcined at 400 °C for 2 h.

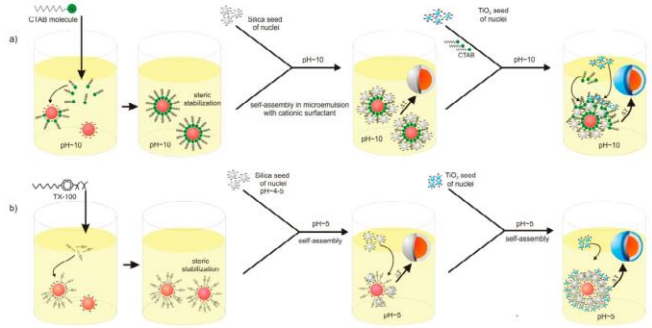

Figure 12. Schematic illustration of magnetic photocatalysts preparation procedure at pH 10 (**a**) and at pH 5 (**b**) in w/o microemulsion.

Another option shown in Figure 12b, modification of ferrite (Fe_3O_4, $CoFe_2O_4$ or $BaFe_{12}O_{19}$) particles with silica interlayer and TiO_2 layer, was performed in TX-100/water/cyclohexane microemulsion. Firstly, ferrite particles were dispersed in 0.2 M TX-100 in cyclohexane. The water content was controlled by fixing the molar ratio of water to surfactant at 30 and the volume ratio between the oil phase and the aqueous phase (o/w) was 15. Then, tetraethylorthosilicate (TEOS) dispersed in microemulsion containing 0.1 M hydrochloric acid in the aqueous phase was added into microemulsion containing magnetic nanoparticles. The molar ratio of TEOS to ferrite was 8:1 and pH of the aqueous phase was adjusted to 5. Obtained Fe_3O_4/SiO_2 particles were covered with commercial TiO_2 (P25, Evonik) or TiO_2 obtained by hydrolysis of TiO_2 precursor (titanium n-butoxide, TBT) in microemulsion system at pH of the aqueos phase adjusted to 5. The molar ratio of ferrite to TiO_2 was 1:4 or 1:2. Finally, microemulsion was destabilized with acetone and obtained ferrite/SiO_2/TiO_2 particles were separated, dried at 80 °C to dry mass and calcined at 400 °C for 2 h.

3.3. Characterization of Magnetic Photocatalysts

XRD analysis were performed using Rigaku Intelligent X-ray diffraction system SmartLab equipped with a sealed tube X-ray generator. Data acquisition conditions were as follows: 2θ range 20–80°, scan speed: $1°\cdot min^{-1}$ and scan step 0.01°. The crystallite size of the photocatalysts in the direction vertical to the corresponding lattice plane was determined using Scherrer's equation

based on the corrected full width at half maximum (FWHM) of the XRD peak and angle of diffraction. Subtraction of the FWHM of the standard was employed as correction method.

To evaluate the light-absorption properties of modified photocatalysts, the diffuse reflectance (DR) spectra were recorded, and the data were converted to obtain the absorption spectra. The band gap energies of photocatalysts were calculated from the corresponding Kubelka-Munk function, $F(R) = \frac{(1-R)^2}{2R}$, where R is reflectance, which is proportional to the absorption of radiation, by plotting $F(R)^{0.5}E_{ph}^{0.5}$ against E_{ph}, where E_{ph} is photon energy. The measurements were carried out on Thermo Scientific Evolution 220 (Waltham, MA, USA) spectrophotometer equipped with PIN-757 integrating sphere.

Nitrogen adsorption-desorption isotherms were recorded at liquid nitrogen temperature (77 K) using Micromeritics Gemini V (model 2365) (Norcross, GA, USA) instrument and the specific surface areas were determined using the Brunauer-Emmett-Teller (BET) method.

XPS analysis was carried out in multichamber ultrahigh vacuum (UHV) system, (Prevac, Rogów, Poland).

The morphology and distribution size of magnetic photocatalysts were observed using Cs-corrected STEM (High Angle Annular Dark Field, HAADF) imaging supplemented with EDXS mapping (JEOL200F, Zaventem, Belgium).

The progress of photocatalytic degradation of organic compounds was measured with application of TOC analyzer (Hach Lange Company, Wroclaw, Poland). The effect of pH on particles surface charge was measured as zeta potential (mV) using Malvern Nano Zetasizer (Malvern Instruments Ltd., Malvern, UK).

Magnetic hysteresis loops were carried out using Physical Properties Measurements System (PPMS, Quantum Design, San Diego, CA, USA). Measurements were performed at temperature 293 K in the range of 0–3 T.

3.4. Measurements of Photocatalytic Activity

In order to evaluate photocatalytic activity, 50 cm^3 of 2×10^{-4} M phenol solution or 6×10^{-5} M carbamazepine solution containing 0.1 g suspended magnetic photocatalyst was stirred and aerated prior and during the photocatalytic process. The suspension of photocatalyst was irradiated using a Xenon lamp (6271H, Oriel, CA, USA), emitting UV–vis light. The power flux at UV range (310–380 nm) was 50 $mW \cdot cm^{-2}$. The 50 cm^3 photoreactor of 3 cm thickness of exposure layer was equipped with a quartz window. The temperature of the aqueous phase during irradiation was kept at 20 °C using a water bath. Aliquots of 1.0 cm^3 of the aqueous suspension were collected at regular time periods during irradiation and filtered through syringe filters (Ø = 0.2 μm) to remove the photocatalyst particles or isolated by magnetically separation (in cycles of degradation) and washed with water. Phenol concentration was estimated by colorimetric method using Thermo 220 Evolution UV-vis Spectrophotometer (Waltham, MA, USA). Moreover, the progress of phenol and carbamazepine photocatalytic degradation was measured by the total organic carbon (TOC) concentration (TOC Analyzer, Shimadzu, Kyoto, Japan). Photocatalytic degradation runs were preceded by blind test in the absence of a photocatalyst or illumination. No degradation of phenol or carbamazepine was observed in the absence of either the photocatalyst or illumination.

4. Conclusions

In this work, we developed a novel method for the preparation of the magnetic photocatalysts with controllable formation core-interlayer-shell structure based on zeta potential changes in aqueous phase. The functionalization of magnetic core with silica interlayer and TiO_2 photocatalyst layer was performed in a w/o microemulsion system using non-ionic (TX-100) and cationic (CTAB) surfactants, depending on the particle surface charge in different pH values. The positively charged ferrite particle can interact in acidic conditions with negatively charged silica, leading to self-assembly of SiO_2 into ferrite shell. Indeed, TiO_2 nanoparticles are positively charged, and thus, interact competitively

with silica particles deposited on a ferrite core. In alkaline conditions, cationic surfactant is used as a binder to form a silica shell on a ferrite core. Moreover, the cationic surfactant also effectively interacts with negatively charged titania species, resulting in the core-interlayer-shell structure of nanocomposite. The composition of the core-interlayer-shell structure of magnetic nanocomposites was confirmed by TEM analysis supplemented with EDXS mapping. Based on XRD data crystalline cubic spinel structure of Fe_3O_4 and $CoFe_2O_4$, magnetic particles with crystallite size of 45 nm and 13 nm was observed. $BaFe_{12}O_{19}$ particles were hexagonal in shape with the random orientation and diameters of the aggregated particles in the range of 40–70 nm. The obtained nanocomposites exhibit superparamagnetic behavior. The best photocatalytic activity in the reaction of phenol and carbamazepine photomineralization was observed for the sample $CoFe_2O_4/SiO_2/TiO_2$_2 obtained by self-assembly of SiO_2 and TiO_2 P25 particles at pH = 5 on the surface of cobalt ferrite. This photocatalyst was as effective in the reaction of phenol degradation as TiO_2 (P25, Evonik), but more easily separable due to superparamagnetic properties. Photocatalytic activity measured in the fourth subsequent cycle showed good reusability and no loss in phenol degradation.

Acknowledgments: This research was financially supported by Polish National Science Centre (Grant No. NCN 2016/23/D/ST5/01021).

Author Contributions: A.Z.-J.: conceived the concept, designed the experiments, analyzed the data, performed zeta potential and XRD analyses, contributed reagents, materials and analysis tools, and drafted the manuscript; Z.B., I.W., S.D.: performed magnetic photocatalyst synthesis; Z.S.: performed the VSM analysis; T.K.: participated in the analysis and interpretation of magnetic properties; G.N.: performed TEM microscopy analysis, J.H. edited and revised the manuscript.

Conflicts of Interest: The authors declare no conflict of interest.

References

1. Guo, Z.; Ma, R.; Li, G. Degradation of phenol by nanomaterial TiO_2 in wastewater. *Chem. Eng. J.* **2006**, *119*, 55–59. [CrossRef]
2. Carabin, A.; Drogui, P.; Robert, D. Photo-degradation of carbamazepine using TiO_2 suspended photocatalysts. *J. Taiwan Inst. Chem. Eng.* **2015**, *54*, 109–117. [CrossRef]
3. He, Y.; Sutton, N.B.; Rijnaarts, H.H.H.; Langenhoff, A.A.M. Degradation of pharmaceuticals in wastewater using immobilized TiO_2 photocatalysis under simulated solar irradiation. *Appl. Catal. B Environ.* **2016**, *182*, 132–141. [CrossRef]
4. Zielińska-Jurek, A.; Zaleska, A. Ag/Pt-modified TiO_2 nanoparticles for toluene photooxidation in the gas phase. *Catal. Today* **2014**, *230*, 104–111. [CrossRef]
5. Vitiello, G.; Pezzella, A.; Zanfardino, A.; Silvestri, B.; Giudicianni, P.; Constantini, A.; Varcamonti, M.; Branda, F.; Luciani, G. Antimicrobial activity of eumelanin-based hybrids: The role of TiO_2 in modulating the structure and biological performance. *Mater. Sci. Eng. C* **2017**, *75*, 454–462. [CrossRef] [PubMed]
6. Jalvo, B.; Faraldos, M.; Bahamonde, A.; Rosal, R. Antimicrobial and antibiofilm efficacy of self-cleaning surfaces functionalized by TiO_2 photocatalytic nanoparticles against *Staphylococcus aureus* and *Pseudomonas putida*. *J. Hazard. Mater.* **2017**, *340*, 160–170. [CrossRef] [PubMed]
7. Xue, X.-D.; Fu, J.-F.; Zhu, W.-F.; Guo, X.-C. Separation of ultrafine TiO_2 from aqueous suspension and its reuse using cross-flow ultrafiltration (CFU). *Desalination* **2008**, *225*, 29–40. [CrossRef]
8. Zielińska-Jurek, A.; Klein, M.; Hupka, J. Enhanced visible light photocatalytic activity of Pt/I-TiO_2 in a slurry system and supported on glass packing. *Sep. Purif. Technol.* **2017**, *189*, 246–252. [CrossRef]
9. Dijkstra, M.F.J.; Michorius, A.; Buwalda, H.; Panneman, H.J.; Winkelman, J.G.M.; Beenackers, A.A.C.M. Comparison of the efficiency of immobilized and suspended systems in photocatalytic degradation. *Catal. Today* **2001**, *66*, 487–494. [CrossRef]
10. Yang, L.; Wang, F.; Hakki, A.; Macphee, D.E.; Liu, P.; Hu, S. The influence of zeolites fly ash bead/TiO_2 composite material surface morphologies on their adsorption and photocatalytic performance. *Appl. Surf. Sci.* **2017**, *392*, 687–696. [CrossRef]

11. Ilkaeva, M.; Krivtsov, I.; Díaz, E.; Amghouzd, Z.; Pati, E.; Khainakove, S.; Garcíaa, J.S.; Ordónez, S. Photocatalytic degradation of 2-(4-methylphenoxy)ethanol over TiO_2 spheres. *J. Hazard. Mater.* **2017**, *332*, 59–69. [CrossRef] [PubMed]
12. Tsai, M.-C.; Yang, M.-H.; Chang, Y.-W.; Tzeng, J.-K.; Lee, C.-Y.; Chiu, H.T.; Chen, H.-C.; Lin, I.-N. Synthesis of porous micro-sized titania cages and their photocatalytic property. *Mater. Chem. Phys.* **2013**, *143*, 60–64. [CrossRef]
13. Dou, L.; Gao, L.; Yang, X.; Song, X. Hierarchical architectures TiO_2: Pollen-inducted synthesis, remarkable crystalline-phase stability, tunable size, and reused photo-catalysis. *J. Hazard. Mater.* **2012**, *203–204*, 363–369. [CrossRef] [PubMed]
14. Hiroshi, F.; Yukiko, H.; Michichiro, Y.; Shoichi, A. Magnetic Photocatalyst. Japanese Patent JP6154620, 13 February 1994.
15. Towata, A.; Sando, M. Photocatalyst Particles Containing Ferromagnetic Metal Particles and Method for Synthesis Thereof. U.S. Patent 5,703,002, 30 August 1997.
16. Beydoun, D.; Amal, R.; Low, G.; McEvoy, S. A Preliminary Investigation into the Synthesis of Titania-Coated Magnetite as a Novel Photocatalyst. In Proceedings of the Third World Congress on Particle Technology, Brighton, UK, 6–9 July 1998; p. 385.
17. Abbas, M.; Rao, B.P.; Reddy, V.; Kim, C. Fe_3O_4/TiO_2 core/shell nanocubes: Single-batch surfactantless synthesis, characterization and efficient catalysts for methylene blue degradation. *Ceram. Int.* **2014**, *40*, 11177–11186. [CrossRef]
18. Wei, J. Synthesis and magnetorheological effect of Fe_3O_4-TiO_2 nanocomposite. *J. Phys. Conf. Ser.* **2009**, *149*, 25–29. [CrossRef]
19. Zhang, L.; Wu, Z.; Chen, L.; Zhang, L.; Li, X.; Xu, H.; Wang, H.; Zhu, G. Preparation of magnetic Fe_3O_4/TiO_2/Ag composite microspheres with enhanced photocatalytic activity. *Solid State Sci.* **2016**, *52*, 42–48. [CrossRef]
20. Beydoun, D.; Amal, R.; Low, G.K.-C.; McEvoy, S. Novel Photocatalyst: Titania-Coated Magnetite. Activity and Photodissolution. *J. Phys. Chem. B* **2000**, *104*, 4387–4396. [CrossRef]
21. Fan, Y.; Ma, C.; Li, W.; Yin, Y. Synthesis and properties of $Fe_3O_4/SiO_2/TiO_2$ nanocomposites by hydrothermal synthetic method. *Mater. Sci. Semicond. Process.* **2012**, *15*, 582–585. [CrossRef]
22. Gad-Allah, T.A.; Fujimura, K.; Kato, S.; Satokawa, S.; Kojima, T. Preparation and characterization of magnetically separable photocatalyst ($TiO_2/SiO_2/Fe_3O_4$): Effect of carbon coating and calcination temperature. *J. Hazard. Mater.* **2008**, *154*, 572–577. [CrossRef] [PubMed]
23. Shi, F.; Li, Y.; Zhang, Q.; Wang, H. Synthesis of $Fe_3O_4/C/TiO_2$ magnetic photocatalyst via vapor phase hydrolysis. *Int. J. Photoenergy* **2012**, *2012*, 1–8. [CrossRef]
24. Yuan, Q.; Li, N.; Geng, W.; Chi, Y.; Li, X. Preparation of magnetically recoverable Fe_3O_4@SiO_2@meso-TiO_2 nanocomposites with enhanced photocatalytic ability. *Mater. Res. Bull.* **2012**, *47*, 2396–2402. [CrossRef]
25. Li, R.; Jia, Y.; Bu, N.; Wu, J.; Zhen, Q. Photocatalytic degradation of methyl blue using Fe_2O_3/TiO_2 composite ceramics. *J. Alloys Compd.* **2015**, *643*, 88–93. [CrossRef]
26. Lee, S.; Drwiega, J.; Wu, C.; Mazyck, D.; Sigmund, W.M. Anatase TiO_2 Nanoparticle Coating on Barium Ferrite Using Titanium Bis-Ammonium Lactato Dihydroxide and Its Use as a Magnetic Photocatalyst. *Chem. Mater.* **2004**, *12*, 1160–1164. [CrossRef]
27. Li, H.; Zhang, Y.; Wang, S.; Wu, Q.; Liu, C. Study on nanomagnets supported TiO_2 photocatalysts prepared by a sol-gel process in reverse microemulsion combining with solvent-thermal technique. *J. Hazard. Mater.* **2009**, *169*, 1045–1053. [CrossRef] [PubMed]
28. Salamat, S.; Younesi, H.; Bahramifar, N. Synthesis of magnetic core–shell Fe_3O_4@TiO_2 nanoparticles from electric arc furnace dust for photocatalytic degradation of steel mill wastewater. *RSC Adv.* **2017**, *7*, 19391–19405. [CrossRef]
29. Prieto-Mahaney, O.O.; Murakami, N.; Abe, R.; Ohtani, B. Correlation between Photocatalytic Activities and Structural and Physical Properties of Titanium(IV) Oxide Powders. *Chem. Lett.* **2009**, *38*, 238–239. [CrossRef]
30. Amano, F.; Nakata, M.; Yamamoto, A.; Tanaka, T. Rutile titanium dioxide prepared by hydrogen reduction of Degussa P25 for highly efficient photocatalytic hydrogen evolution. *Catal. Sci. Technol.* **2016**, *6*, 5693–5699. [CrossRef]
31. Fagerlund, G. Determination of specific surface by the BET method. *Mater. Constr.* **1973**, *6*, 239–245. [CrossRef]

32. Liu, H.; Jia, Z.; Ji, S.; Zheng, Y.; Li, M.; Yang, H. Synthesis of $TiO_2/SiO_2@Fe_3O_4$ magnetic microspheres and their properties of photocatalytic degradation dyestuff. *Catal. Today* **2011**, *175*, 293–298. [CrossRef]
33. Chi, Y.; Yuan, Q.; Li, Y.; Zhao, L.; Li, N.; Li, X.; Yan, W. Magnetically separable $Fe_3O_4@SiO_2@TiO_2$-Ag microspheres with well-designed nanostructure and enhanced photocatalytic activity. *J. Hazard. Mater.* **2013**, *262*, 404–411. [CrossRef] [PubMed]
34. Fu, W.; Yang, H.; Li, M.; Chang, L.; Yu, Q.; Xu, J.; Zou, G. Preparation and photocatalytic characteristics of core-shell structure $TiO_2/BaFe_{12}O_{19}$ nanoparticles. *Mater. Lett.* **2006**, *60*, 2723–2727. [CrossRef]
35. Dubowik, J.; Gościańska, I. Micromagnetic Approach to Exchange Bias. *Acta Phys. Pol. A* **2015**, *127*, 147–152. [CrossRef]
36. Petracic, O. Superparamagnetic nanoparticle ensembles. *Superlattices Microstruct.* **2010**, *47*, 569–578. [CrossRef]
37. Haneda, K.; Morrish, A.H. Magnetic Properties of $BaFe_{12}O_{19}$ Small Particles. *IEEE Trans. Magn.* **1989**, *25*, 2597–2601. [CrossRef]
38. Torres, T.E.; Lima, E., Jr.; Mayoral, A.; Ibarra, A.; Marquina, C.; Ibarra, M.R.; Goya, G.F. Validity of the Néel-Arrhenius model for highly anisotropic $Co_xFe_{3-x}O_4$ nanoparticles. *J. Appl. Phys.* **2015**, *118*, 183902. [CrossRef]
39. Su, R.; Bechstein, R.; Sø, L.; Vang, R.T.; Sillassen, M.; Esbjörnsson, B.; Palmqvist, A.; Besenbacher, F. How the Anatase-to-Rutile Ratio Influences the Photoreactivity of TiO_2. *J. Phys. Chem. C* **2011**, *115*, 24287–24292. [CrossRef]
40. Ohno, T.; Sarukawa, K.; Tokieda, K.; Matsumura, M. Morphology of a TiO_2 Photocatalyst (Degussa, P-25) Consisting of Anatase and Rutile Crystalline Phases. *J. Catal.* **2001**, *203*, 82–86. [CrossRef]
41. Rui, Z.; Wu, S.; Peng, C.; Ji, H. Comparison of TiO_2 Degussa P25 with anatase and rutile crystalline phases for methane combustion. *Chem. Eng. J.* **2014**, *243*, 254–264. [CrossRef]
42. Kawahara, T.; Konishi, Y.; Tada, H.; Tohge, N.; Nishii, J.; Ito, S. A Patterned TiO_2(Anatase)/TiO_2(Rutile) Bilayer-Type Photocatalyst: Effect of the Anatase/Rutile Junction on the Photocatalytic Activity. *Angew. Chem.* **2002**, *114*, 2935–2937. [CrossRef]
43. Zielińska-Jurek, A.; Wei, Z.; Wysocka, I.; Szweda, P.; Kowalska, E. The effect of nanoparticles size on photocatalytic and antimicrobial properties of Ag-Pt/TiO_2 photocatalysts. *Appl. Surf. Sci.* **2015**, *353*, 317–325. [CrossRef]
44. Zielińska-Jurek, A.; Bielan, Z.; Wysocka, I.; Strychalska, J.; Janczarek, M.; Klimczuk, T. Magnetic semiconductor photocatalysts for the degradation of recalcitrant chemicals from flow back water. *J. Environ. Manag.* **2017**, *195*, 157–165. [CrossRef] [PubMed]
45. Zhen, G.; Muir, B.W.; Moffat, B.A.; Harbour, P.; Murray, K.S.; Moubaraki, B.; Suzuki, K.; Madsen, I.; Agron-Olshina, N.; Waddington, L. Comparative study of magnetic behavior of spherical and cubic superparamagnetic iron oxide nanoparticles. *J. Phys. Chem. C* **2011**, *115*, 327–334. [CrossRef]
46. Larumbe, S.; Gómez-Polo, C.; Pérez-Landazábal, J.; Pastor, J.M. Effect of a SiO_2 coating on the magnetic properties of Fe_3O_4 nanoparticles. *J. Phys. Condens Matter.* **2012**, *24*, 1–6. [CrossRef] [PubMed]

6. Sposób otrzymywania fotokatalizatora magnetycznego wielowarstwowego

Anna Zielińska-Jurek, Zuzanna Bielan

Polish patents no. PL. 233343, PL. 233344, PL. 233345 (2019)

P6

RZECZPOSPOLITA POLSKA

Urząd Patentowy Rzeczypospolitej Polskiej

(12) **OPIS PATENTOWY** (19) **PL** (11) **233343** (13) **B1**

(21) Numer zgłoszenia: **423293**

(22) Data zgłoszenia: **28.10.2017**

(51) Int.Cl.
B01J 37/03 (2006.01)
B01J 35/02 (2006.01)
B01J 21/06 (2006.01)
B01J 23/00 (2006.01)

(54) **Sposób otrzymywania warstwowego fotokatalizatora magnetycznego**

(43) Zgłoszenie ogłoszono:
06.05.2019 BUP 10/19

(45) O udzieleniu patentu ogłoszono:
30.09.2019 WUP 09/19

(73) Uprawniony z patentu:
POLITECHNIKA GDAŃSKA, Gdańsk, PL

(72) Twórca(y) wynalazku:
ANNA ZIELIŃSKA-JUREK, Otomin, PL
ZUZANNA BIELAN, Tczew, PL

(74) Pełnomocnik:
rzecz. pat. Małgorzata Kluczyk

PL 233343 B1

Opis wynalazku

Przedmiotem wynalazku jest sposób otrzymywania warstwowych fotokatalizatorów magnetycznych o strukturze wielowarstwowej, aktywnych w zakresie promieniowania UV i Vis, mających zastosowanie zwłaszcza w reakcji fotokatalitycznej degradacji wybranych związków organicznych i nieorganicznych.

Konwencjonalne metody oczyszczania ścieków, płynów technologicznych nie zawsze są skuteczne i efektywne w odniesieniu do usuwania z nich substancji trudno degradowalnych, niepodatnych na rozkład biologiczny, takich jak: pestycydy, wielopierścieniowe węglowodory aromatyczne, związki chloroorganiczne oraz barwniki. Efektywną metodą usuwania zanieczyszczeń z takich ścieków i płynów technologicznych są procesy zaawansowanego utleniania, które cechuje wytwarzanie in-situ utleniaczy o najwyższym potencjale utleniającym, takich jak: rodniki hydroksylowe, aniony nadtlenkowe, tlen singletowy oraz nadtlenek wodoru. Spośród najbardziej efektywnych metod zaawansowanego utleniania należy wymienić proces fotokatalizy, w którym degradacja zanieczyszczeń odbywa się w obecności fotokatalizatora, poddanego działaniu promieniowania elektromagnetycznego. Najczęściej opisywanym fotokatalizatorem, z uwagi na niską cenę oraz wysoką aktywność fotokatalityczną, jest tlenek tytanu(IV), rozdrobniony do postaci cząstek o nanometrycznych rozmiarach, co zapewnia dużą powierzchnię właściwą i zwiększa efektywność degradacji zanieczyszczeń poprzez zwiększenie powierzchni kontaktu fotokatalizator – zanieczyszczenie. Wielkość cząstek TiO_2 generuje jednak trudności w jego separacji, po procesie oczyszczania, przyczyniając się do wzrostu kosztów prowadzenia procesu, poprzez stosowanie drogich metod separacji m.in. ultrafiltracji.

Jednym z najnowszych i efektywnych rozwiązań zagadnienia separacji fotokatalizatora po procesie oczyszczania i jego ponownego zastosowania w procesie, wykluczającym konieczność immobilizacji na nośniku stałym jest preparatyka nanokompozytu, który poza wysoką efektywnością rozkładu zanieczyszczeń w reakcji fotokatalitycznej posiada dodatkowe właściwości, umożliwiające jego separację z wodnej zawiesiny, z zastosowaniem pola magnetycznego.

Znane są sposoby otrzymywania fotokatalizatorów o właściwościach magnetycznych, które jednak w wyniku bezpośredniego kontaktu materiału magnetycznego zawierającego jony metalu, szczególnie żelaza podatne są na ługowanie chemiczne w fazie wodnej o odczynie kwasowym (pH<7). Prowadzi to często do wtórnego zanieczyszczenia ścieków lub w wyniku kontaktu z powierzchnią fotokatalizatora do jego zatrucia i w konsekwencji obniżenia efektywności rozkładu zanieczyszczeń obecnych w fazie wodnej metodą fotokatalityczną. Ponadto w trakcie procesu fotokatalitycznego może następować fotochemiczne ługowanie jonów żelaza do roztworu, będące efektem reakcji wygenerowanych nośników ładunku na powierzchni półprzewodnika (np. TiO_2) z cząsteczką tlenu lub wody, które zdolne są do utleniania żelaza lub innego metalu znajdującego się na powierzchni cząstki magnetycznej. W tym odniesieniu pokrycie powierzchni kompozytu inertną warstwą oddzielającą magnetyczny rdzeń od warstwy fotokatalizatora pozwala na wielokrotne zastosowanie otrzymanego fotokatalizatora w procesie oczyszczania ścieków lub płynów technologicznych, nie zmieniając jego właściwości fotokatalitycznych oraz magnetycznych.

Z dokumentacji zgłoszeniowej CN102357363A znany jest sposób preparatyki fotokatalizatora $TiO_2/SiO_2/Fe_3O_4$ o właściwościach magnetycznych aktywnego w zakresie światła widzialnego. Nanocząstki magnetyczne otrzymano metodą strąceniową w wyniku dodawania do wodnego roztworu $FeCl_3 \cdot 6H_2O$ i $FeSO_4$ amoniaku w temperaturze 40–60°C w atmosferze gazu obojętnego, azotu. Otrzymany osad cząstek magnetycznych dyspergowano w alkoholu etylowym, dodawano TEOS w ilości od 0,5% do 10% molowych i mieszano w temperaturze 50°C–60°C. Hydrolizę krzemionki przeprowadzano dodając wodny roztwór kwasu solnego, a następnie po 30 min mieszania dodano amoniak i kontynuowano mieszanie przez 10 h. Stosunek wagowy TEOS do amoniaku wynosił 2:3. Następnie do wody dejonizowanej wprowadzono prekursor TiO_2 – siarczan tytanylu, mocznik oraz otrzymane cząstki magnetyczne i prowadzono reakcję hydrotermalną w temperaturze 120–200°C przez 5–18 h. Otrzymane cząstki charakteryzowały się magnetycznością 3 $emu \cdot g^{-1}$.

Z dokumentacji patentowej CN1103637C znany jest sposób preparatyki fotokatalizatorów magnetycznych, których rdzeń stanowi związek o właściwościach magnetycznych, o wielkości cząstek od 5 nm do 10 μm otrzymany w wyniku dyspergowania cząstek magnetycznych z grupy: Fe_3O_4, γ-Fe_2O_3, CrO_2, Co-Fe_2O_3, $BaFe_{12}O_{19}$ w roztworze wodnym o pH 11, które następnie wkraplano do roztworu krzemianu sodu i żywicy kationowej o pH 10. Całość poddawano działaniu ultradźwięków, mieszano, suszono i kalcynowano w temperaturze 600°C przez 1 h. Otrzymane cząstki magnetyczne pokryte warstwą inertną krzemionki po suszeniu ucierano z półprzewodnikiem takim jak: TiO_2, SnO_2, ZnO, Cds czy

WO_3 z dodatkiem wody, otrzymując pastę fotokatalizatora, którą następnie suszono i kalcynowano w temperaturze 500°C przez 1 h.

Znane są sposoby otrzymywania fotokatalizatorów magnetycznych o strukturze rdzeń-otoczka. Według tych sposobów można otrzymywać cząstki o wielkości rzędu od kilku nm do kilkudziesięciu μm. Jednak często magnetyczność otrzymanych nanokompozytów jest niewielka (poniżej 5 $emu \cdot g^{-1}$), co nie pozwala na efektywną separację magnetyczną w krótkim czasie fotokatalizatora z fazy wodnej. Ponadto otrzymywanie fotokatalizatora magnetycznego w środowisku o odczynie kwasowym, dla którego cząstki magnetyczne oraz warstwy fotokatalitycznej (np. TiO_2) charakteryzują się zwiększonym powierzchniowym ładunkiem dodatnim, wpływa na ich wzajemne odpychanie i nie prowadzi do otrzymania pożądanej struktury rdzeń-otoczka nanokompozytu. Procesy wytwarzania cząstek magnetycznych impregnowanych warstwą inertną oraz warstwą fotokatalityczną prowadzone są wieloetapowo w kolejnych etapach polegających na (1) otrzymaniu cząstek magnetycznych i ich obróbce termicznej, (2) dyspergowaniu wysuszonych cząstek magnetycznych w mieszaninie reakcyjnej, (3) osadzeniu cząstek warstwy inertnej i ich ponownej obróbce termicznej, a następnie (4) osadzeniu cząstek fotokatalizatora, suszeniu i kalcynacji otrzymanego nanokompozytu.

W tym odniesieniu należy wskazać, że dotychczas nie jest znany sposób otrzymywania fotokatalizatorów magnetycznych, według którego struktura nanokompozytu może być dowolnie zaprojektowana i otrzymana w oparciu o pomiar potencjału elektrokinetycznego (zeta) poszczególnych komponentów układu: materiału magnetycznego, warstwy inertnej oraz fotokatalizatora, a następnie odpowiedni dobór pH, w jakim należy przeprowadzać adhezję poszczególnych warstw na powierzchni rdzenia magnetycznego, w celu otrzymania struktury rdzeń-otoczka lub struktury wielowarstwowej.

Sposób wytwarzania fotokatalizatora magnetycznego charakteryzuje się według wynalazku tym, że preparatyka cząstek magnetycznych, wytwarzanie warstwy inertnej oraz warstwy fotokatalizatora mogą być prowadzone w jednym układzie, bez konieczności separacji poszczególnych jego komponentów. Proces przeprowadza się w oparciu o zmianę właściwości powierzchniowych cząstek w funkcji pH. Sposób otrzymywania fotokatalizatorów magnetycznych prowadzi się również w układzie mikroemulsji w/o, jednak można również stosować w tym celu roztwory wodne oraz roztwory wodne surfaktantów.

W przedstawionym sposobie otrzymywania nanokompozytów magnetycznych według wynalazku, do roztworu wodnego wprowadza się prekursory cząstek magnetycznych korzystnie w atmosferze gazu obojętnego, korzystnie azotu i/lub argonu, i/lub amoniaku, dodaje się odczynnik strącający cząstki magnetyczne i jednocześnie podwyższający pH, w zakresie od 7 do 14, korzystnie do wartości 8–12, z grupy: wodorotlenki metali grupy I i II A układu okresowego pierwiastków, amoniak, sole amonowe, aminy, otrzymując zawiesinę cząstek magnetycznych. Jako cząstki magnetyczne stosuje się dowolny ferryt spinelowy, korzystnie z grupy: MFe_2O_4 (M=Mn, Zn, Fe), $CoFe_{2-x}M_xO_4$ (M=Zn^{2+}, Mn^{2+}), γ-Fe_2O_3, dowolny ferryt heksagonalny, korzystnie $BaFe_{12}O_{19}$, $BaFe_{12}O_{19}$-$M_2Fe_4O_8$ (M=Mn, Fe, Zn), związki z grupy magnesów organicznych, pył żelazowy lub stopy metali i ich nanocząstki o właściwościach magnetycznych, takie jak: Fe-Pt, Co-Pt, Fe-Ni, Fe-Co, Ni-CeO_2, korzystnie Fe-Ni. Zawiesinę cząstek magnetycznych w wodzie i/lub alkoholu miesza się korzystnie w atmosferze gazu obojętnego lub tlenku węgla(IV), sporządza się drugą mieszaninę w ten sposób, że sporządza się alkoholowy i/lub wodny roztwór substancji obniżającej pH z grupy: kwasów karboksylowych i/lub kwasów nieorganicznych, korzystnie kwas solny i/lub kwas octowy i/lub kwas cytrynowy i/lub kwas askorbinowy o pH w zakresie od 1 do 7, korzystnie od 3 do 6, do którego dodaje się składnik warstwy inertnej w postaci węgla korzystnie w postaci grafitu lub grafenu, polimeru poli(N-izopropyloakryloamidu) glikolu polietylenowego lub polidimetylosiloksanu lub prekursora składnika warstwy inertnej, takiego jak tetraetyloortokrzemian (TEOS) i/lub tetrametoksysilan (TMOS) w stosunku molowym składnika warstwy inertnej do cząstek magnetycznych wynoszącym w zakresie od 0,01:1 do 20:1, korzystnie od 0,5:1 do 10:1. Następnie do zawiesiny cząstek magnetycznych wkrapla się drugą mieszaninę i ustala się pH poniżej 7, korzystnie w zakresie od 3 do 6, całość miesza się, a następnie dodaje się cząstki fotokatalityczne z grupy: TiO_2, WO_3, ZnO, SnO_2, CdS, korzystnie TiO_2, korzystnie w postaci prekursora półprzewodnika cząstek fotokatalitycznych, korzystnie tetrabutylo tytanian i/lub tetraizopropylo tytanian i/lub siarczan tytanylu i/lub czterochlorek tytanu w takiej ilości, aby stosunek molowy półprzewodnika do cząstek magnetycznych wynosił od 0,1:1 do 30:1, korzystnie w zakresie od 0,5:1 do 4:1. Cząstki fotokatalityczne korzystnie modyfikuje się powierzchniowo nanocząstkami metali szlachetnych lub bimetali, korzystnie Pt-Cu, Pt-Pd, Pd-Cu, Au-Pt, Au-Pd, Ag-Pt, Ag-Cu w ilości od 0,01 do 10% molowych w stosunku do półprzewodnika, korzystnie od 0,01 do 1% molowych lub cząstki fotokatalityczne korzystnie domieszkuje się niemetalem z grupy azot, siarka, bor, jod, węgiel w ilości od 0,01 do 30% wagowych w stosunku

do półprzewodnika, korzystnie od 0,01 do 15% wagowych lub cząstki fotokatalityczne korzystnie domieszkuje się niemetalem z grupy azot, siarka, bor, jod, węgiel w ilości od 0,01 do 30% wagowych w stosunku do półprzewodnika, korzystnie od 0,01 do 15% wagowych i dodatkowo modyfikuje się powierzchniowo w znany sposób nanocząstkami metali, korzystnie platyny, miedzi, palladu, srebra, złota, rutenu w ilości od 0,01 do 10% molowych w stosunku do półprzewodnika, korzystnie od 0,01 do 1% molowych. Stopień pokrycia cząstek magnetycznych warstwą inertną i warstwą fotokatalityczną monitoruje się mierząc potencjał zeta powstałego układu dyspersyjnego. Potencjał zeta dla cząstek magnetycznych pokrytych krzemionką w środowisku kwasowym przyjmuje wartość ujemną, natomiast po wprowadzeniu do układu cząstek warstwy fotokatalitycznej i ich adsorpcji na powierzchni cząstek magnetycznych, potencjał zeta przyjmuje wartość dodatnią. Po co najmniej 10 min mieszania, lub uzyskaniu dodatniej wartości potencjału zeta dla cząstek pokrytych warstwą inertną i TiO_2, otrzymane cząstki separuje się za pomocą pola magnetycznego, przemywa się wodą, suszy się do stałej masy, w temperaturze 60–90°C i kalcynuje się w temperaturze 250–1000°C przez 0,5–5 godzin.

Projektowane nanokompozyty o właściwościach fotokatalitycznych i magnetycznych według wynalazku korzystnie otrzymywane są w wyniku preparatyki z zastosowaniem związków powierzchniowo czynnych niejonowych, pozwalających na efektywną adhezję poszczególnych warstw na powierzchni rdzenia magnetycznego, korzystnie przeprowadza się reakcję w układzie mikroemulsji w/o. W mikroemulsji nanokrople fazy wodnej zdyspergowane są w fazie ciągłej – olejowej, dodatkowo stabilizowanej i chronionej przed aglomeracją przez surfaktant na granicy faz w/o. Każda z kropel stanowi mikroreaktor, a wielkość tworzących się cząstek jest ograniczona poprzez wielkość kropli fazy wewnętrznej. Dzięki temu można kontrolować wielkość otrzymywanych cząstek materiału magnetycznego, nukleację i wzrost cząstek fotokatalizatora magnetycznego zgodnie z zamierzonym oczekiwaniem.

W przedstawionym sposobie otrzymywania warstwowego fotokatalizatora magnetycznego według wynalazku do wodnego i/lub alkoholowego roztworu surfaktantu niejonowego, korzystnie eteru p-1,1,3,3-tetrametylobutylofenylowo polietylenoglikolowym (TX-100), monostearynian sorbitanu, monolaurynianu sorbitanu (Tween 80) w stężeniu od 0,01M do 3M wprowadza się cząstki magnetyczne. Jako cząstki magnetyczne stosuje się dowolny ferryt spinelowy, korzystnie z grupy: MFe_2O_4 (M=Mn, Zn, Fe), $CoFe_{2-x}M_xO_4$ (M=Zn^{2+}, Mn^{2+}), γ-Fe_2O_3, dowolny ferryt heksagonalny, korzystnie $BaFe_{12}O_{19}$, $BaFe_{12}O_{19}$-$M_2Fe_4O_8$ (M=Mn, Fe, Zn), związki z grupy magnesów organicznych, pył żelazowy lub stopy metali i ich nanocząstki o właściwościach magnetycznych, takie jak: Fe-Pt, Co-Pt, Fe-Ni, Fe-Co, Ni-CeO_2, korzystnie Fe-Ni. Następnie sporządza się drugą mieszaninę zawierającą alkoholowy i/lub wodny roztwór surfaktantu niejonowego, korzystnie eteru p-1,1,3,3-tetrametylobutylofenylowo polietylenoglikolowym (TX-100), monostearynian sorbitanu, monolaurynianu sorbitanu (Tween 80) w stężeniu od 0,01M do 3M zawierający substancję obniżającą pH z grupy: kwasów karboksylowych i/lub kwasów nieorganicznych, korzystnie kwas solny i/lub kwas octowy i/lub kwas cytrynowy i/lub kwas askorbinowy o pH w zakresie od 1 do 7, korzystnie od 3 do 6, do którego dodaje się składnik warstwy inertnej w postaci węgla korzystnie w postaci grafitu lub grafenu, polimeru poli(N-izopropyloakryloamidu), glikolu polietylenowego lub polidimetylosiloksanu lub tetraetyloortokrzemianu (TEOS) i/lub tetrametoksysilanu (TMOS) w stosunku molowym składnika warstwy inertnej do cząstek magnetycznych wynoszącym w zakresie od 0,01:1 do 20:1, korzystnie od 0,5:1 do 10:1. Następnie do zawiesiny zawierającej cząstki magnetyczne wkrapla się drugą mieszaninę i ustala się pH poniżej 7, korzystnie w zakresie od 3 do 6, całość miesza się, a następnie dodaje się cząstki fotokatalityczne półprzewodników z grupy: tlenek tytanu (IV) TiO_2, tlenek wolframu (VI) WO_3, tlenek cynku ZnO, dwutlenek cyny SnO_2, siarczek kadmu CdS, korzystnie TiO_2, korzystnie w postaci prekursora półprzewodnika cząstek fotokatalitycznych, korzystnie tetrabutylo tytanian i/lub tetraizopropyło tytanian i/lub siarczan tytanylu i/lub czterochlorek tytanu, w takiej ilości, aby stosunek molowy cząstek fotokatalitycznych do cząstek magnetycznych wynosił od 0,1:1 do 30:1, korzystnie w zakresie od 0,5:1 do 4:1. Cząstki fotokatalityczne korzystnie modyfikuje się powierzchniowo nanocząstkami metali szlachetnych lub bimetali, korzystnie Pt-Cu, Pt- Pd, Pd-Cu, Au-Pt, Au-Pd, Ag-Pt, Ag-Cu w ilości od 0,01 do 10% molowych w stosunku do półprzewodnika, korzystnie od 0,01 do 1% molowych lub cząstki fotokatalityczne korzystnie domieszkuje się niemetalem z grupy azot, siarka, bor, jod, węgiel w ilości od 0,01 do 30% wagowych w stosunku do półprzewodnika, korzystnie od 0,01 do 15% wagowych lub cząstki fotokatalityczne korzystnie domieszkuje się niemetalem z grupy azot, siarka, bor, jod, węgiel w ilości od 0,01 do 30% wagowych w stosunku do półprzewodnika, korzystnie od 0,01 do 15% wagowych i dodatkowo modyfikuje się powierzchniowo w znany sposób nanocząstkami metali, korzystnie platyny, miedzi, palladu, srebra, złota, rutenu w ilości od 0,01 do 10% molowych w stosunku do półprzewodnika, korzystnie od 0,01 do 1% molowych. Następnie po co najmniej 10 min mieszania

lub uzyskaniu dodatniej wartości potencjału zeta dla cząstek fotokatalizatora magnetycznego, otrzymane cząstki separuje się za pomocą pola magnetycznego, przemywa się wodą, suszy się do stałej masy, w temperaturze 60–90°C i kalcynuje się w temperaturze 250–1000°C przez 0,5–5 godzin.

W przedstawionym sposobie otrzymywania warstwowego fotokatalizatora magnetycznego według wynalazku otrzymywanie cząstek magnetycznych korzystnie prowadzi się w mikroemulsji w/o lub układzie odwróconych miceli. Sporządza się mikroemulsję w/o składającą się z fazy wodnej, która zawiera roztwór soli metali stanowiące prekursory cząstek magnetycznych oraz fazę olejową, która zawiera ciekłe węglowodory korzystnie cykloheksan i/lub oktan i/lub izooktan i/lub heptan oraz surfaktant niejonowy korzystnie eter p-1,1,3,3-tetrametylobutylofenylowo polietylenoglikolowym, monooleinian polioksyetylenosorbitanu (Polisorbat 80), monooleinian sorbitanu (Span 80), monostearynian sorbitanu, monolaurynianem sorbitanu (Tween 80) w stężeniu od 0,1M do 10M w stosunku do fazy olejowej korzystnie cykloheksanu i/lub izooktanu i/lub heptanu, i/lub oktanu i/lub ko-surfaktant, korzystnie izopropanol i/lub n-butanol i/lub heksanol o stężeniu od 0,1M do 10M w stosunku do fazy olejowej, do której dodaje się mikroemulsję w/o stabilizowaną surfaktantem niejonowym, korzystnie eter p-1,1,3,3-tetrametylobutylofenylowo polietylenoglikolowym, monooleinian polioksyetylenosorbitanu (Polisorbat 80), monooleinian sorbitanu (Span 80), monostearynian sorbitanu, monolaurynianem sorbitanu (Tween 80) w stężeniu od 0,1M do 10M w stosunku do fazy olejowej korzystnie cykloheksanu i/lub izooktanu i/lub heptanu, i/lub oktanu i/lub ko-surfaktantem, korzystnie izopropanolem i/lub n-butanolem i/lub heksanolem o stężeniu od 0,1M do 10M w stosunku do fazy olejowej, zawierającą w fazie wodnej substancję podwyższającą pH w zakresie od 7 do 14, korzystnie do wartości w zakresie od 8 do 12, z grupy: wodorotlenki metali grupy I i II A układu okresowego pierwiastków, amoniak, sole amonowe, aminy. Całość miesza się otrzymując mikroemulsję zawierającą zdyspergowane cząstki magnetyczne. Sposób otrzymywania cząstek fotokatalizatora magnetycznego w mikroemulsji w/o charakteryzuje się tym, że sporządza się pierwszą mikroemulsję w/o zawierającą zawiesinę cząstek magnetycznych oraz surfaktant niejonowy, korzystnie eter p-1,1,3,3-tetrametylobutylofenylowo polietylenoglikolowym, monooleinian polioksyetylenosorbitanu (Polisorbat 80), monooleinian sorbitanu (Span 80), monostearynian sorbitanu, monolaurynianem sorbitanu (Tween 80) w stężeniu od 0,1M do 10M w stosunku do fazy olejowej korzystnie cykloheksanu i/lub izooktanu i/lub heptanu, i/lub oktanu i/lub ko-surfaktant, korzystnie izopropanol i/lub n-butanol i/lub heksanol o stężeniu od 0,1M do 10M w stosunku do fazy olejowej. Jako cząstki magnetyczne stosuje się dowolny ferryt spinelowy, korzystnie z grupy: MFe_2O_4 (M=Mn, Zn, Fe), $CoFe_{2-x}M_xO_4$ (M=Zn^{2+}, Mn^{2+}), γ-Fe_2O_3, dowolny ferryt heksagonalny, korzystnie $BaFe_{12}0_{19}$, $BaFe_{12}O_{19}$-$M_2Fe_4O_8$ (M=Mn, Fe, Zn), związki z grupy magnesów organicznych, pył żelazowy lub stopy metali i ich nanocząstki o właściwościach magnetycznych, takie jak: Fe-Pt, Co-Pt, Fe-Ni, Fe-Co, Ni-CeO_2, korzystnie Fe-Ni. Oddzielnie sporządza się drugą mikroemulsję w/o zawierającą surfaktant niejonowy korzystnie eter p-1,1,3,3-tetrametylobutylofenylowo polietylenoglikolowym, monooleinian polioksyetylenosorbitanu (Polisorbat 80), monooleinian sorbitanu (Span 80), monostearynian sorbitanu, monolaurynianem sorbitanu (Tween 80) w stężeniu od 0,1M do 10M w stosunku do fazy olejowej korzystnie cykloheksanu i/lub izooktanu lub i/heptanu i/lub oktanu i/lub ko-surfaktant, korzystnie izopropanol i/lub n-butanol i/lub heksanol o stężeniu od 0,1M do 10M w stosunku do fazy olejowej oraz w fazie wodnej substancję obniżającą pH z grupy kwasów organicznych i/lub nieorganicznych, korzystnie kwas cytrynowy i/lub kwas solny i/lub kwas askorbinowy o stężeniu od 0,01 do 10M, korzystnie 1M, o pH poniżej 7 korzystnie od 3 do 6, następnie do drugiej mikroemulsji dodaje się składnik warstwy inertnej w postaci substancji z grupy krzemionki, polimeru poli(N-izopropyloakryloamidu) glikolu polietylenowego lub węgla korzystnie w postaci grafitu lub grafenu lub prekursora składnika warstwy inertnej, takiego jak tetraetyloortokrzemian (TEOS) i/lub tetrametoksysilan (TMOS), w stosunku molowym składnika warstwy inertnej do cząstek magnetycznych wynoszącym od 0,01:1 do 20:1, korzystnie od 1:1 do 10:1, następnie miesza się razem pierwszą mikroemulsję z drugą mikroemulsją cały czas utrzymując pH poniżej 7, korzystnie w zakresie od 3 do 6, po czym dodaje się cząstki fotokatalityczne półprzewodników z grupy: tlenek tytanu (IV) TiO_2, tlenek wolframu (VI) WO_3, tlenek cynku ZnO, dwutlenek cyny SnO_2, siarczek kadmu CdS, korzystnie TiO_2 korzystnie w postaci prekursora półprzewodnika, korzystnie tetrabutylo tytanian i/lub tetraizopropylo tytanian i/lub siarczan tytanylu i/lub czterochlorek tytanu, w takiej ilości, aby stosunek molowy cząstek fotokatalitycznych do cząstek magnetycznych wynosił od 0,1:1 do 30:1, korzystnie w zakresie od 1:1 do 4:1, cały czas utrzymując pH poniżej 7 korzystnie od 3 do 6. Cząstki fotokatalityczne korzystnie modyfikuje się powierzchniowo nanocząstkami metali szlachetnych lub bimetali, korzystnie Pt-Cu, Pt-Pd, Pd-Cu, Au-Pt, Au-Pd, Ag-Pt, Ag-Cu w ilości od 0,01 do 10% molowych w stosunku do półprzewodnika, korzystnie od 0,01 do 1% molowych lub cząstki fotokatalityczne korzystnie domieszkuje się

niemetalem z grupy azot, siarka, bor, jod, węgiel w ilości od 0,01 do 30% wagowych w stosunku do półprzewodnika, korzystnie od 0,01 do 15% wagowych lub cząstki fotokatalityczne korzystnie domieszkuje się niemetalem z grupy azot, siarka, bor, jod, węgiel w ilości od 0,01 do 30% wagowych w stosunku do półprzewodnika, korzystnie od 0,01 do 15% wagowych i dodatkowo modyfikuje się powierzchniowo w znany sposób nanocząstkami metali, korzystnie platyny, miedzi, palladu, srebra, złota, rutenu w ilości od 0,01 do 10% molowych w stosunku do półprzewodnika, korzystnie od 0,01 do 1% molowych. Cząstki fotokalityczne korzystnie dodaje się w postaci mikroemulsji w/o (mikroemulsji trzeciej) zawierającej surfaktant niejonowy korzystnie eter p-1,1,3,3-tetrametylobutylofenylowo polietylenoglikolowym, monooleinian polioksyetylenosorbitanu (Polisorbat 80), monooleinian sorbitanu (Span 80), monostearynian sorbitanu, monolaurynianem sorbitanu (Tween 80) w stężeniu od 0,1M do 10M w stosunku do fazy olejowej korzystnie cykloheksanu i/lub izooktanu lub i/heptanu i/lub oktanu, i/lub ko-surfaktant, korzystnie izopropanol i/lub n-butanol i/lub heksanol o stężeniu od 0,1M do 10M w stosunku do fazy olejowej, w takiej ilości aby stosunek molowy półprzewodnika do cząstek magnetycznych wynosił od 0,1:1 do 30:1, korzystnie w zakresie od 1:1 do 4:1, o pH o wartości poniżej 7, korzystnie 3 do 6 do mikroemulsji powstałej ze zmieszania pierwszej mikroemulsji zawierającej cząstki magnetyczne i drugiej mikroemulsji zawierającej składnik warstwy inertnej i substancję obniżającą pH. Następnie po co najmniej 10 min mieszania lub uzyskaniu dodatniej wartości potencjału zeta, otrzymane cząstki separuje się za pomocą pola magnetycznego, przemywa się wodą, suszy się w temperaturze 60–90°C i kalcynuje się w temperaturze 250–1000°C przez 0,5–5 godzin.

Sposób według wynalazku charakteryzuje się tym, że otrzymany nanokompozyt może wykazywać aktywność w zakresie UV i Vis w wyniku domieszkowania struktury objętościowej półprzewodnika za pomocą związków niemetali, korzystnie z grupy: mocznik, i/lub tiomocznik, i/lub hydrazyna, i/lub amoniak, i/lub kwas jodowy, i/lub jodek potasu, i/lub fluorowodór i/lub jonów metali, korzystnie związków niklu, i/lub kobaltu, i/lub żelaza, i/lub cynku, i/lub rutenu, i/lub wolframu, i/lub miedzi, lub modyfikacji powierzchni za pomocą nanocząstek metali szlachetnych, korzystnie platyny, i/lub palladu, i/lub złota, i/lub srebra oraz nanocząstek metali grup przejściowych, korzystnie miedzi, i/lub rutenu, i/lub cyrkonu, i/lub rodu, i/lub wanadu. W tym celu do mieszaniny reakcyjnej przed dodaniem cząstek fotokatalizatora z grupy: TiO_2, WO_3, ZnO, SnO_2, CdS, i/lub prekursora półprzewodnika, korzystnie tetrabutylo tytanianu, i/lub tetraizopropylo tytanianu, i/lub siarczan tytanylu, i/lub czterochlorek tytanu wprowadza się prekursor nanocząstek metalu i/lub prekursor niemetali z grupy azot, siarka, bor, jod, węgiel w ilości od 0,01 do 30% wagowych w stosunku do TiO_2, korzystnie od 0,01 do 15% wagowych i/lub prekursor cząstek platyny, miedzi, palladu w ilości od 0,01 do 10% molowych w stosunku do TiO_2, korzystnie od 0,01 do 1% molowych, korzystnie otrzymując strukturę warstwy fotokatalitycznej I-TiO_2, N-TiO_2, S-TiO_2, I,C-TiO_2, B-TiO_2, Pt/I-TiO_2, Pt/N-TiO_2, Pd/-I-TiO_2, Pd/N-TiO_2, Cu/I-TiO_2, Cu/N-TiO_2, Pt-Cu-TiO_2, Pt-Pd-TiO_2, Pd-Cu-TiO_2, Au-Pt-TiO_2, Au-Pd-TiO_2, Ag-Pt-TiO_2, Ag-Cu-TiO_2.

Dzięki wykorzystaniu sposobu według wynalazku w stosunkowo prosty sposób otrzymuje się fotokatalizatory magnetyczne, prowadząc syntezę w jednym układzie, bez konieczności separacji poszczególnych jego komponentów w oparciu o adhezję w środowisku kwasowym cząstek warstwy inertnej i warstwy fotokatalizatora w roztworze wodnym lub roztworze wodnym surfaktantu niejonowego lub mikroemulsji w/o stabilizowanej surfaktantem niejonowym. Otrzymane według sposobu opisanego w wynalazku fotokatalizatory magnetyczne można odseparować z fazy wodnej po przyłożeniu gradientu pola magnetycznego. Pętle histerezy dla wybranych fotokatalizatorów magnetycznych wskazują, że nanokompozyty charakteryzują się wysokim momentem magnetycznym wynoszącym od 15 do 60 $emu \cdot g^{-1}$. Otrzymane fotokatalizatory magnetyczne wykazują wysoką efektywność degradacji związków organicznych np. fenolu, w tym również związków niepodatnych na rozkład biologiczny, obecnych w ściekach przemysłowych, odbiornikach wodnych takich jak: etodolak, karbamazepina, hydrochlorotiazyd. Charakterystykę właściwości magnetycznych i fotokatalitycznych wybranych nanokompozytów otrzymanych według sposobu wykonania omówionego w niniejszym wynalazku oraz szczegółowy opis wykonania przedstawiono w przykładach wykonania i na rysunku, na którym fig. 1 przedstawia zmianę potencjału elektrokinetycznego (zeta) w funkcji pH dla (a) cząstek magnetycznych Fe_3O_4, fotokatalizatora TiO_2 i cząstek SiO_2 oraz (b) dla cząstek $CoFe_2O_4$, fotokatalizatora TiO_2 i cząstek SiO_2, fig. 2 przedstawia wykresy histerezy magnetycznej dla fotokatalizatora magnetycznego (a) $TiO_2/SiO_2/CoFe_2O_4$ oraz (b) $TiO_2/SiO_2/BaFe_{12}O_{19}$, fig. 3 przedstawia separację cząstek fotokatalizatora po 1 min (a) oraz po czasie 5 minut (b) od przyłożenia magnesu neodymowego, fig. 4 przedstawia zdjęcia mikroskopowe TEM z mappingiem struktur rdzeń-otoczka nanokompozytu magnetycznego otrzymanego sposobem według wynalazku, fig. 5 przedstawia histerezy magnetyczne dla nanokompozytu Fe_3O_4/SiO_2, fig. 6 przedstawia

histerezę magnetyczną dla nanokompozytu I-TiO_2/Fe_3O_4/SiO_2, fig. 7 przedstawia histerezę magnetyczną dla nanokompozytu Pd/I-TiO_2/SiO_2/$BaFe_{12}O_9$.

Przykład 1

Sposób otrzymywania fotokatalizatora magnetycznego warstwowego
Pt-Cu/TiO_2/SiO_2/$CoFe_2O_4$ *w mikroemulsji w/o aktywnego w świetle widzialnym*

Do 200 cm^3 0,2M TX-100 (Triton X-100) w cykloheksanie wprowadza się roztwór wodny zawierający $FeSO_4 \cdot 7H_2O$ i $CoCl_2$ w stosunku molowym Fe^{2+} do Co^{2+} wynoszącym 2:1. Następnie dodaje się jako ko-surfaktant 0,5M heksanol, całość miesza się 30 min w atmosferze gazu obojętnego. Następnie do 100 cm^3 0,2M TX-100 w cykloheksanie wprowadza się roztwór wodny NaOH oraz 0,5M heksanol. Współczynnik R w obu mikroemulsjach, określający stosunek ilości wody do surfaktantu wynosi 20, natomiast stosunek molowy Fe^{2+}:Co^{2+}:OH^- wynosi 1:0,5:2. Do pierwszej mikroemulsji dodaje się drugą mikroemulsję i otrzymuje się koloid cząstek magnetycznych $CoFe_2O_4$. Moment magnetyczny otrzymanych cząstek wynosi 40 $emu \cdot g^{-1}$. Następnie sporządza się trzecią mikroemulsję, dodając do 0,2M TX-100 w cykloheksanie, 0,5M heksanol oraz roztwór wodny 3M kwasu cytrynowego tak, aby współczynnik R określający stosunek ilości wody do surfaktantu wynosił 20. Cały czas mieszając do mikroemulsji trzeciej wkrapla się 15,4 cm^3 tetraetyloortokrzemian (TEOS), a następnie ustala się wartość pH do wartości 5, dodając 0,3 cm^3 1M kwasu cytrynowego. Do otrzymanego układu mikroemulsji w/o zawierającego cząstki magnetyczne wprowadza się mikroemulsję trzecią i ustala wartość pH w granicach 5–5,5. Po 15 min. wartość potencjału zeta cząstek wynosiła -20 mV. Następnie do układu zawierającego cząstki magnetyczne pokryte warstwą inertną krzemionki dodawany jest prekursor tlenku tytanu(IV), tetrabutylo tytanian, przy wartości pH wynoszącej 5. Stosunek molowy półprzewodnika do cząstek magnetycznych ($CoFe_2O_4$) wynosi 1:1. W ten sposób otrzymuje się fotokatalizator magnetyczny aktywny w zakresie promieniowania UV. Wartość potencjału zeta po 15 min mieszania wynosiła +40 mV. W celu aktywacji fotokatalizatora w zakresie światła widzialnego, otrzymany nanokompozyt modyfikuje się powierzchniowo cząstkami bimetalicznymi Pt-Cu. Do mikroemulsji zawierającej fotokatalizator magnetyczny dodaje się 0,36 cm^3 0,05M roztworu kwasu heksachloroplatynowego tak, aby stosunek molowy Pt:TiO_2 wynosił 0,05% oraz 3,5 cm^3 0,025 M azotanu miedzi(III). Cały czas mieszając do układu wkrapla się borowodorek sodu w nadmiarze molowym w stosunku do jonów platyny i miedzi wynoszącym 1,5. Otrzymane cząstki fotokatalizatora separuje się za pomocą pola magnetycznego, przemywa się wodą, suszy się w temperaturze 80°C i kalcynuje się w temperaturze 400°C przez 2 godziny. Otrzymany według przedstawionego przykładu wykonania fotokatalizator Pt-Cu/TiO_2/SiO_2/$CoFe_2O_4$ (patrz Rysunek 3) posiada doskonałe właściwości magnetyczne, jak również charakteryzuje się wysoką aktywnością fotokatalityczną w zakresie promieniowania UV-Vis oraz Vis.

Efektywność fotokatalityczną zbadano w reakcji degradacji fenolu oraz karbamazepiny, analizując ubytek badanego związku w czasie oraz stopień mineralizacji zanieczyszczeń organicznych obecnych w fazie wodnej. Stwierdzono, że po 30 minutach naświetlania promieniowaniem z zakresu widzialnego (λ>420 nm) degradacji ulega 100% fenolu oraz w czasie 120 min 100% karbamazepiny, a stopień mineralizacji dla analizowanych związków wynosi odpowiednio 95% oraz 86%.

Przykład 2

Sposób otrzymywania fotokatalizatora magnetycznego warstwowego
I-TiO_2/SiO_2/Fe_3O_4 *w mikroemulsji* w/o *aktywnego w świetle widzialnym*

Do 200 cm^3 0,2M TX-100 w cykloheksanie wprowadza się roztwór wodny zawierający $FeSO_4 \cdot 7H_2O$ i $FeCl_3$ w stosunku molowym Fe^{3+} do Fe^{2+} wynoszącym 2:1. Następnie dodaje się 0,5M heksanol, całość miesza się 30 min w atmosferze gazu obojętnego. Następnie otrzymuje się drugą mikroemulsję dodając do 100 cm^3 0,2M TX-100 w cykloheksanie roztwór wody amoniakalnej oraz 0,5M heksanol. Współczynnik R określający stosunek ilości wody do surfaktantu wynosi 30, a stosunek molowy Fe^{3+}:Fe^{2+}:OH^- wynosi 2:1:8. Do pierwszej mikroemulsji dodaje się drugą mikroemulsję, zawierającą amoniak jako odczynnik strącający tak, aby wartość pH wynosiła 10. Następnie sporządza się mikroemulsję trzecią 0,2M TX-100 w cykloheksanie, zawierającą w fazie zdyspergowanej 0,2M roztwór wodny kwasu solnego. Współczynnik R określający stosunek ilości wody do surfaktantu w trzeciej mikroemulsji wynosi 30, następnie do mikroemulsji trzeciej wprowadza się tetraetyloortokrzemian. Stosunek molowy TEOS do Fe_3O_4 wynosi 8:1. Po 1 h mieszania do mikroemulsji zawierającej cząstki magnetyczne wprowadza się mikroemulsję trzecią, utrzymując wartość pH w granicach 5–6. Otrzymane cząstki Fe_3O_4/SiO_2 separuje się za pomocą pola magnetycznego, przemywa się wodą, suszy się w temperaturze 80°C i kalcynuje się w temperaturze 500°C przez 1 godzinę. Zdjęcia mikroskopowe TEM uzyskanego nanokompozytu o strukturze rdzeń-otoczka przedstawiono na Fig. 4.

Właściwości magnetyczne otrzymanego nanokompozytu przedstawiono na Fig. 5. Natężenie koercji bliskie jest zeru, co wskazuje na właściwości superparamagnetyczne otrzymanych cząstek Fe_3O_4/SiO_2. Otrzymany nanokompozyt może być zastosowany w diagnostyce medycznej.

W celu nadania właściwości fotokatalitycznych w świetle widzialnym do mikroemulsji 0,2M TX-100 w cykloheksanie zawierającej 0,5M heksanol oraz zawierającej cząstki magnetyczne (Fe_3O_4) pokryte inertną warstwą SiO_2 wprowadza się mikroemulsję czwartą zawierającą 0,2M Triton X-100 w cykloheksanie, 0,5M heksanol oraz roztwór kwasu jodowego zdyspergowany w fazie wodnej, kontrolując wartość pH w granicach 5–5,5 za pomocą kwasu solnego. Następnie do mikroemulsji czwartej wkrapla się prekursor TiO_2 (TBT) tak, aby stosunek molowy TiO_2 do HIO_3 wynosił 15:1. Następnie mikroemulsję czwartą dodaje się do mikroemulsji zawierającej cząstki magnetyczne pokryte inertną warstwą krzemionki, kontrolując wartość pH fazy wodnej w granicach 5–6, dodając ewentualnie 0,1M HCl. Stosunek molowy TiO_2 do Fe_3O_4 wynosi 2:1. Otrzymaną zawiesinę fotokatalizatora aktywnego w zakresie promieniowania widzialnego, separuje się w znany sposób, suszy się w temperaturze 60°C i kalcynuje w temperaturze 300°C przez 1 h.

Właściwości fotokatalityczne zbadano w reakcji degradacji fenolu oraz karbamazepiny – leku przeciwpadaczkowego, który jest sklasyfikowany w systemie związków farmaceutycznych, jako związek niepodatny na degradację biologiczną. Stwierdzono, że w wyniku naświetlania promieniowaniem z zakresu Vis (λ>420 nm) w czasie 1 h degradacji uległo odpowiednio 100% fenolu oraz 95% karbamazepiny. Jak pokazano na Fig. 5, magnetyczność nanokompozytu I-$TiO_2/SiO_2/Fe_3O_4$ była porównywalna do właściwości magnetycznych Fe_3O_4/SiO_2 i wyniosła 15 $emu \cdot g^{-1}$.

Przykład 3

Sposób otrzymywania fotokatalizatora magnetycznego warstwowego Cu/TiO_2/PEG-PNIPAm/Fe-Ni *w wodzie charakteryzującego się aktywnością w świetle widzialnym*

Cząstki magnetyczne Fe-Ni otrzymuje się w wyniku chemicznego strącania w roztworze wodnym soli metali zgodnie z reakcją przedstawioną w równaniu 1, poniżej:

$$2Fe^{2+} Ni^{2+} + 2H_2O + BH_4^- \rightarrow 2Fe\text{-}Ni\downarrow + BO_2^- + 4H^+ + 2H_2\uparrow$$

[1]

W ty celu do 100 cm^3 wody wprowadza się sole metali $FeCl_2$ i $NiCl_2$ w stosunku molowym określonym zgodnie ze stechiometrią reakcji, Fe^{2+} do Ni^{2+} wynoszącym 2:1. Całość miesza się w atmosferze gazu obojętnego, azotu. Następnie dodaje się 20 cm^3 1M borowodorku sodu tak, aby stosunek molowy Fe^{2+}:Ni^{2+}:BH_4^- wynosił 2:1:1. Następnie sporządza się mieszaninę drugą 0,01M kwasu solnego o pH 3,5, do której wprowadza się prekursor warstwy intertnej w postaci 2,5% roztworu wodnego poli(N-izopropyloakryloamidu) glikolu polietylenowego tak, aby zawartość polimeru w stosunku do cząstek Fe-Ni wynosiła 0,5%. Mieszaninę drugą dodaje się do zawiesiny cząstek Fe-Ni, tak aby wartość pH wynosiła 5 i otrzymuje zawiesinę zawierającą cząstki magnetyczne pokryte warstwą inertną polimeru. Następnie przygotowuje się zawiesinę trzecią, zawierającą fotokatalizator Cu-TiO_2. W tym celu do 20 cm^3 roztworu wodnego azotanu miedzi(III) dodaje się cząstki TiO_2 P25 tak, aby zawartość cząstek miedzi w stosunku do TiO_2 wynosiła 0,5% mol. Następnie redukuje się miedź na powierzchni TiO_2 za pomocą 0,1M roztworu borowodorku sodu w 1,5-krotnym nadmiarze molowym $NaBH_4$ do jonów Cu^{2+}. Do zawiesiny cząstek magnetycznych Fe-Ni pokrytych warstwą polimeru dodaje się zawiesinę trzecią zawierającą cząstki fotokatalizatora Cu-TiO_2, przy wartości pH wynoszącej 5–6. Stosunek molowy TiO_2 do Fe-Ni wynosi 0,5:1. Otrzymany fotokatalizator magnetyczny Cu/TiO_2/PEG-PNIPAm/Fe-Ni separuje się, przemywa się wodą i suszy się w temperaturze 70°C do suchej masy. Magnetyczność otrzymanego nanokompozytu wynosi 70 $emu \cdot g^{-1}$. Stwierdzono, że efektywność degradacji fenolu po 30 min naświetlania światłem widzialnym (λ>450 nm) wynosiła 100%, a stopień mineralizacji 95%.

Przykład 4

Sposób otrzymywania fotokatalizatora magnetycznego $TiO_2/SiO_2/Fe_3O_4$ *aktywnego w zakresie promieniowania UV*

Do 200 cm^3 0,2M TX-100 w cykloheksanie wprowadza się zdyspergowane w wodzie cząstki magnetytu (Fe_3O_4) o wielkości 50 nm. Do otrzymanej mikroemulsji dodaje się tetraetyloortokrzemian. Stosunek molowy TEOS do Fe_3O_4 wynosi 10:1. Następnie sporządza się mikroemulsję o takim samym składzie fazy ciągłej, zawierającej w fazie zdyspergowanej 0,2M roztwór wodny kwasu askorbinowego. Drugą mikroemulsję dodaje się do pierwszej, korygując pH fazy wodnej do wartości 6. Współczynnik R określający stosunek molowy wody do surfaktantu dla obydwu mikroemulsji wynosi 30. Po 1 h mieszania do mikroemulsji zawierającej cząstki magnetyczne pokryte warstwą krzemionki wprowadza tlenek tytanu(IV) P25 firmy Evonik, przy wartości pH wynoszącej 5, korygowanej za pomocą kwasu solnego.

Stosunek molowy półprzewodnika do cząstek magnetycznych wynosi 2:1. W ten sposób otrzymuje się fotokatalizator magnetyczny aktywny w zakresie promieniowania UV o strukturze wielowarstwowej, przedstawiony na zdjęciu wykonanym za pomocą wysokorozdzielczego mikroskopu transmisyjnego, patrz fig. 7.

Magnetyczność otrzymanego nanokompozytu wynosi 10 emu·g^{-1}. Stwierdzono, że efektywność degradacji fenolu po 30 min naświetlania światłem UV-Vis wynosiła 100%, stopień mineralizacji (TOC/TOC$_o$) wynosi 86%, a efektywność mineralizacji karbamazepiny 85% w czasie 120 min naświetlania promieniowanie w zakresie UV-Vis (natężenie promieniowania 30 mW·cm^{-2}).

Przykład 5

Sposób otrzymywania fotokatalizatora magnetycznego $ZnO/SiO_2/Fe_2O_3$ *w mikroemulsji w/o, charakteryzującego się aktywnością w zakresie promieniowania UV*

Do 200 cm^3 0,05M surfaktantu niejonowego Span 80 w heptanie wprowadza się zdyspergowane w wodzie cząstki hematytu (Fe_2O_3) o wielkości 45 nm. Następnie sporządza się 50 cm^3 mikroemulsji 0,05M Span 80 w heptanie, zawierającą w fazie wodnej 0,5M kwas askorbinowy, do której wprowadza się tetraetyloortokrzemian, pH mikroemulsji powinno wynosić 3. Współczynnik R określający stosunek molowy wody do surfaktantu dla obydwu mikroemulsji wynosi 20. Stosunek molowy TEOS do Fe_2O_3 wynosi 10:1. Do otrzymanego układu koloidalnego zawierającego cząstki magnetyczne wprowadza się mikroemulsję drugą zawierającą cząstki SiO_2 i koryguje ewentualnie wartość pH za pomocą 0,1M HCl do wartości 4. Po 1 h mieszania do otrzymanego układu koloidalnego zawierającego cząstki magnetyczne pokryte warstwą inertną krzemionki dodawany jest półprzewodnik, tlenek cynku(II), korygując jeśli to konieczne pH do wartości 4, za pomocą octanu amonu. Stosunek molowy półprzewodnika do związku magnetycznego wynosi 1,75:1. Następnie otrzymane cząstki separuje się za pomocą pola magnetycznego, przemywa się wodą, suszy się w temperaturze 80°C do suchej masy. W ten sposób otrzymuje się fotokatalizator magnetyczny $ZnO/SiO_2/Fe_2O_3$ aktywny w zakresie promieniowania UV. Właściwości fotokatalityczne zbadano w reakcji degradacji fenolu. Stwierdzono, że w wyniku naświetlania promieniowaniem z zakresu UV (λ<400 nm) w czasie 120 min naświetlania degradacji uległo 80% fenolu, a magnetyczność nanokompozytu $ZnO/SiO_2/Fe_2O_3$ wynosi 7 emu·g^{-1}.

Przykład 6

Sposób otrzymywania fotokatalizatora magnetycznego $TiO_2/SiO_2/Fe_3O_4$ *aktywnego w zakresie promieniowania UV*

Do 0,18M Tween 80 w wodzie dodaje się 20 g $Fe(NO_3)_3 \cdot 9H_2O$ oraz 10 g $FeSO_4 \cdot 7H_2O$, całość miesza się w atmosferze gazu obojętnego, azotu. Dodaje się wodę amoniakalną w 0,18M Tween 80 do wartości pH wynoszącej 10. Oddzielnie sporządza się mieszaninę drugą zawierającą roztwór alkoholu etylowego oraz TEOS i do mieszaniny drugiej dodaje się 0,18M Tween 80 w wodzie i 0,1M kwas azotowy tak, aby wartość pH mieszaniny drugiej wynosiła 3. Stosunek molowy TEOS do Fe_3O_4 wynosi 4:1. Otrzymany koloid SiO_2 w mieszaninie drugiej dodaje się do zawiesiny cząstek magnetycznych w wodzie, ustalając wartość pH 4. Następnie dodaje się 1 g TiO_2 P25, otrzymując fotokatalizator magnetyczny $TiO_2/SiO_2/Fe_3O_4$. Właściwości fotokatalityczne zbadano w reakcji degradacji fenolu. Stwierdzono, że w wyniku naświetlania promieniowaniem z zakresu UV 0,2 mM roztworu wodnego fenolu zawierającego 1 g fotokatalizatora, w czasie 30 min degradacji uległo 100% fenolu. Magnetyczność nanokompozytu $TiO_2/SiO_2/Fe_3O_4$ wynosiła 49 emu·g^{-1}.

Przykład 7

Sposób otrzymywania fotokatalizatora magnetycznego $Pt\text{-}TiO_2/SiO_2/Fe_3O_4$ *aktywnego w zakresie promieniowania UV i Vis*

Do 0,18M Tween 80 w wodzie dodaje się 3 g cząstek Fe-Ni o wielkości 10 nm. Oddzielnie sporządza się 50 cm^3 0,18M Tween 80 zawierającego 0,05M kwas solny, do którego dodaje się 16 cm^3 TMOS. Mieszaninę drugą dodaje się do zawiesiny cząstek Fe-Ni, tak aby wartość pH wynosiła 5–6 i otrzymuje zawiesinę zawierającą cząstki magnetyczne pokryte warstwą krzemionki. Następnie przygotowuje się zawiesinę trzecią, zawierającą 0,18M Tween 80 w wodzie, zawierającej K_2PtCl_4, do którego dodaje się 1 g TiO_2 ST-01 (Ishikara) tak, aby zawartość cząstek platyny w stosunku do TiO_2 wynosiła 0,05% mol. Platynę redukuje się na powierzchni TiO_2 za pomocą 0,1M roztworu borowodorku sodu w 1,5-krotnym nadmiarze molowym $NaBH_4$ do jonów Pt^{2+}. Do zawiesiny cząstek magnetycznych Fe-Ni pokrytych warstwą krzemionki dodaje się zawiesinę trzecią zawierającą cząstki fotokatalizatora $Pt\text{-}TiO_2$, przy wartości pH wynoszącej 5–6. Otrzymany fotokatalizator magnetyczny $Pt/TiO_2/SiO_2/Fe\text{-}Ni$ separuje się, przemywa się wodą i suszy się w temperaturze 70°C do suchej masy. Magnetyczność

otrzymanego nanokompozytu wynosi 46 emu·g^{-1}. Stwierdzono, że efektywność degradacji fenolu po 30 min naświetlania światłem widzialnym (λ>450 nm) wynosiła 100%.

Przykład 8

Sposób otrzymywania fotokatalizatora magnetycznego warstwowego Pt/I-TiO_2/SiO_2/$BaFe_{12}O_{19}$ aktywnego w świetle widzialnym

Do 100 cm^3 wody wprowadza się cząstki magnetyczne $BaFe_{12}O_{19}$ o wielkości 12 nm, zawiesinę poddaje się działaniu ultradźwięków przez 10 min. Oddzielnie sporządza się roztwór 0,1M kwasu askorbinowego o pH 3,5, do którego wprowadza się prekursor warstwy intertnej tetraetyloortokrzemian (TEOS) tak, aby zawartość TEOS w stosunku do cząstek $BaFe_{12}O_{19}$ wynosiła 4:1. Mieszaninę drugą dodaje się do zawiesiny cząstek magnetycznych, tak aby wartość pH wynosiła 4,5. Następnie przygotowuje się zawiesinę trzecią, wprowadzając do 10 cm^3 tetraizopropylotytanianu zdyspergowanego w alkoholu etylowym 6 cm^3 6 mM roztworu wodnego kwasu jodowego. Następnie po 30 min mieszania dodaje się 0,5 cm^3 K_2PtCl_4 tak, aby zawartość platyny do TiO_2 wynosiła 0,05% molowych oraz po 30 min mieszania dodaje się 0,5 cm^3 borowodorku sodu w nadmiarze molowym w stosunku do jonów platyny wynoszącym 1,5. Do zawiesiny cząstek magnetycznych $BaFe_{12}O_{19}$ pokrytych warstwą krzemionki dodaje się zawiesinę trzecią zawierającą cząstki fotokatalizatora Pt/I-TiO_2, korygując wartość pH w zakresie pomiędzy 4–5. Otrzymany fotokatalizator magnetyczny Pt/I-TiO_2/SiO_2/$BaFe_{12}O_{19}$ separuje się, przemywa się wodą i suszy się w temperaturze 70°C do suchej masy i kalcynuje w temperaturze 300°C przez 1 h. Magnetyczność otrzymanego nanokompozytu wynosi 65 emu·g^{-1}. Stwierdzono, że efektywność degradacji fenolu po 30 min. naświetlania światłem widzialnym (λ>420 nm) wynosiła 100%, a stopień mineralizacji 98%.

Przykład 9

Sposób otrzymywania fotokatalizatora magnetycznego warstwowego Pt/TiO_2/grafen/$BaFe_{12}O_{19}$ aktywnego w UV-Vis

Do 100 cm^3 wody wprowadza się cząstki magnetyczne $BaFe_{12}O_{19}$ o wielkości 12 nm, zawiesinę poddaje się działaniu ultradźwięków przez 10 min. Oddzielnie sporządza się zawiesinę drugą zawierającą roztwór 0,2M kwasu askorbinowego o pH 3,5, do którego wprowadza się cząstki grafenu lub węgla w ilości 3% wag. a stosunek molowy grafenu lub węgla do cząstek $BaFe_{12}O_{19}$ wynosił 0,1:1. Zawiesinę drugą dodaje się do zawiesiny cząstek magnetycznych, tak aby wartość pH wynosiła 6. Następnie przygotowuje się zawiesinę trzecią, wprowadzając do 10 cm^3 tetraizopropylotytanianu zdyspergowanego w alkoholu etylowym 6 cm^3 6 mM roztworu wodnego kwasu jodowego. Do zawiesiny cząstek magnetycznych $BaFe_{12}O_{19}$ pokrytych warstwą krzemionki dodaje się zawiesinę trzecią zawierającą cząstki fotokatalizatora I-TiO_2, korygując wartość pH w zakresie pomiędzy 5–6 za pomocą 0,2M kwasu askorbinowego. Wartość potencjału zeta cząstek I-TiO_2/grafen/$BaFe_{12}O_{19}$ wynosi +32 mV. Następnie po 30 min mieszania dodaje się 0,5 cm^3 K_2PtCl_4 tak, aby zawartość platyny do TiO_2 wynosiła 0,05% molowych oraz po 30 min mieszania dodaje się 0,5 cm^3 borowodorku sodu w nadmiarze molowym w stosunku do jonów platyny wynoszącym 1,5. Otrzymany fotokatalizator magnetyczny Pt/I-TiO_2/-/SiO_2/$BaFe_{12}O_{19}$ separuje się, przemywa się wodą i suszy się w temperaturze 70°C do suchej masy i kalcynuje w temperaturze 300°C przez 1 h. Magnetyczność otrzymanego nanokompozytu wynosi 65 emu·g^{-1}. Stwierdzono, że efektywność degradacji fenolu po 30 min naświetlania światłem widzialnym (λ>420 nm) wynosiła 100%, a stopień mineralizacji 98%.

Zastrzeżenia patentowe

1. Sposób otrzymywania warstwowego fotokatalizatora magnetycznego polegający na utworzeniu inertnej warstwy wokół cząstki magnetycznej, którą następnie pokrywa się cząstkami fotokatalitycznymi, **znamienny tym**, że sporządza się zawiesinę cząstek magnetycznych w wodzie, którą miesza się korzystnie w atmosferze gazu obojętnego lub tlenku węgla(IV) oraz sporządza się drugą mieszaninę w ten sposób, że sporządza się alkoholowy i/lub wodny roztwór substancji obniżającej pH z grupy: kwasów karboksylowych i/lub kwasów nieorganicznych, korzystnie kwas solny i/lub kwas octowy i/lub kwas cytrynowy i/lub kwas askorbinowy, o pH w zakresie od 1 do 7, korzystnie od 3 do 6, do którego dodaje się składnik warstwy inertnej w postaci polimeru poli(N-izopropyloakryloamidu) glikolu polietylenowego i/lub polidimetylosiloksanu i/lub krzemionki lub węgla korzystnie w postaci grafitu lub grafenu lub prekursora składnika warstwy inertnej, takiego jak tetraetyloortokrzemian (TEOS) i/lub tetrameto-

ksysilan (TMOS), w stosunku molowym składnika warstwy inertnej do cząstek magnetycznych wynoszącym w zakresie od 0,01:1 do 20:1, korzystnie od 0,5:1 do 10:1, następnie do zawiesiny zawierającej cząstki magnetyczne wkrapla się drugą mieszaninę i ustala się pH poniżej 7, korzystnie w zakresie od 3 do 6, całość miesza się, a następnie dodaje się cząstki fotokatalityczne półprzewodników z grupy: tlenek tytanu(IV) TiO_2, tlenek wolframu(VI) WO_3, tlenek cynku ZnO, dwutlenek cyny SnO_2, siarczek kadmu CdS, korzystnie TiO_2, korzystnie w postaci prekursora półprzewodnika cząstek fotokatalitycznych, korzystnie tetrabutylo tytanian i/lub tetraizopropylo tytanian i/lub siarczan tytanylu i/lub czterochlorek tytanu, w takiej ilości, aby stosunek molowy cząstek fotokatalitycznych do cząstek magnetycznych wynosił od 0,1:1 do 30:1, korzystnie w zakresie od 0,5:1 do 4:1, po czym po co najmniej 10 min mieszania lub uzyskaniu dodatniej wartości potencjału zeta, otrzymane cząstki separuje się za pomocą pola magnetycznego, przemywa się wodą, suszy się w temperaturze 60–90°C i kalcynuje się w temperaturze 250–1000°C przez 0,5–5 godzin.

2. Sposób według zastrz. 1, **znamienny tym**, że jako cząstki magnetyczne stosuje się dowolny ferryt spinelowy, korzystnie z grupy: MFe_2O_4 (M=Mn, Zn, Fe), $CoFe_{2-x}M_xO_4$ (M=Zn^{2+}, Mn^{2+}), γ-Fe_2O_3, dowolny ferryt heksagonalny, korzystnie $BaFe_{12}O_{19}$, $BaFe_{12}O_{19}$-$M_2Fe_4O_8$ (M=Mn, Fe, Zn), związki z grupy magnesów organicznych, pył żelazowy lub stopy metali i ich nanocząstki o właściwościach magnetycznych, takie jak: Fe-Pt, Co-Pt, Fe-Ni, Fe-Co, Ni-CeO_2, korzystnie Fe-Ni.
3. Sposób według zastrz. 1, **znamienny tym**, że jako cząstki fotokatalityczne stosuje się cząstki fotokatalityczne zmodyfikowane powierzchniowo nanocząstkami metali szlachetnych lub bimetali, korzystnie Pt-Cu, Pt-Pd, Pd-Cu, Au-Pt, Au-Pd, Ag-Pt, Ag-Cu w ilości od 0,01 do 10% molowych w stosunku do półprzewodnika, korzystnie od 0,01 do 1% molowych.
4. Sposób według zastrz. 1, **znamienny tym**, że cząstki fotokatalityczne domieszkuje się niemetalem z grupy azot, siarka, bor, jod, węgiel w ilości od 0,01 do 30% wagowych w stosunku do półprzewodnika, korzystnie od 0,01 do 15% wagowych.
5. Sposób według zastrz. 4, **znamienny tym**, że cząstki fotokatalityczne dodatkowo modyfikuje się powierzchniowo w znany sposób nanocząstkami metali korzystnie platyny, miedzi, palladu w ilości od 0,01 do 10% molowych w stosunku do półprzewodnika, korzystnie od 0,01 do 1% molowych.
6. Sposób według zastrz. 1, **znamienny tym**, że zawiesinę cząstek magnetycznych sporządza się w roztworze wodnym surfaktantu niejonowego, korzystnie eteru p-1,1,3,3-tetrametylobutylofenylowo polietylenoglikolowy (TX-100), monostearynianu sorbitanu, monolaurynianu sorbitanu (Tween 80) w stężeniu od 0,01M do 3M, jak również do drugiej mieszaniny dodaje się roztwór wodny surfaktantu niejonowego, korzystnie eteru p-1,1,3,3-tetrametylobutylofenylowo polietylenoglikolowy (TX-100), monostearynianu sorbitanu, monolaurynianu sorbitanu (Tween 80) w stężeniu od 0,01M do 3M.
7. Sposób otrzymywania warstwowego fotokatalizatora magnetycznego polegający na utworzeniu inertnej warstwy wokół cząstki magnetycznej, którą następnie pokrywa się cząstkami fotokatalitycznymi, **znamienny tym**, że sporządza się pierwszą mikroemulsję w/o zawierającą zawiesinę cząstek magnetycznych oraz surfaktant niejonowy, korzystnie eter p-1,1,3,3-tetrametylobutylofenylowo polietylenoglikolowym, monooleinian polioksyetylenosorbitanu (Polisorbat 80), monooleinian sorbitanu (Span 80), monostearynian sorbitanu, monolaurynianem sorbitanu (Tween 80) w stężeniu od 0,1M do 10M w stosunku do fazy olejowej korzystnie cykloheksanu i/lub izooktanu i/lub heptanu, i/lub oktanu, sporządza się drugą mikroemulsję w/o zawierającą surfaktant niejonowy korzystnie eter p-1,1,3,3-tetrametylobutylofenylowo polietylenoglikolowym, monooleinian polioksyetylenosorbitanu (Polisorbat 80), monooleinian sorbitanu (Span 80), monostearynian sorbitanu, monolaurynianem sorbitanu (Tween 80) w stężeniu od 0,1M do 10M w stosunku do fazy olejowej korzystnie cykloheksanu i/lub izooktanu lub i/heptanu i/lub oktanu oraz w fazie wodnej substancję obniżającą pH z grupy kwasów organicznych i/lub nieorganicznych, korzystnie kwas cytrynowy i/lub kwas solny i/lub kwas askorbinowy o stężeniu od 0,01 do 10M, korzystnie 1M, o pH poniżej 7 korzystnie od 3 do 6, następnie do drugiej mikroemulsji dodaje się składnik warstwy inertnej w postaci substancji z grupy krzemionki, polimeru poli(N-izopropyloakryloamidu) glikolu polietylenowego lub węgla korzystnie w postaci grafitu lub grafenu lub prekursora składnika warstwy inertnej, takiego jak

tetraetyloortokrzemian (TEOS) i/lub tetrametoksysilan (TMOS), w stosunku molowym składnika warstwy inertnej do cząstek magnetycznych wynoszącym od 0,01:1 do 20:1, korzystnie od 1:1 do 10:1, następnie miesza się razem pierwszą mikroemulsję z drugą mikroemulsją cały czas utrzymując pH poniżej 7 korzystnie w zakresie od 3 do 6, po czym dodaje się cząstki fotokatalityczne półprzewodników z grupy: tlenek tytanu(IV) TiO_2, tlenek wolframu(VI) WO_3, tlenek cynku ZnO, dwutlenek cyny SnO_2, siarczek kadmu CdS, korzystnie TiO_2 korzystnie w postaci prekursora półprzewodnika, korzystnie tetrabutylo tytanian i/lub tetraizopropylo tytanian i/lub siarczan tytanylu i/lub czterochlorek tytanu, w takiej ilości, aby stosunek molowy cząstek fotokatalitycznych do cząstek magnetycznych wynosił od 0,1:1 do 30:1, korzystnie w zakresie od 1:1 do 4:1, cały czas utrzymując pH poniżej 7 korzystnie od 3 do 6, po czym po co najmniej 10 min mieszania lub uzyskaniu dodatniej wartości potencjału zeta, otrzymane cząstki separuje się za pomocą pola magnetycznego, przemywa się wodą, suszy się w temperaturze 60–90°C i kalcynuje się w temperaturze 250–1000°C przez 0,5–5 godzin.

8. Sposób według zastrz. 7, **znamienny tym**, że cząstki fotokalityczne dodaje się w postaci mikroemulsji w/o zawierającej surfaktant niejonowy korzystnie eter p-1,1,3,3-tetrametylobutylofenylowo polietylenoglikolowym, monooleinian polioksyetylenosorbitanu (Polisorbat 80), monooleinian sorbitanu (Span 80), monostearynian sorbitanu, monolaurynianem sorbitanu (Tween 80) w stężeniu od 0,1M do 10M w stosunku do fazy olejowej korzystnie cykloheksanu lub izooktanu lub heptanu lub oktanu, w takiej ilości aby stosunek molowy półprzewodnika do cząstek magnetycznych wynosił od 0,1:1 do 30:1, korzystnie w zakresie od 1:1 do 4:1, o pH o wartości poniżej 7 korzystnie 3 do 6.
9. Sposób według zastrz. 7 albo 8, **znamienny tym**, że do pierwszej mikroemulsji i/lub do drugiej mikroemulsji dodaje się ko-surfaktant, korzystnie izopropanol i/lub n-butanol i/lub heksanol o stężeniu od 0,1M do 10M w stosunku do fazy olejowej.
10. Sposób według zastrz. 7 albo 8, **znamienny tym**, że jako cząstki magnetyczne stosuje się dowolny ferryt spinelowy, korzystnie z grupy: MFe_2O_4 (M=Mn, Zn, Fe), $CoFe_{2-x}M_xO_4$ (M=Zn^{2+}, Mn^{2+}), γ-Fe_2O_3, dowolny ferryt heksagonalny, korzystnie $BaFe_{12}O_{19}$, $BaFe_{12}O_{19}$-$M_2Fe_4O_8$ (M=Mn, Fe, Zn), związki z grupy magnesów organicznych, pył żelazowy lub stopy metali i ich nanocząstki o właściwościach magnetycznych, takie jak: Fe-Pt, Co-Pt, Fe-Ni, Fe-Co, Ni-CeO_2, korzystnie Fe-Ni.
11. Sposób według zastrz. 7 albo 8, **znamienny tym**, że jako cząstki fotokatalityczne stosuje się cząstki fotokatalityczne zmodyfikowane powierzchniowo nanocząstkami metali szlachetnych lub bimetali, korzystnie Pt-Cu, Pt-Pd, Pd-Cu, Au-Pt, Au-Pd, Ag-Pt, Ag-Cu w ilości od 0,01 do 10% molowych w stosunku do półprzewodnika, korzystnie od 0,01 do 1% molowych.
12. Sposób według zastrz. 7 albo 8, **znamienny tym**, że cząstki fotokatalityczne domieszkuje się niemetalem z grupy azot, siarka, bor, jod, węgiel w ilości od 0,01 do 30% wagowych w stosunku do półprzewodnika, korzystnie od 0,01 do 15% wagowych.
13. Sposób według zastrz. 12, **znamienny tym**, że cząstki fotokatalityczne dodatkowo modyfikuje się powierzchniowo w znany sposób nanocząstkami metali korzystnie platyny, miedzi, palladu w ilości od 0,01 do 10% molowych w stosunku do półprzewodnika, korzystnie od 0,01 do 1% molowych.

Rysunki

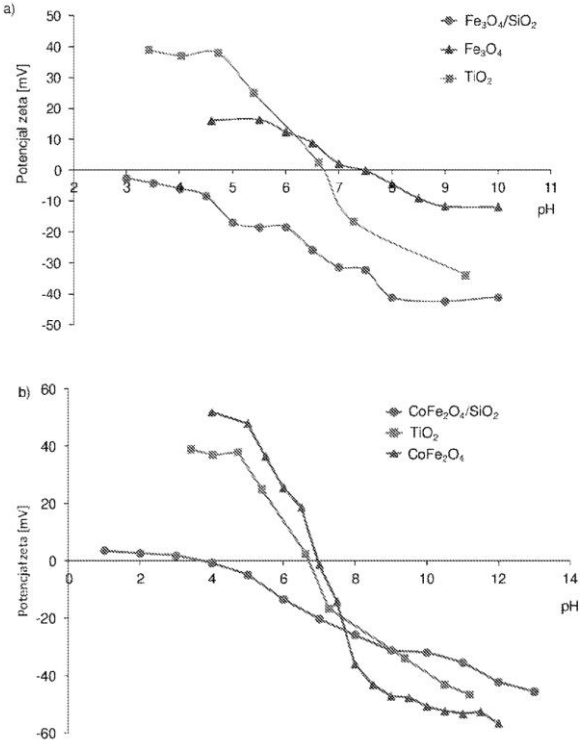

Fig. 1

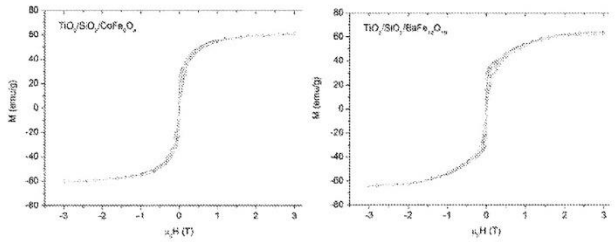

Fig. 2

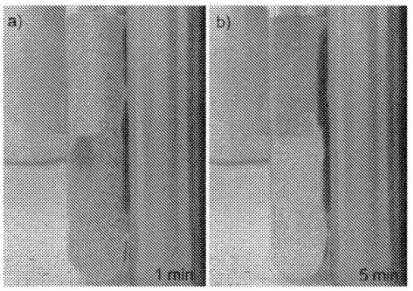

Fig. 3

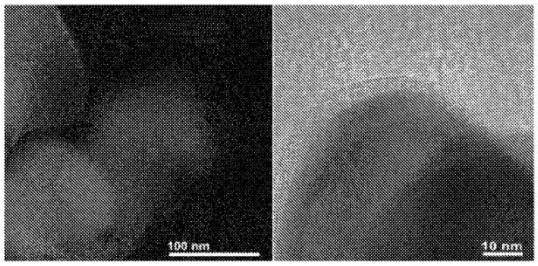

Fig. 4

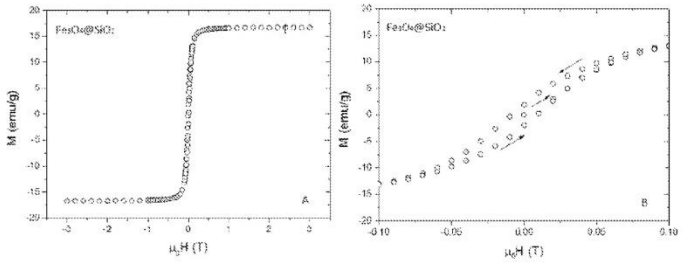

Fig. 5

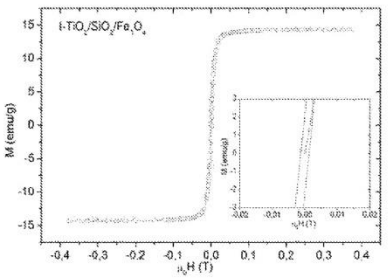

Fig. 6

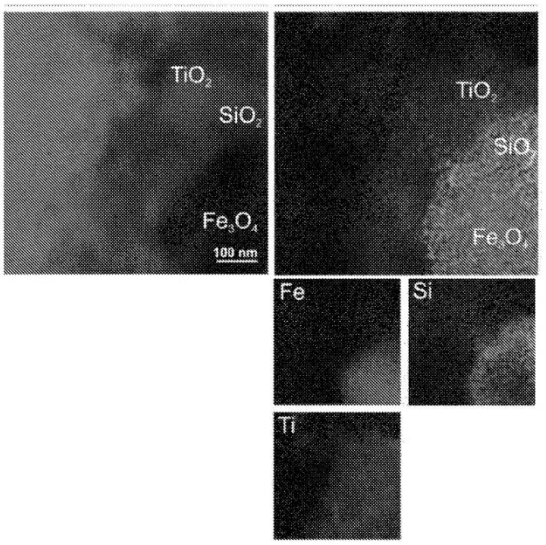

Fig. 7

Departament Wydawnictw UPRP
Cena 4,92 zł (w tym 23% VAT)

RZECZPOSPOLITA POLSKA

Urząd Patentowy Rzeczypospolitej Polskiej

(12) **OPIS PATENTOWY** (19) **PL** (11) **233344** (13) **B1**

(21) Numer zgłoszenia: **423294**

(22) Data zgłoszenia: **28.10.2017**

(51) Int.Cl.
B01J 37/03 (2006.01)
B01J 35/02 (2006.01)
B01J 21/06 (2006.01)
B01J 23/00 (2006.01)

(54) **Sposób otrzymywania warstwowego fotokatalizatora magnetycznego**

(43) Zgłoszenie ogłoszono:
06.05.2019 BUP 10/19

(45) O udzieleniu patentu ogłoszono:
30.09.2019 WUP 09/19

(73) Uprawniony z patentu:
POLITECHNIKA GDAŃSKA, Gdańsk, PL

(72) Twórca(y) wynalazku:
ANNA ZIELIŃSKA-JUREK, Otomin, PL
ZUZANNA BIELAN, Tczew, PL

(74) Pełnomocnik:
rzecz. pat. Małgorzata Kluczyk

PL 233344 B1

Opis wynalazku

Przedmiotem wynalazku jest sposób otrzymywania warstwowych fotokatalizatorów magnetycznych o strukturze wielowarstwowej, aktywnych w zakresie promieniowania UV i Vis, mających zastosowanie zwłaszcza w reakcji fotokatalitycznej degradacji wybranych związków organicznych i nieorganicznych.

Z opisu zgłoszenia patentowego CN1200959A znany jest sposób otrzymywania fotokatalizatorów magnetycznych, zgodnie z którym do roztworu prekursorów cząstek magnetycznych wprowadza się prekursor lub cząstki półprzewodnika takiego jak: TiO_2, SnO_2, ZnO, CdS, WO_3 i przeprowadza współstrącanie w pH wynoszącym w zakresie od 9 do 12. Materiał o właściwościach magnetycznych, korzystnie występuje w postaci cząstek Fe_3O_4, γ-Fe_2O_3, CrO_2, Co-γ-Fe_2O_3, $BaFe_{12}O_{19}$. Zgodnie z innym sposobem według wynalazku fotokatalizator magnetyczny otrzymuje się w wyniku ucierania wcześniej osobno otrzymanych cząstek magnetycznych i fotokatalizatora, a następnie ich kalcynacji w temperaturze 500–900°C.

Z opisu zgłoszenia patentowego US20140131288A1 znany jest sposób otrzymywania fotokatalizatorów aktywnych w świetle widzialnym, ultrafioletowym lub podczerwonym o właściwościach superparamagnetycznych. Cząstki magnetyczne o wielkości w zakresie od 0.01 μm do 100 μm otrzymywano metodą starzenia oksydacyjnego soli żelaza w pH zasadowym, korygowanym za pomocą roztworów KOH oraz KNO_3, prowadząc reakcję w temperaturze 90°C. Następnie otrzymane cząstki magnetyczne dyspergowano w alkoholu etylowym z wodą amoniakalną i wprowadzano tetraetylokrzemian (TEOS). Do wytworzonych cząstek magnetycznych pokrytych inertną warstwą SiO_2 wprowadzano prekursor TiO_2, tetraizopropylo tytanian w alkoholu etylowym i podgrzewano do 85°C przez 90 min. Otrzymane cząstki separowano, suszono i kalcynowano w temperaturze 500°C przez 2 h. Zgodnie z innym sposobem według wynalazku fotokatalizator o właściwościach superparamagnetycznych otrzymano w wyniku wieloetapowej reakcji hydrotermalnej. Najpierw jony $FeCl_3$ dyspergowano w roztworze wodnym z dodatkiem cytrynianu sodu, mocznika oraz poliakrylamidu i poddawano reakcji hydrotermalnej w temperaturze 200°C przez 16 h. Otrzymane cząstki o właściwościach superparamagnetycznych odseparowano, suszono, a następnie ponownie dyspergowano w roztworze alkoholu etylowego z dodatkiem wody amoniakalnej, do której wprowadzono tetraetylokrzemian. Reakcję prowadzono przez 18 h, a następnie powstałe cząstki impregnowane SiO_2 odseparowano, suszono i dyspergowano w roztworze wodnym alkoholu etylowego z dodatkiem hydroksypropylocelulozy, dodawano prekursor TiO_2, tetrabutylo tytanian (TBOT) i ogrzewano w temperaturze 85°C przez 90 min. Cząstki odseparowano i ponownie zdyspergowano w wodzie dejonizowanej, poddając reakcji hydrotermalnej w 180°C przez 90 min. W ostatnim etapie fotokatalizator suszono i kalcynowano w 500°C przez 3 h. Warstwa fotokatalityczna według wynalazku może być domieszkowana węglem lub modyfikowana metalami z grupy Au, Ag, Fe, Ni, Cu, Pt oraz Pd w celu uzyskania aktywności w zakresie widzialnym.

Znane są sposoby otrzymywania fotokatalizatorów magnetycznych o strukturze rdzeń-otoczka. Według tych sposobów można otrzymywać cząstki o wielkości rzędu od kilku nm do kilkudziesięciu μm. Jednak często magnetyczność otrzymanych nanokompozytów jest niewielka (poniżej 5 $emu \cdot g^{-1}$), co nie pozwala na efektywną separację w krótkim czasie fotokatalizatora z fazy wodnej. Ponadto prowadzenie preparatyki cząstek fotokatalizatora magnetycznego w pH zasadowym, dla którego cząstki magnetyczne, inertnej warstwy (np. krzemionki) oraz warstwy fotokatalitycznej (np. TiO_2) charakteryzują się zwiększonym powierzchniowym ładunkiem ujemnym, jak pokazano na fig. 1, powoduje, że cząstki jednoimiennie naładowane odpychają się nie tworząc pożądanej struktury rdzeń – otoczka lub wielowarstwowej. Natomiast domieszkowanie struktury objętościowej za pomocą cząstek o właściwościach magnetycznych (jony żelaza, kobaltu, niklu) może prowadzić do ługowania kationów metalu do roztworu lub zatrucia powierzchni fotokatalizatora w kolejnych cyklach oczyszczania strumienia fazy wodnej lub gazowej, dlatego ważne jest zastosowanie warstwy inertnej pomiędzy rdzeniem magnetycznym, a warstwą fotokatalityczną.

Sposób wytwarzania fotokatalizatora magnetycznego charakteryzuje się według wynalazku tym, że preparatyka cząstek magnetycznych, wytwarzanie warstwy inertnej oraz warstwy fotokatalizatora zachodzi w jednym układzie, bez konieczności separacji poszczególnych jego komponentów. Sposób otrzymywania fotokatalizatorów magnetycznych korzystnie prowadzi się w układzie mikroemulsji w/o, jednak można również stosować w tym celu roztwory wodne, roztwory wodne alkoholi i/lub roztwory wodne surfaktantów kationowych lub kationowych związków o charakterze polimerów w środowisku zasadowym.

W przedstawionym sposobie otrzymywania warstwowych fotokatalizatorów magnetycznych o strukturze wielowarstwowej do wody i/lub alkoholu wprowadza się surfaktant kationowy, korzystnie bromek heksadecetylo-trimetyloamoniowy (CTAB) i/lub chlorek heksadecylo-trimetyloamoniowy (CTAC), bromek tetradecylotrimetyloamoniowy (TTAB), chlorek dodecylotrimetyloamoniowy (DTAC), bromek heksadecylopirydyniowy (CPB) tak, aby jego stężenie wynosiło od 0,01M do 10M, korzystnie od 0,02 do 0,2M i/lub kopolimer kationowy, korzystnie polidimetyloaminoepichlorohydrynę w ilości od 0,01 do 30% wag., polichlorek diallilodimetyloamoniowy (PDDAC) w ilości od 0,1 do 20% wag., korzystnie 5% wag. i/lub polietylenoiminę (PEI) w ilości od 0,01 do 20% wag., korzystnie od 1 do 5% wag. Do mieszaniny dodaje się cząstki magnetyczne lub sole metali, stanowiące prekursory cząstek magnetycznych, korzystnie w atmosferze gazu obojętnego, azotu lub argonu lub amoniaku. Jako cząstki magnetyczne stosuje się dowolny ferryt spinelowy, korzystnie z grupy: MFe_2O_4 (M=Mn, Zn, Fe), $CoFe_{2-x}M_xO_4$ ($M=Zn^{2+}$, Mn^{2+}), γ-Fe_2O_3, dowolny ferryt heksagonalny, korzystnie $BaFe_{12}O_{19}$, $BaFe_{12}O_{19}$-$M_2Fe_4O_8$ (M=Mn, Fe, Zn), związki z grupy magnesów organicznych, pył żelazowy lub stopy metali i ich nanocząstki o właściwościach magnetycznych, takie jak: Fe-Pt, Co-Pt, Fe-Ni, Fe-Co, Ni-CeO_2, korzystnie Fe-Ni. Całość miesza się i dodaje się substancję podwyższającą pH, w zakresie od 7 do 14, korzystnie w zakresie od 8 do 10, z grupy: wodorotlenki metali grupy I i II A układu okresowego pierwiastków, amoniak, sole amonowe, aminy, w takiej ilości, aby pH mieszaniny reakcyjnej wynosiło od 7 do 14, korzystnie od 8 do 10, po czym w warunkach kontrolowania pH mieszaniny, wprowadza się składnik warstwy inertnej w postaci polimeru poli(N-izopropyloakryloamidu) glikolu polietylenowego lub polidimetylosiloksanu i/lub krzemianu sodu i/lub krzemionki lub węgla korzystnie w postaci grafitu lub grafenu lub prekursora składnika warstwy inertnej, takiego jak tetraetyloortokrzemian (TEOS) i/lub tetrametoksysilan (TMOS), w takiej ilości, aby stosunek molowy składnika warstwy inertnej do cząstek magnetycznych wynosił od 0,01:1 do 20:1, korzystnie od 1:1 do 10:1. Całość miesza się w pH zasadowym, otrzymując cząstki magnetyczne pokryte inertną warstwą polimeru lub krzemionki stabilizowane surfaktantem kationowym i/lub kopolimerem kationowym. Oddzielnie sporządza się roztwór wodny i/lub alkoholowy zawierający surfaktant kationowy, korzystnie bromek cetylo-trimetyloamoniowy i/lub chlorek heksadecylo-trimetyloamoniowy i/lub kopolimer kationowy, korzystnie polidimetyloaminoepichlorohydrynę, polichlorek diallilodimetyloamoniowy i/lub polietylenoiminę, do którego następnie dodaje się cząstki fotokatalityczne półprzewodników z grupy: tlenek tytanu(IV) TiO_2, tlenek wolframu(VI) WO_3, tlenek cynku ZnO, dwutlenek cyny SnO_2, siarczek kadmu CdS, korzystnie TiO_2 korzystnie w postaci prekursora półprzewodnika, korzystnie tetrabutylo tytanian i/lub tetraizopropylo tytanian i/lub siarczan tytanylu i/lub czterochlorek tytanu przy wartości pH wynoszącej w zakresie od 7 do 14, korzystnie od 8 do 10, w takiej ilości, aby stosunek molowy półprzewodnika do cząstek magnetycznych wynosił w zakresie od 0,05:1 do 30:1, korzystnie w zakresie od 1:1 do 4:1. Cząstki fotokatalityczne korzystnie modyfikuje się powierzchniowo nanocząstkami metali szlachetnych lub bimetali, korzystnie Pt-Cu, Pt-Pd, Pd-Cu, Au-Pt, Au-Pd, Ag-Pt, Ag-Cu w ilości od 0,01 do 10% molowych w stosunku do półprzewodnika, korzystnie od 0,01 do 1% molowych lub cząstki fotokatalityczne korzystnie domieszkuje się niemetalem z grupy azot, siarka, bor, jod, węgiel w ilości od 0,01 do 30% wagowych w stosunku do półprzewodnika, korzystnie od 0,01 do 15% wagowych lub cząstki fotokatalityczne korzystnie domieszkuje się niemetalem z grupy azot, siarka, bor, jod, węgiel w ilości od 0,01 do 30% wagowych w stosunku do półprzewodnika, korzystnie od 0,01 do 15% wagowych i dodatkowo modyfikuje się powierzchniowo w znany sposób nanocząstkami metali, korzystnie platyny, miedzi, palladu, srebra, złota, rutenu w ilości od 0,01 do 10% molowych w stosunku do półprzewodnika, korzystnie od 0,01 do 1% molowych. Obie mieszaniny miesza się ze sobą przez co najmniej 10 min, ustalając wartość pH powyżej 7, korzystnie w zakresie od 8 do 10. Następnie otrzymane cząstki separuje się za pomocą pola magnetycznego, przemywa się wodą, suszy się do stałej masy w temperaturze 60–90°C i kalcynuje się w temperaturze 250–1000°C przez 0,5–5 godzin.

Projektowane nanokompozyty o właściwościach fotokatalitycznych i magnetycznych według wynalazku są otrzymywane w wyniku preparatyki w środowisku zasadowym z zastosowaniem kationowych związków powierzchniowo czynnych, pozwalających na efektywną adhezję poszczególnych warstw na powierzchni rdzenia magnetycznego, korzystnie przeprowadza się reakcję w układzie mikroemulsji w/o. W mikroemulsji nanokrople fazy wodnej zdyspergowane są w fazie ciągłej – olejowej, dodatkowo stabilizowanej i chronionej przed aglomeracją przez surfaktant na granicy faz w/o.

W przedstawionym sposobie preparatykę cząstek przeprowadza się w układzie odwróconych miceli lub mikroemulsji w/o. Do fazy olejowej, która zawiera ciekłe węglowodory, korzystnie cykloheksan

i/lub izooktan i/lub heptan i/lub oktan, ko-surfaktant, korzystnie izopropanol, i/lub n-butanol, i/lub heksanol w ilości od 1 do 30% obj. oraz surfaktant, korzystnie z grupy: bromek cetylo-trimetyloamoniowy (CTAB), chlorek heksadecylo-trimetyloamoniowy (CTAC), chlorek dodecylo-trimetyloamoniowy (DTAC), bromek tetradecylotrimetyloamoniowy (TTAB) w stężeniu od 0,1M do 10M, korzystnie od 0,2M do 0,5M dodaje się fazę wodną zawierającą sole metali, będące prekursorem cząstek magnetycznych. Następnie sporządza się mikroemulsję w/o zawierającą w fazie wodnej substancję podwyższającą pH z grupy: amoniak i/lub sole amonowe i/lub aminy i/lub wodorotlenek metalu z I i II grupy układu okresowego pierwiastków, a w fazie olejowej ciekłe węglowodory, korzystnie cykloheksan i/lub izooktan i/lub heptan, i/lub oktan oraz surfaktant kationowy, korzystnie z grupy: bromek cetylo-trimetyloamoniowy (CTAB), chlorek heksadecylo-trimetyloamoniowy (CTAC), chlorek dodecylo-trimetyloamoniowy (DTAC), bromek tetradecylotrimetyloamoniowy (TTAB), o stężeniu od 0,1M do 10M, korzystnie od 0,2M do 0,5M, w stosunku do fazy olejowej, i/lub kopolimer kationowy, korzystnie polidimetyloaminoepichlorohydrynę w ilości od 0,01 do 30% wag., polichlorek diallilodimetyloamoniowy (PDDAC) w ilości od 0,1 do 20% wag., korzystnie 0,5% wag. i/lub polietylenoiminy (PEI) w ilości od 0,01 do 20% wag., korzystnie od 1 do 5% wag., tak aby pH wynosiło od 7 do 14, korzystnie od 8 do 12, którą miesza się korzystnie w atmosferze gazu obojętnego. Następnie do mikroemulsji zawierającej sole metali zdyspergowane w fazie wodnej wkrapla się mikroemulsję zawierającą w fazie wodnej substancję podwyższającą pH z grupy: wodorotlenki metali grupy I i II A układu okresowego pierwiastków, amoniak, sole amonowe, aminy, w takiej ilości, aby pH mieszaniny reakcyjnej wynosiło od 7 do 14, korzystnie od 8 do 12. Następnie miesza się obydwie mikroemulsję, otrzymując zawiesinę cząstek magnetycznych. Sposób otrzymywania fotokatalizatora magnetycznego w układzie odwróconych miceli lub mikroemulsji w/o charakteryzuje się tym, że sporządza się, jak opisano powyżej pierwszą mikroemulsję w/o zawierającą cząstki magnetyczne lub do mikroemulsji w/o zawierające surfaktant kationowy korzystnie z grupy: bromek cetylo-trimetyloamoniowy (CTAB), chlorek heksadecylo-trimetyloamoniowy (CTAC), chlorek dodecylo-trimetyloamoniowy (DTAC), bromek tetradecylotrimetyloamoniowy (TTAB), o stężeniu od 0,1M do 10M, korzystnie od 0,2M do 0,5M, w stosunku do fazy olejowej, ciekłe węglowodory, korzystnie cykloheksan i/lub izooktan i/lub heptan i/lub oktan oraz ko-surfaktant, korzystnie izopropanol, n-butanol lub heksanol w ilości od 1 do 30% obj., dodaje się cząstki magnetyczne. Jako cząstki magnetyczne stosuje się dowolny ferryt spinelowy, korzystnie z grupy: MFe_2O_4 (M=Mn, Zn, Fe), $CoFe_{2-x}M_xO_4$ (M=Zn^{2+}, Mn^{2+}), γ-Fe_2O_3, dowolny ferryt heksagonalny, korzystnie $BaFe_{12}O_{19}$, $BaFe_{12}O_{19}$-$M_2Fe_4O_8$ (M=Mn, Fe, Zn), związki z grupy magnesów organicznych, pył żelazowy lub stopy metali i ich nanocząstki o właściwościach magnetycznych, takie jak: Fe-Pt, Co-Pt, Fe-Ni, Fe-Co, Ni-CeO_2, korzystnie Fe-Ni. Oddzielnie sporządza się drugą mikroemulsję w/o zawierającą w fazie wodnej substancję podwyższającą pH z grupy: amoniak i/lub sole amonowe i/lub aminy i/lub wodorotlenek metalu z I i II grupy układu okresowego pierwiastków, a w fazie olejowej ciekłe węglowodory, korzystnie cykloheksan i/lub izooktan i/lub heptan, i/lub oktan oraz surfaktant kationowy, korzystnie z grupy: bromek cetylo-trimetyloamoniowy (CTAB), chlorek heksadecylo-trimetyloamoniowy (CTAC), chlorek dodecylo-trimetyloamoniowy (DTAC), bromek tetradecylotrimetyloamoniowy (TTAB), o stężeniu od 0,1M do 10M, korzystnie od 0,2M do 0,5M, w stosunku do fazy olejowej, i/lub kopolimer kationowy, korzystnie polidimetyloaminoepichlorohydrynę w ilości od 0,01 do 30% wag., polichlorek diallilodimetyloamoniowy (PDDAC) w ilości od 0,1 do 20% wag., korzystnie 0,5% wag. i/lub polietylenoiminy (PEI) w ilości od 0,01 do 20% wag., korzystnie od 1 do 5% wag., tak aby pH wynosiło od 7 do 14, korzystnie od 8 do 12, którą korzystnie miesza się w atmosferze gazu obojętnego, po czym wprowadza się składnik warstwy inertnej w postaci polidimetylosiloksanu i/lub krzemianu sodu i/lub krzemionki lub węgla korzystnie w postaci polimeru poli(N-izopropyloakryloamidu) glikolu polietylenowego lub grafitu lub prekursora składnika warstwy inertnej, takiego jak tetraetyloortokrzemian (TEOS) i/lub tetrametoksysilan (TMOS), w ilości takiej, aby stosunek molowy składnika warstwy inertnej do cząstek magnetycznych wynosił od 0,01:1 do 20:1, korzystnie od 1:1 do 10:1, po czym drugą mikroemulsję dodaje się do pierwszej i miesza się utrzymując pH w zakresie od 7 do 14 korzystnie od 8 do 12, a następnie dodaje się cząstki fotokatalityczne półprzewodników z grupy: tlenek tytanu(IV) TiO_2, tlenek wolframu(VI) WO_3, tlenek cynku ZnO, dwutlenek cyny SnO_2, siarczek kadmu CdS, korzystnie TiO_2 korzystnie w postaci prekursora półprzewodnika, korzystnie tetrabutylo tytanian i/lub tetraizopropylo tytanian i/lub siarczan tytanylu i/lub czterochlorek tytanu przy wartości pH wynoszącej w zakresie od 7 do 14, korzystnie od 8 do 12, w takiej ilości, aby stosunek molowy półprzewodnika do cząstek magnetycznych wynosił w zakresie od 0,05:1 do 30:1, korzystnie w zakresie od 1:1 do 4:1. Cząstki fotokatalityczne korzystnie dodaje się do mikroemulsji zawierającej cząstki magnetyczne pokryte inertną warstwą w postaci mikroemulsji w/o (trzeciej) o pH w zakresie od 7 do 14, korzystnie od 8 do 12, stabilizowanej

surfaktantem kationowym i/lub kopolimerem kationowym, korzystnie polidimetyloaminoepichlorohydryną w ilości od 0,01 do 30% wag., polichlorkiem diallilodimetyloamoniowym (PDDAC) w ilości od 0,1 do 20% wag., korzystnie 0,5% wag. i/lub polietylenoiminą (PEI) w ilości od 0,01 do 20% wag. Cząstki fotokatalityczne korzystnie modyfikuje się powierzchniowo nanocząstkami metali szlachetnych lub bimetali, korzystnie Pt-Cu, Pt-Pd, Pd-Cu, Au-Pt, Au-Pd, Ag-Pt, Ag-Cu w ilości od 0,01 do 10% molowych w stosunku do półprzewodnika, korzystnie od 0,01 do 1% molowych lub cząstki fotokatalityczne korzystnie domieszkuje się niemetalem z grupy azot, siarka, bor, jod, węgiel w ilości od 0,01 do 30% wagowych w stosunku do półprzewodnika, korzystnie od 0,01 do 15% wagowych lub cząstki fotokatalityczne korzystnie domieszkuje się niemetalem z grupy azot, siarka, bor, jod, węgiel w ilości od 0,01 do 30% wagowych w stosunku do półprzewodnika, korzystnie od 0,01 do 15% wagowych i dodatkowo modyfikuje się powierzchniowo w znany sposób nanocząstkami metali, korzystnie platyny, miedzi, palladu, srebra, złota, rutenu w ilości od 0,01 do 10% molowych w stosunku do półprzewodnika, korzystnie od 0,01 do 1% molowych. Następnie całość miesza się ze sobą przez co najmniej 10 min, a następnie otrzymane cząstki fotokatalizatora magnetycznego separuje się za pomocą pola magnetycznego, przemywa się wodą, suszy się do stałej masy korzystnie w temperaturze 60–90°C i kalcynuje się w temperaturze 250–1000°C przez 0,5–5 godzin.

Sposób według wynalazku charakteryzuje się tym, że otrzymany nanokompozyt może wykazywać aktywność w zakresie UV i Vis w wyniku domieszkowania struktury objętościowej półprzewodnika za pomocą związków niemetali, korzystnie z grupy: mocznik, i/lub tiomocznik, i/lub hydrazyna, i/lub amoniak, i/lub kwas jodowy, i/lub jodek potasu, i/lub fluorowodór i/lub jonów metali, korzystnie związków niklu, i/lub kobaltu, i/lub żelaza, i/lub cynku, i/lub rutenu, i/lub wolframu, i/lub miedzi, lub modyfikacji powierzchni za pomocą nanocząstek metali szlachetnych, korzystnie platyny, i/lub palladu, i/lub złota, i/lub srebra oraz nanocząstek metali grup przejściowych, korzystnie miedzi, i/lub rutenu, i/lub cyrkonu, i/lub rodu, i/lub wanadu. W tym celu do mieszaniny reakcyjnej przed dodaniem cząstek fotokatalizatora z grupy: TiO_2, WO_3, ZnO, SnO_2, Cds, i/lub prekursora półprzewodnika, korzystnie tetrabutylo tytanianu, i/lub tetraizopropylo tytanianu, i/lub siarczan tytanylu, i/lub czterochlorek tytanu wprowadza się prekursor nanocząstek metalu i/lub prekursor niemetali z grupy azot, siarka, bor, jod, węgiel w ilości od 0,01 do 30% wagowych w stosunku do TiO_2, korzystnie od 0,01 do 15% wagowych i/lub prekursor cząstek platyny, miedzi, palladu w ilości od 0,01 do 10% molowych w stosunku do TiO_2, korzystnie od 0,01 do 1% molowych, korzystnie otrzymując strukturę warstwy fotokatalitycznej I-TiO_2, N-TiO_2, S-TiO_2, I,C-TiO_2, B-TiO_2, Pt/I-TiO_2, Pt/N-TiO_2, Pd/-I-TiO_2, Pd/N-TiO_2, Cu/I-TiO_2, Cu/N-TiO_2, Pt-Cu-TiO_2, Pt-Pd-TiO_2, Pd-Cu-TiO_2, Au-Pt-TiO_2, Au-Pd-TiO_2, Ag-Pt-TiO_2, Ag-Cu-TiO_2 stosując metodę mikroemulsyjną, zol-żel lub hydrotermalną.

W wariancie realizacji wynalazku modyfikację powierzchniową nanocząstkami metalu szlachetnego, i/lub jonami metali i/lub domieszkowanie niemetalem półprzewodnika z grupy: TiO_2, WO_3, ZnO, SnO_2, CdS, i/lub prekursora półprzewodnika przeprowadza się in-situ w mieszaninie reakcyjnej zawierającej cząstki magnetyczne pokryte inertną warstwą. W tym celu do mieszaniny reakcyjnej zawierającej cząstki magnetyczne pokryte warstwą inertną dodaje się prekursor półprzewodnika i/lub nanocząstki półprzewodnika oraz roztwory kwasów i/lub soli metali i/lub niemetali tak, aby stosunek domieszki do półprzewodnika wynosił od 0,01 do 30% wag. Modyfikację cząstkami metali korzystnie prowadzi się poprzez redukcję chemiczną za pomocą mocnego reduktora, korzystnie borowodorku sodu lub redukcję termiczną w temperaturze od 300°C do 1000°C.

Dzięki wykorzystaniu sposobu według wynalazku otrzymuje się fotokatalizator magnetyczny wielowarstwowy w jednym układzie, bez konieczności separacji poszczególnych jego komponentów w oparciu o adhezję w środowisku zasadowym cząstek warstwy inertnej i warstwy fotokatalizatora stabilizowanych kationowym surfaktantem i/lub kopolimerem kationowym. Otrzymane według sposobu opisanego w wynalazku fotokatalizatory magnetyczne można separować z fazy wodnej po przyłożeniu gradientu pola magnetycznego. Pętle histerezy dla wybranych fotokatalizatorów magnetycznych wskazują, że nanokompozyty są superparamagnetyczne oraz charakteryzują się wysokim momentem magnetycznym wynoszącym od 15 do 60 $emu \cdot g^{-1}$. Otrzymane fotokatalizatory magnetyczne wykazują wysoką efektywność degradacji związków organicznych np. fenolu, kwasu benzoesowego, w tym również związków niepodatnych na rozkład biologiczny, takich jak: etodolak, karbamazepina, hydrochlorotiazyd, obecnych w ściekach przemysłowych oraz w śladowych ilościach w wodach powierzchniowych.

Charakterystykę właściwości magnetycznych i fotokatalitycznych wybranych nanokompozytów otrzymanych według sposobu wykonania omówionego w niniejszym wynalazku oraz szczegółowy opis wykonania przedstawiono w przykładach wykonania i na rysunku, na którym fig. 1 przedstawia zmianę

potencjału zeta w funkcji pH dla (a) cząstek magnetycznych $BaFe_{12}O_{19}$, fotokatalizatora TiO_2 i cząstek SiO_2 oraz (b) dla cząstek $CoFe_2O_4$, fotokatalizatora TiO_2 i cząstek SiO_2, fig. 2 przedstawia wykresy histerezy magnetycznej dla fotokatalizatora magnetycznego $TiO_2/SiO_2/BaFe_{12}O_{19}$.

Przykład 1

Sposób otrzymywania fotokatalizatora magnetycznego Pt/N-$TiO_2/SiO_2/CoFe_2O_4$ *w mikroemulsji w/o, charakteryzującego się aktywnością w zakresie promieniowania widzialnego*

Pierwszą mikroemulsję otrzymuje się poprzez dodanie surfaktantu CTAB do n-butanolu, który stanowi ko-surfaktant. Następnie dodaje się CTAB i n-butanol do izooktanu w stosunku molowym CTAB:n-butanol:izooktan wynoszącym 1:4:8. Do 200 cm^3 0,45M CTAB w izooktanie wkrapla się roztwór wodny zawierający $FeSO_4 \cdot 7H_2O$ i $CoCl_2$ w stosunku molowym Fe^{2+} do Co^{2+} wynoszącym 2:1. Stosunek objętości fazy olejowej do fazy wodnej wynosi 8:1. Całość miesza się 30 min w atmosferze gazu obojętnego, azotu. Następnie do pierwszej mikroemulsji dodaje się drugą mikroemulsję zawierającą CTAB:n-butanol:izooktan w proporcji molowej 1:4:8 oraz zdyspergowany w fazie wodnej odczynnik strącający, NaOH tak, aby stosunek molowy $Fe^{2+}:Co^{2+}:OH^-$ wynosił 1:0,5:2. Strącanie cząstek magnetycznych przeprowadza się przy pH fazy wodnej równym 10. Po 30 min mieszania w atmosferze gazu obojętnego otrzymuje się koloid cząstek magnetycznych $CoFe_2O_4$. Oddzielnie sporządza się trzecią mikroemulsję o takim samym składzie CTAB:n-butanol:izooktan wynoszącym 1:4:8, zawierającą w fazie wodnej 3M trietyloaminę (TEA). Stosunek objętości fazy olejowej do fazy wodnej w mikroemulsji trzeciej wynosi 8:1. Następnie do mikroemulsji trzeciej wkrapla się tetrametoksysilan. Stosunek molowy TMOS:$CoFe_2O_4$ wynosi 5, a TEA do TMOS wynosi 10. Do mikroemulsji w/o zawierającej cząstki magnetyczne dodaje się mikroemulsję trzecią zawierającą cząstki krzemionki. Następnie otrzymuje się mikroemulsję czwartą CTAB:n-butanol:izooktan w stosunku molowym 1:4:8, do której wprowadza się prekursor tlenku tytanu(IV), tetrabutylo tytanian i mocznik, przy wartości pH wynoszącej 11. Stosunek molowy Ti:N wynosi 1:4, a półprzewodnika do związku magnetycznego wynosi 2:1. Do układu wprowadza się 0,25 cm^3 0,048M K_2PtCl_4 tak, aby zawartość cząstek platyny w stosunku do TiO_2 wynosiła 0,05% mol. Następnie mikroemulsję czwartą dodaje się do układu koloidalnego cząstek magnetycznych pokrytych inertną warstwą krzemionki i miesza korzystnie przez 1 h. Otrzymane cząstki fotokatalizatora Pt/N-$TiO_2/SiO_2/CoFe_2O_4$ separuje się za pomocą pola magnetycznego, przemywa się wodą, suszy się w temperaturze 80°C i kalcynuje się w temperaturze 400°C przez 2 godziny. Moment magnetyczny otrzymanych cząstek wynosi 40 $emu \cdot g^{-1}$.

Efektywność fotokatalityczną zbadano w reakcji degradacji fenolu oraz etodolaku. Stwierdzono, że po 30 min naświetlania promieniowaniem z zakresu widzialnego (λ>420 nm) degradacji ulega 100% fenolu oraz 45% etodolaku, zaś stopień mineralizacji związków wynosi odpowiednio 88% oraz 20%.

Przykład 2

Sposób otrzymywania fotokatalizatora magnetycznego $TiO_2/SiO_2/BaFe_{12}O_9$ oraz Pd/I-$TiO_2/SiO_2/BaFe_{12}O_9$ *w mikroemulsji w/o, charakteryzującego się aktywnością w zakresie promieniowania UV i Vis*

Do 200 cm^3 mikroemulsji 0,5M CTAB i n-butanolu w izooktanie, w stosunku molowym CTAB: n-butanol:izooktan wynoszącym 1:4:8 wkrapla się roztwór wodny prekursorów ferrytu barowego $Fe(NO_3)_3$ i $Ba(NO_3)_3$. Stosunek molowy jonów Ba^{2+} do Fe^{3+} wynosi 1:10, natomiast stosunek objętości fazy olejowej do fazy wodnej 9:1. Całość miesza się 30 min w atmosferze gazu obojętnego, azotu. Następnie do pierwszej mikroemulsji dodaje się drugą mikroemulsję zawierającą CTAB:n-butanol:izooktan w proporcji molowej 1:4:8 oraz zdyspergowany w fazie wodnej odczynnik strącający, 5M NH_4OH. Strącanie cząstek magnetycznych przeprowadza się przy pH fazy wodnej równym 11. Po 1 h mieszania w atmosferze gazu obojętnego wprowadza się TEOS. Stosunek molowy TEOS:$BaFe_{12}O_9$ wynosi 12. Do koloidu cząstek magnetycznych pokrytych inertną warstwą krzemionki dodaje się 0,5% wag. polichlorku diallilodimetyloamoniowego (PDDA), a następnie cząstki magnetyczne pokrywa się warstwą fotokatalizatora. W tym celu sporządza się 50 cm^3 mikroemulsji CTAB:n-butanol:izooktan w proporcji molowej 1:4:8, do której dodaje się prekursor TiO_2 tetraizopropylotytanianu (TIP). Stosunek molowy półprzewodnika do związku magnetycznego wynosi 1:1.

Alternatywnie, w celu uzyskania aktywności fotokatalizatora w świetle widzianym oddzielnie sporządza się 50 cm^3 mikroemulsji 0,5M CTAB, n-butanol w izooktanie, w stosunku molowym CTAB: n-butanol:izooktan wynoszącym 1:4:8, wprowadzając do fazy wodnej 6 mM kwas jodowy, 10 cm^3 tetraizopropylotytanianu. Następnie po 30 min mieszania dodaje się 0,5 cm^3 $PdCl_2$ tak, aby zawartość palladu do TiO_2 wynosiła 0,05% molowych oraz po 30 min mieszania dodaje się 0,5 cm^3 borowodorku sodu w nadmiarze molowym w stosunku do jonów palladu wynoszącym 1,5. Otrzymaną mikroemulsję trzecią

zawierającą cząstki fotokatalizatora domieszkowane jodem i modyfikowane powierzchniowo palladem dodaje się do mikroemulsji zawierającej cząstki $BaFe_{12}O_9/SiO_2$, wartość pH powinna wynosić powyżej 8 (0,1M NH_4OH). Otrzymane cząstki fotokatalizatora magnetycznego separuje się w znany sposób, suszy do stałej masy i kalcynuje w temperaturze 300°C, otrzymując fotokatalizator $Pd/I\text{-}TiO_2/SiO_2/BaFe_{12}O_9$, separowalny w polu magnetycznym.

Właściwości fotokatalityczne zbadano w reakcji degradacji fenolu oraz hydrochlorotiazydu. Stwierdzono, że w wyniku naświetlania promieniowaniem z zakresu widzialnego (λ>420 nm) w czasie 40 min naświetlania degradacji uległo 100% fenolu, zaś w czasie 2 h zdegradowało 70% hydrochlorotiazydu. Jak pokazano na Fig. 2, magnetyczność nanokompozytu $TiO_2/SiO_2/BaFe_{12}O_9$ wynosi 43 $emu \cdot g^{-1}$.

Przykład 3

Sposób otrzymywania fotokatalizatora magnetycznego $Ag\text{-}TiO_2/SiO_2/Fe/Fe_3O_4$ *w mikroemulsji w/o, charakteryzującego się aktywnością w zakresie UV-Vis*

Do 100 cm^3 0,5M CTAC w n-oktanie wprowadza się zdyspergowane uprzednio za pomocą ultradźwięków w wodzie cząstki pyłu żelazowego (Fe) o wielkości 0,1 μm. Stosunek molowy CTAC do kosurfaktantu, n-butanolu oraz n-oktanu CTAC:n-butanokizooktan wynosi 1:5:12. Stosunek objętości fazy olejowej do fazy wodnej wynosi 12:1. Po 1 h mieszania wytwarza się warstwa pasywująca tlenku żelaza(II) żelaza(III) na powierzchni Fe. Do układu koloidalnego dodaje się tetraetyloortokrzemian. Stosunek molowy TEOS do Fe wynosi 12:1. Następnie koryguje się pH fazy wodnej mikroemulsji w/o do wartości 12, wkraplając 50 cm^3 mikroemulsji o takim samym składzie, zawierającej w fazie wodnej odczynnik strącający cząstki SiO_2, 5M NaOH. Po 1 h mieszania do otrzymanej mikroemulsji w/o zawierającej cząstki magnetyczne pokryte warstwą inertną krzemionki dodawany jest fotokatalizator. W celu sporządza się trzecią mikroemulsję CTAC:n-butanol:izooktan w stosunku molowym wynoszącym 1:5:12, która zawiera w fazie wodnej 0,35M roztwór azotanu srebra. Zawartość cząstek srebra osadzonych na powierzchni TiO_2 wynosi 2,5% mol. Do mikroemulsji trzeciej dodaje się jest tetraizopropylo tytanian (TIP) i wprowadza się odczynnik redukujący, hydrazynę tak, aby stosunek molowy hydrazyny do Ag^+ wynosił 2:1. Następnie do zawiesiny cząstek magnetycznych pokrytych krzemionką wprowadza się mikroemulsję zawierającej cząstki $Ag\text{-}TiO_2$ przy wartości pH 10,5 korygowanej za pomocą wody amoniakalnej. Otrzymane cząstki fotokatalizatora $Ag\text{-}TiO_2/SiO_2/Fe/Fe_3O_4$ separuje się i suszy w znany sposób oraz kalcynuje się w temperaturze 400°C przez 1 godzinę. Moment magnetyczny otrzymanych cząstek wynosi 16 $emu \cdot g^{-1}$.

Zaobserwowano, że stopień redukcji fenolu po 60 min naświetlania promieniowaniem z zakresu widzialnego (λ>420 nm) wodnego roztworu 0,2 mM fenolu zawierającego 1 $g \cdot dm^{-3}$ fotokatalizatora $Ag\text{-}TiO_2/SiO_2/Fe/Fe_3O_4$ wynosi 85%, zaś efekt biobójczy zbadany na szczepach bakterii: *Escherichia coli* ATCC 10536 i *Staphylococcus aureus* ATCC 6538 oraz grzybów *Candida albicans* ATCC 10231 zaobserwowano przy zawartości 250 mg fotokatalizatora na 1 dm^3 fazy wodnej.

Przykład 4

Sposób otrzymywania fotokatalizatora magnetycznego $ZnO/SiO_2/CoFe_2O_4$ *aktywnego w zakresie promieniowania UV*

Do 0,1M bromku tetradecylotrimetyloamoniowego (TTAB) w wodzie dodaje się $FeSO_4 \cdot 7H_2O$ i $CoCl_2$ w stosunku molowym Fe^{2+} do Co^{2+} wynoszącym 2:1, całość miesza się 30 min w atmosferze gazu obojętnego i wprowadza się roztwór wodny NaOH tak, aby stosunek molowy $Fe^{2+}:Co^{2+}:OH^-$ wynosi 1:0,5:2. Następnie dodaje się 0,1M trietyloaminę (TEA) do pH fazy wodnej wynoszącego 11 i wkrapla się tetrametoksysilan. Stosunek molowy $TMOS:CoFe_2O_4$ wynosi 6, a TEA do TMOS wynosi 10. Następnie do cząstek magnetycznych pokrytych warstwą inertną dodawany jest roztwór trzeci 0,1M TTAB zawierający zdyspergowane cząstki ZnO. Stosunek molowy półprzewodnika do związku magnetycznego wynosi 1:1. Zawiesinę fotokatalizatora wprowadza się do układu koloidalnego cząstek magnetycznych pokrytych warstwą inertną, korygując wartość pH do 10. Otrzymane cząstki fotokatalizatora $ZnO/SiO_2/CoFe_2O_4$ separuje się za pomocą pola magnetycznego, przemywa się wodą i suszy się w temperaturze 80°C. Moment magnetyczny otrzymanych cząstek wynosi 20 $emu \cdot g^{-1}$. Efektywność fotokatalityczną zbadano w reakcji degradacji kwasu benzoesowego. Stwierdzono, że po 60 min naświetlania promieniowaniem z zakresu UV degradacji ulega 95% kwasu benzoesowego, zaś stopień mineralizacji związków wynosił 83%.

Przykład 5

Sposób otrzymywania fotokatalizatora magnetycznego $TiO_2/SiO_2/MnFe_2O_4$ *aktywnego w zakresie promieniowania UV*

Do 0,05M chlorku dodecylotrimetyloamoniowego (DTAC) dodaje się cząstki magnetyczne $MnFe_2O_4$. Oddzielnie sporządza się roztwór 0,05M DTAC, do którego wprowadza się 1M wodę amoniakalną do wartości pH 8 i wkrapla się TEOS. Stosunek molowy TEOS:$MnFe_2O_4$ wynosi 3. Następnie do cząstek magnetycznych dodawany jest koloid cząstek SiO_2. Oddzielnie sporządza się 20 cm^3 roztwór wodny DTAC, do którego wprowadza się TiO_2 P25 i 1% wag. polietylenoiminy. Stosunek molowy półprzewodnika do związku magnetycznego wynosi 0,5:1. Zawiesinę fotokatalizatora wprowadza się do układu koloidalnego cząstek magnetycznych pokrytych warstwą inertną, korgując wartość pH do 8. Otrzymane cząstki fotokatalizatora $TiO_2/SiO_2/MnFe_2O_4$ separuje się za pomocą pola magnetycznego, przemywa się wodą i suszy się w temperaturze 80°C. Moment magnetyczny otrzymanych cząstek wynosi 56 $emu \cdot g^{-1}$. Efektywność fotokatalityczną zbadano w reakcji degradacji fenolu. Stwierdzono, że po 25 min naświetlania promieniowaniem z zakresu UV degradacji ulega 100% fenolu, zaś stopień mineralizacji związków wynosił 95%.

Przykład 6

Sposób otrzymywania fotokatalizatora magnetycznego $TiO_2/C/MnFe_2O_4$ lub TiO_2/PEG-PNIPAm/$MnFe_2O_4$ *aktywnego w zakresie promieniowania UV*

Postępuje się jak w przykładzie 5, przy czym jako składnik warstwy inertnej dodaje się cząstki grafenu w ilości 2% molowych lub polimer poli(N-izopropyloakryloamidu) glikolu polietylenowego w ilości 5% molowych.

Przykład 7

Sposób otrzymywania fotokatalizatora magnetycznego Pd/$TiO_2/C/MnFe_2O_4$ lub Pd/TiO_2/PEG-PNIPAm/$MnFe_2O_4$ *aktywnego w zakresie promieniowania UV i Vis*

Postępuje się jak w przykładzie 5, przy czym jako składnik warstwy inertnej dodaje się cząstki grafenu w ilości 2% molowych lub polimer poli(N-izopropyloakryloamidu) glikolu polietylenowego w ilości 5% molowych. Otrzymane cząstki fotokatalizatora $TiO_2/C/MnFe_2O_4$ lub TiO_2/PEG-PNIPAm/$MnFe_2O_4$ modyfikuje się palladem, dodając do wodnej zawiesiny cząstek fotokatalizatora magnetycznego 0,5 cm^3 $PdCl_2$ tak, aby zawartość palladu do TiO_2 wynosiła 0,1% molowych. Następnie dodaje się 5 cm^3 borowodorku sodu w nadmiarze molowym w stosunku do jonów palladu wynoszącym 1,5. Otrzymane cząstki fotokatalizatora Pd/$TiO_2/C/MnFe_2O_4$ lub Pd/TiO_2/PEG-PNIPAm/$MnFe_2O_4$ separuje się za pomocą pola magnetycznego, przemywa się wodą i suszy się do stałej masy. Efektywność fotokatalityczną zbadano w reakcji degradacji benzochinonu. Stwierdzono, że po 40 min naświetlania promieniowaniem z zakresu UV-Vis degradacji ulega 70% i 65% benzochinonu dla Pd/$TiO_2/C/MnFe_2O_4$ lub Pd/TiO_2/PEG-PNIPAm/$MnFe_2O_4$.

Zastrzeżenia patentowe

1. Sposób otrzymywania warstwowego fotokatalizatora magnetycznego polegający na utworzeniu inertnej warstwy wokół cząstki magnetycznej, którą następnie pokrywa się cząstkami fotokatalitycznymi, **znamienny tym**, że sporządza się mieszaninę reakcyjną, w której korzystnie w atmosferze gazu obojętnego lub amoniaku do wody i/lub alkoholu dodaje się surfaktant kationowy, korzystnie bromek heksadecetylo-trimetyloamoniowy (CTAB) i/lub chlorek heksadecylo-trimetyloamoniowy (CTAC), bromek tetradecylotrimetyloamoniowy (TTAB) i/lub chlorek dodecylotrimetyloamoniowy (DTAC) i/lub bromek heksadecylopirydyniowy (CPB) o stężeniu od 0,01M do 10M, korzystnie od 0,02M do 0,2M, i/lub kopolimer kationowy, korzystnie polidimetyloaminoepichlorohydrynę w ilości od 0,01 do 30% wag., polichlorek diallilodimetyloamoniowy (PDDAC) w ilości od 0,1 do 20% wag., korzystnie 0,5% wag., i/lub polietylenoiminę (PEI) w ilości od 0,01 do 20% wag., korzystnie od 1 do 5% wag., oraz cząstki magnetyczne, po czym całość miesza się, a następnie dodaje się substancję podwyższającą pH z grupy: wodorotlenki metali grupy I i II A układu okresowego pierwiastków, amoniak, sole amonowe, aminy, w takiej ilości, aby pH mieszaniny reakcyjnej wynosiło od 7 do 14, korzystnie od 8 do 10, po czym w warunkach kontrolowania pH mieszaniny, wprowadza się składnik warstwy inertnej w postaci polimeru poli(N-izopropyloakryloamidu), glikolu polietylenowego lub polidimetylosiloksanu i/lub krzemianu sodu i/lub krzemionki lub węgla korzystnie w postaci grafitu

lub grafenu lub prekursora składnika warstwy inertnej, takiego jak tetraetyloortokrzemian (TEOS) i/lub tetrametoksysilan (TMOS), w takiej ilości, aby stosunek molowy składnika warstwy inertnej do cząstek magnetycznych wynosił od 0,01:1 do 20:1, korzystnie od 1:1 do 10:1, przy czym całość miesza się utrzymując zasadowy poziom pH, zaś oddzielnie sporządza się roztwór wodny i/lub alkoholowy zawierający surfaktant kationowy, korzystnie bromek cetylotrimetyloamoniowy i/lub chlorek heksadecylo-trimetyloamoniowy i/lub kopolimer kationowy, korzystnie polidimetyloaminoepichlorohydrynę, polichlorek diallilodimetyloamoniowy i/lub polietylenoiminę, do którego następnie dodaje się cząstki fotokatalityczne półprzewodników z grupy: tlenek tytanu(IV) TiO_2, tlenek wolframu(VI) WO_3, tlenek cynku ZnO, dwutlenek cyny SnO_2, siarczek kadmu CdS, korzystnie TiO_2 korzystnie w postaci prekursora półprzewodnika, korzystnie tetrabutylo tytanian i/lub tetraizopropylo tytanian i/lub siarczan tytanylu i/lub czterochlorek tytanu przy wartości pH wynoszącej w zakresie od 7 do 14, korzystnie od 8 do 10, w takiej ilości, aby stosunek molowy półprzewodnika do cząstek magnetycznych wynosił w zakresie od 0,05:1 do 30:1, korzystnie w zakresie od 1:1 do 4:1, po czym obie mieszaniny miesza się ze sobą przez co najmniej 10 min, a następnie otrzymane cząstki separuje się za pomocą pola magnetycznego, przemywa się wodą, suszy się do stałej masy w temperaturze 60–90°C i kalcynuje się w temperaturze 250–1000°C przez 0,5–5 godzin.

2. Sposób według zastrz. 1, **znamienny tym**, że jako cząstki magnetyczne stosuje się dowolny ferryt spinelowy, korzystnie z grupy: MFe_2O_4 (M=Mn, Zn, Fe), $CoFe_{2-x}M_xO_4$ (M=Zn^{2+}, Mn^{2+}), γ-Fe_2O_3, dowolny ferryt heksagonalny, korzystnie $BaFe_{12}O_{19}$, $BaFe_{12}O_{19}$-$M_2Fe_4O_8$ (M=Mn, Fe, Zn), związki z grupy magnesów organicznych, pył żelazowy lub stopy metali i ich nanocząstki o właściwościach magnetycznych, takie jak: Fe-Pt, Co-Pt, Fe-Ni, Fe-Co, Ni-CeO_2, korzystnie Fe-Ni.
3. Sposób według zastrz. 1, **znamienny tym**, że jako cząstki fotokatalityczne stosuje się cząstki fotokatalityczne zmodyfikowane powierzchniowo nanocząstkami metali szlachetnych lub bimetali, korzystnie Pt-Cu, Pt-Pd, Pd-Cu, Au-Pt, Au-Pd, Ag-Pt, Ag-Cu w ilości od 0,01 do 10% molowych w stosunku do półprzewodnika, korzystnie od 0,01 do 1% molowych.
4. Sposób według zastrz. 1, **znamienny tym**, że cząstki fotokatalityczne domieszkuje się niemetalem z grupy azot, siarka, bor, jod, węgiel w ilości od 0,01 do 30% wagowych w stosunku do półprzewodnika, korzystnie od 0,01 do 15% wagowych.
5. Sposób według zastrz. 4, **znamienny tym**, że cząstki fotokatalityczne dodatkowo modyfikuje się powierzchniowo w znany sposób nanocząstkami metali korzystnie platyny, miedzi, palladu w ilości od 0,01 do 10% molowych w stosunku do półprzewodnika, korzystnie od 0,01 do 1% molowych.
6. Sposób otrzymywania warstwowego fotokatalizatora magnetycznego polegający na utworzeniu inertnej warstwy wokół cząstki magnetycznej, którą następnie pokrywa się cząstkami fotokatalitycznymi, **znamienny tym**, że sporządza się pierwszą mikroemulsję w/o zawierającą cząstki magnetyczne oraz surfaktant kationowy korzystnie z grupy: bromek cetylo-trimetyloamoniowy (CTAB), chlorek heksadecylo-trimetyloamoniowy (CTAC), chlorek dodecylo-trimetyloamoniowy (DTAC), bromek tetradecylotrimetyloamoniowy (TTAB), o stężeniu od 0,1M do 10M, korzystnie od 0,2M do 0,5M, w stosunku do fazy olejowej, ciekłe węglowodory, korzystnie cykloheksan i/lub izooktan i/lub heptan i/lub oktan oraz ko-surfaktant, korzystnie izopropanol, n-butanol lub heksanol w ilości od 1 do 30% obj., przy czym oddzielnie sporządza się drugą mikroemulsję w/o zawierającą w fazie wodnej substancję podwyższającą pH z grupy: amoniak i/lub sole amonowe i/lub aminy i/lub wodorotlenek metalu z I i II grupy układu okresowego pierwiastków, a w fazie olejowej ciekłe węglowodory, korzystnie cykloheksan i/lub izooktan i/lub heptan, i/lub oktan oraz surfaktant kationowy, korzystnie z grupy: bromek cetylotrimetyloamoniowy (CTAB), chlorek heksadecylo-trimetyloamoniowy (CTAC), chlorek dodecylo-trimetyloamoniowy (DTAC), bromek tetradecylotrimetyloamoniowy (TTAB), o stężeniu od 0,1M do 10M, korzystnie od 0,2M do 0,5M, w stosunku do fazy olejowej, i/lub kopolimer kationowy, korzystnie polidimetyloaminoepichlorohydrynę w ilości od 0,01 do 30% wag., polichlorek diallilodimetyloamoniowy (PDDAC) w ilości od 0,1 do 20% wag., korzystnie 0,5% wag. i/lub polietylenoiminy (PEI) w ilości od 0,01 do 20% wag., korzystnie od 1 do 5% wag., tak aby pH wynosiło od 7 do 14, korzystnie od 8 do 12, którą korzystnie miesza się w atmosferze gazu obojętnego, po czym wprowadza się składnik warstwy inertnej w postaci polidimetylosiloksanu

i/lub krzemianu sodu i/lub krzemionki lub węgla korzystnie w postaci polimeru poli(N-izopropyloakryloamidu) glikolu polietylenowego lub grafitu lub prekursora składnika warstwy inertnej, takiego jak tetraetyloortokrzemian (TEOS) i/lub tetrametoksysilan (TMOS), w ilości takiej, aby stosunek molowy składnika warstwy inertnej do cząstek magnetycznych wynosił od 0,01:1 do 20:1, korzystnie od 1:1 do 10:1, po czym drugą mikroemulsję dodaje się do pierwszej i miesza się utrzymując pH w zakresie od 7 do 14 korzystnie od 8 do 12, a następnie dodaje się cząstki fotokatalityczne półprzewodników z grupy: tlenek tytanu(IV) TiO_2, tlenek wolframu(VI) WO_3, tlenek cynku ZnO, dwutlenek cyny SnO_2, siarczek kadmu CdS, korzystnie TiO_2 korzystnie w postaci prekursora półprzewodnika, korzystnie tetrabutylo tytanian i/lub tetraizopropylo tytanian i/lub siarczan tytanylu i/lub czterochlorek tytanu przy wartości pH wynoszącej w zakresie od 7 do 14, korzystnie od 8 do 12, w takiej ilości, aby stosunek molowy półprzewodnika do cząstek magnetycznych wynosił w zakresie od 0,05:1 do 30:1, korzystnie w zakresie od 1:1 do 4:1, po czym całość miesza się przez co najmniej 10 min, a następnie otrzymane cząstki separuje się za pomocą pola magnetycznego, przemywa się wodą, suszy się w temperaturze 60–90°C i kalcynuje się w temperaturze 250–1000°C przez 0,5–5 godzin.

7. Sposób, według zastrz. 6, **znamienny tym**, że cząstki fotokatalityczne dodaje się w postaci mikroemulsji w/o o pH w zakresie od 7 do 14, korzystnie od 8 do 12, stabilizowanej surfaktantem kationowym i/lub kopolimerem kationowym, korzystnie polidimetyloaminoepichlorohydryną w ilości od 0,01 do 30% wag., polichlorkiem diallilodimetyloamoniowym (PDDAC) w ilości od 0,1 do 20% wag., korzystnie 0,5% wag. i/lub polietylenoiminą (PEI) w ilości od 0,01 do 20% wag.
8. Sposób według zastrz. 6 albo 7, **znamienny tym**, że jako cząstki fotokatalityczne stosuje się cząstki fotokatalityczne zmodyfikowane powierzchniowo nanocząstkami metali szlachetnych lub bimetali, korzystnie Pt-Cu, Pt-Pd, Pd-Cu, Au-Pt, Au-Pd, Ag-Pt, Ag-Cu w ilości od 0,01 do 10% molowych w stosunku do półprzewodnika, korzystnie od 0,01 do 1% molowych.
9. Sposób według zastrz. 6 albo 7, **znamienny tym**, że cząstki fotokatalityczne domieszkuje się niemetalem z grupy azot, siarka, bor, jod, węgiel w ilości od 0,01 do 30% wagowych w stosunku do półprzewodnika, korzystnie od 0,01 do 15% wagowych.
10. Sposób według zastrz. 9, **znamienny tym**, że cząstki fotokatalityczne dodatkowo modyfikuje się powierzchniowo w znany sposób nanocząstkami metali korzystnie platyny, miedzi, palladu w ilości od 0,01 do 10% molowych w stosunku do półprzewodnika, korzystnie od 0,01 do 1% molowych.
11. Sposób według zastrz. 6 albo 7, **znamienny tym**, że jako cząstki magnetyczne stosuje się dowolny ferryt spinelowy, korzystnie z grupy: MFe_2O_4 (M=Mn, Zn, Fe), $CoFe_{2-x}M_xO_4$ (M=Zn^{2+}, Mn^{2+}), γ-Fe_2O_3, dowolny ferryt heksagonalny, korzystnie $BaFe_{12}O_{19}$, $BaFe_{12}O_{19}$-$M_2Fe_4O_8$ (M=Mn, Fe, Zn), związki z grupy magnesów organicznych, pył żelazowy lub stopy metali i ich nanocząstki o właściwościach magnetycznych, takie jak: Fe-Pt, Co-Pt, Fe-Ni, Fe-Co, Ni-CeO_2, korzystnie Fe-Ni.

Rysunki

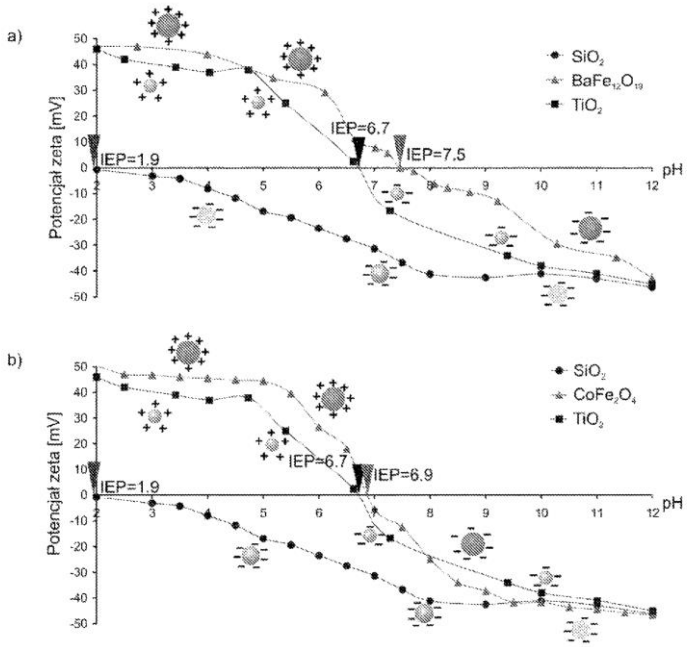

Fig. 1

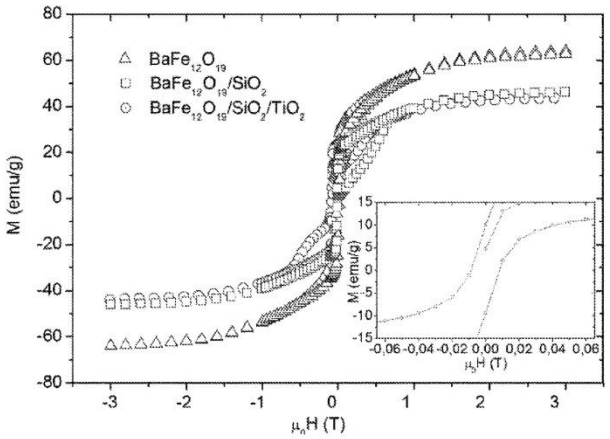

Fig. 2

Departament Wydawnictw UPRP
Cena 4,92 zł (w tym 23% VAT)

RZECZPOSPOLITA POLSKA

Urząd Patentowy Rzeczypospolitej Polskiej

(12) **OPIS PATENTOWY** (19) **PL** (11) **233345** (13) **B1**

(21) Numer zgłoszenia: **423295**

(22) Data zgłoszenia: **28.10.2017**

(51) Int.Cl.
B01J 37/03 (2006.01)
B01J 35/02 (2006.01)
B01J 21/06 (2006.01)
B01J 23/00 (2006.01)

(54) **Sposób otrzymywania warstwowego fotokatalizatora magnetycznego**

(43) Zgłoszenie ogłoszono:
06.05.2019 BUP 10/19

(45) O udzieleniu patentu ogłoszono:
30.09.2019 WUP 09/19

(73) Uprawniony z patentu:
POLITECHNIKA GDAŃSKA, Gdańsk, PL

(72) Twórca(y) wynalazku:
ANNA ZIELIŃSKA-JUREK, Otomin, PL
ZUZANNA BIELAN, Tczew, PL

(74) Pełnomocnik:
rzecz. pat. Małgorzata Kluczyk

PL 233345 B1

Opis wynalazku

Przedmiotem wynalazku jest sposób otrzymywania warstwowych fotokatalizatorów magnetycznych, aktywnych w zakresie promieniowania UV i Vis, mających zastosowanie zwłaszcza w reakcji fotokatalitycznej degradacji wybranych związków organicznych i nieorganicznych.

Z dokumentacji zgłoszeniowej CN101816937A znany jest sposób preparatyki fotokatalizatora TiO_2/Fe_3O_4 o właściwościach magnetycznych aktywnego w zakresie promieniowania UV. Zgodnie z opisem zgłoszeniowym fotokatalizator magnetyczny otrzymuje się dwuetapowo w wyniku współstrącania jonów Fe^{3+} oraz Fe^{2+} w pH wynoszącym 11 za pomocą amoniaku, w roztworze wodnym dodecylobenzenosulfonianu sodu (SDBS), anionowego związku powierzchniowo czynnego. Stosunek jonów Fe^{3+} do Fe^{2+} wynosi 1,8, temperatura reakcji 60°C, zaś stężenie surfaktantu 10% zawartości żelaza w układzie koloidalnym. Otrzymane cząstki magnetyczne odseparowano i suszono w temperaturze 80°C przez 48 h, a następnie wprowadzano do bezwodnego alkoholu etylowego zawierającego prekursor TiO_2-tetrabutylo tytanian (TBOT), dodawano wodę, w celu zainicjowania reakcji hydrolizy w pH wynoszącym 3, które korygowano za pomocą kwasu azotowego(V). Otrzymany nanokompozyt suszono i kalcynowano w 450°C przez 2 h.

Z opisu patentowego US7504130B1 znany jest sposób preparatyki nanokompozytu $TiO_2/NiFe_2O_4$ o strukturze rdzeń-otoczka metodą strąceniową w układzie odwróconych miceli. W tym sposobie w celu otrzymania fotokatalizatora magnetycznego, do fazy organicznej (izooktan) zawierającej surfaktant (0,5M AOT) wprowadzano wodne roztwory chlorku żelaza(II) oraz chlorku niklu(II). Następnie wkraplano drugą mikroemulsję zawierającą w fazie zdyspergowanej 30% roztwór wody amoniakalnej. Do otrzymanego koloidu $NiFe_2O_4$ dodawano roztwór prekursora TiO_2, korzystnie $TiCl_4$ w HCl w stosunku molowym TiO_2:$NiFe_2O_4$ wynoszącym 1:1. Następnie otrzymane cząstki przepłukiwano izopropanolem, separowano i suszono w temperaturze 90°C przez 30 min. Magnetyczność otrzymanych cząstek $NiFe_2O_4$ wynosiła 25 $emu \cdot g^{-1}$, a nanokompozytów $TiO_2/NiFe_2O_4$ 4 $emu \cdot g^{-1}$.

Znane są sposoby otrzymywania fotokatalizatorów magnetycznych o strukturze rdzeń-otoczka, które jednak w wyniku bezpośredniego kontaktu materiału magnetycznego z warstwą fotokatalityczną mogą ulegać reakcjom związanym z fotochemicznym ługowaniem jonów żelaza do roztworu, w wyniku reakcji wygenerowanych nośników ładunku na powierzchni półprzewodnika (np. TiO_2) z cząsteczką tlenu lub wody, które zdolne są do utleniania żelaza lub innego metalu znajdującego się na powierzchni cząstki magnetycznej. W tym odniesieniu wytworzenie w strukturze nanokompozytu inertnej warstwy oddzielającej magnetyczny rdzeń od powierzchni fotokatalizatora pozwala na wielokrotne zastosowanie otrzymanego fotokatalizatora w procesie oczyszczania ścieków lub płynów technologicznych, nie zmieniając jego właściwości fotokatalitycznych oraz magnetycznych.

Sposób wytwarzania warstwowego fotokatalizatora magnetycznego w roztworze wodnym i/lub alkoholowym surfaktantu anionowego korzystnie 2-etyloheksylosulfonobursztynianu sodu (AOT), i/lub soli sodowej kwasu dodecylosiarkowego (SDS) w stężeniu od 0,01M do 10M, korzystnie od 0,02 do 0,3M polegający na tym, że sporządza się mieszaninę reakcyjną, w której korzystnie w atmosferze gazu obojętnego do wodnego i/lub alkoholowego roztworu surfaktantu anionowego, korzystnie 2-etyloheksylosulfonobursztynianu sodu (AOT) i/lub soli sodowej kwasu dodecylosiarkowego (SDS) o stężeniu od 0,01M do 10M, korzystnie od 0,02M do 0,3M dodaje się prekursory cząstek magnetycznych, po czym całość miesza się, dodaje substancję podwyższającą pH powyżej 7 z grupy: wodorotlenki metali grupy I i II A układu okresowego pierwiastków, amoniak, sole amonowe, aminy, w takiej ilości, aby pH mieszaniny reakcyjnej wynosiło od 7 do 14, korzystnie od 8 do 10, otrzymując cząstki magnetyczne. Sposób otrzymywania fotokatalizatora magnetycznego w roztworze wodnym i/lub alkoholowym surfaktantu anionowego korzystnie 2-etyloheksylosulfonobursztynianu sodu (AOT), i/lub soli sodowej kwasu dodecylosiarkowego (SDS) w stężeniu od 0,01M do 10M, korzystnie od 0,02 do 0,3M charakteryzuje się tym, że sporządza się, jak opisano powyżej mieszaninę zawierającą cząstki magnetyczne lub do wodnego i/lub alkoholowego roztworu surfaktantu anionowego, korzystnie 2-etyloheksylosulfonobursztynianu sodu (AOT) i/lub soli sodowej kwasu dodecylosiarkowego (SDS) o stężeniu od 0,01M do 10M, korzystnie od 0,02M do 0,3M dodaje się cząstki magnetyczne, po czym całość miesza się korzystnie w atmosferze gazu obojętnego. Jako cząstki magnetyczne stosuje się dowolny ferryt spinelowy, korzystnie z grupy: MFe_2O_4 (M=Mn, Zn, Fe), $CoFe_{2-x}M_xO_4$ (M=Zn^{2+}, Mn^{2+}), γ-Fe_2O_3, dowolny ferryt heksagonalny, korzystnie $BaFe_{12}O_{19}$, $BaFe_{12}O_{19}$-$M_2Fe_4O_8$ (M=Mn, Fe, Zn), związki z grupy magnesów organicznych, pył żelazowy lub stopy metali i ich nanocząstki o właściwościach magnetycznych, takie jak: Fe-Pt,

Co-Pt, Fe-Ni, Fe-Co, Ni-CeO_2, korzystnie Fe-Ni. Oddzielnie sporządza się drugą mieszaninę w ten sposób, że sporządza się alkoholowy i/lub wodny roztwór substancji podwyższającej pH z grupy: wodorotlenki metali grupy I i II A układu okresowego pierwiastków, amoniak, sole amonowe, aminy, w takiej ilości, aby pH mieszaniny reakcyjnej wynosiło od 7 do 14, korzystnie od 8 do 10, do której dodaje się składnik warstwy inertnej w postaci polimeru poli(N-izopropyloakryloamidu) glikolu polietylenowego, polidimetylosiloksanu i/lub krzemianu sodu i/lub kopolimeru glikolu polietylowego i/lub krzemionki lub węgla korzystnie w postaci grafitu lub grafenu lub prekursora składnika warstwy inertnej, takiego jak tetraetyloortokrzemian (TEOS) i/lub tetrametoksysilan (TMOS), w takiej ilości, aby stosunek molowy składnika warstwy inertnej do cząstek magnetycznych wynosił od 0,01:1 do 30:1, korzystnie od 0,5:1 do 10:1, a następnie dodaje się kopolimer kationowy w ilości od 0,01 do 30% wag., korzystnie polidimetyloaminoepichlorohydrynę i/lub polichlorek diallilodimetyloamoniowy (PDDAC) korzystnie w ilości 5% wag. i/lub polietylenoiminę (PEI) korzystnie w ilości od 1 do 5% wag., i/lub surfaktant kationowy, po czym do zawiesiny zawierającej cząstki magnetyczne wkrapla się drugą mieszaninę i ustala się pH powyżej 7, korzystnie w zakresie od 8 do 10, całość miesza się, a następnie sporządza się roztwór trzeci surfaktantu anionowego, korzystnie 2-etyloheksylosulfonobursztynianu sodu (AOT) i/lub soli sodowej kwasu dodecylosiarkowego (SDS) o stężeniu od 0,01M do 10M, korzystnie od 0,02M do 0,3M, zawierający substancję z grupy kwasów organicznych i/lub nieorganicznych w takiej ilości, aby pH wynosiło od 1 do 7, korzystnie od 3 do 6, zawierający cząstki fotokatalityczne półprzewodników z grupy: tlenek tytanu(IV) TiO_2, tlenek wolframu(VI) WO_3, tlenek cynku ZnO, dwutlenek cyny SnO_2, siarczek kadmu CdS, korzystnie TiO_2 korzystnie w postaci prekursora półprzewodnika, korzystnie tetrabutylo tytanian i/lub tetraizopropylo tytanian i/lub siarczan tytanylu i/lub czterochlorek tytanu, w takiej ilości, aby stosunek molowy cząstek fotokatalitycznych do cząstek magnetycznych wynosił od 1:1 do 30:1, korzystnie w zakresie od 1:1 do 4:1. Cząstki fotokatalityczne korzystnie modyfikuje się powierzchniowo nanocząstkami metali szlachetnych lub bimetali, korzystnie Pt-Cu, Pt-Pd, Pd-Cu, Au-Pt, Au-Pd, Ag-Pt, Ag-Cu w ilości od 0,01 do 10% molowych w stosunku do półprzewodnika, korzystnie od 0,01 do 1% molowych lub cząstki fotokatalityczne korzystnie domieszkuje się niemetalem z grupy azot, siarka, bor, jod, węgiel w ilości od 0,01 do 30% wagowych w stosunku do półprzewodnika, korzystnie od 0,01 do 15% wagowych lub cząstki fotokatalityczne korzystnie domieszkuje się niemetalem z grupy azot, siarka, bor, jod, węgiel w ilości od 0,01 do 30% wagowych w stosunku do półprzewodnika, korzystnie od 0,01 do 15% wagowych i dodatkowo modyfikuje się powierzchniowo w znany sposób nanocząstkami metali, korzystnie platyny, miedzi, palladu, srebra, złota, rutenu w ilości od 0,01 do 10% molowych w stosunku do półprzewodnika, korzystnie od 0,01 do 1% molowych. Następnie mieszaninę trzecią dodaje się do mieszaniny utworzonej z pierwszej i drugiej, utrzymując pH poniżej 7, korzystnie w zakresie od 3 do 6, po czym po co najmniej 10 min mieszania lub uzyskaniu dodatniej wartości potencjału zeta, otrzymane cząstki separuje się za pomocą pola magnetycznego, przemywa się wodą, suszy się do stałej masy, korzystnie w temperaturze 60–90°C i kalcynuje się w temperaturze 250–1000°C przez 0,5–5 godzin.

Sposób wytwarzania warstwowego fotokatalizatora magnetycznego w mikroemulsji w/o lub układzie odwróconych miceli stabilizowanym surfaktantem anionowym, korzystnie 2-etyloheksylosulfonobursztynianem sodu w stężeniu od 0,01M do 10M korzystnie w cykloheksanie i/lub izooktanie i/lub heptanie i/lub oktanie i/lub ko-surfaktantem, korzystnie izopropanolem i/lub n-butanolem i/lub heksanolem o stężeniu od 0,1M do 10M w stosunku do fazy olejowej. W tym celu sporządza się pierwszą mikroemulsję, korzystnie w atmosferze gazu obojętnego zawierającą cząstki magnetyczne, surfaktant anionowy, korzystnie 2-etyloheksylosulfonobursztynian sodu w stężeniu od 0,1M do 10M w stosunku do fazy olejowej, i/lub ko-surfaktant, korzystnie izopropanol i/lub n-butanol i/lub heksanol o stężeniu od 0,1M do 10M w stosunku do fazy olejowej, ciekłe węglowodory, korzystnie cykloheksan i/lub izooktan i/lub heptan i/lub oktan. Jako cząstki magnetyczne stosuje się dowolny ferryt spinelowy, korzystnie z grupy: MFe_2O_4 (M=Mn, Zn, Fe), $CoFe_{2-x}M_xO_4$ (M=Zn^{2+}, Mn^{2+}), γ-Fe_2O_3, dowolny ferryt heksagonalny, korzystnie $BaFe_{12}O_{19}$, $BaFe_{12}O_{19}$-$M_2Fe_4O_8$ (M=Mn, Fe, Zn), związki z grupy magnesów organicznych, pył żelazowy lub stopy metali i ich nanocząstki o właściwościach magnetycznych, takie jak: Fe-Pt, Co-Pt, Fe-Ni, Fe-Co, Ni-CeO_2, korzystnie Fe-Ni. Oddzielnie sporządza się drugą mikroemulsję w/o zawierającą surfaktant anionowy, korzystnie 2-etyloheksylosulfonobursztynian sodu w stężeniu od 0,1M do 10M w stosunku do fazy olejowej, i/lub ko-surfaktant, korzystnie izopropanol i/lub n-butanol i/lub heksanol o stężeniu od 0,1M do 10M w stosunku do fazy olejowej, ciekłe węglowodory, korzystnie cykloheksan i/lub izooktan i/lub heptan i/lub oktan, do której wprowadza się składnik warstwy inertnej w postaci polimeru poli(N-izopropyloakryloamidu) glikolu polietylenowego lub polidimetylosiloksanu i/lub krzemianu sodu i/lub krzemionki lub węgla lub grafitu lub grafenu lub prekursora składnika warstwy

inertnej, takiego jak tetraetyloortokrzemian (TEOS) i/lub tetrametoksysilan (TMOS), w ilości takiej, aby stosunek molowy składnika warstwy inertnej do cząstek magnetycznych wynosił od 0,01:1 do 20:1, korzystnie od 1:1 do 10:1, a następnie dodaje się w fazie wodnej substancję podwyższającą pH z grupy: amoniak i/lub sole amonowe i/lub aminy i/lub wodorotlenek metalu z I i II grupy układu okresowego pierwiastków, tak aby pH wynosiło od 7 do 14, korzystnie od 8 do 12, po czym cały czas mieszając wprowadza się kopolimer kationowy, korzystnie polidimetyloaminoepichlorohydrynę w ilości od 0,01 do 30% wag., polichlorek diallilodimetyloamoniowy (PDDAC) w ilości od 0,1 do 20% wag., korzystnie 0,5% wag. i/lub polietylenoiminy (PEI) w ilości od 0,01 do 20% wag., korzystnie od 1 do 5% wag., po czym drugą mikroemulsję dodaje się do pierwszej i miesza się utrzymując pH w zakresie od 7 do 14 korzystnie od 8 do 12, sporządza się trzecią mikroemulsję w/o zawierającą surfaktant anionowy, korzystnie 2-etyloheksylosulfonobursztynian sodu (AOT) w stężeniu od 0,1M do 10M, korzystnie w cykloheksanie i/lub izooktanie, i/lub heptanie, i/lub oktanie, i/lub ko-surfaktant, korzystnie izopropanol i/lub n-butanol i/lub heksanol o stężeniu od 0,1M do 10M w stosunku do fazy olejowej, w fazie wodnej zawierającą substancję z grupy kwasów organicznych i/lub nieorganicznych w takiej ilości, aby pH wynosiło od 1 do 7, korzystnie od 3 do 6, zawierającą cząstki fotokatalityczne półprzewodników z grupy: tlenek tytanu (IV) TiO_2, tlenek wolframu (VI) WO_3, tlenek cynku ZnO, dwutlenek cyny SnO_2, siarczek kadmu CdS, korzystnie TiO_2 korzystnie w postaci prekursora półprzewodnika, korzystnie tetrabutylo tytanian i/lub tetraizopropylo tytanian i/lub siarczan tytanylu i/lub czterochlorek tytanu, w takiej ilości, aby stosunek molowy cząstek fotokatalitycznych do cząstek magnetycznych wynosił od 1:1 do 30:1, korzystnie w zakresie od 1:1 do 4:1. Cząstki fotokatalityczne korzystnie modyfikuje się powierzchniowo nanocząstkami metali szlachetnych lub bimetali, korzystnie Pt-Cu, Pt-Pd, Pd-Cu, Au-Pt, Au-Pd, Ag-Pt, Ag-Cu w ilości od 0,01 do 10% molowych w stosunku do półprzewodnika, korzystnie od 0,01 do 1% molowych lub cząstki fotokatalityczne korzystnie domieszkuje się niemetalem z grupy azot, siarka, bor, jod, węgiel w ilości od 0,01 do 30% wagowych w stosunku do półprzewodnika, korzystnie od 0,01 do 15% wagowych lub cząstki fotokatalityczne korzystnie domieszkuje się niemetalem z grupy azot, siarka, bor, jod, węgiel w ilości od 0,01 do 30% wagowych w stosunku do półprzewodnika, korzystnie od 0,01 do 15% wagowych i dodatkowo modyfikuje się powierzchniowo w znany sposób nanocząstkami metali, korzystnie platyny, miedzi, palladu, srebra, złota, rutenu w ilości od 0,01 do 10% molowych w stosunku do półprzewodnika, korzystnie od 0,01 do 1% molowych. Następnie mieszamy trzecią mikroemulsję z mikroemulsję utworzoną z pierwszej i drugiej mikroemulsji, a następnie po co najmniej 10 min mieszania lub uzyskaniu dodatniej wartości potencjału zeta, otrzymane cząstki fotokatalizatora magnetycznego separuje się za pomocą pola magnetycznego, przemywa się wodą, suszy się do stałej masy i kalcynuje się w temperaturze 250–1000°C przez 0,5–5 godzin.

Sposób według wynalazku charakteryzuje się tym, że otrzymany nanokompozyt może wykazywać aktywność w zakresie UV i Vis w wyniku domieszkowania struktury objętościowej półprzewodnika za pomocą związków niemetali, korzystnie z grupy: mocznik, i/lub tiomocznik, i/lub hydrazyna, i/lub amoniak, i/lub kwas jodowy, i/lub jodek potasu, i/lub fluorowodór i/lub jonów metali, korzystnie związków niklu, i/lub kobaltu, i/lub żelaza, i/lub cynku, i/lub rutenu, i/lub wolframu, i/lub miedzi, lub modyfikacji powierzchni za pomocą nanocząstek metali szlachetnych, korzystnie platyny, i/lub palladu, i/lub złota, i/lub srebra oraz nanocząstek metali grup przejściowych, korzystnie miedzi, i/lub rutenu, i/lub cyrkonu, i/lub rodu, i/lub wanadu. W tym celu do mieszaniny reakcyjnej przed dodaniem cząstek fotokatalizatora z grupy: TiO_2, WO_3, ZnO, SnO_2, CdS, i/lub prekursora półprzewodnika, korzystnie tetrabutylo tytanianu, i/lub tetraizopropylo tytanianu, i/lub siarczan tytanylu, i/lub czterochlorek tytanu wprowadza się prekursor nanocząstek metalu i/lub prekursor niemetali z grupy azot, siarka, bor, jod, węgiel w ilości od 0,01 do 30% wagowych w stosunku do TiO_2, korzystnie od 0,01 do 15% wagowych i/lub prekursor cząstek platyny, miedzi, palladu w ilości od 0,01 do 10% molowych w stosunku do TiO_2, korzystnie od 0,01 do 1% molowych, korzystnie otrzymując strukturę warstwy fotokatalitycznej I-TiO_2, N-TiO_2, S-TiO_2, I,C-TiO_2, B-TiO_2, Pt/I-TiO_2, Pt/N-TiO_2, Pd/-I-TiO_2, Pd/N-TiO_2, Cu/I-TiO_2, Cu/N-TiO_2, Pt-Cu-TiO_2, Pt-Pd-TiO_2, Pd-Cu-TiO_2, Au-Pt-TiO_2, Au-Pd-TiO_2, Ag-Pt-TiO_2, Ag-Cu-TiO_2 stosując metodą mikroemulsyjną, zol-żel lub hydrotermalną.

W wariancie realizacji wynalazku modyfikację powierzchniową nanocząstkami metalu szlachetnego, i/lub jonami metali i/lub domieszkowanie niemetalem półprzewodnika z grupy: TiO_2, WO_3, ZnO, SnO_2, CdS, i/lub prekursora półprzewodnika przeprowadza się w mieszaninie reakcyjnej zawierającej cząstki magnetyczne pokryte inertną warstwą. W tym celu do mieszaniny reakcyjnej zawierającej cząstki magnetyczne pokryte warstwą inertną dodaje się prekursor półprzewodnika i/lub nanocząstki półprze-

wodnika oraz roztwory kwasów i/lub soli metali i/lub niemetali tak, aby stosunek domieszki do półprzewodnika wynosił od 0,01 do 30% wag. Modyfikację cząstkami metali korzystnie prowadzi się poprzez redukcję chemiczną za pomocą mocnego reduktora, korzystnie borowodorku sodu lub redukcję termiczną w temperaturze od 300 do 1000°C.

Dzięki wykorzystaniu sposobu według wynalazku otrzymuje się fotokatalizator magnetyczny wielowarstwowy w jednym układzie, bez konieczności separacji poszczególnych jego komponentów. Otrzymane według sposobu opisanego w wynalazku fotokatalizatory magnetyczne można odseparować z fazy wodnej po przyłożeniu gradientu pola magnetycznego. Pętle histerezy dla wybranych fotokatalizatorów magnetycznych wskazują, że nanokompozyty są superparamagnetyczne oraz charakteryzują się wysokim momentem magnetycznym wynoszącym od 15 do 60 emu·g^{-1}. Otrzymane fotokatalizatory magnetyczne wykazują wysoką efektywność degradacji związków organicznych np. fenolu, w tym również związków niepodatnych na rozkład biologiczny, obecnych w ściekach farmaceutycznych takich jak: etodolak, karbamazepina, hydrochlorotiazyd oraz zanieczyszczeń obecnych w płynie technologicznym po wydobyciu węglowodorów niekonwencjonalnych. Charakterystykę właściwości magnetycznych i fotokatalitycznych wybranych nanokompozytów otrzymanych według sposobu wykonania omówionego w niniejszym wynalazku oraz szczegółowy opis wykonania przedstawiono w przykładach i na rysunku, na którym fig. 1 przedstawia zmianę potencjału zeta w funkcji pH dla cząstek magnetycznych Fe_3O_4, SiO_2 i TiO_2 fig. 2 przedstawia wykresy histerezy magnetycznej dla fotokatalizatora magnetycznego $TiO_2/SiO_2/Fe_3O_4$.

Przykład 1

Sposób otrzymywania fotokatalizatora magnetycznego Pt-Pd/TiO_2/SiO_2/Fe_3O_4 *w mikroemulsji w/o aktywnego w zakresie promieniowania UV i Vis*

Do 100 cm^3 0,2M AOT w oktanie dodaje się roztwór wodny zawierający $FeSO_4 \cdot 7H_2O$ i $FeCl_3$ w stosunku molowym Fe^{3+} do Fe^{2+} wynoszącym 2:1. Całość miesza się 30 min w atmosferze gazu obojętnego, azotu. Do pierwszej mikroemulsji dodaje się drugą mikroemulsję, zawierającą amoniak jako odczynnik strącający i substancję podwyższającą pH do 10. Współczynnik R określający stosunek ilości wody do surfaktantu wynosi 4, a stosunek molowy Fe^{3+}:Fe^{2+}:OH^- wynosi 2:1:10. Następnie otrzymuje się trzecią mikroemulsję dodając do 50 cm^3 0,2M AOT w oktanie wody amoniakalnej oraz prekursor cząstek SiO_2 TEOS. Stosunek molowy TEOS do Fe_3O_4 wynosi 10:1. Do mikroemulsji trzeciej dodaje się 0,75 cm^3 roztworu wodnego 50% polietylenoiminy (PEI), po czym trzecią mikroemulsję dodaje się do mikroemulsji w/o powstałej z połączenia mikroemulsji pierwszej i drugiej, utrzymując pH w zakresie 9–9,5. Następnie sporządza się mikroemulsję czwartą 0,2M AOT w oktanie zawierającą w fazie zdyspergowanej 0,1M kwas solny, do której wkrapla się prekursor TiO_2 tetrachlorotytanian tak, aby stosunek molowy TiO_2 do Fe_3O_4 wynosił 2:1. Po 30 min mieszania dodaje się 0,5 cm^3 H_2PtCl_6 i 0,5 cm^3 $PdCl_2$ tak, aby zawartość platyny do TiO_2 wynosiła 0,05% molowych, a zawartość palladu do TiO_2 wynosiła 0,5% molowych. Do mikroemulsji zawierającej cząstki magnetyczne impregnowane krzemionką (mikroemulsja powstała po połączeniu 3 i mieszaniny 1 i 2) wprowadza się mikroemulsję czwartą zawierającą substancję korygującą pH oraz cząstki fotokatalityczne. Wartość pH układu koloidalnego po połączeniu mikroemulsji utrzymuje się w zakresie od 5,5 do 6, a potencjał zeta cząstek wynosi +45 mV. Otrzymaną zawiesinę fotokatalizatora magnetycznego aktywnego w zakresie promieniowania widzialnego, separuje się w znany sposób, suszy się w temperaturze 80°C i kalcynuje w temperaturze 400°C przez 1 h. Właściwości fotokatalityczne zbadano w reakcji degradacji fenolu oraz pirydyny. Stwierdzono, że w wyniku naświetlania promieniowaniem z zakresu UV-Vis w czasie 1 h degradacji uległo odpowiednio 100% fenolu oraz 80% pirydyny, a stopień mineralizacji fenolu i pirydyny wynosił odpowiednio 95% oraz 69%. Magnetyczność nanokompozytu Pt-Pd/TiO_2/SiO_2/Fe_3O_4 wynosiła 34 emu·g^{-1}.

Przykład 2

Sposób otrzymywania fotokatalizatora magnetycznego B-TiO_2/SiO_2/$BaFe_{12}O_{19}$ *w mikroemulsji w/o, charakteryzującego się aktywnością w zakresie Vis*

Do 100 cm^3 0,3M AOT w cykloheksanie dodaje się cząstki $BaFe_{12}O_{19}$ o wielkości 50 nm. Współczynnik R określający stosunek ilości wody do surfaktantu wynosi 5. Następnie otrzymuje się oddzielnie mikroemulsję zawierającą 0,3M AOT w cykloheksanie oraz 2,7 cm^3 wodorotlenku sodu tak, aby pH fazy wodnej mikroemulsji wynosiło 10, dodaje się prekursor cząstek SiO_2 TEOS. Stosunek molowy TEOS do Fe_3O_4 wynosi 12:1. Po 2 h mieszania dodaje się 1,8 cm^3 35% wodnego roztworu polichlorku diallilodimetyloamoniowego (PDDA). Mikroemulsję drugą miesza się z mikroemulsją pierwszą zawierającą cząstki magnetyczne. Następnie sporządza się mikroemulsję trzecią 0,3M AOT w cykloheksanie zawierającą w fazie zdyspergowanej 0,1 cm^3 kwasu azotowego oraz 0,5 cm^3 H_3BO_3, do której wprowadza się

cząstki TiO_2 tak, aby stosunek molowy TiO_2 do $BaFe_{12}O_{19}$ wynosił 3:1, a zawartość boru wynosiła 2% wag. w stosunku do TiO_2. Mikroemulsję trzecią dodaje się do koloidu cząstek magnetycznych impregnowanych krzemionką. Otrzymaną zawiesinę fotokatalizatora B-TiO_2/SiO_2/$BaFe_{12}O_{19}$ aktywnego w zakresie promieniowania widzialnego, separuje się i suszy w znany sposób oraz kalcynuje w temperaturze 400°C przez 1 h. Właściwości fotokatalityczne zbadano w reakcji degradacji fenolu. Stwierdzono, że w wyniku naświetlania promieniowaniem z zakresu Vis (λ>420 nm) 0,2 mM roztworu wodnego fenolu zawierającego 1 g fotokatalizatora, w czasie 1 h degradacji uległo 62% fenolu. Magnetyczność nanokompozytu B-TiO_2/SiO_2/$BaFe_{12}O_{19}$ wynosiła 46 emu·g^{-1}.

Przykład 3

Sposób otrzymywania fotokatalizatora magnetycznego Pd-TiO_2/SiO_2/Fe_3O_4 *aktywnego w zakresie promieniowania UV i Vis*

Do 0,01M dodecylosiarczanu sodu (SDS) dodaje się roztwór wodny zawierający $FeSO_4 \cdot 7H_2O$ i $FeCl_3$ w stosunku molowym Fe^{3+} do Fe^{2+} wynoszącym 2:1. Całość miesza się 30 min w atmosferze gazu obojętnego, azotu i dodaje się wodę amoniakalną do pH 12, tworząc mieszaninę pierwszą zawierającą cząstki magnetyczne. Następnie sporządza się 20% roztwór wodny polietylenoiminy (PEI) (mieszanina druga), do której dodaje się prekursor cząstek SiO_2 TEOS i wodę amoniakalną do pH 11. Stosunek molowy TEOS do Fe_3O_4 wynosi 7:1, a stosunek wagowy PEI do Fe_3O_4 wynosi 0,1% wag. Następnie miesza się ze sobą mieszaninę pierwszą i drugą, otrzymując zawiesinę cząstek magnetycznych impregnowanych krzemionką. Oddzielnie sporządza się mieszaninę trzecią, zawierającą 0,01M roztwór SDS, do którego wprowadza się kwas octowy i dodaje się do 50 cm^3 alkoholu etylowego zawierającego tetraizopropylo tytanian tak, aby stosunek molowy TiO_2 do Fe_3O_4 wynosił 6:1. Następnie do układu zawierającego cząstki magnetyczne pokryte warstwą inertną wprowadza się mieszaninę trzecią, korygując pH w zakresie od 4,5 do 5,5 za pomocą kwasu octowego. Po 30 min mieszania dodaje się 0,5 cm^3 $PdCl_2$ tak, aby zawartość palladu do TiO_2 wynosiła 0,2% molowych. Otrzymaną zawiesinę fotokatalizatora aktywnego w zakresie promieniowania widzialnego, separuje się w znany sposób, suszy się w temperaturze 80°C i kalcynuje w temperaturze 400°C przez 1 h. Właściwości fotokatalityczne zbadano w reakcji degradacji fenolu oraz karbamazepiny. Stwierdzono, że w wyniku naświetlania promieniowaniem z zakresu UV-Vis w czasie 1 h degradacji uległo odpowiednio 100% fenolu oraz 85% karbamazepiny, a stopień mineralizacji fenolu i pirydyny wynosił odpowiednio 95% oraz 83%. Magnetyczność nanokompozytu Pd-TiO_2/SiO_2/Fe_3O_4 wynosiła 26 emu·g^{-1}.

Przykład 4

Sposób otrzymywania fotokatalizatora magnetycznego Pd/I-TiO_2/SiO_2/Fe_3O_4 *aktywnego w zakresie promieniowania Vis*

Do 0,05M lauryloeterosiarczanu sodu wprowadza się zdyspergowane w wodzie cząstki magnetytu (Fe_3O_4) o wielkości 10 nm. Następnie sporządza się mieszaninę drugą zawierającą 30% roztwór wodny polidimetyloaminoepichlorohydryny, do którego dodaje się prekursor cząstek SiO_2 TEOS, korygując pH do wartości 10 za pomocą wody amoniakalnej. Stosunek molowy TEOS do Fe_3O_4 wynosi 4:1, a stosunek wagowy polidimetyloaminoepichlorohydryny do Fe_3O_4 wynosi 0,5% wag. Mieszaninę drugą dodaje się do pierwszej otrzymując cząstki magnetyczne impregnowane krzemionką. Oddzielnie sporządza się mieszaninę trzecią, zawierającą 0,05M roztwór lauryloeterosiarczanu sodu i kwasu azotowego (pH 2), który wprowadza się do tetraizopropylo tytanianu, dodaje się kwas jodowy tak, aby stosunek molowy TiO_2 do HIO_3 wynosił 10:1 i ustala wartość pH w zakresie od 4,5 do 5,5. Po 30 min mieszania dodaje się 0,5 cm^3 $PdCl_2$ tak, aby zawartość palladu do TiO_2 wynosiła 0,5% molowych. Następnie do układu zawierającego cząstki magnetyczne pokryte warstwą inertną wprowadza się mieszaninę trzecią. Otrzymaną zawiesinę fotokatalizatora aktywnego w zakresie promieniowania widzialnego, separuje się w znany sposób, suszy się w temperaturze 80°C i kalcynuje w temperaturze 400°C przez 1 h. Właściwości fotokatalityczne zbadano w reakcji degradacji fenolu i hydrochlorotiazydu. Stwierdzono, że w wyniku naświetlania promieniowaniem z zakresu Vis (λ<400 nm) w czasie 30 min naświetlania degradacji ulega 100% fenolu oraz 80% kwasu benzoesowego, a magnetyczność nanokompozytu Pd/I-TiO_2/SiO_2/Fe_3O_4 wynosi 46 emu·g^{-1}.

Przykład 5

Sposób otrzymywania fotokatalizatora magnetycznego Pd/i-TiO_2/SiO_2/Fe-Ni *aktywnego w zakresie promieniowania Vis*

Postępuje się jak w przykładzie 4, przy czym jako cząstki magnetyczne dodaje się nanocząstki Fe-Ni o wielkości 10 nm tak, aby stosunek molowy TiO_2 do Fe-Ni wynosił 0,5:1, a stosunek molowy

TEOS do Fe-Ni wynosi 1:1. Efektywność degradacji fenolu wynosiła 100% w trakcie 30 min naświetlania, a magnetyzacja 67 emu/g.

Przykład 6

Sposób otrzymywania fotokatalizatora magnetycznego Cu-TiO_2/SiO_2/Fe_3O_4 *aktywnego w zakresie promieniowania Vis*

Do 0,01M dodecylosiarczanu sodu (SDS) dodaje się roztwór wodny zawierający $FeSO_4 \cdot 7H_2O$ i $FeCl_3$ w stosunku molowym Fe^{3+} do Fe^{2+} wynoszącym 2:1. Całość miesza się 30 min w atmosferze gazu obojętnego, azotu i dodaje się wodę amoniakalną do pH 10. Następnie otrzymuje się mieszaninę drugą zawierającą 0,02M roztwór wodny chlorku dodecylotrimetyloamoniowego (DTAC), do której dodaje się prekursor cząstek SiO_2 TEOS w pH zasadowym, korygowanym 1M NaOH do wartości 9. Stosunek molowy TEOS do Fe_3O_4 wynosi 6:1. Następnie mieszaninę drugą zawierającą cząstki krzemionki dodaje się do mieszaniny pierwszej zawierającej cząstki magnetyczne. Oddzielnie sporządza się mieszaninę trzecią zawierającą 0,01M roztwór SDS, do którego wprowadza się kwas azotowy i dodaje się do 50 cm^3 alkoholu etylowego zawierającego tetraizopropylo tytanian tak, aby stosunek molowy TiO_2 do Fe_3O_4 wynosił 1:1, a pH wynosiło 3. Po 30 min mieszania do mieszaniny trzeciej dodaje się $Cu(NO_3)_2$ tak, aby zawartość miedzi do TiO_2 wynosiła 0,1% molowych. Otrzymaną zawiesinę fotokatalizatora (mieszaninę trzecią) dodaje się do zawiesiny cząstek magnetycznych impregnowanych krzemionką, ustalając wartość pH 5. Zawiesinę fotokatalizatora magnetycznego aktywnego w zakresie promieniowania widzialnego, separuje się w znany sposób, suszy się do stałej masy i kalcynuje w temperaturze 400°C przez 1 h. Właściwości fotokatalityczne zbadano w reakcji degradacji fenolu oraz karbamazepiny. Stwierdzono, że w wyniku naświetlania promieniowaniem z zakresu Vis w czasie 1 h degradacji uległo odpowiednio 69% fenolu oraz 58% karbamazepiny, a stopień mineralizacji fenolu i pirydyny wynosił odpowiednio 54% oraz 49%. Magnetyczność nanokompozytu Cu-TiO_2/SiO_2/Fe_3O_4 wynosiła 16 emu·g^{-1}.

Przykład 7

Sposób otrzymywania fotokatalizatora magnetycznego Cu-TiO_2/SiO_2/Fe_3O_4 *aktywnego w zakresie promieniowania Vis*

Do 0,01M dodecylosiarczanu sodu (SDS) dodaje się roztwór wodny zawierający $Fe_3O_4 \cdot 7H_2O$ i $FeCl_3$ w stosunku molowym Fe^{3+} do Fe^{2+} wynoszącym 2:1. Całość miesza się 30 min w atmosferze gazu obojętnego, azotu i dodaje się wodę amoniakalną do pH 10. Następnie wprowadza się 0,02M chlorku dodecylotrimetyloamoniowego (DTAC) oraz dodaje się prekursor cząstek SiO_2 TEOS w pH zasadowym, korygowanym 1M NaOH do pH 9. Stosunek molowy TEOS do Fe_3O_4 wynosi 6:1. Następnie mieszaninę drugą zawierającą cząstki krzemionki dodaje się do mieszaniny pierwszej zawierającej cząstki magnetyczne. Oddzielnie sporządza się 0,01M roztwór SDS, do którego wprowadza się kwas azotowy i dodaje się do 50 cm^3 alkoholu etylowego zawierającego tetraizopropylo tytanian tak, aby stosunek molowy TiO_2 do Fe_3O_4 wynosił 1:1. Następnie do układu zawierającego cząstki magnetyczne pokryte warstwą inertną wprowadza się koloid TiO_2, korygując pH w zakresie od 3,5 do 4. Po 30 min mieszania dodaje się $Cu(NO_3)_2$ tak, aby zawartość miedzi do TiO_2 wynosiła 0,1% molowych. Otrzymaną zawiesinę fotokatalizatora aktywnego w zakresie promieniowania widzialnego, separuje się w znany sposób, suszy się do stałej masy i kalcynuje w temperaturze 400°C przez 1 h. Właściwości fotokatalityczne zbadano w reakcji degradacji fenolu oraz karbamazepiny. Stwierdzono, że w wyniku naświetlania promieniowaniem z zakresu Vis w czasie 1 h degradacji uległo odpowiednio 69% fenolu oraz 58% karbamazepiny, a stopień mineralizacji fenolu i pirydyny wynosił odpowiednio 54% oraz 49%. Magnetyczność nanokompozytu Cu-TiO_2/SiO_2/Fe_3O_4 wynosiła 16 emu·g^{-1}.

Zastrzeżenia patentowe

1. Sposób otrzymywania warstwowego fotokatalizatora magnetycznego polegający na utworzeniu inertnej warstwy wokół cząstki magnetycznej, którą następnie pokrywa się cząstkami fotokatalitycznymi, **znamienny tym**, że w atmosferze gazu obojętnego lub tlenku węgla(IV) sporządza się, cały czas mieszając, mieszaninę reakcyjną, w której korzystnie w atmosferze gazu obojętnego do wodnego i/lub alkoholowego roztworu surfaktantu anionowego, korzystnie 2-etyloheksylosulfonobursztynianu sodu (AOT) i/lub soli sodowej kwasu dodecylosiarkowego (SDS) o stężeniu od 0,01M do 10M, korzystnie od 0,02M do 0,3M dodaje się cząstki magnetyczne, po czym całość miesza się, a następnie sporządza się drugą mieszaninę w ten sposób, że sporządza się alkoholowy i/lub wodny roztwór substancji podwyższającej pH z grupy:

wodorotlenki metali grupy I i II A układu okresowego pierwiastków, amoniak, sole amonowe, aminy, w takiej ilości, aby pH mieszaniny reakcyjnej wynosiło od 7 do 14, korzystnie od 8 do 10, do której dodaje się składnik warstwy inertnej w postaci polimeru poli(N-izopropyloakryloamidu), glikolu polietylenowego, polidimetylosiloksanu i/lub krzemianu sodu i/lub kopolimeru glikolu polietylowego i/lub krzemionki lub węgla korzystnie w postaci grafitu lub grafenu lub prekursora składnika warstwy inertnej, takiego jak tetraetyloortokrzemian (TEOS) i/lub tetrametoksysilan (TMOS), w takiej ilości, aby stosunek molowy składnika warstwy inertnej do cząstek magnetycznych wynosił od 0,01:1 do 30:1, korzystnie od 0,5:1 do 10:1, a następnie cały czas mieszając dodaje się kopolimer kationowy w ilości od 0,01 do 30% wag., korzystnie polidimetyloaminoepichlorohydrynę i/lub polichlorek diallilodimetyloamoniowy (PDDAC) korzystnie w ilości 5% wag. i/lub polietylenoiminę (PEI) korzystnie w ilości od 1 do 5% wag., i/lub surfaktant kationowy, po czym do zawiesiny zawierającej cząstki magnetyczne wkrapla się drugą mieszaninę i ustala się pH powyżej 7, korzystnie w zakresie od 8 do 10, całość miesza się, a następnie sporządza się roztwór trzeci surfaktantu anionowego, korzystnie 2-etyloheksylosulfonobursztynianu sodu (AOT) i/lub soli sodowej kwasu dodecylosiarkowego (SDS) o stężeniu od 0,01M do 10M, korzystnie od 0,02M do 0,3M, zawierający substancję z grupy kwasów organicznych i/lub nieorganicznych w takiej ilości, aby pH wynosiło od 1 do 7, korzystnie od 3 do 6, zawierający cząstki fotokatalityczne półprzewodników z grupy: tlenek tytanu(IV) TiO_2, tlenek wolframu(VI) WO_3, tlenek cynku ZnO, dwutlenek cyny SnO_2, siarczek kadmu CdS, korzystnie TiO_2 korzystnie w postaci prekursora półprzewodnika, korzystnie tetrabutylo tytanian i/lub tetraizopropylo tytanian i/lub siarczan tytanylu i/lub czterochlorek tytanu, w takiej ilości, aby stosunek molowy cząstek fotokatalitycznych do cząstek magnetycznych wynosił od 1:1 do 30:1, korzystnie w zakresie od 1:1 do 4:1, po czym mieszaninę trzecią dodaje się do mieszaniny utworzonej z pierwszej i drugiej, utrzymując pH poniżej 7, korzystnie w zakresie od 3 do 6, po czym po co najmniej 10 min mieszania lub uzyskaniu dodatniej wartości potencjału zeta, otrzymane cząstki separuje się za pomocą pola magnetycznego, przemywa się wodą, suszy się do stałej masy, korzystnie w temperaturze 60–90°C i kalcynuje się w temperaturze 250–1000°C przez 0,5–5 godzin.

2. Sposób według zastrz. 1, **znamienny tym**, że w mieszaninie 2 zamiast kopolimeru kationowego dodaje się surfaktant kationowy, korzystnie bromek heksadecetylo-trimetyloamoniowy (CTAB) i/lub chlorek heksadecylo-trimetyloamoniowy (CTAC), bromek tetradecylotrimetyloamoniowy (HAB) i/lub chlorek dodecylotrimetyloamoniowy (DTAC) i/lub bromek heksadecylopirydyniowy (CPB) o stężeniu od 0,01M do 3M, korzystnie od 0,02M do 0,5M.
3. Sposób według zastrz. 1, **znamienny tym**, że jako cząstki magnetyczne stosuje się dowolny ferryt spinelowy, korzystnie z grupy: MFe_2O_4 (M=Mn, Zn, Fe), $CoFe_{2-x}M_xO_4$ (M=Zn^{2+}, Mn^{2+}), γ-Fe_2O_3, dowolny ferryt heksagonalny, korzystnie $BaFe_{12}O_{19}$, $BaFe_{12}O_{19}$-$M_2Fe_4O_8$ (M=Mn, Fe, Zn), związki z grupy magnesów organicznych, pył żelazowy lub stopy metali i ich nanocząstki o właściwościach magnetycznych, takie jak: Fe-Pt, Co-Pt, Fe-Ni, Fe-Co, Ni-CeO_2, korzystnie Fe-Ni.
4. Sposób według zastrz. 1, **znamienny tym**, że jako cząstki fotokatalityczne stosuje się cząstki fotokatalityczne zmodyfikowane powierzchniowo nanocząstkami metali szlachetnych lub bimetali, korzystnie Pt-Cu, Pt-Pd, Pd-Cu, Au-Pt, Au-Pd, Ag-Pt, Ag-Cu w ilości od 0,01 do 10% molowych w stosunku do półprzewodnika, korzystnie od 0,01 do 1% molowych.
5. Sposób według zastrz. 1, **znamienny tym**, że cząstki fotokatalityczne domieszkuje się niemetalem z grupy azot, siarka, bor, jod, węgiel w ilości od 0,01 do 30% wagowych w stosunku do półprzewodnika, korzystnie od 0,01 do 15% wagowych.
6. Sposób według zastrz. 5, **znamienny tym**, że cząstki fotokatalityczne dodatkowo modyfikuje się powierzchniowo w znany sposób nanocząstkami metali korzystnie platyny, miedzi, palladu w ilości od 0,01 do 10% molowych w stosunku do półprzewodnika, korzystnie od 0,01 do 1% molowych.
7. Sposób otrzymywania warstwowego fotokatalizatora magnetycznego polegający na utworzeniu inertnej warstwy wokół cząstki magnetycznej, którą następnie pokrywa się cząstkami fotokatalitycznymi, **znamienny tym**, że sporządza się pierwszą mikroemulsję korzystnie w atmosferze gazu obojętnego, zawierającą cząstki magnetyczne, surfaktant anionowy, korzystnie 2-etyloheksylosulfonobursztynian sodu w stężeniu od 0,1M do 10M w stosunku do fazy olejowej, ciekłe węglowodory, korzystnie cykloheksan i/lub izooktan i/lub heptan i/lub oktan, przy

czym oddzielnie sporządza się drugą mikroemulsję w/o zawierającą surfaktant anionowy, korzystnie 2-etyloheksylosulfonobursztynian sodu w stężeniu od 0,1M do 10M w stosunku do fazy olejowej, ciekłe węglowodory, korzystnie cykloheksan i/lub izooktan i/lub heptan i/lub oktan, do której wprowadza się składnik warstwy inertnej w postaci polimeru poli(N-izopropyloakryloamidu) glikolu polietylenowego lub polidimetylosiloksanu i/lub krzemianu sodu i/lub krzemionki lub węgla lub grafitu lub grafenu lub prekursora składnika warstwy inertnej, takiego jak tetraetyloortokrzemian (TEOS) i/lub tetrametoksysilan (TMOS), w ilości takiej, aby stosunek molowy składnika warstwy inertnej do cząstek magnetycznych wynosił od 0,01:1 do 20:1, korzystnie od 1:1 do 10:1, dodaje się w fazie wodnej substancję podwyższającą pH z grupy: amoniak i/lub sole amonowe i/lub aminy i/lub wodorotlenek metalu z I i II grupy układu okresowego pierwiastków, tak aby pH wynosiło od 7 do 14, korzystnie od 8 do 12, po czym cały czas mieszając wprowadza się kopolimer kationowy, korzystnie polidimetyloaminoepichlorohydrynę w ilości od 0,01 do 30% wag., polichlorek diallilodimetyloamoniowy (PDDAC) w ilości od 0,1 do 20% wag., korzystnie 0,5% wag. i/lub polietylenoiminy (PEI) w ilości od 0,01 do 20% wag., korzystnie od 1 do 5% wag., po czym drugą mikroemulsję dodaje się do pierwszej i miesza się utrzymując pH w zakresie od 7 do 14 korzystnie od 8 do 12, sporządza się trzecią mikroemulsję w/o zawierającą surfaktant anionowy, korzystnie 2-etyloheksylosulfonobursztynian sodu (AOT) w stężeniu od 0,1M do 10M, korzystnie w cykloheksanie i/lub izooktanie, i/lub heptanie, i/lub oktanie, w fazie wodnej zawierającą substancję z grupy kwasów organicznych i/lub nieorganicznych w takiej ilości, aby pH wynosiło od 1 do 7, korzystnie od 3 do 6, zawierającą cząstki fotokatalityczne półprzewodników z grupy: tlenek tytanu(IV) TiO_2, tlenek wolframu(VI) WO_3, tlenek cynku ZnO, dwutlenek cyny SnO_2, siarczek kadmu CdS, korzystnie TiO_2 korzystnie w postaci prekursora półprzewodnika, korzystnie tetrabutylo tytanian i/lub tetraizopropylo tytanian i/lub siarczan tytanylu i/lub czterochlorek tytanu, w takiej ilości, aby stosunek molowy cząstek fotokatalitycznych do cząstek magnetycznych wynosił od 1:1 do 30:1, korzystnie w zakresie od 1:1 do 4:1, po czym mieszamy trzecią mikroemulsję z mikroemulsją utworzoną z pierwszej i drugiej mikroemulsji, a następnie po co najmniej 10 min mieszania lub uzyskaniu dodatniej wartości potencjału zeta, otrzymane cząstki separuje się za pomocą pola magnetycznego, przemywa się wodą, suszy się do stałej masy i kalcynuje się w temperaturze 250–1000°C przez 0,5–5 godzin.

8. Sposób według zastrz. 7, **znamienny tym**, że jako cząstki magnetyczne stosuje się dowolny ferryt spinelowy, korzystnie z grupy: MFe_2O_4 (M=Mn, Zn, Fe), $CoFe_{2-x}M_xO_4$ (M=Zn^{2+}, Mn^{2+}), γ-Fe_2O_3, dowolny ferryt heksagonalny, korzystnie $BaFe_{12}O_{19}$, $BaFe_{12}O_{19}$-$M_2Fe_4O_8$ (M=Mn, Fe, Zn), związki z grupy magnesów organicznych, pył żelazowy lub stopy metali i ich nanocząstki o właściwościach magnetycznych, takie jak: Fe-Pt, Co-Pt, Fe-Ni, Fe-Co, Ni-CeO_2, korzystnie Fe-Ni.
9. Sposób według zastrz. 7, **znamienny tym**, że do pierwszej mikroemulsji i/lub do drugiej mikroemulsji i/lub do trzeciej mikroemulsji dodaje się ko-surfaktant, korzystnie izopropanol i/lub n-butanol i/lub heksanol o stężeniu od 0,1M do 10M w stosunku do fazy olejowej.
10. Sposób według zastrz. 7, **znamienny tym**, że jako cząstki fotokatalityczne stosuje się cząstki fotokatalityczne zmodyfikowane powierzchniowo nanocząstkami metali szlachetnych lub bimetali, korzystnie Pt-Cu, Pt-Pd, Pd-Cu, Au-Pt, Au-Pd, Ag-Pt, Ag-Cu w ilości od 0,01 do 10% molowych w stosunku do półprzewodnika, korzystnie od 0,01 do 1% molowych.
11. Sposób według zastrz. 7, **znamienny tym**, że cząstki fotokatalityczne domieszkuje się niemetalem z grupy azot, siarka, bor, jod, węgiel w ilości od 0,01 do 30% wagowych w stosunku do półprzewodnika, korzystnie od 0,01 do 15% wagowych.
12. Sposób według zastrz. 11, **znamienny tym**, że cząstki fotokatalityczne dodatkowo modyfikuje się powierzchniowo w znany sposób nanocząstkami metali korzystnie platyny, miedzi, palladu w ilości od 0,01 do 10% molowych w stosunku do półprzewodnika, korzystnie od 0,01 do 1% molowych.

Rysunki

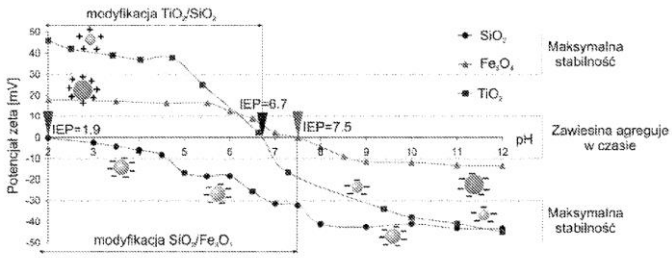

Fig. 1

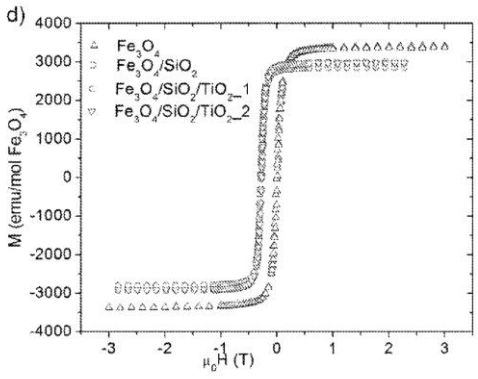

Fig. 2

Departament Wydawnictw UPRP
Cena 2,46 zł (w tym 23% VAT)

7. Mono- and bimetallic (Pt/Cu) titanium(IV) oxide core-shell photocatalysts with UV/Vis light activity and magnetic separability

Zuzanna Bielan, Ewa Kowalska, Szymon Dudziak, Kunlei Wang, Bunsho Ohtani, Anna Zielińska-Jurek

Catalysis Today (2020), Accepted, Journal preprint

DOI: 10.1016/j.cattod.2020.05.034

P7

Journal Pre-proof

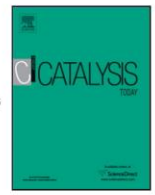

Mono- and bimetallic (Pt/Cu) titanium(IV) oxide core-shell photocatalysts with UV/Vis light activity and magnetic separability

Zuzanna Bielan (Conceptualization) (Visualization) (Investigation) (Writing - original draft), Ewa Kowalska (Supervision) (Resources) (Writing - review and editing), Szymon Dudziak (Formal analysis) (Validation), Kunlei Wang (Investigation), Bunsho Ohtani (Supervision) (Resources), Anna Zielińska-Jurek (Conceptualization) (Supervision) (Writing - review and editing)

PII:	S0920-5861(20)30315-1
DOI:	https://doi.org/10.1016/j.cattod.2020.05.034
Reference:	CATTOD 12884
To appear in:	*Catalysis Today*
Received Date:	1 October 2019
Revised Date:	27 April 2020
Accepted Date:	7 May 2020

Please cite this article as: Bielan Z, Kowalska E, Dudziak S, Wang K, Ohtani B, Zielińska-Jurek A, Mono- and bimetallic (Pt/Cu) titanium(IV) oxide core-shell photocatalysts with UV/Vis light activity and magnetic separability, *Catalysis Today* (2020), doi: https://doi.org/10.1016/j.cattod.2020.05.034

GDAŃSK UNIVERSITY OF TECHNOLOGY
FACULTY OF CHEMISTRY

Mono- and bimetallic (Pt/Cu) titanium(IV) oxide core-shell photocatalysts with UV/Vis light activity and magnetic separability

Zuzanna Bielan[a,b,*], Ewa Kowalska[b], Szymon Dudziak[a], Kunlei Wang[b], Bunsho Ohtani[b], Anna Zielińska-Jurek[a]

[a] *Department of Process Engineering and Chemical Technology, Chemical Faculty, Gdansk University of Technology, 80-233 Gdansk, Poland*

[b] *Institute for Catalysis (ICAT), Hokkaido University, N21, W10, 001-0021 Sapporo, Japan*

* Corresponding author Tel.: + 48 58 347 13 90 (ZB)

e-mail address: bielan_chan@onet.eu (ZB)

Graphical abstract

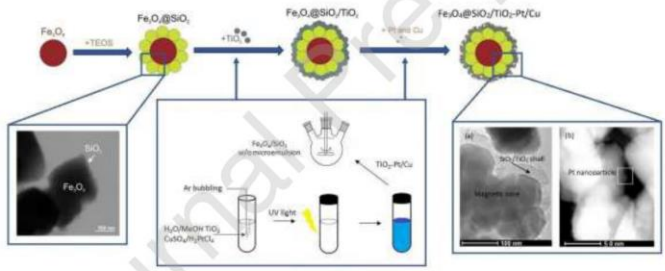

Highlights

- Preparation of magnetically separable $TiO_2/SiO_2/Fe_3O_4$ nanocomposites
- Core-interlayer-shell structure of bimetal-modified magnetic photocatalysts
- High photocatalytic activity of metal-modified magnetic photocatalysts
- $Fe_3O_4@SiO_2/TiO_2$-M revealed high stability after subsequent cycles of degradation

Abstract

Titanium(IV) oxide is one of the most widely investigated photocatalysts. However, separation of nano-sized particulate titania might result in profitless technologies for commercial applications. Additionally, bare titania is almost inactive under the Vis range of solar spectrum due to its wide bandgap. Therefore, the present study aims to prepare novel core-interlayer-shell TiO_2 magnetic photocatalysts modified with metal nanoparticles (Pt, Cu), which exhibit both photocatalytic and magnetic properties, making it easily separable within the magnetic field. Accordingly, the core-shell structure of Fe_3O_4@SiO_2/TiO_2 was obtained in water/TX100/cyclohexane microemulsion. Platinum and copper were photodeposited on four TiO_2 templates and characterized by X-ray diffractometry (XRD), X-ray photoelectron spectroscopy (XPS), specific surface area (BET) measurement and diffuse reflectance spectroscopy (DR-UV/Vis). Photoactivity was studied in the reaction of phenol, acetic acid, and methanol degradation under UV/Vis irradiation, using both polychromatic and monochromatic irradiation (action spectrum analysis). The core-interlayer-shell structure of Pt and Cu modified magnetic photocatalysts was confirmed using scanning transmission electron microscopy (STEM). Magnetic photocatalysts modified with platinum and copper revealed improved photoactivity both in oxidation and reduction photocatalytic reactions, as compared to unmodified Fe_3O_4@SiO_2/TiO_2 photocatalysts. Finally, the correlation between physicochemical properties and photocatalytic activities of Fe_3O_4@SiO_2/TiO_2-Pt/Cu photocatalysts was investigated. For the first time, the effect of metals' loading on the efficiency of phenol degradation and mineralization (TOC removal), and quantum efficiency of reaction in the presence of magnetic photocatalysts were analyzed. It was found that phenol can be

efficiently decomposed (ca. 100%) during 60 min of UV/Vis irradiation for the photocatalyst recovered within the magnetic field during three subsequent degradation cycles.

Keywords: Pt-Cu-modified magnetic photocatalyst, core-shell structure, quantum efficiency, magnetic separation, titania

1. Introduction

In recent years, the importance of photocatalysis using TiO_2 nanoparticles has been increasing in various fields, e.g., wastewater treatment [1], air purification [2], and energy conversion [3], due to their low price, stability, chemical inertness and high photocatalytic efficiency. Nevertheless, there are three limitations to the scaling-up of titania photocatalytic reactions. Firstly, TiO_2 is activated almost only by ultraviolet (UV) light, due to its wide bandgap (ca. 3.0-3.2 eV, depending on polymorphic form) [4–6]. Therefore, the application of artificial irradiation sources (UV lamps) instead of sunlight radiation might increase the costs of the purification process.

The second shortcoming of titania, typical for all semiconductors, is the fast recombination of charge carriers, resulting in much lower than expected quantum yields of photocatalytic reactions. In this regard, much attention has been paid to increase the light absorption in the visible range and to inhibit the recombination rate. Various methods of titania modifications have been proposed, such as surface modification with noble metals (Pt, Ag, Au, Pd) [7–10], doping with non-metals (N, S, C, P, B, I, F) [11–16], heterojunction with other semiconductors [17,18] and sensitization with color compounds (e.g., dyes [19]). Among them, surface modification with noble metals has been the most prevalent since A. Bard [20] introduced it for enhancement of activity under UV irradiation. Recently, noble metal nanoparticles have been used for titania modification to absorb visible light due to localized surface plasmon resonance (LSPR) properties [21,22]. Moreover, the deposition of metallic nanoparticles on the TiO_2 surface could increase photocatalytic activity by (i) reducing the electron-hole recombination,

(ii) increasing the efficiency of interfacial charge transfer, and (iii) generating charge carriers due to light interaction [23–27]. However, the addition of high content of noble metals (1-5%), mainly platinum and gold, could also generate high costs of photocatalyst preparation and even result in an activity decrease due to the "shielding effect." Hence, it is possible to reduce the amount of expensive noble metals by creating bimetallic systems with cheaper metals, e.g., copper or silver [28,29], which also can enhance photocatalytic activity due to synergistic effect between both metals [30–32].

The third challenge in photocatalysis is a separation of semiconductor nanoparticles from post-process suspension. Owing to nanometric particle size, TiO_2 could be detached from the photocatalytic batch system almost only by highly expensive ultrafiltration [33,34]. Alternatively, nanoparticles have been immobilized on solid substrates, such as glass, sand, ceramic balls, zeolites, activated carbon, or optical fibers [35]. However, it should be pointed out that photocatalyst immobilization usually results in a significant decrease in specific surface area and thus decrease in photocatalytic activity. For example, Zielińska-Jurek et al. showed that TiO_2 activity decreased by ca. 30% after its impregnation on a glass substrate [36]. Moreover, the immobilized TiO_2 layer is often unstable, and due to abrasion might be detached during the photocatalytic reactions [37,38]. Therefore, other methods of photocatalyst recovery have been intensively investigated, and magnetic separation is considered as the most prospective. For example, the modification of titanium(IV) oxide with Fe_3O_4 [39,40] and γ-Fe_2O_3 [41,42], as well as other compounds exhibiting magnetic properties [43–45] has been proposed for effective photocatalyst separation from the reaction suspension.

Considering these limitations, in this study, the modification of magnetic titania photocatalyst with noble/semi-noble metals has been proposed, which should result in the preparation of highly active photocatalyst at a wide range of irradiation and easily separation. In the last years, only a few reports regarding metal modified TiO_2 loaded on a magnetic core

material have been reported. For example, Li et al. [46] prepared hierarchical Fe_3O_4@SiO_2@TiO_2@Pt photocatalyst with highly active nanoplatelets of titania with exposed (001) facets. As a photocatalytic shell, Ag-modified TiO_2 was also used [47,48]. However, mono- and bimetal modification of various titanium(IV) oxide templates loaded on magnetic cores has not been reported yet. Moreover, the majority of the reported studies for the photocatalytic activity of magnetic nanocomposites were investigated in the reaction of organic dyes degradation [49–53], which has been considered as unsuitable due to sensitization mechanism by dyes [54,55].

Therefore, the aim of the present study was preparation and characterization of the mono- and bi-metal modified TiO_2 photocatalysts of different polymorphic compositions, additionally deposited on magnetic particles (Fe_3O_4), forming a core-shell structure. An inert silica layer in the structure of the magnetic photocatalyst was introduced to prevent leaching of iron ions into the solution. The effect of noble and semi-noble metals' loading, TiO_2 template on photooxidation of phenol, acetic acid, and methanol dehydrogenation was investigated. Furthermore, for the first time for metal-modified TiO_2 matrices embedded on a magnetic core, quantum efficiency was determined in the phenol oxidation reaction under monochromatic irradiation in the range of 320-620 nm.

2. Materials and methods

Commercial titania samples: ST01 (ST-01, Ishihara Sangyo, Osaka, Japan), ST41 (ST-41, Ishihara Sangyo), and FP6 (Showa Denko K.K., Tokyo, Japan) were supplied as photocatalysts' shell matrix. Other chemicals, including titanium n-butoxide (TBT, 96.0%), cetyltrimethylammonium bromide (CTAB, 98%), magnetite (Fe_3O_4, particles size of about 50 nm, 97%), tetraethyl orthosilicate (TEOS, 99%), chloroplatinic acid hexahydrate (99%), copper(II) sulfate (99.9%), cyclohexane, acetone, methanol, 2-propanol, acetic acid, ammonium hydroxide solution (25%), acetonitrile (HPLC grade), phosphoric acid (HPLC

grade, 85%) and phenol (99.5%) were purchased from Wako Pure Chemicals (Osaka, Japan). All materials were used as received without further purification.

2.1. Preparation of TiO_2-M photocatalysts

Four different types of titania (commercial: ST01, ST41 and FP6, and self-prepared TBT - from titanium n-butoxide hydrolysis) were modified with platinum and/or copper nanoparticles using photodeposition method. The complete procedure was described in our Data in Brief article [56].

2.2. Preparation of magnetic Fe_3O_4@SiO_2/TiO_2-M photocatalysts

The TiO_2-M nanoparticles were deposited on spinel ferrite particles as a thin photocatalytic active shell. Magnetite (Fe_3O_4) was chosen as a core of the designed composite due to its high magnetic properties, which enables to separate obtained photocatalyst in an external magnetic field. Silica was used as an inert interlayer to isolate Fe_3O_4 from TiO_2 and suppress possible electron transfer between them. The magnetic photocatalysts were obtained in w/o microemulsion system based on changes in the particles' surface charge as a function of pH value, which was described in previously published work [57].

In the first part, commercially available Fe_3O_4 nanoparticles with nominate particles diameter of about 50 nm were dispersed in water at pH 10. After this, the prepared suspension was introduced to cyclohexane/isopropanol (100:6 volume ratio) solution in the presence of cationic surfactant, cetyltrimethylammonium bromide (CTAB), creating stable w/o microemulsion system with water nanodroplets dispersed in the continuous oil phase. The molar ratio between water and surfactant content was set at 30. After 2 h of microemulsion stabilization, a corresponding amount of tetraethyl orthosilicate (TEOS) and precipitating agent (ammonia) were added into the microemulsion, resulting in the formation of SiO_2 interlayer. The molar ratios of TEOS to Fe_3O_4 and NH_4OH to TEOS were 8:1 and 16:1, respectively. After 12-h mixing, microemulsion was destabilized by acetone addition and obtained nanocomposite

Fe_3O_4@SiO_2 was separated, washed with ethanol and water, dried at 70 °C to dry mass and calcined at 400 °C for 2 h. Two different types of Fe_3O_4@SiO_2 magnetic matrices were synthesized, marked as z2 and z3, differing by the adding order of TEOS and ammonia, i.e., NH_4OH first and TEOS first, respectively.

In a second step, previously obtained Fe_3O_4@SiO_2 particles were coupled with pure TiO_2 or TiO_2-M to create photocatalytically active shells. As previously, a reversed-phase microemulsion system at pH 10 was used. The Fe_3O_4:TiO_2 molar ratio was set to 1:2. The junction between the magnetic/silica core and the photocatalytic layer was promoted by their opposite surface charges, provided by the presence of CTAB at basic pH. Fe_3O_4@SiO_2/TiO_2 and Fe_3O_4@SiO_2/TiO_2-M samples, after their separation and purification using water and ethanol, were dried at 70 °C to dry mass and calcined at 400 °C for 2 h.

2.3. Characterization of obtained photocatalysts

XRD analyses were performed using the Rigaku Intelligent X-ray diffraction system SmartLab (Tokyo, Japan) equipped with a sealed tube X-ray generator (a copper target; operated at 40 kV and 30 mA). Data were collected in the 2θ range of 5-80°. Scan speed and scan steps were fixed at $1^{o} \cdot min^{-1}$ and 0.01°, respectively. The analysis was based on the International Centre for Diffraction Data (ICDD) database. The crystallite size of the photocatalysts in the vertical direction to the corresponding lattice plane was determined using Scherrer's equation, with Scherrer's constant equals 0.891. Quantitative analysis, including phase composition with standard deviation, was calculated using the Reference Intensity Ratio (RIR) method from the most intensive independent peak of each phase.

Nitrogen adsorption-desorption isotherms (BET method for the specific surface area) were recorded using the Micromeritics Gemini V (model 2365) (Norcross, GA, USA) instrument at 77 K (liquid nitrogen temperature).

The light-absorption properties were measured using diffuse reflectance (DR) spectroscopy, and the data were converted to obtain absorption spectra. The bandgap energy of photocatalysts was calculated from the corresponding Kubelka-Munk function, $F(R)^{0.5}E_{ph}^{0.5}$ against E_{ph}, where E_{ph} is photon energy. The measurements were carried out on JASCO V-670 (Tokyo, Japan), equipped with a PIN-757 integrating sphere. As a reference, BaSO4 or respective bare titania was used.

Samples morphology, as well as core-shell structures formation, were determined by scanning transmission electron microscopy (STEM) equipped with energy-dispersive X-ray spectroscopy (EDS; HITACHI, HD-2000, Tokyo, Japan).

The oxidation states of elements, especially platinum and copper, were determined by XPS measurements on JEOL JPC-9010MC X-ray spectrometer (JEOL Ltd, Tokyo, Japan).

2.4. Measurements of photocatalytic activity

Photocatalytic activity of obtained samples was evaluated in three reaction systems: (1) phenol degradation reaction under UV-Vis irradiation, (2) decomposition of acetic acid under UV-Vis irradiation, and (3) dehydrogenation of methanol under UV-Vis irradiation. For phenol degradation reaction, the 300 W xenon lamp (LOT Oriel, Darmstadt, Germany) was used. A 0.05 g (1 g·dm^{-3}) of a magnetic nanocomposite, where 0.02 g corresponds to photocatalytic active TiO_2, together with 20 mg·dm^{-3} phenol solution was added to 50 cm^3 quartz photoreactor with an exposure layer thickness of 3 cm, and obtained suspension was stirred in darkness for 30 min to provide adsorption-desorption stabilization. After equilibrium was established, photocatalyst suspension was irradiated (60 mW·cm^{-2}) for 60 min under continuously stirring. The constant temperature of the aqueous phase was kept at 20 °C using a thermostated water bath. Every 10 min of irradiation, 1.0 cm^3 of suspension was collected and filtered through a syringe filter (pore size: 0.2 µm) for the removal of photocatalysts particles. The concentration of phenol and formed intermediates was estimated using a reversed-phase high-performance

liquid chromatography (HPLC) system, equipped with a C18 chromatography column with bound residual silane groups (Phenomenex, model 00F-4435-E0) and a UV-Vis detector with a DAD photodiodes array (model SPD-M20A, Shimadzu). The tests were carried out at 45 °C and under isocratic flow conditions of 0.3 ml·min^{-1} and volume composition of the mobile phase of 70% acetonitrile, 29.5% water, and 0.5% orthophosphoric acid. Qualitative and quantitative analysis was performed based on previously made measurements of relevant substance standards [58] and using the method of an external calibration curve. Total organic carbon (TOC) was measured using TOC-L analyzer (Shimadzu, Kyoto, Japan).

For acetic acid decomposition, 0.05 g of nanocomposite (including 0.02 g of pure or metal-modified TiO_2) was suspended in 5 cm^3 of 5 vol% aqueous acetic acid solution. The 30 cm^3 testing tube with as prepared suspension was sealed with a rubber septum and irradiated for 60 min using the 400 W mercury lamp (Hamamatsu Photonics, Hamamatsu, Japan) under continuous stirring and temperature control. Every 20 min, liberated CO_2 in a gas phase was estimated chromatographically using a Shimadzu GC-8A Chromatograph (Shimadzu Corporation, Kyoto, Japan) equipped with thermal conductivity detector (TCD) and Porapak Q column (Agilent Technologies, Santa Clara, CA, USA).

For methanol dehydrogenation, 0.05 g of nanocomposite (0.02 g of TiO_2) was suspended in 5 cm^3 in methanol-water solution (volume ratio 50:50). The obtained suspension was first purged with argon for oxygen removal, and the testing tube was sealed with a rubber septum and irradiated for 1 h using mercury lamp (same reaction system as that used for acetic acid decomposition). Generated hydrogen was determined every 15 min using a Shimadzu GC-8A Chromatograph with TCD detector and MS-5A column (Agilent Technologies).

Additional photoactivity measurements for pure TiO_2 matrices and unmodified Fe_3O_4@SiO_2/TiO_2 nanocomposites were performed in reaction of 4-nitrophenol reduction to 4-aminophenol, based on the studies by Imamura et all. [59] and Brezova et all. [60]. To 50 cm^3

quartz photoreactor, 0.1 g (1 g·dm^{-3}) of pure TiO_2 or magnetic nanocomposite, where 0.04 g corresponds to photocatalytic active TiO_2, was added together with 50 cm^3 500 μM 4-nitrophenol solution in methanol. Oxygen was removed from suspension using nitrogen purging. After complete oxygen removal, the mixture was irradiated for 1 h using 300-W xenon lamp with light intensity set to 30 mW·cm^2. Every 10 min, 1.0 cm^3 of suspension was collected, filtered through a syringe filter, and analyzed using high-performance liquid chromatography (HPLC) system. The measurement of 4-nitrophenol and 4-aminophenol concentration was performed at 45 °C and under isocratic flow conditions of 1 cm^3·min^{-1} and volume composition of the mobile phase of 60% water, 39.5% acetonitrile and 0.5% orthophosphoric acid.

2.5. Quantum efficiency of photocatalytic phenol degradation

Apparent quantum efficiency was determined in phenol oxidation reaction under monochromatic irradiation. The generation of 1,4-benzoquinone (BQ; intermediate phenol product) was quantified at seven irradiation wavelengths: 320, 380, 440, 450, 500, 560, and 620 nm. 0.03 g of nanocomposite (0.012 g of photocatalytic active TiO_2) and 3 cm^3 of phenol solution (c = 20 mg·dm^{-3}) were placed in a quartz cuvette and irradiated with monochromatic light emitted by a diffraction grading type illuminator Jasco CRM-FD (Jasco Corporation, Tokyo, Japan). Irradiation intensity was set in the range of 7.2 - 9.9 mW·cm^{-2} and measured using a Hioki 3664 Optical Power Meter (Hioki EE Corporation, Nagano, Japan). The concentration of formed BQ was determined chromatographically using the Shimadzu LC-6A system equipped with the WAKOSIL-II 5C18 AR column (FUJIFILM Wako Pure Chemical Corporation, Osaka, Japan) and a UV-Vis detector (model SPD-6A, Shimadzu). The tests were performed at 45 °C and under isocratic flow conditions of 1 cm^3·min^{-1} and volume composition of the mobile phase of 70% water, 29.5% acetonitrile, and 0.5% orthophosphoric acid. The detection wavelength was set at 254 nm.

3. Results and discussion

3.1. Physicochemical characterization of obtained nanocomposites

Exemplary XRD patterns for Fe_3O_4@SiO_2/TiO_2-M samples are presented in Fig.1a-b with detailed crystal phase composition and crystallite sizes for all samples being listed in Tables S1-S6 in Supplementary Material. For magnetic composites, the presence of crystalline phases of both magnetite and TiO_2 was detected in all patterns, with the diffraction peaks for Fe_3O_4 inverse cubic spinel structure at 30.1°, 35.6°, 43.3°, 57.2°, 62.8° (ICDD card No 9002319) and anatase as main TiO_2 polymorph at 25°, 37.8°, 47.9°, 53.8°, 54.9°, 62.6°, 68.7° and 70° (ICDD card No 9009086). The content of magnetite crystalline phases varied from 28.3% to 35% for ST01 and FP6 samples, respectively, for composites without deposited metals. For Fe_3O_4@SiO_2/TBT-M nanocomposites, in opposite to previously described TiO_2-M [56], the brookite phase was not detected probably due to additional thermal annealing process after preparation of the core-shell structure of magnetic photocatalyst. Interestingly, the content of the rutile phase in the FP6 sample decreased significantly after the preparation of magnetic nanocomposites. For example, the anatase to rutile ratio increased from 3.6 for bare FP6 sample to 45.7 for magnetic composite containing 0.5% Cu ([56] and Table S4 in Supplementary Material). Therefore, brookite – anatase transition, as well as amorphous phase – anatase transition related to additional calcination of Fe_3O_4@SiO_2/TiO_2-M nanocomposites, is proposed as one of the possibilities [61]. The presence of amorphous silica was confirmed by enlargement of the patterns between 15 and 25 reflection angles [53,62]. The presence of platinum and copper was not approved by XRD analysis (no peaks for platinum or copper) due to their low content (0.05-0.5 mol%) and nanometric size. No other crystalline phases were identified in the patterns, which indicated the crystal purity of the obtained composites.

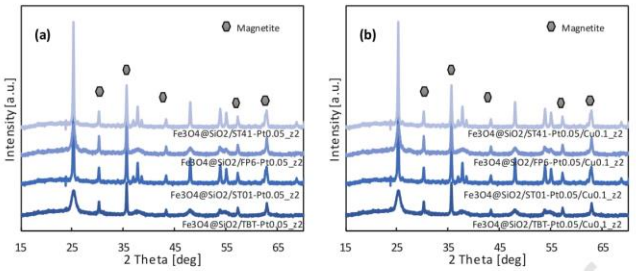

Fig. 1. XRD patterns of mono-metal (a) and bi-metal (b) Fe_3O_4@SiO_2/TiO_2-M magnetic photocatalysts

The photoabsorption properties of the prepared magnetic materials were studied by diffuse reflectance spectroscopy, and exemplary data are shown in Fig. 2. As a representative for magnetic nanocomposite, Fe_3O_4@SiO_2/TBT-Pt0.05_z2 was compared with the metal-modified TBT matrix. The light absorption was extended in the range above 400 nm for the obtained nanocomposites. Previously, the red-shifted light absorption was observed for TiO_2-SiO_2 shell coating the magnetic core [63]. The absorption at the Vis range for TBT-Cu0.5 and TBT-Pt0.05, presented by Bielan et al. [56], confirmed that noble metals were successfully deposited on the titania surface. Although for platinum the plasmonic peaks could be observed for all Pt-modified samples (spectra with bare titania as a reference) with maximum absorption at ca. 380-420 nm [64], the copper exists as an oxidation state-mixed form (i.e., zero-valent, Cu_2O and CuO), because of its easy oxidation in air, as already reported for other Cu-modified titania samples [65,66].

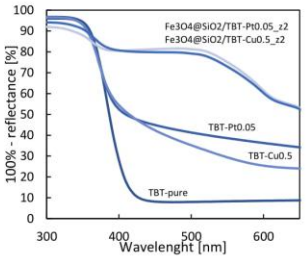

Fig. 2. Exemplary DR-UV/Vis spectra of nanocomposites with $BaSO_4$ as a reference.

The specific surface area (BET) data for the obtained magnetic core-shell titania-based nanocomposites are presented in Tables S7-S8 in the Supplementary Materials. After introducing titania photocatalyst (bare or modified) on the Fe_3O_4@SiO_2 magnetic core, the specific surface area increased significantly due to the presence of a highly porous silica interlayer (Table S7). It was found that the highest BET for monometallic samples was obtained for magnetic nanocomposites modified with 0.05 mol% of Pt reaching 160, 170, 110, and 119 $m^2 \cdot g^{-1}$ for TBT, ST01, FP6, and ST41, respectively, suggesting the presence of non-aggregated fine nanoclusters of platinum. There was no meaningful difference between the BET specific surface area of mono- and bimetallic magnetic nanocomposites.

The STEM analyses were performed to confirm the core-shell structure as well as the presence of platinum and copper on the titania surface. The exemplary results for Fe_3O_4@SiO_2/TBT-Pt0.05_z2 sample as a representative magnetic nanocomposite are presented in Fig. 3.

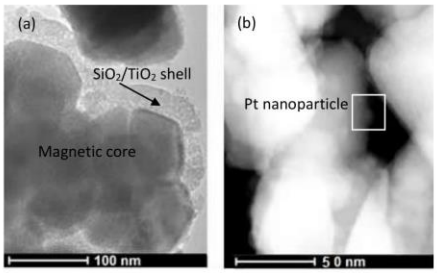

Fig. 3. STEM images of Fe_3O_4@SiO_2/TBT-Pt0.05_z2 nanocomposite

The analysis confirmed the formation of a photocatalytic coating on the magnetic Fe_3O_4 core. Magnetite particles with a size of about 50 nm tended to agglomerate, which led to creating about 20 nm SiO_2/TiO_2 shell on the entire agglomerated surface. Pt nanoparticles of the average diameter smaller than 10 nm were uniformly distributed on the surface.

The surface properties and oxidation state of elements were investigated by X-ray photoelectron spectroscopy (XPS), and the obtained results for three different magnetic nanocomposites containing ST01 titania shell are shown in Table 1 and Fig. 4.

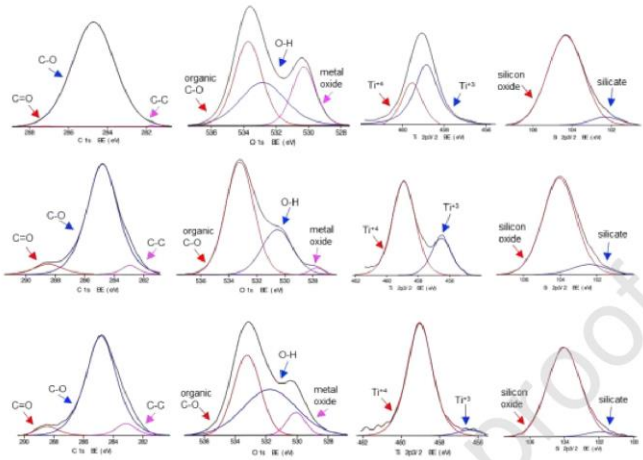

Fig. 3. Deconvolution of X-ray photoelectron spectroscopy (XPS) spectra for C 1s, O 1s, Ti $2p_{3/2}$ and Si $2p_{3/2}$ for Fe_3O_4@SiO_2/ST01-s_z2, Fe_3O_4@SiO_2/ST01-Pt0.05_z2 and Fe_3O_4@SiO_2/ST01-Pt0.05/Cu0.1_z2 samples (from the top)

Table 1. X-ray photoelectron spectroscopy (XPS) analysis of Ti, O, C, Fe, Si, Pt and Cu

Sample	Content (at.%)						
	Ti 2p	O 1s	C 1s	Fe 2p	Si 2p	Pt 4f	Cu 2p
Fe_3O_4@SiO_2/ST01-s_z2	3.12	34.07	50.36	1.87	10.59	-	-
Fe_3O_4@SiO_2/ST01-Pt0.05_z2	8.21	50.56	24.15	0.09	16.96	0.04	-
Fe_3O_4@SiO_2/ST01-Pt0.05/Cu0.1_z2	3.34	36.58	48.85	0.02	10.97	0.11	0.11

Although the same content of platinum was used for modification, the surface content of platinum was almost three times higher in the magnetic bimetallic nanocomposite, which might suggests that co-deposition of copper could result in formation of larger nanoparticles than that in the case of simple Pt deposition on fine titania (probably nano-sized Pt clusters). The presence of copper was confirmed in the bimetallic sample, reaching 0.11 at. %. Iron content

ranged from 0.02 at.% for Fe_3O_4@SiO_2/ST01-Pt0.05/Cu0.1_z2 to 1.87 at.% for Fe_3O_4@SiO_2/ST01-s_z2, which was expected for core-shell nanostructure, and confirmed that the core was composed of magnetite. The Fe 2p signal was deconvoluted into 709 and 711 eV peaks, corresponding to FeO and Fe_2O_3 co-present in magnetite. The comparison between magnetic samples also suggested that platinum might replace oxygen (the smallest O/(Ti+Si) ratio), as already published for other titania samples [50]. Interestingly, the highest O/(Ti+Si) ratio for bimetallic magnetic composite confirmed the presence of copper oxides rather than zero-valent copper. The Ti 2p peak could be divided into 456 eV and 459 eV binding energies and identified as Ti^{3+} and Ti^{4+}, respectively. Ti^{4+} was a dominant surface state for the most samples. However, it should be pointed out that the Ti^{3+} content in magnetic composites was quite high, suggesting titanium reduction during the microemulsion method. Silicon (Si 2p) appeared in two forms: silicate (102 eV) and silicon oxide (104 eV), among which SiO_2 state is dominant (90-96%). Carbon was detected in all analyzed samples and varied from 24.15 to even 50.36 at.%, which is typical for all titania (and others) samples, and mainly originated from carbon(IV) oxide adsorption from surrounding air.

The oxygen to titanium and titanium/silicon ratio exceeded the expected one (2.0 considering only SiO_2 and/or TiO_2, as Fe_3O_4 core is almost undetectable) for nearly all analyzed samples, reaching 2.5, 2.0 and 2.6 for ST01: bare on magnetic core, modified with 0.05 mol% Pt on magnetite and modified with 0.05 mol% Pt and 0.1 mol% Cu on magnetic core, respectively. The enrichment of the surface with oxygen (mainly in the form of hydroxyl groups) is common and often reported for different titania photocatalysts [67].

3.2. Photoactivity of mono- and bimetallic Fe_3O_4@SiO_2/TiO_2 nanocomposites

Firstly, photoactivity of core-shell non-metal modified Fe_3O_4@SiO_2/TiO_2 nanocomposites was studied in methanol dehydrogenation and acetic acid decomposition. The obtained results, in comparison with pure TiO_2 matrices, are shown in Fig. 5a-d.

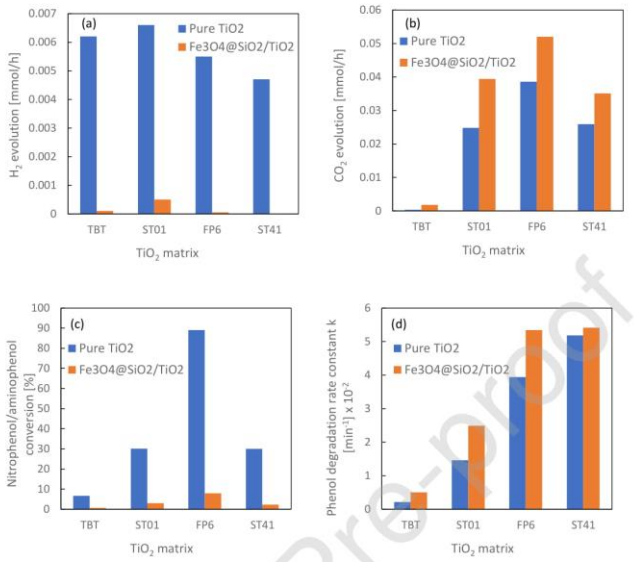

Fig. 5. H_2 evolution (a) and acetic acid oxidation to CO_2 (b) as well as nitrophenol/aminophenol conversion percentage (c) and phenol oxidation rate constant k (d) as a function of TiO_2 matrix for pure TiO_2 and Fe_3O_4@SiO_2/TiO_2 nanocomposites

Performed observations remained similar to pure TiO_2-M systems [56] with the highest activity towards H_2 generation and acetic acid oxidation to CO_2 for samples containing anatase particles in the shell layer, pure ST01, and FP6 respectively. However, some differences were visible considering the exact value of the monitored process, with H_2 evolution being especially suppressed. On the other hand, the efficiency of acetic acid decomposition was promoted for Fe_3O4@SiO_2 surface coated with TiO_2 particles (Fig. 5b), which suggests that obtained magnetic nanocomposites are more suitable for oxidation processes rather than reduction due to the development of the specific surface area and formation of TiO_2-SiO_2 photocatalytic layer

for Fe_3O_4@SiO_2/TiO_2 nanocomposites in opposite to pure TiO_2 particles. For further confirmation of the presented thesis, additional measurements of photocatalytic activity in the reduction of 4-nitrophenol to 4-aminophenol as well as phenol oxidation reaction were performed. The described dependencies are shown in Figure 5 c,d. For phenol oxidation reaction, presented as constant rate k, the core-shell magnetic photocatalysts revealed significantly higher activity than pure TiO_2 matrices, while the opposite trend was observed for photoconversion of 4-nitrophenol to 4-aminophenol, with the highest efficiency for FP6 matrix.

Further differences were also observed for magnetic photocatalysts modified with Pt and Cu nanoparticles, as presented in Fig. 6 a,d.

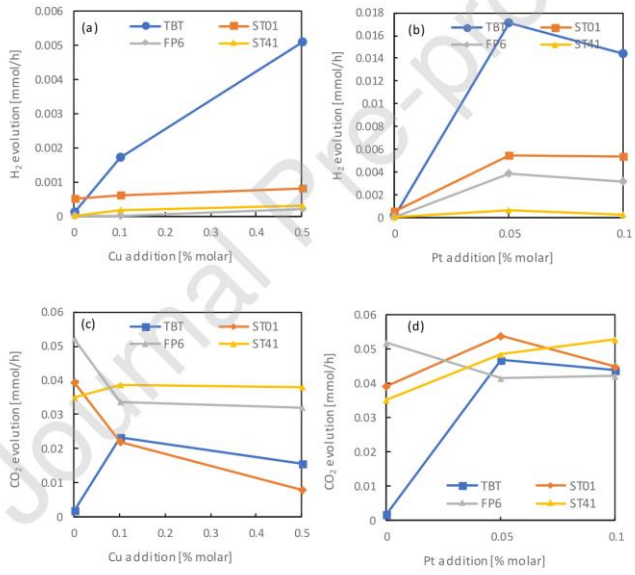

Fig. 6. The effect of metal loading on photocatalytic activity for: H_2 evolution (a-b), and acetic acid oxidation to CO_2 (CO_2 evolution) (c-d) for monometallic Fe_3O_4@SiO_2/TiO_2-M samples

Regarding H_2 evolution, a strong trend to promote the process in TBT-based systems was observed both for Cu and Pt modified samples; however, as presented in Fig. 6a-b, nearly ten times higher activity was observed for Pt-modified magnetic photocatalysts than for Cu-modified magnetic nanocomposites. Moreover, very little difference was observed between 0.05% and 0.1% platinum loading, which led to the observation that the metal presence, rather than its concentration, is the main factor affecting process efficiency in overall results. Regarding acetic acid degradation, the highest efficiency was observed for ST41 based samples, with no dependence on the character of the modification. In general, Cu presence decreased process efficiency in most cases, and pure FP6 matrices (a mixture of anatase and rutile) allowed to achieve a high degradation rate, while ST41 (anatase particles) synergizes with Pt nanoparticles. Moreover, TiO_2 particles obtained from TBT hydrolysis (fine anatase NPs), as well as, commercial TiO_2 ST01 consist also fine anatase particles modified with both Cu and Pt exhibited higher photoactivity than FP6 (mixture of anatase and rutile NPs) and ST41 (large anatase NPs), being weak or almost not affected by the presence of modifications. In the case of H_2 evolution, TiO_2 metal-modification allows to markedly improvement of process efficiency in Fe_3O_4@SiO_2/TBT core-shell systems since practically no activity was observed for samples without deposited metal nanoparticles (see in Figure 6). However, for acetic acid degradation, a strong matrix effect was observed, leading to the highest activity of ST41 and FP6 -based samples, despite them being less affected by both metals. Ultimately it can be stated that FP6 based composites, consists a mixture of anatase and rutile, possess the highest activity towards acetic acid degradation, while ST41 (large anatase NPs) achieved its maximum after modification with Pt nanoparticles only.Additional analyses were performed to evaluate the possible effect of combining Fe_3O_4@SiO_2 cores with TiO_2-M photocatalysts based on different TiO_2 matrices. It was found that both z2 (sample obtained by adding NH_4OH to TEOS), and z3 (sample obtained by addition of and TEOS/NH_4OH) are suitable for further modification, with

almost the same efficiency towards acetic acid degradation and some increase in H_2 generation in favor of z3 matrice, as shown in Fig. 7a-b.

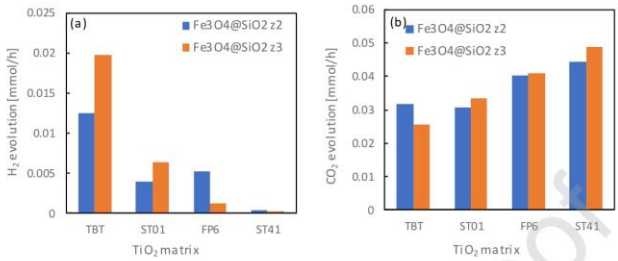

Fig. 7. H_2 (a) and acetic acid oxidation to CO_2 (b) for Fe_3O_4@SiO_2/TiO_2-M nanocomposites as a function of different Fe_3O_4@SiO_2 magnetic cores

Further analysis showed that the TBT-based photocatalyst layer in the structure of magnetic composite was especially active towards H_2 generation when combined with the z3 sample, while FP6 worked well with the z2 sample. Since, as presented in Data in Brief, TBT-based TiO_2-M photocatalysts were found to be favorable for H_2 production in general, this explains why in overall results, magnetic core material covered with TiO_2 anatase obtained from TBT (TBT shell samples) were more suitable and highly active in hydrogen evolution. On the other hand, no significant interactions between Fe_3O_4@SiO_2 magnetic samples and all TiO_2-M photocatalytic matrices were observed for acetic acid oxidation.

Finally, to confirm the observed dependencies, additional analyses of phenol oxidation were performed for mono- and bimetallic Fe_3O_4@SiO_2/TiO_2-M samples. Their overall results, presented as phenol degradation rate constant k and TOC removal, were compared with previously described acetic acid degradation efficiency. Obtained results, presented in Fig. 8 a-h, were in good agreement with the ones described for acetic acid, showing a high positive effect of Pt addition, together with its negative interactions with Cu and no impact of

Fe_3O_4@SiO_2 core selection. The selection of TiO_2 matrix also showed a similar impact to previously described. The highest activity was noticed for magnetic composites containing the photocatalyst layer of TiO_2 FP6 (a mixture of anatase and rutile) as well as TiO_2 ST41 (large anatase particles).

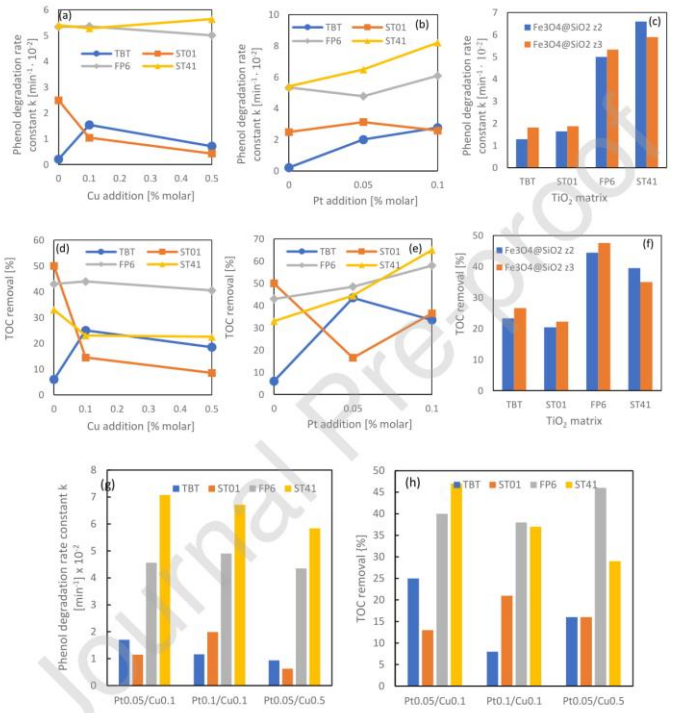

Fig. 8. Phenol degradation rate constant k and TOC removal for mono- (a-f) and bimetallic (g-h) nanocomposites. The effect of TiO_2 matrix, Fe_3O_4@SiO_2 matrices as well as Cu and Pt content.

Analyzed results are in good agreement with the study reported by Zielińska-Jurek et al. [68]. Large decahedral anatase particles (DAP) with crystalline size about 70 nm modified with 0.1 mol% of Pt nanoparticles exhibited the highest photocatalytic activity in phenol degradation reaction in UV-Vis irradiation range. It is also worth mentioning that Pt nanoparticles embedded on DAP surface were much bigger (17 nm) than nanoparticles on other TiO_2 matrices (ca. 5 nm). Similar high activity for ST41 TiO_2 was presented by Ohno et al. in the photocatalytic oxidation of adamantane [69]. Different situation was reported by Xie et al. [70] in their work regarding CO_2 reduction by various titania phases. Moreover, anatase/rutile and anatase/brookite mixed phases semiconductors could form a phase junction, where electrons could migrate from a higher conduction band (CB) to lower CB, promoting photogenerated charge carriers' separation [70–72]. Moreover, for methanol dehydrogenation the presence and properties of co-catalyst (noble metals) are the most crucial for being reaction centers [73].

3.3.Quantum efficiency analysis

The dependence of phenol degradation quantum efficiency on the irradiation wavelength (action spectrum) is presented in Fig. 9. Quantum efficiency was determined for mono- and bimetallic ST01-M and corresponding Fe_3O_4@SiO_2/ST01-M magnetic photocatalysts.

In the UV light range, the highest quantum yields were achieved by bimetallic photocatalysts, in which the ST01 surface was simultaneously modified with platinum and copper. For Fe_3O_4@SiO_2/ST01-M magnetic nanocomposites, bimetallic Fe_3O_4@SiO_2/ST01-Pt0.05/Cu0.1_z2 had almost twice as high performance as Fe_3O_4@SiO_2/ST01-Pt0.05_z2 (with only platinum in its structure). The ST01-Cu0.1 photocatalyst had the lowest quantum efficiency among the modified semiconductors. It is obvious that co-presence of platinum and copper results in a significant enhancement of Vis response. Although in the case of platinum, the mechanism is clear, i.e., platinum works as an electron sink (well-known since Bard studies [20]), the mechanism for copper-modified titania is not so obvious [74], including p-n junction,

Z-scheme electron transfer, Schottky barrier formation, and more complex charge carriers' transfer between various forms of copper (Cu_2O, CuO, Cu_xO, Cu) and titania. It has been proposed that Z-scheme electron transfer would be the most advisable (i.e., recombination of electrons from conduction band (CB) of titania with holes from valence band (VB) of copper oxides), resulting in highly reactive electrons in CB of copper oxides (more negative potential than that in titania) and holes in VB of titania (more positive potential than that in copper oxides) [18]. The present study suggests that in UV light range the co-presence of platinum might result in the formation of efficient Z-scheme photocatalyst., i.e., second-generation Z-scheme (all-solid-state (ASS) Z-scheme), in which platinum could work as an efficient conductor between copper oxide and titania [75].

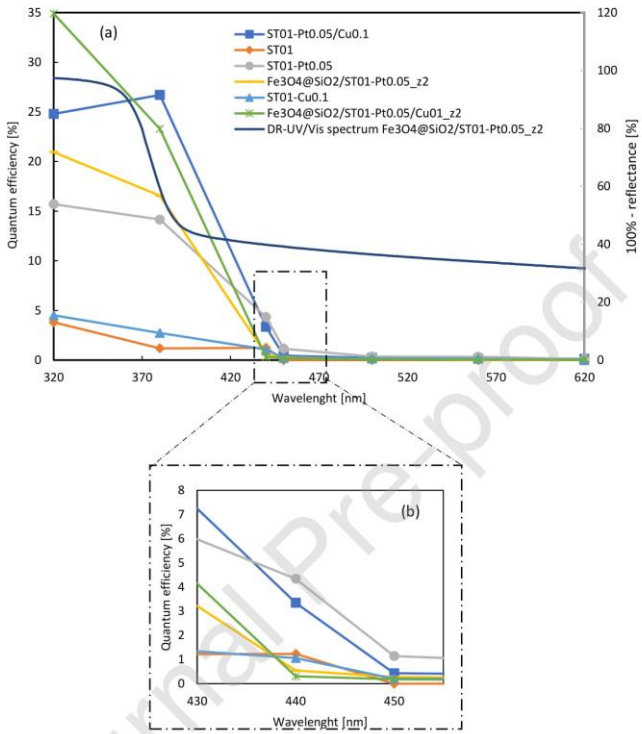

Fig. 9. Action spectra of phenol degradation for obtained nanocomposites: (a) at whole range of irradiation, and (b) at 430 - 455 nm field (magnification).

In the visible light range (> 420 nm), an apparent decrease in quantum efficiency was observed because of insufficient excitation of titania (absorption edge at ca. 400 nm). The slight activity even at 440 nm for bare titania could be explained by defects' presence, typical for almost all commercial titania samples ("self-doped" titania), which might result in slight Vis

response, i.e., excitation to/from defects (such defects have already been reported for ST01 at ca. 0-0.4 eV below CB bottom by reverse double-beam photoacoustic spectroscopy [76]). Platinum-modified samples showed the highest Vis activity confirming that plasmon resonance of platinum should activate titania [28]. Moreover, the Vis activity for magnetic composites was much lower comparing to TiO_2-M, which may result from competitive charge carriers' transfer between metal nanoparticles as well as titania. The previous study on hybrid photocatalysts (ruthenium complexes and plasmonic nanoparticles [77]) and some bimetallic photocatalysts (Au(core)/Ag(shell) [78]) indicated the enhanced charge carriers' recombination instead of their efficient separation in the case of photocatalysts modified by two modifiers. Based on our previous studies [28–30,68], the Pt particle size, which depends on (i) TiO_2 support type, (ii) reducing agent, (iii) annealing temperature, and (iv) metallic structure on TiO_2 support is crucial in Vis light activity. Therefore, the additional calcination of Fe_3O_4@SiO_2/TiO_2-M nanocomposites could have resulted in metal particles re-arrangement, their aggregation, and finally, in the observed lower photocatalytic activity compared to TiO_2-M photocatalysts.

3.4. Reusability of magnetic nanocomposites

The reusability of magnetic nanocomposites was studied in phenol degradation reaction in three subsequent cycles. Bimetallic Fe_3O_4@SiO_2/ST41-Pt0.05/Cu0.1_z2 was selected due to its excellent photocatalytic activity. After each 60 min cycle, nanocomposite was separated using a magnetic field and used in another run without any treatment. The obtained results are presented in Fig. 10. No loss in degradation was observed after three cycles of phenol degradation process. Thus, the magnetic nanocomposites revealed excellent stability and reusability.

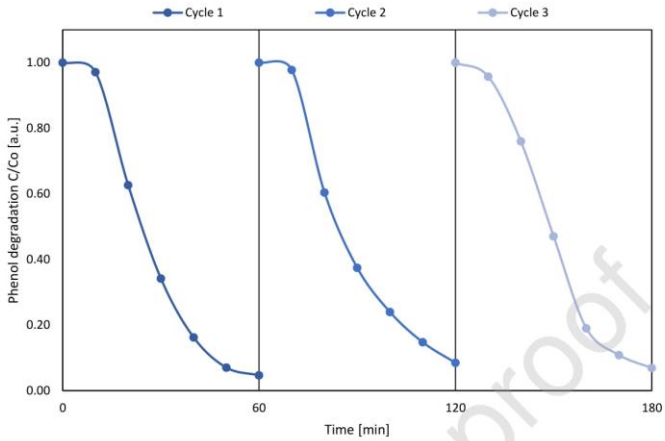

Fig. 10. Phenol degradation efficiency measured in three subsequent cycles in the presence of Fe_3O_4@SiO_2/ST41-Pt0.05/Cu0.1_z2

4. Conclusions

Mono- and bimetallic magnetic nanocomposites Fe_3O_4@SiO_2/TiO_2-M were successfully prepared using w/o microemulsion method. The core-interlayer-shell structure, where core was magnetic Fe_3O_4, inert interlayer was SiO_2, and a shell was composed of TiO_2 modified with Pt and Cu, allowed to increase both photocatalytic activity and separability. Action spectra for phenol decomposition correlated with corresponding absorption spectra for Pt-modified titania, and thus confirming that even its low content (0.05 mol%) could activate titania under Vis irradiation due to plasmon resonance of platinum. However, the co-existence of copper and platinum nanoparticles was beneficial only under UV light. In the Vis range decrease in activity was observed, suggesting that their co-deposition might work as charge carriers' recombination center. The most important finding was that introducing of magnetic nanoparticles as a core for

Fe_3O_4@SiO_2/TiO_2 and Fe_3O_4@SiO_2/TiO_2-M did not negatively influence the photocatalytic performance, as reported for immobilized photocatalysts. What is more, Fe_3O_4@SiO_2/TiO_2 revealed higher photocatalytic activity than pure TiO_2 in oxidation reactions (phenol and acetic acid decomposition). Moreover, along with excellent photocatalytic properties in the solar spectrum range, the outstanding stability, tested in three subsequent cycles of phenol decontamination, suggested the possibility of commercial application of magnetic nanocomposites for environmental purification.

CRediT author statement:

Zuzanna Bielan: Conceptualization, Visualization, Investigation, Writing-Original Draft

Ewa Kowalska: Supervision, Resources, Writing – Review and Editing

Szymon Dudziak: Formal analysis, Validation

Kunlei Wang: Investigation

Bunsho Ohtani: Supervision, Resources

Anna Zielińska-Jurek: Conceptualization, Supervision, Writing – Review and Editing

Declaration of interests

The authors declare that they have no known competing financial interests or personal relationships that could have appeared to influence the work reported in this paper.

Acknowledgements

This work was supported by the Polish National Science Centre (Grant No. NCN 2016/23/D/ST5/01021) and Gdansk University of Technology by InterPhD II (POWER) project (No. POWR.03.02.00-IP.08-00-DOK/16). Z.B. would like to highly acknowledge Dr. Maya Endo-Kimura from the Institute for Catalysis, Hokkaido University, Japan, for the inestimable help during conducting research.

References

[1] J.A. Fernandez, A. Suan, J.C. Ramirez, J. Robles, J.C. Salcedo, A.M. Pedroza, C.E. Daza, Treatment of real wastewater with TiO2-films sensitized by a natural-dye obtained from Picramnia sellowii, J. Environ. Chem. Eng. 4 (2016) 2848–2856. doi:10.1016/j.jece.2016.05.037.

[2] I. Wysocka, A. Markowska-Szczupak, P. Szweda, J. Ryl, M. Endo-Kimura, E. Kowlaska, G. Nowaczyk, A. Zielińska-Jurek, Gas- phase removal of indoor volatile organic compounds and airborne microorganisms over mono - and bimetal - modified (Pt , Cu , Ag) titanium(IV) oxide nanocomposites, Indoor Air. 00 (2019) 1–14. doi:10.1111/ina.12595.

[3] M. Matsuoka, M. Kitano, M. Takeuchi, K. Tsujimaru, M. Anpo, J.M. Thomas, Photocatalysis for new energy production. Recent advances in photocatalytic water splitting reactions for hydrogen production, Catal. Today. 122 (2007) 51–61. doi:10.1016/j.cattod.2007.01.042.

[4] A. Ofiarska, A. Pieczyńska, A. Fiszka Borzyszkowska, P. Stepnowski, E.M. Siedlecka, Pt-TiO2-assisted photocatalytic degradation of the cytostatic drugs ifosfamide and cyclophosphamide under artificial sunlight, Chem. Eng. J. 285 (2016) 417–427. doi:10.1016/j.cej.2015.09.109.

[5] A. Zielińska-Jurek, Z. Wei, I. Wysocka, P. Szweda, E. Kowalska, The effect of nanoparticles size on photocatalytic and antimicrobial properties of Ag-Pt/TiO<inf>2</inf> photocatalysts, Appl. Surf. Sci. 353 (2015) 317–325. doi:10.1016/j.apsusc.2015.06.065.

[6] M. Długokęcka, J. Łuczak, Ż. Polkowska, A. Zaleska-Medynska, The effect of microemulsion composition on the morphology of Pd nanoparticles deposited at the surface of TiO2 and photoactivity of Pd-TiO2, Appl. Surf. Sci. 405 (2017) 220–230. doi:10.1016/j.apsusc.2017.02.014.

[7] M. Klein, E. Grabowska, A. Zaleska, Noble metal modified TiO2 for photocatalytic air purification, Physicochem. Probl. Miner. Process. 51 (2015) 49–57.

[8] E. Grabowska, M. Marchelek, T. Klimczuk, G. Trykowski, A. Zaleska-Medynska, Noble metal modified TiO2 microspheres: surface properties and photocatalytic activity under UV–vis and visible light, J. Mol. Catal. A Chem. 423 (2016) 191–206. doi:10.1016/j.molcata.2016.06.021.

[9] E. Borowska, J.F. Gomes, R.C. Martins, R.M. Quinta-Ferreira, H. Horn, M. Gmurek, Solar Photocatalytic Degradation of Sulfamethoxazole by TiO2 Modified with Noble Metals, Catalysts. 9 (2019) 1–19.

[10] M. Endo, Z. Wei, K. Wang, B. Karabiyik, K. Yoshiiri, P. Rokicka, B. Ohtani, A. Markowska-Szczupak, E. Kowalska, Noble metal-modified titania with visible-light activity for the decomposition of microorganisms, Beilstein J. Nanotechnol. 9 (2018) 829–841. doi:10.3762/bjnano.9.77.

[11] H. Irie, Y. Watanabe, K. Hashimoto, Nitrogen-Concentration Dependence on Photocatalytic Activity of TiO2-xNx Powders, J. Phys. Chem. B. 107 (2003) 5483–5486.

[12] Y. Li, D. Hwang, H.N. Lee, S. Kim, Synthesis and characterization of carbon-doped titania as an artificial solar light sensitive photocatalyst, Chem. Phys. Lett. 404 (2005) 25–29. doi:10.1016/j.cplett.2005.01.062.

[13] L. Korosi, I. Dekany, Preparation and investigation of structural and photocatalytic properties of phosphate modified titanium dioxide, Colloids Surfaces A Physicochem. Eng. Asp. 280 (2006) 146–154. doi:10.1016/j.colsurfa.2006.01.052.

[14] S. Moon, H. Mametsuka, S. Tabata, E. Suzuki, Photocatalytic production of hydrogen from water using TiO2 and B/TiO2, Catal. Today. 58 (2000) 125–132.

[15] N. Rahimi, R.A. Pax, E.M.A. Gray, Review of functional titanium oxides. I: TiO2 and

its modifications, Prog. Solid State Chem. 44 (2016) 86–105. doi:10.1016/j.progsolidstchem.2016.07.002.

[16] J.C. Yu, J. Yu, W. Ho, Z. Jiang, L. Zhang, Effects of F-Doping on the Photocatalytic Activity and Microstructures of Nanocrystalline TiO2 Powders, Chem. Mater. 14 (2002) 3808–3816.

[17] M. Endo-Kimura, M. Janczarek, Z. Bielan, D. Zhang, K. Wang, A. Markowska-Szczupak, E. Kowalska, Photocatalytic and Antimicrobial Properties of Ag2O/TiO2 Heterojunction, ChemEngineering. 3 (2019) 1–18. doi:10.3390/chemengineering3010003.

[18] M. Janczarek, M. Endo, D. Zhang, K. Wang, E. Kowalska, Enhanced Photocatalytic and Antimicrobial Performance of Cuprous Oxide/Titania: The Effect of Titania Matrix, Materials (Basel). 11 (2018) 1–21. doi:10.3390/ma11112069.

[19] Z. Wang, X. Lang, Visible Light Photocatalysis of Dye-Sensitized TiO2: The Selective Aerobic Oxidation of Amines to Imines, Appl. Catal. B Environ. 224 (2018) 404–409. doi:10.1016/j.apcatb.2017.10.002.

[20] A.J. Bard, Photoelectrochemistry and heterogeneous photocatalysis at semiconductors, J. Photochem. 10 (1979) 59–75.

[21] E. Kowalska, R. Abe, B. Ohtani, Visible light-induced photocatalytic reaction of gold-modified titanium(IV) oxide particles: action spectrum analysis, Chem. Commun. 2 (2009) 241–243. doi:10.1039/b815679d.

[22] E. Kowalska, O.O. Prieto-Mahaney, R. Abe, B. Ohtani, Visible-light-induced photocatalysis through surface plasmon excitation of gold on titania surfaces, Phys. Chem. Chem. Phys. 12 (2010) 2344–2355. doi:10.1039/b917399d.

[23] X. Hou, J. Ma, A. Liu, D. Li, M. Huang, X. Deng, Visible light active TiO2 films prepared by electron beam deposition of noble metals, Nucl. Instrum. Methods Phys.

Res. B. 268 (2010) 550–554. doi:10.1016/j.nimb.2009.12.010.

[24] S. Sakthivel, M.V. Shankar, M. Palanichamy, B. Arabindoo, D.W. Bahnemann, V. Murugesan, Enhancement of photocatalytic activity by metal deposition: characterisation and photonic efficiency of Pt , Au and Pd deposited on TiO2 catalyst, Water Res. 38 (2004) 3001–3008. doi:10.1016/j.watres.2004.04.046.

[25] H. Fan, C. Lu, W.W. Lee, M. Chiou, C. Chen, Mechanistic pathways differences between P25-TiO2 and Pt-TiO2 mediated CV photodegradation, J. Hazard. Mater. 185 (2011) 227–235. doi:10.1016/j.jhazmat.2010.09.022.

[26] E. Kowalska, H. Remita, C. Colbeau-Justin, J. Hupka, J. Belloni, Modification of Titanium Dioxide with Platinum Ions and Clusters: Application in Photocatalysis, J. Phys. Chem. C. 112 (2008) 1124–1131.

[27] M. Ni, M.K.H. Leung, D.Y.C. Leung, K. Sumathy, A review and recent developments in photocatalytic water-splitting using TiO2 for hydrogen production, Renew. Sustain. Energy Rev. 11 (2007) 401–425. doi:10.1016/j.rser.2005.01.009.

[28] A. Zielińska-Jurek, A. Zaleska, Ag/Pt-modified TiO2 nanoparticles for toluene photooxidation in the gas phase, Catal. Today. 230 (2014) 104–111. doi:10.1016/j.cattod.2013.11.044.

[29] I. Wysocka, E. Kowalska, J. Ryl, G. Nowaczyk, A. Zielińska-Jurek, Morphology, Photocatalytic and Antimicrobial Properties of TiO2 Modified with Mono- and Bimetallic Copper , Platinum and Silver Nanoparticles, Nanomaterials. 9 (2019) 1–23.

[30] A. Zielińska-Jurek, Progress, Challenge, and Perspective of Bimetallic TiO2 -Based Photocatalysts, J. Nanomater. 2014 (2014) 1–17.

[31] Y. Shiraishi, H. Sakamoto, Y. Sugano, S. Ichikawa, T. Hirai, Pt-Cu Bimetallic Alloy Nanoparticles Supported on Anatase TiO2: Highly Active Catalysts for Aerobic Oxidation Driven by Visible Light, ACS Catal. 7 (2013) 9287–9297.

doi:10.1021/nn403954p.

[32] S. Shuang, R. Lv, Z. Xie, Z. Zhang, Surface Plasmon Enhanced Photocatalysis of Au/Pt-decorated TiO 2 Nanopillar Arrays, Sci. Rep. 6 (2016) 1–8. doi:10.1038/srep26670.

[33] C.F. Liriano-Jorge, U. Sohmen, A. Özkan, H. Gulyas, R. Otterpohl, TiO2 Photocatalyst Nanoparticle Separation: Flocculation in Different Matrices and Use of Powdered Activated Carbon as a Precoat in Low-Cost Fabric Filtration, Adv. Mater. Sci. Eng. 2014 (2014) 1–12.

[34] S.-A. Lee, K.-H. Choo, C.-H. Lee, H.-I. Lee, T. Hyeon, W. Choi, H.-H. Kwon, Use of Ultrafiltration Membranes for the Separation of TiO2 Photocatalysts in Drinking Water Treatment, Ind. Eng. Chem. Res. 40 (2001) 1712–1719.

[35] Q. Zhang, H. Wang, X. Fan, F. Lv, S. Chen, X. Quan, Fabrication of TiO2 nanofiber membranes by a simple dip-coating technique for water treatment, Surf. Coatings Technol. 298 (2016) 45–52. doi:10.1016/j.surfcoat.2016.04.054.

[36] A. Zielińska-Jurek, M. Klein, J. Hupka, Enhanced visible light photocatalytic activity of Pt/I-TiO2in a slurry system and supported on glass packing, Sep. Purif. Technol. 189 (2017) 246–252. doi:10.1016/j.seppur.2017.08.018.

[37] J.H. Wei, C.J. Leng, X.Z. Zhang, W.H. Li, Z.Y. Liu, J. Shi, Synthesis and magnetorheological effect of Fe3O4-TiO2 nanocomposite, J. Phys. Conf. Ser. 149 (2009) 25–29.

[38] X. Zhang, H. Wang, C. Yang, D. Du, Y. Lin, Preparation, characterization of Fe3O4 at TiO2 magnetic nanoparticles and their application for immunoassay of biomarker of exposure to organophosphorus pesticides, Biosens. Bioelectron. 41 (2013) 669–674. doi:10.1016/j.bios.2012.09.047.

[39] J. Wang, J. Yang, X. Li, D. Wang, B. Wei, H. Song, X. Li, S. Fu, Preparation and

photocatalytic properties of magnetically reusable Fe3O4@ZnO core/shell nanoparticles, Phys. E. 75 (2016) 66–71. doi:10.1016/j.physe.2015.08.040.

[40] T.A. Gad-Allah, S. Kato, S. Satokawa, T. Kojima, Treatment of synthetic dyes wastewater utilizing a magnetically separable photocatalyst (TiO2/SiO2/Fe3O4): Parametric and kinetic studies, Desalination. 244 (2009) 1–11. doi:10.1016/j.desal.2008.04.031.

[41] M.E. Hassan, Y. Chen, G. Liu, D. Zhu, J. Cai, Heterogeneous photo-Fenton degradation of methyl orange by Fe 2 O 3 / TiO 2 nanoparticles under visible light, J. Water Process Eng. 12 (2016) 52–57. doi:10.1016/j.jwpe.2016.05.014.

[42] R. Li, Y. Jia, N. Bu, J. Wu, Q. Zhen, Photocatalytic degradation of methyl blue using Fe2O3/TiO2 composite ceramics, J. Alloys Compd. 643 (2015) 88–93. doi:10.1016/j.jallcom.2015.03.266.

[43] W. Fu, H. Yang, M. Li, L. Chang, Q. Yu, J. Xu, G. Zou, Preparation and photocatalytic characteristics of core-shell structure TiO2/BaFe12O19 nanoparticles, Mater. Lett. 60 (2006) 2723–2727. doi:10.1016/j.matlet.2006.01.078.

[44] F. Bavarsiha, M. Rajabi, M. Montazeri-Pour, Synthesis of SrFe12O19/SiO2/TiO2 composites with core/shell/shell nano-structure and evaluation of their photo-catalytic efficiency for degradation of methylene blue, J. Mater. Sci. Mater. Electron. 29 (2018) 1877–1887. doi:10.1007/s10854-017-8098-5.

[45] S.W. Lee, J. Drwiega, C.Y. Wu, D. Mazyck, W.M. Sigmund, Anatase TiO2 Nanoparticle Coating on Barium Ferrite Using Titanium Bis-Ammonium Lactato Dihydroxide and Its Use as a Magnetic Photocatalyst, Chem. Mater. 16 (2004) 1160–1164. doi:10.1021/cm0351902.

[46] X. Li, D. Liu, S. Song, H. Zhang, Fe3O4@SiO2@TiO2@Pt Hierarchical Core−Shell Microspheres: Controlled Synthesis, Enhanced Degradation System, and Rapid

Magnetic Separation to Recycle, Cryst. Growth Des. 14 (2014) 5506–5511. doi:10.1021/cg501164c.

[47] J. Zhan, H. Zhang, G. Zhu, Magnetic photocatalysts of cenospheres coated with Fe3O 4/TiO2 core/shell nanoparticles decorated with Ag nanopartilces, Ceram. Int. 40 (2014) 8547–8559. doi:10.1016/j.ceramint.2014.01.069.

[48] L. Zhang, Z. Wu, L. Chen, L. Zhang, X. Li, H. Xu, H. Wang, G. Zhu, Preparation of magnetic Fe3O4/TiO2/Ag composite microspheres with enhanced photocatalytic activity, Solid State Sci. 52 (2016) 42–48. doi:10.1016/j.solidstatesciences.2015.12.006.

[49] G. Liu, F. He, J. Zhang, L. Li, F. Li, L. Chen, Y. Huang, Yolk-shell structured Fe3O4CF-TiO2 microspheres with surface fluorinated as recyclable visible-light driven photocatalysts, Appl. Catal. B Environ. 150–151 (2014) 515–522. doi:10.1016/j.apcatb.2013.12.050.

[50] F. Shi, Y. Li, Q. Zhang, H. Wang, Synthesis of Fe3O4/C/TiO2 magnetic photocatalyst via vapor phase hydrolysis, Int. J. Photoenergy. 2012 (2012). doi:10.1155/2012/365401.

[51] T.A. Gad-Allah, S. Kato, S. Satokawa, T. Kojima, Role of core diameter and silica content in photocatalytic activity of TiO2/SiO2/Fe3O4 composite, Solid State Sci. 9 (2007) 737–743. doi:10.1016/j.solidstatesciences.2007.05.012.

[52] J. Cui, T. He, X. Zhang, Synthesis of Fe3O4@SiO2@Ption–TiO2 hybrid composites with high efficient UV–visible light photoactivity, Catal. Commun. 40 (2013) 66–70. doi:10.1016/j.catcom.2013.06.009.

[53] H. Liu, Z. Jia, S. Ji, Y. Zheng, M. Li, H. Yang, Synthesis of TiO2/SiO2@Fe3O4 magnetic microspheres and their properties of photocatalytic degradation dyestuff, Catal. Today. 175 (2011) 293–298. doi:10.1016/j.cattod.2011.04.042.

[54] X. Yan, T. Ohno, K. Nishijima, R. Abe, B. Ohtani, Is methylene blue an appropriate substrate for a photocatalytic activity test? A study with visible-light responsive titania, Chem. Phys. Lett. 429 (2006) 606–610. doi:10.1016/j.cplett.2006.08.081.

[55] N. Barbero, D. Vione, Why Dyes Should Not Be Used to Test the Photocatalytic Activity of Semiconductor Oxides, Environ. Sci. Technol. 50 (2016) 2130–2131. doi:10.1021/acs.est.6b00213.

[56] Z. Bielan, E. Kowalska, S. Dudziak, K. Wang, B. Ohtani, A. Zielinska-Jurek, Mono- and bimetallic (Pt/Cu) titanium(IV) oxide photocatalysts. Physicochemical and photocatalytic data for magnetic nanocomposites' shell, Data Br. (n.d.).

[57] A. Zielińska-Jurek, Z. Bielan, S. Dudziak, I. Wolak, Z. Sobczak, T. Klimczuk, G. Nowaczyk, J. Hupka, Design and Application of Magnetic Photocatalysts for Water Treatment. The Effect of Particle Charge on Surface Functionality, Catalysts. 7 (2017) 1–18. doi:10.3390/catal7120360.

[58] I. Wysocka, E. Kowalska, K. Trzciński, M. Łapiński, G. Nowaczyk, A. Zielińska-Jurek, UV-Vis-Induced Degradation of Phenol over Magnetic Photocatalysts Modified with Pt , Pd , Cu and Au Nanoparticles, Nanomaterials. 8 (2018) 1–20. doi:10.3390/nano8010028.

[59] K. Imamura, T. Yoshikawa, K. Hashimoto, H. Kominami, Environmental Stoichiometric production of aminobenzenes and ketones by photocatalytic reduction of nitrobenzenes in secondary alcoholic suspension of titanium(IV) oxide under metal-free conditions, Appl. Catal. B Environ. 134–135 (2013) 193–197. doi:10.1016/j.apcatb.2013.01.015.

[60] V. Brezova, A. Blazkova, I. Surina, B. Havlinova, Solvent effect on the photocatalytic reduction of 4-nitrophenol in titanium dioxide suspensions, J. Photochem. Photobiol. A Chem. 107 (1997) 233–237.

[61] A. Di Paola, M. Bellardita, L. Palmisano, Brookite, the Least Known TiO2 Photocatalyst, Catalysts. 3 (2013) 36–73. doi:10.3390/catal3010036.

[62] Y. Chi, Q. Yuan, Y. Li, L. Zhao, N. Li, X. Li, W. Yan, Magnetically separable Fe3O4@SiO2@TiO2-Ag microspheres with well-designed nanostructure and enhanced photocatalytic activity, J. Hazard. Mater. 262 (2013) 404–411. doi:10.1016/j.jhazmat.2013.08.077.

[63] E. Mrotek, S. Dudziak, I. Malinowska, D. Pelczarski, Z. Ryżyńska, A. Zielińska-Jurek, Improved degradation of etodolac in the presence of core-shell ZnFe2O4/SiO2/TiO2 magnetic photocatalyst, Sci. Total Environ. 724 (2020) 1–12. doi:10.1016/j.scitotenv.2020.138167.

[64] Y. Shiraishi, D. Tsukamoto, Y. Sugano, A. Shiro, S. Ichikawa, S. Tanaka, T. Hirai, Platinum Nanoparticles Supported on Anatase Titanium Dioxide as Highly Active Catalysts for Aerobic Oxidation under Visible Light Irradiation, ACS Catal. 2 (2012) 1984–1992. doi:10.1021/cs300407e.

[65] Z. Wei, M. Endo, K. Wang, E. Charbit, A. Markowska-szczupak, B. Ohtani, E. Kowalska, Noble metal-modified octahedral anatase titania particles with enhanced activity for decomposition of chemical and microbiological pollutants, Chem. Eng. J. 318 (2017) 121–134. doi:10.1016/j.cej.2016.05.138.

[66] M. Janczarek, Z. Wei, M. Endo, B. Ohtani, E. Kowalska, Silver- and copper-modified decahedral anatase titania particles as visible light-responsive plasmonic photocatalyst, J. Photonics Energy. 7 (2016) 1–16. doi:10.1117/1.JPE.7.012008.

[67] I. Krivtsov, M. Ilkaeva, E. Salas-Colera, Z. Amghouz, J.R. Garc, E. Diaz, S. Ordonez, S. Villar-Rodil, Consequences of Nitrogen Doping and Oxygen Enrichment on Titanium Local Order and Photocatalytic Performance of TiO2 Anatase, J. Phys. Chem. C. 121 (2017) 6770–6780. doi:10.1021/acs.jpcc.7b00354.

[68] A. Zielińska-Jurek, Z. Wei, M. Janczarek, I. Wysocka, E. Kowalska, Size- Controlled Synthesis of Pt Particles on TiO2 Surface: Physicochemical Characteristic and Photocatalytic Activity, Catalysts. 9 (2019) 1–18. doi:10.3390/catal9110940.

[69] T. Ohno, M. Akiyoshi, T. Umebayashi, K. Asai, T. Mitsui, M. Matsumura, Preparation of S-doped TiO2 photocatalysts and their photocatalytic activities under visible light, Appl. Catal. A Gen. 265 (2004) 115–121. doi:10.1246/cl.2003.364.

[70] S. Xie, Q. Zhang, G. Liu, Y. Wang, Photocatalytic and photoelectrocatalytic reduction of CO2 using heterogeneous catalysts with controlled nanostructures, Chem. Commun. 52 (2016) 35–59. doi:10.1039/C5CC07613G.

[71] J. Zhang, Q. Xu, Z. Feng, M. Li, C. Li, Importance of the Relationship between Surface Phases and Photocatalytic Activity of TiO2, Angew. Chemie. 47 (2008) 2006–2009. doi:10.1002/anie.200704788.

[72] G. Li, S. Ciston, Z. V. Saponjic, L. Chen, N.M. Dimitrijevic, T. Rajh, K.A. Gray, Synthesizing mixed-phase TiO2 nanocomposites using a hydrothermal method for photo-oxidation and photoreduction applications, J. Catal. 253 (2008) 105–110. doi:10.1016/j.jcat.2007.10.014.

[73] K. Wang, Z. Wei, B. Ohtani, E. Kowalska, Interparticle electron transfer in methanol dehydrogenation on platinum- loaded titania particles prepared from P25, Catal. Today. 303 (2018) 327–333. doi:10.1016/j.cattod.2017.08.046.

[74] M. Janczarek, E. Kowalska, On the Origin of Enhanced Photocatalytic Activity of Copper- Modified Titania in the Oxidative Reaction Systems, Catalysts. 7 (2017) 1–26. doi:10.3390/catal7110317.

[75] J. Low, C. Jiang, B. Cheng, S. Wageh, A.A. Al-ghamdi, J. Yu, A Review of Direct Z-Scheme Photocatalysts, Small Methods. 1 (2017) 1700080–1700101. doi:10.1002/smtd.201700080.

[76] K. Wang, M. Endo-Kimura, R. Belchi, D. Zhang, A. Habert, J. Boucle, B. Ohtani, E. Kowalska, N. Herlin-Boime, Carbon/Graphene-Modified Titania with Enhanced Photocatalytic Activity under UV and Vis Irradiation, Materials (Basel). 12 (2019) 1–19.

[77] E. Kowalska, K. Yoshiiri, Z. Wei, S. Zheng, E. Kastl, H. Remita, B. Ohtani, S. Rau, Hybrid photocatalysts composed of titania modified with plasmonic nanoparticles and ruthenium complexes for decomposition of organic compounds, App. Catal. B Environ. 178 (2015) 133–143.

[78] E. Kowalska, Z. Wei, B. Karabiyik, A. Herissan, M. Janczarek, M. Endo, H. Remita, B. Ohtani, Silver-modified titania with enhanced photocatalytic and antimicrobial properties under UV and visible light irradiation, Catal. Today. 252 (2015) 136–142. doi:10.1016/j.cattod.2014.10.038.

References

1. Lekkerkerker-Teunissen K., Benotti M. J., Snyder S. A., Van Dijk H. C., *Transformation of atrazine, carbamazepine, diclofenac and sulfamethoxazole by low and medium pressure UV and UV/H_2O_2 treatment*, Separation and Purification Technology, (2012), 96, 33–43.

2. Wang X., Zhang L., *Kinetic study of hydroxyl radical formation in a continuous hydroxyl generation system*, RSC Advances, (2018), 8, 40632–40638.

3. Kubiak A., Siwińska-Ciesielczyk K., Jesionowski T., *Titania-Based Hybrid Materials with ZnO, ZrO_2 and MoS_2: A Review*, Materials, (2018), 11, 1–56.

4. Zhang Y., Ram M. K., Stefanakos E. K., Goswami D. Y., *Synthesis, characterization, and applications of ZnO nanowires*, Journal of Nanomaterials, (2012), 2012.

5. Mioduska J., Zielinska-Jurek A., Janczarek M., Hupka J., *The Effect of Calcination Temperature on Structure and Photocatalytic Properties of WO_3/TiO_2 Nanocomposites*, Journal of Nanomaterials, (2016), 2016, 1–8.

6. Kim S. P., Choi M. Y., Choi H. C., *Photocatalytic activity of SnO_2 nanoparticles in methylene blue degradation*, Materials Research Bulletin, (2016), 74, 85–89.

7. Frame F. A., Carroll E. C., Larsen D. S., Sarahan M., Browning N. D., Osterloh F. E., *First demonstration of CdSe as a photocatalyst for hydrogen evolution from water under UV and visible light*, Chemical Communications, (2008), 2206–2208.

8. Lee G.-J., Wu J. J., *Recent developments in ZnS photocatalysts from synthesis to photocatalytic applications — A review*, Powder Technology, (2017), 318, 8–22.

9. Leinen M. B., Dede D., Khan M. U., Çağlayan M., Koçak Y., Demir H. V., Ozensoy E., *CdTe Quantum Dot-Functionalized P25 Titania Composite with Enhanced Photocatalytic NO_2 Storage Selectivity under UV and VIS Irradiation*, ACS Applied Materials & Interfaces, (2019), 11, 865–879.

10. Naeem K., Ã F. O., *Preparation of Fe^{3+} -doped TiO_2 nanoparticles and its photocatalytic activity under UV light*, Physica B: Physics of Condensed Matter, (2010), 405, 221–226.

11. Fujishima A., Honda K., *Electrochemical Photolysis of Water at Semiconductor Electrode*, Nature, (1972), 238, 37–38.

12. Carey J. H., Lawrence J., Tosine H. M., *Photodechlorination of PCB's in the Presence of Titanium Dioxide in Aqueous Suspencion*, Bulletin of Environmental Contamination and Toxicology, (1976), 16, 697–701.

13. Chekin F., Bagheri S., Bee S., Hamid A., *Synthesis of Pt doped TiO_2 nanoparticles : Characterization and application for electrocatalytic oxidation of L-methionine*, Sensors & Actuators: B. Chemical, (2013), 177, 898–903.

14. Hanaor D. A. H., Sorrell C. C., *Review of the anatase to rutile phase transformation*, Journal of Materials Science, (2011), 46, 855–874.

15. Simonarson G., Sommer S., Lotsari A., Elgh B., Iversen B. B., Palmqvist A. E. C., *Evolution of the Polymorph Selectivity of Titania Formation under Acidic and Low-Temperature Conditions*, ACS Omega, (2019), 4, 5750–5757.

16. Žunič V., Vukomanović M., Škapin S. D., Suvorov D., Kovač J., *Photocatalytic properties of TiO_2 and TiO2/Pt: A sol-precipitation, sonochemical and hydrothermal approach*, Ultrasonics Sonochemistry, (2014), 21, 367–375.

17. Addamo M., Augugliaro V., Di Paola a, Garcia-Lopez E., Loddo V., Marci G., Molinari R., Palmisano L., Schiavello M., *Preparation, characterization, and photoactivity of polycrystalline nanostructured TiO_2 catalysts*, Journal of Physical Chemistry B, (2004), 108, 3303–3310.

18. Zalas M., *Synthesis of N-doped template-free mesoporous titania for visible light photocatalytic applications*, Catalysis Today, (2014), 230, 91–96.

19. Mills A., Wang J., Ollis D. F., *Dependence of the kinetics of liquid-phase photocatalyzed reactions on oxygen concentration and light intensity*, Journal of

Catalysis, (2006), 243, 1–6.

20. Chen D., Li F., Ray A. K., *External and internal mass transfer effect on photocatalytic degradation*, Catalysis Today, (2001), 66, 475–485.

21. Gaya I. U., Abdullah H. A., *Heterogeneous Photocatalytic Degradation of Organic Contaminants Over Titanium Dioxide : A Review of Fundamentals , Progress and Problems*, Journal of Photochemistry and Photobiology C: Photochemistry Reviews, (2008), 9, 1–12.

22. Serpone N., *Is the Band Gap of Pristine TiO_2 Narrowed by Anion- and Cation-Doping of Titanium Dioxide in Second-Generation Photocatalysts?*, Journal of Physical Chemistry B, (2006), 110, 24287–24293.

23. Zhang L., Tse M. S., Tan O. K., *Facile in situ synthesis of visible light-active Pt/C-TiO_2 nanoparticles for environmental remediation*, Journal of Environmental Chemical Engineering, (2014), 2, 1214–1220.

24. Suwannaruang T., Kamonsuangkasem K., Kidkhunthod P., Chirawatkul P., Saiyasombat C., Chanlek N., Wantala K., *Influence of nitrogen content levels on structural properties and photocatalytic activities of nanorice-like N-doped TiO_2 with various calcination temperatures*, Materials Research Bulletin, (2018), 105, 265–276.

25. Yang Y., Ni D., Yao Y., Zhong Y., Ma Y., Yao J., *High photocatalytic activity of carbon doped TiO_2 prepared by fast combustion of organic capping ligands*, RSC Advances, (2015), 5, 93635–93643.

26. Xie R., Lei D., Zhan Y., Liu B., Tsang C. H. A., Zeng Y., Li K., Leung D. Y. C., Huang H., *Efficient photocatalytic oxidation of gaseous toluene over F-doped TiO_2 in a wet scrubbing process*, Chemical Engineering Journal, (2020), 386, 121025.

27. Filippatos P.-P., Kelaidis N., Vasilopoulou M., Davazoglou D., Lath N. N., Chroneos A., *Defect processes in F and Cl doped anatase TiO_2*, Scientific Reports, (2019), 9, 19970.

28. Boningari T., Inturi S. N. R., Suidan M., Smirniotis P. G., *Novel one-step synthesis of sulfur doped-TiO_2 by flame spray pyrolysis for visible light photocatalytic degradation of acetaldehyde*, Chemical Engineering Journal, (2018), 339, 249–258.

29. Deng W., Ning S., Lin Q., Zhang H., Zhou T., Lin H., Long J., Lin Q., Wang X., *I-TiO_2/PVC film with highly photocatalytic antibacterial activity under visible light*, Colloids and Surfaces B: Biointerfaces, (2016), 144, 196–202.

30. Jaafar N. F., Jalil A. A., Triwahyono S., *Visible-light photoactivity of plasmonic silver supported on mesoporous TiO_2 nanoparticles (Ag-MTN) for enhanced degradation of 2-chlorophenol: Limitation of Ag-Ti interaction*, Applied Surface Science, (2017), 392, 1068–1077.

31. Endo M., Wei Z., Wang K., Karabiyik B., Yoshiiri K., Rokicka P., Ohtani B., Markowska-Szczupak A., Kowalska E., *Noble metal-modified titania with visible-light activity for the decomposition of microorganisms*, Beilstein Journal of Nanotechnology, (2018), 9, 829–841.

32. Huang J. G., Guo X. T., Wang B., Li L. Y., Zhao M. X., Dong L. L., Liu X. J., Huang Y. T., *Synthesis and photocatalytic activity of Mo-doped TiO_2 nanoparticles*, Journal of Spectroscopy, (2015), 2015.

33. Zeng G., Zhang Q., Liu Y., Zhang S., Guo J., *Preparation of TiO_2 and Fe-TiO_2 with an Impinging Stream-Rotating Packed Bed by the Precipitation Method for the Photodegradation of Gaseous Toluene*, Nanomaterials, (2019), 9, 1173.

34. Wysocka I., Markowska-Szczupak A., Szweda P., Ryl J., Endo-Kimura M., Kowlaska E., Nowaczyk G., Zielińska-Jurek A., *Gas-phase removal of indoor volatile organic compounds and airborne microorganisms over mono - and bimetal - modified (Pt, Cu, Ag) titanium(IV) oxide nanocomposites*, Indoor Air, (2019), 00, 1–14.

35. Długokęcka M., Łuczak J., Polkowska Ż., Zaleska-Medynska A., *The effect of microemulsion composition on the morphology of Pd nanoparticles deposited at the surface of TiO_2 and photoactivity of Pd-TiO_2*, Applied Surface Science, (2017),

405, 220–230.

36. Lee J.-S., Won D.-I., Jung W.-J., Son H.-J., Pac C., Kang S. O., *Widely Controllable Syngas Production by a Dye-Sensitized TiO_2 Hybrid System with ReI and CoIII Catalysts under Visible-Light Irradiation*, Angewandte Chemie, (2017), 56, 976–980.

37. Diaz-Angulo J., Gomez-Bonilla I., Jimenez-Tohapanta C., Mueses M., Pinzon M., Machuca-Martinez F., *Visible-light activation of TiO_2 by dye-sensitization for degradation of pharmaceutical compounds*, Photochemical and Photobiological Sciences, (2019), 18, 897–904.

38. Endo-Kimura M., Janczarek M., Bielan Z., Zhang D., Wang K., Markowska-Szczupak A., Kowalska E., *Photocatalytic and Antimicrobial Properties of Ag_2O/TiO_2 Heterojunction*, ChemEngineering, (2019), 3, 1–18.

39. Kubiak A., Siwińska-Ciesielczyk K., Bielan Z., Zielińska-Jurek A., Jesionowski T., *Synthesis of highly crystalline photocatalysts based on - TiO_2 and ZnO for the degradation of organic impurities under visible-light irradiation*, Adsorption, (2019), 25, 1–17.

40. Kubiak A., Bielan Z., Kubacka M., Gabała E., Zgoła-Grześkowiak A., Janczarek M., Zalas M., Zielińska-Jurek A., Siwińska-Ciesielczyk K., Jesionowski T., *Microwave-assisted synthesis of a TiO_2-CuO heterojunction with enhanced photocatalytic activity against tetracycline*, Applied Surface Science, (2020), 520, 1–15.

41. Wu Q., Huang F., Zhao M., Xu J., Zhou J., Wang Y., *Ultra-small yellow defective TiO_2 nanoparticles for co-catalyst free photocatalytic hydrogen production*, Nano Energy, (2016), 24, 63–71.

42. Kang X., Liu S., Dai Z., He Y., Song X., Tan Z., *Titanium Dioxide: From Engineering to Applications*, Catalysts, (2019), 9, 1–32.

43. Lin L., Huang J., Li X., Abass M. A., Zhang S., *Effective Surface Disorder Engineering of Metal Oxide Nanocrystals for Improved Photocatalysis*, Applied

Catalysis B, Environmental, (2017), 203, 615–624.

44. Wysocka I., Kowalska E., Ryl J., Nowaczyk G., Zielińska-Jurek A., *Morphology, Photocatalytic and Antimicrobial Properties of TiO_2 Modified with Mono- and Bimetallic Copper , Platinum and Silver Nanoparticles*, Nanomaterials, (2019), 9, 1–23.

45. Klein M., Grabowska E., Zaleska A., *Noble metal modified TiO_2 for photocatalytic air purification*, Physicochemical Problems of Mineral Processing, (2015), 51, 49–57.

46. Janczarek M., Wei Z., Endo M., Ohtani B., Kowalska E., *Silver- and copper-modified decahedral anatase titania particles as visible light-responsive plasmonic photocatalyst*, Journal of Photonics for Energy, (2016), 7, 1–16.

47. Wei Z., Janczarek M., Endo M., Wang K., Balcytis A., Nitta A., Mendez-Medrano M. G., Colbeau-Justin C., Juodkazis S., Ohtani B., Kowlaska E., *Noble Metal-Modified Faceted Anatase Titania Photocatalysts: Octahedron versus Decahedron*, Applied Catalysis B : Environmental, (2018), 237, 574–587.

48. Pillai Z. S., Kamat P. V, *What Factors Control the Size and Shape of Silver Nanoparticles in the Citrate Ion Reduction Method ?*, Journal of Physical Chemistry B, (2004), 108, 945–951.

49. Langhammer C., Larsson E. M., *Nanoplasmonic In Situ Spectroscopy for Catalysis Applications*, ACS Catalysis, (2012), 2, 2036–2045.

50. Zoric I., Zach M., Kasemo B., Langhammer C., *Gold, Platinum, and Aluminum Nanodisk Plasmons: Material Independence, Subradiance, and Damping Mechanisms*, ACS Nano, (2011), 5, 2535–2546.

51. Hou X., Ma J., Liu A., Li D., Huang M., Deng X., *Visible light active TiO_2 films prepared by electron beam deposition of noble metals*, Nuclear Instruments and Methods in Physics Research B, (2010), 268, 550–554.

52. Sakthivel S., Shankar M. V., Palanichamy M., Arabindoo B., Bahnemann D.

W., Murugesan V., *Enhancement of photocatalytic activity by metal deposition: characterisation and photonic efficiency of Pt , Au and Pd deposited on TiO_2 catalyst*, Water Research, (2004), 38, 3001–3008.

53. Fan H., Lu C., Lee W. W., Chiou M., Chen C., *Mechanistic pathways differences between P25-TiO_2 and Pt-TiO_2 mediated CV photodegradation*, Journal of Hazardous Materials, (2011), 185, 227–235.

54. Kowalska E., Remita H., Colbeau-Justin C., Hupka J., Belloni J., *Modification of Titanium Dioxide with Platinum Ions and Clusters: Application in Photocatalysis*, Journal of Physical Chemistry C, (2008), 112, 1124–1131.

55. Ni M., Leung M. K. H., Leung D. Y. C., Sumathy K., *A review and recent developments in photocatalytic water-splitting using TiO_2 for hydrogen production*, Renewable & Sustainable Energy Reviews, (2007), 11, 401–425.

56. Wei Z., Endo M., Wang K., Charbit E., Markowska-szczupak A., Ohtani B., Kowalska E., *Noble metal-modified octahedral anatase titania particles with enhanced activity for decomposition of chemical and microbiological pollutants*, Chemical Engineering Journal, (2017), 318, 121–134.

57. Zielińska-Jurek A., Wei Z., Janczarek M., Wysocka I., Kowalska E., *Size-Controlled Synthesis of Pt Particles on TiO_2 Surface: Physicochemical Characteristic and Photocatalytic Activity*, Catalysts, (2019), 9, 1–18.

58. Zuo F., Bozhilov K., Dillon R. J., Wang L., Smith P., Zhao X., Bardeen C., Feng P., *Active Facets on Titanium(III)-Doped TiO_2: An Effective Strategy to Improve the Visible-Light Photocatalytic Activity*, Angewandte Chemie, (2012), 51, 6223–6226.

59. Ullattil S. G., Narendranath S. B., Pillai S. C., Periyat P., *Black TiO_2 Nanomaterials: A Review of Recent Advances*, Chemical Engineering Journal, (2018), 343, 708–736.

60. Lettieri S., Gargiulo V., Alfe M., Amati M., Zeller P., Maraloiu V.-A., Borbone F., Muñoz-García A. B., Pavone M., Maddalena P., *A Simple Ethanol Refluxing*

Method for Production of Blue Colored Titanium Dioxide with Oxygen Vacancies and Visible Light-Driven Photocatalytic Properties, The Journal of Physical Chemistry C, (2020), 124, 3564–3576.

61. Nowotny M. K., Bak T., Nowotny J., Sorrell C. C., *Titanium vacancies in nonstoichiometric TiO_2 single crystal*, Physica Status Solidi B, (2005), 242, 88–90.

62. Bak T., Nowotny J., Nowotny M. K., *Defect Disorder of Titanium Dioxide*, Journal of Physical Chemistry B, (2006), 110, 21560–21567.

63. Yamazaki-Nishida S., Read H. W., Nagano J. K., Jarosch T., Eddy C., Cervera-March S., Anderson M. A., *Gas Phase Photocatalytic Degradation on TiO_2 Pellets of Volatile Chlorinated Organic Compounds from a Soil Vapor Extraction Well*, Journal of Soil Contamination, (1994), 3, 1–16.

64. Sabin F., Turk T., Vogler A., *Photo-oxidation of organic compounds in the presence of titanium dioxide: determination of the efficiency*, Journal of Photochemistry & Photobiology A: Chemistry, (1992), 63, 99–106.

65. Ullah S., Ferreira-Neto E. P., Pasa A. a., Alcântara C. C. J., Acuña J. J. S., Bilmes S. a., Martínez Ricci M. L., Landers R., Fermino T. Z., Rodrigues-Filho U. P., *Enhanced photocatalytic properties of core@shell SiO_2@TiO_2 nanoparticles*, Applied Catalysis B: Environmental, (2015), 179, 333–343.

66. Xue X. dong, Fu J. feng, Zhu W. fang, Guo X. chao, *Separation of ultrafine TiO_2 from aqueous suspension and its reuse using cross-flow ultrafiltration (CFU)*, Desalination, (2008), 225, 29–40.

67. Zielińska-Jurek A., Klein M., Hupka J., *Enhanced visible light photocatalytic activity of Pt/I-TiO_2 in a slurry system and supported on glass packing*, Separation and Purification Technology, (2017), 189, 246–252.

68. Cunha D. L., Kuznetsov A., Achete C. A., da Hora Machado E. A., Marques M., *Immobilized TiO_2 on glass spheres applied to heterogeneous photocatalysis: photoactivity, leaching and regeneration process*, PeerJ, (2018), 6, 4464.

69. Ray S., Lalman J. A., *Fabrication and characterization of an immobilized titanium dioxide (TiO_2) nanofiber photocatalyst*, Materials Today: Proceedings, (2016), 3, 1582–1591.

70. Zhang Q., Wang H., Fan X., Lv F., Chen S., Quan X., *Fabrication of TiO_2 nanofiber membranes by a simple dip-coating technique for water treatment*, Surface and Coatings Technology, (2016), 298, 45–52.

71. Fernandez J. A., Suan A., Ramirez J. C., Robles J., Salcedo J. C., Pedroza A. M., Daza C. E., *Treatment of real wastewater with TiO_2-films sensitized by a natural-dye obtained from Picramnia sellowii*, Journal of Environmental Chemical Engineering, (2016), 4, 2848–2856.

72. Dijkstra M. F. J., Michorius A., Buwalda H., Panneman H. J., Winkelman J. G. M., Beenackers A. A. C. M., *Comparison of the efficiency of immobilized and suspended systems in photocatalytic degradation*, Catalysis Today, (2001), 66, 487–494.

73. Silva F. V, *A Comparison of Slurry and Immobilized TiO_2 in the Photocatalytic Degradation of Phenol*, (2012), 280, 275–280.

74. Dong H., Zeng G., Tang L., Fan C., Zhang C., He X., He Y., *An overview on limitations of TiO_2-based particles for photocatalytic degradation of organic pollutants and the corresponding countermeasures*, Water Research, (2015), 79, 128–146.

75. Dadfar M. R., Seyyed Ebrahimi S. A., Masoudpanah S. M., *Sol–Gel Synthesis and Characterization of $SrFe_{12}O_{19}/TiO_2$ Nanocomposites*, Journal of Superconductivity and Novel Magnetism, (2014), 28, 89–94.

76. Wang H., Xu Y., Jing L., Huang S., Zhao Y., He M., Xu H., Li H., *Novel magnetic $BaFe_{12}O_{19}/g\text{-}C_3N_4$ composites with enhanced thermocatalytic and photo-Fenton activity under visible-light*, Journal of Alloys and Compounds, (2017), 710, 510–518.

77. Li Z. D., Wang H. L., Wei X. N., Liu X. Y., Yang Y. F., Jiang W. F., *Preparation*

and photocatalytic performance of magnetic Fe_3O_4@TiO_2 core-shell microspheres supported by silica aerogels from industrial fly ash, Journal of Alloys and Compounds, (2016), 659, 240–247.

78. Mallesh S., Sunny A., Vasundhara M., Srinivas V., *Structure and magnetic properties of ZnO coated MnZn ferrite nanoparticles*, Journal of Magnetism and Magnetic Materials, (2016), 418, 112–117.

79. Li W., Deng Y., Wu Z., Qian X., Yang J., Wang Y., Gu D., Zhang F., Tu B., Zhao D., *Hydrothermal Etching Assisted Crystallization: A Facile Route to Functional Yolk-Shell Titanate Microspheres with Ultrathin Nanosheets-Assembled Double Shells*, Journal of the American Chemical Society, (2011), 133, 15830–15833.

80. Mohammadi-Aghdam S., Sarkhosh B., Tajoddin N. N., *Recyclable-Fe_3O_4/SiO_2/TiO_2/Cu nanocomposites: synthesis, characterization and investigation of the photocatalytic and magnetic property*, Journal of Materials Science: Materials in Electronics, (2017), 28, 9456–9463.

81. Mrotek E., Dudziak S., Malinowska I., Pelczarski D., Ryżyńska Z., Zielińska-Jurek A., *Improved degradation of etodolac in the presence of core-shell $ZnFe_2O_4$/SiO_2/TiO_2 magnetic photocatalyst*, Science of the Total Environment, (2020), 724, 1–12.

82. Dudziak S., Ryżyńska Z., Bielan Z., Ryl J., Klimczuk T., Zielińska-Jurek A., *Pseudo-superparamagnetic behaviour of barium hexaferrite particles*, RSC Advances, (2020), 10, 18784–18796.

83. Qiu J., Gu M., *Magnetic nanocomposite thin films of $BaFe_{12}O_{19}$ and TiO_2 prepared by sol-gel method*, Applied Surface Science, (2005), 252, 888–892.

84. Blaney L., *Magnetite (Fe_3O_4): Properties, Synthesis, and Applications*, Lehigh Review, (2007), 15, 33–81.

85. Lee J. S., Cha J. M., Yoon H. Y., Lee J. K., Kim Y. K., *Magnetic multi-granule nanoclusters: A model system that exhibits universal size effect of magnetic*

coercivity, Scientific Reports, (2015), 5.

86. Wu W., Jiang C., Roy V. A. L., *Recent Progress in Magnetic Iron Oxide-Semiconductro Composite Nanomaterials as Promising Photocatalysts*, Nanoscale, (2015), 7, 38–58.

87. Beketova D., Motola M., Sopha H., Michalicka J., Cicmancova V., Dvorak F., Hromádko L., Frumarova B., Stoica M., Macak J. M., *One-Step Decoration of TiO_2 Nanotubes with Fe_3O_4 Nanoparticles: Synthesis, and Photocatalytic, and magnetic properties*, ACS Applied Nano Materials, (2020), 3, 1553–1563.

88. Guanghong Z., Hongyan D., Yufu Z., Yuebin L., Peng L., *High Visible-light Photocatalytic Activity of γ-Fe_2O_3/TiO_2 Nanotube Heterojunction Arrays*, Rare Metal Materials and Engineering, (2016), 45, 1117–1121.

89. Beydoun D., Amal R., Low G. K.-C., McEvoy S., *Novel Photocatalyst: Titania-Coated Magnetite. Activity and Photodissolution*, The Journal of Physical Chemistry B, (2000), 104, 4387–4396.

90. Zielińska-Jurek A., Bielan Z., Wysocka I., Strychalska J., Janczarek M., Klimczuk T., *Magnetic semiconductor photocatalysts for the degradation of recalcitrant chemicals from flow back water*, Journal of Environmental Management, (2016), 1–9.

91. Bavarsiha F., Rajabi M., Montazeri-Pour M., *Synthesis of $SrFe_{12}O_{19}$/SiO_2/TiO_2 composites with core/shell/shell nano-structure and evaluation of their photo-catalytic efficiency for degradation of methylene blue*, Journal of Materials Science: Materials in Electronics, (2018), 29, 1877–1887.

92. Jia Y., Liu J., Cha S., Choi S., Chang Y. C., Liu C., *Magnetically separable Au-TiO_2/nanocube $ZnFe_2O_4$ composite for chlortetracycline removal in wastewater under visible light*, Journal of Industrial and Engineering Chemistry, (2017), 47, 303–314.

93. Zheng L., Pi F., Wang Y., Xu H., Zhang Y., Sun X., *Photocatalytic degradation of Acephate, Omethoate, and Methyl parathion by Fe_3O_4@SiO_2@mTiO_2*

nanomicrospheres, Journal of Hazardous Materials, (2016), 315, 11–22.

94. Kunarti E. S., Syoufian A., Budi I. S., Pradipta A. R., *Preparation and Properties of $Fe_3O_4/SiO_2/TiO_2$ Core-Shell Nanocomposite as Recoverable Photocatalyst*, Asian Journal of Chemistry, (2016), 28, 1343–1346.

95. Khatiri R., Reyhani A., Mortazavi S. Z., Hossainalipour M., *Preparation and characterization of Fe_3O_4/SiO_2/APTES core-shell nanoparticles*, (2012), 12–14.

96. Li C., Tan J., Fan X., Zhang B., Zhang H., Zhang Q., *Magnetically separable one dimensional Fe_3O_4/P(MAA-DVB)/TiO_2 nanochains: Preparation, characterization and photocatalytic activity*, Ceramics International, (2015), 41, 3860–3868.

97. Sibi M. G., Verma D., Kim J., *Magnetic core–shell nanocatalysts: promising versatile catalysts for organic and photocatalytic reactions*, Catalysis Reviews, (2019), 62, 163–311.

98. Hou Y., Wang Y., Yuan H., Chen H., Chen G., Shen J., Li L., *The enhanced catalytic degradation of $SiO_2/Fe_3O_4/C@TiO_2$ photo-Fenton system on p-nitrophenol*, Journal of Nanoparticle Research, (2016), 18, 343.

99. Zhang Q., Meng G., Wu J., Li D., Liu Z., *Study on enhanced photocatalytic activity of magnetically recoverable $Fe_3O_4@C@TiO_2$ nanocomposites with core–shell nanostructure*, Optical Materials, (2015), 46, 52–58.

100. Rånby B., *Photodegradation and photo-oxidation of synthetic polymers*, Journal of Analytical and Applied Pyrolysis, (1989), 15, 237–247.

101. Yun C. S., Javier A., Jennings T., Fisher M., Hira S., Peterson S., Hopkins B., Reich N. O., Strouse G. F., *Nanometal Surface Energy Transfer in Optical Rulers, Breaking the FRET Barrier*, Journal of Americal Chemical Society, (2005), 127, 3115–3119.

102. Zhou J., Ren F., Zhang S., Wu W., Xiao X., Liu Y., Jiang C., *SiO_2-Ag-SiO_2-TiO_2 multi-shell structures: Plasmon enhanced photocatalysts with wide-spectral-response*, Journal of Materials Chemistry A, (2013), 1, 13128.

103. Kowalska E., Wei Z., Karabiyik B., Janczarek M., Endo M., Wang K., Rokicka P., Markowska-Szczupak A., Ohtani B., *Development of Plasmonic Photocatalysts for Environmental Application*, Advances in Science and Technology, (2014), 93, 174–183.

104. Kowalska E., Wei Z., Karabiyik B., Herissan A., Janczarek M., Endo M., Remita H., Ohtani B., *Silver-modified titania with enhanced photocatalytic and antimicrobial properties under UV and visible light irradiation*, Catalysis Today, (2015), 252, 136–142.

105. Prieto-Mahaney O. O., Murakami N., Abe R., Ohtani B., *Correlation between Photocatalytic Activities and Structural and Physical Properties of Titanium(IV) Oxide Powders*, Chemistry Letters, (2009), 38, 238–239.

106. Moroz P., Boddy A., Zamkov M., *Challenges and Prospects of Photocatalytic Applications Utilizing Semiconductor Nanocrystals*, Frontiers in Chemistry, (2018), 6, 353.

107. Ohtani B., Prieto-Mahaney O. O., Li D., Abe R., *What is Degussa (Evonic) P25? Crystalline composition analysis, reconstruction from isolated pure particles and photocatalytic activity test*, Journal of Photochemistry and Photobiology A: Chemistry, (2010), 216, 179–182.

108. Pi Y., Li X., Xia Q., Wu J., Li Y., Xiao J., Li Z., *Adsorptive and photocatalytic removal of Persistent Organic Pollutants (POPs) in water by metal-organic frameworks (MOFs)*, Chemical Engineering Journal, (2018), 337, 351–371.

109. Clara M., Strenn B., Kreuzinger N., *Carbamazepine as a possible anthropogenic marker in the aquatic environment: investigations on the behaviour of Carbamazepine in wastewater treatment and during groundwater infiltration*, Water Research, (2004), 38, 947–954.

110. Nawaz M., Miran W., Jang J., Lee D. S., *One-step hydrothermal synthesis of porous 3D reduced graphene oxide/TiO_2 aerogel for carbamazepine photodegradation in aqueous solution*, Applied Catalysis B, Environmental, (2017), 203, 85–95.

111. Li S., Wang Z., Zhao X., Yang X., Liang G., Xie X., *Insight into enhanced carbamazepine photodegradation over biochar-based magnetic photocatalyst Fe_3O_4/BiOBr/BC under visible LED light irradiation*, Chemical Engineering Journal, (2019), 360, 600–611.

112. Awfa D., Ateia M., Fujii M., Johnson M. S., Yoshimura C., *Photodegradation of pharmaceuticals and personal care products in water treatment using carbonaceous-TiO_2 composites: A critical review of recent literature*, Water Research, (2018), 142, 26–45.

113. Mestre A. S., Carvalho A. P., *Photocatalytic Degradation of Pharmaceuticals Carbamazepine, Diclofenac, and Sulfamethoxazole by Semiconductor and Carbon Materials: A Review*, Molecules, (2019), 24, 3702.

114. Imanishi A., Okamura T., Ohashi N., Nakamura R., *Mechanism of Water Photooxidation Reaction at Atomically Flat TiO_2 (Rutile) (110) and (100) Surfaces : Dependence on Solution pH*, Journal of Americal Chemical Society, (2007), 2, 11569–11578.

115. Toor A. P., Verma A., Jotshi C. K., Bajpai P. K., Singh V., *Photocatalytic degradation of Direct Yellow 12 dye using UV/TiO_2 in a shallow pond slurry reactor*, Dyes and Pigments, (2006), 68, 53–60.

116. Ofiarska A., Pieczyńska A., Fiszka Borzyszkowska A., Stepnowski P., Siedlecka E. M., *Pt-TiO_2-assisted photocatalytic degradation of the cytostatic drugs ifosfamide and cyclophosphamide under artificial sunlight*, Chemical Engineering Journal, (2016), 285, 417–427.

117. Morgan B. J., Watson G. W., *Polaronic trapping of electrons and holes by native defects in anatase TiO_2*, Physical Review B - Condensed Matter and Materials Physics, (2009), 80, 2–5.

List of academic achievements

JCR-listed publications

[1] Z. Bielan, A. Sulowska, S. Dudziak, K. Siuzdak, J. Ryl, A. Zielińska-Jurek, Defective TiO_2 Core-Shell Magnetic Photocatalyst Modified with Plasmonic Nanoparticles for Visible Light-Induced Photocatalytic Activity, *Catalysts.* 10 (2020) 672. **Q2, IF 3.444, 100 points**

[2] Z. Bielan, S. Dudziak, A. Sulowska, D. Pelczarski, J. Ryl, A. Zielińska-Jurek, Preparation and Characterization of Defective TiO_2. The Effect of the Reaction Environment on Titanium Vacancies Formation, *Materials*. 13 (2020) 2763. **Q2, IF 2.972, 140 points**

[3] A. Kubiak, Z. Bielan, A. Bartkowiak, E. Gabała, A. Piasecki, M. Zalas, A. Zielińska-Jurek, M. Janczarek, K. Siwińska-Ciesielczyk, T. Jesionowski, Synthesis of Titanium Dioxide *via* Surfactant-Assisted Microwave Method for Photocatalytic and Dye-Sensitized Solar Cells Applications, *Catalysts.* 10 (2020) 586. **Q2, IF 3.444, 100 points**

[4] Z. Bielan, E. Kowalska, S. Dudziak, K. Wang, B. Ohtani, A. Zielińska-Jurek, Mono- and bimetallic (Pt/Cu) titanium(IV) oxide photocatalysts. Physicochemical and photocatalytic data of magnetic nanocomposites' shell, *Data in Brief*. 31 (2020) 105814. **Q1, IF 0.93, 40 points**

[5] Z. Bielan, E. Kowalska, S. Dudziak, K. Wang, B. Ohtani, A. Zielińska-Jurek, Mono- and bimetallic (Pt/Cu) titanium(IV) oxide core-shell photocatalysts with UV/Vis light activity and magnetic separability, *Catalysis Today*. (2020). **Q1, IF 4.888, 140 points**

[6] S. Dudziak, Z. Ryżyńska, Z. Bielan, J. Ryl, T. Klimczuk, A. Zielińska-Jurek, Pseudo-superparamagnetic behavior of barium hexaferrite particles, *RSC Advances.* 10 (2020) 18784. **Q1, IF 3.049, 100 points**

[7] A. Kubiak, Z. Bielan, M. Kubacka, E. Gabała, A. Zgoła-Grześkowiak, M. Janczarek, M. Zalas, A. Zielińska-Jurek, K. Siwińska-Ciesielczyk, T. Jesionowski, Microwave-assisted synthesis of a TiO_2-CuO heterojunction with enhanced photocatalytic activity against tetracycline, *Applied Surface Science*. 520 (2020) 146344. **Q1, IF 5.155, 140 points**

[8] A. Kubiak, K. Siwińska-Ciesielczyk, Z. Bielan, A. Zielińska-Jurek, T. Jesionowski, Synthesis of highly crystalline photocatalysts based on TiO_2 and ZnO for the degradation of organic impurities under visible light irradiation, *Adsorption*. 25 (2019) 309-325. **Q2, IF 1.731, 70 points, citations: 10**

[9] A. Zielińska-Jurek, Z. Bielan, S. Dudziak, I. Wolak, Z. Sobczak, T. Klimczuk, G. Nowaczyk, J. Hupka, Design and Application of Magnetic Photocatalysts for Water Treatment. The Effect of Particle Charge on Surface Functionality, *Catalysts*. 7 (2017) 360. **Q2, IF 3.465, 100 points, citations: 13**

[10] A. Zielińska-Jurek, Z. Bielan, I. Wysocka, J. Strychalska, M. Janczarek, T. Klimczuk, Magnetic semiconductor photocatalysts for the degradation of recalcitrant chemicals from flow back water, *Journal of Environmental Management*. 195 part 2 (2017) 157-165. **Q1, IF 4.005, 100 points, citations: 17**

Σ IF = 38.857 **Σ citations = 40 (Web of Science)** **Σ Ministry points = 1030**

Reviewer for:

- Chemical Engineering Journal
- SN Applied Science
- Micro & Nano Letters
- IET Nanobiotechnology
- Inorganic and Nano-Metal Chemistry
- International Journal of Photochemistry and Photobiology

Chapters and articles in non-JCR listed journals

[1] M. Endo-Kimura, M. Janczarek, Z. Bielan, D. Zhang, K. Wang, A. Markowska-Szczupak, E. Kowalska, Photocatalytic and Antimicrobial Properties of Ag_2O/TiO_2 Heterojunction. *ChemEngineering*. 3 (2019) 3, **5 points**

[2] Z. Bielan, A. Zielińska-Jurek, Magnetyczne fotokatalizatory na bazie TiO_2 do degradacji zanieczyszczeń organicznych w fazie wodnej, Chapter in post-conference monography: *Problematyka z zakresu nauk o środowisku – przegląd i badania*. Lublin 2019. ISBN 978-83-65932-93-8

Conferences

[1] Z. Bielan, I. Wysocka, J. Strychalska, M. Janczarek, J. Hupka, A. Zielińska-Jurek, Preparation and characterization of magnetic TiO_2 nanoparticles and their utilization for the degradation of organic pollutants in water, *The 3rd International Conference on Photocatalytic and Advanced Oxidation Technologies for Treatment of Water, Air, Soil and Surfaces (PAOT-3)*, 1-4 September 2015, Gdansk, Poland, poster

[2] A. Zielińska-Jurek, I. Wysocka , Z. Bielan, , J. Strychalska-Nowak, J. Hupka, Magnetic semiconductor photocatalysts for the degradation of recalcitrant chemicals form flow back water, *European Conference on Environmental Applications of Advanced Oxidation Process*, 21-24 October 2015, Athens, Greece, oral speech

[3] Z. Bielan, A. Zielińska-Jurek, J. Hupka, Magnetic and photocatalytic properties of Fe_3O_4/TiO_2 nanocomposites, *The XI Summer School for Postgraduate Students and Young Researches „Interfacial phenomena in theory and practise"*, 19-24 June 2016, Rybaki near Kościerzyna, Poland, oral speech

[4] Z. Bielan, A. Zielińska-Jurek, J. Hupka, J-TiO_2 and Fe_3O_4/J-TiO_2 photocatalysts and their environmental applications, *13th International Symposium on Catalysis*, 19-23 September 2016, Siófok, Hungary, poster

[5] Z. Bielan, A. Zielińska-Jurek, Photocatalytical degradation of organic pollutants from flow back water, *The XII Summer School for Postgraduate Students and Young Researchers „Interfacial Phenomena in Theory and Practice"*, 25-30 June 2017, Rybaki near Kościerzyna, Poland, oral speech

[6] I. Wolak, Z. Bielan, A. Zielińska-Jurek, Application of Magnetic Spinel Ferrites Modified by TiO_2 for Degradation of Pharmaceuticals, *The XII Summer School for Postgraduate Students and Young Researchers „Interfacial Phenomena in Theory and Practice"*, 25-30 June 2017, Rybaki near Kościerzyna, Poland, poster

[7] S. Dudziak, Z. Bielan, A. Zielińska-Jurek, Characterization of Hexagonal Ferrites Modified with TiO_2 and their Application in Heterogeneous Photocatalysis, *The XII Summer School for Postgraduate Students and Young Researchers „Interfacial Phenomena in Theory and Practice"*, 25-30 June 2017, Rybaki near Kościerzyna, Poland, poster

[8] A. Zielińska-Jurek, I. Wysocka, Z. Bielan, P. Jurek, A. Hänel, J. Hupka, Investigation on Photocatalytic Degradation of Selected Pollutants Using Bench-Scale Reactors, *The 2nd International Conference on New Photocatalytic Materials for Environment, Energy and Sustainability (NPM-2)*, 3-6 July 2017, Ljubljana, Slovenia, oral speech

[9] A. Zielińska-Jurek, I. Wysocka, Z. Bielan, P. Jurek, J. Hupka, New Photocatalysts for Environmentally Friendly Recycling of Water in the Production of Hydrocarbons, *The 2nd International Conference on New Photocatalytic Materials for Environment, Energy and Sustainability (NPM-2)*, 3-6 June 2017, Ljubljana, Slovenia, poster

[10] A. Zielińska-Jurek, Z. Bielan, I. Wysocka, S. Dudziak, I. Wolak, Magnetic photocatalysts for water treatment, *Symposium on Nanomaterials for Environmental Purification and Energy Conversion (SNEPEC)*, 20-21 February 2018, Sapporo, Japan, oral speech

[11] A. Zielińska-Jurek, Z. Bielan, S. Dudziak, I. Wolak, J. Hupka, Design, preparation and characterization of magnetic photocatalysts, *3rd International Symposium on Energy and Environmental Photocatalytic Materials (EEPM-3)*, 15-19 May 2018, Kraków, Poland, oral speech

[12] Z. Bielan, Z. Sobczak, A. Zielińska-Jurek, Preparation and characterization of core-interlayer-shell magnetic photocatalysts for degradation of organic pollutants, *3rd International Symposium on Energy and Environmental Photocatalytic Materials (EEPM-3)*, 15-19 May 2018, Kraków, Poland, poster

[13] Z. Bielan, S. Dudziak, I. Wolak, Z. Sobczak, A. Zielińska-Jurek, A magnetically recoverable photocatalyst prepared by supporting TiO2 nanoparticles on a ferromagnetic oxide core@silica shell composite, *The XIII Summer School for Postrgraduate Students and Young Researches „Interfacial Phenomena in Theory and Practice"*, 25-29 June 2018, Rybaki near Kościerzyna, Poland, oral speech

[14] Z. Bielan, A. Zielińska-Jurek, E. Kowalska, TiO_2-based magnetic nanocomposites with core-shell structure, *9th CSE Summer School*, 14-15 July 2018, Sapporo, Japan, poster

[15] Z. Bielan, I. Wolak, A. Zielińska-Jurek, A magnetically recoverable photocatalyst prepared by supporting TiO_2 nanoparticles on a ferromagnetic oxide core@silica shell composite, *Pre-conference of TOCAT8 and the 5th International Symposium of Institute for Catalysis (ICAT)*, 3-4 August 2018, Sapporo, Japan, poster

[16] Z. Bielan, E. Kowalska, A. Zielińska-Jurek, TiO_2-based magnetic nanocomposites with core-shell structure, *CSE International Student Symposium 2018*, 27 August 2018, Sapporo, Japan, poster

[17] Z. Bielan, A. Zielińska-Jurek, Otrzymywanie i charakterystyka nanokompozytów o właściwościach magnetycznych i fotokatalitycznych, *IX Kongres Technologii Chemicznej (TECHEM IX)*, 3-7 September 2018, Gdańsk, Poland, poster

[18] Z. Bielan, A. Zielińska-Jurek, B. Ohtani, E. Kowalska, Titania-based magnetic nanocomposites with core-shell structure, 第24回シンポジウム「光触媒反応の最近の展開」*(24th Symposium "Recent technical solutions in the field of photocatalysis")*, 30 November 2018, Tokyo, Japan, poster

[19] Z. Bielan, A. Zielińska-Jurek, Magnetyczne fotokatalizatory na bazie TiO_2 do degradacji zanieczyszczeń organicznych w fazie wodnej, *Ogólnopolska Konferencja Naukowa „Ochrona Środowiska – Rozwiązania i Perspektywy"*, 17 May 2019, Lublin, Poland, oral speech

[20] Z. Bielan, E. Kowalska, B. Ohtani, A. Zielińska-Jurek, Magnetically separable and visible light active photocatalysts for effective pollutants degradation, *6th European Conference on Environmental Applications of Advanced Oxidation Processes (EAAOP-6)*, 26-30 June 2019, Portoroz, Slovenia, oral speech

[21] A. Zielińska-Jurek, S. Dudziak, Z. Bielan, A. Sulowska, I. Malinowska, I. Wysocka, Magnetic photocatalysts for water treatment, *6th European Conference on Environmental Applications of Advanced Oxidation Processes (EAAOP-6)*, 26-30 June 2019, Portoroz, Slovenia, oral speech

[22] S. Dudziak, Z. Bielan, A. Sulowska, A. Zielińska-Jurek, Kinetics and degradation pathways of carbamazepine. A comparative study using visible light active TiO_2 photocatalysts, *6th European Conference on Environmental Applications of Advanced Oxidation Processes (EAAOP-6)*, 26-30 June 2019, Portoroz, Slovenia, poster

Patents

[1] A. Zielińska-Jurek, Z. Bielan, Sposób otrzymywania fotokatalizatora magnetycznego wielowarstwowego, 2019. No: PL. 233343

[2] A. Zielińska-Jurek, Z. Bielan, Sposób otrzymywania fotokatalizatora magnetycznego wielowarstwowego, 2019. No: PL. 233344

[3] A. Zielińska-Jurek, Z. Bielan, Sposób otrzymywania fotokatalizatora magnetycznego wielowarstwowego, 2019. No: PL. 233345

Internships

July – December 2018: Hokkaido University, Institute for Catalysis (ICAT), Photocatalytic Research Division, Sapporo, Japan, supervisor prof. Ewa Kowalska – funded by the PO WER program.

Scholarships

2017-20 The National Centre for Research and Development Scholarship for Interdisciplinary, International PhD Studies (the PO WER 3.2 program)

2016-17 Pro-quality Scholarship for best PhD Students

2015-16 Gdańsk University of Technology Rector's Scholarship for best PhD Students

Awards

[1] Award for the presentation during *The XII Summer School for Postgraduate Students and Young Researchers "Interfacial Phenomena in Theory and Practice"*; 25-30 June 2017; Rybaki near Kościerzyna, Poland

[2] Award in the *13th Poland National Competition "Student-Inventor 2018"*

[3] Gold medal for the invention: Method of obtaining a layered magnetic photocatalyst during the *International Warsaw Invention Show (IWIS)*; 15-17 October 2018; Warsaw, Poland

GDAŃSK UNIVERSITY OF TECHNOLOGY

FACULTY OF CHEMISTRY

Co-authors' statements of contribution

GDAŃSK UNIVERSITY OF TECHNOLOGY
FACULTY OF CHEMISTRY

mgr inż. Zuzanna Bielan
Department of Process Engineering
and Chemical Technology
Faculty of Chemistry
Gdansk University of Technology
Gabriela Narutowicza 11/12
80-233 Gdańsk, Poland

September 1, 2020

Statement of contribution

I have contributed to the publications which constitute a part of my PhD dissertation in the following way:

- Anna Zielińska-Jurek, Zuzanna Bielan, Izabela Wysocka, Judyta Strychalska, Marcin Janczarek, Tomasz Klimczuk, Magnetic semiconductor photocatalysts for the degradation of recalcitrant chemicals from flow back water, *Journal of Environmental Management*. 195 (2017) 157;

In the above study I have prepared Fe_3O_4/TiO_2 and $Fe_3O_4@SiO_2/TiO_2$ samples with different Fe_3O_4/TiO_2 and Fe_3O_4/SiO_2 molar ratios, characterized obtained photocatalysts with use of XRD, BET surface area and DR-UV/Vis spectroscopy analysis as well as investigate the photocatalytic activity in degradation of pyridine, phenol and 4-heptanone under UV-Vis irradiation.

- Anna Zielińska-Jurek, Zuzanna Bielan, Szymon Dudziak, Izabela Wolak, Zuzanna Sobczak, Tomasz Klimczuk, Grzegorz Nowaczyk, Jan Hupka, Design and Application of Magnetic Photocatalysts for Water Treatment.

The Effect of Particle Charge on Surface Functionality, *Catalysts*. 7 (2017) 360;

In the above study I have prepared the Fe_3O_4-based magnetic photocatalysts samples and was co-responsible with other authors for their physicochemical and photocatalytic analysis.

- Zuzanna Bielan, Ewa Kowalska, Szymon Dudziak, Kunlei Wang, Bunsho Ohtani, Anna Zielińska-Jurek, Mono- and bimetallic (Pt/Cu) titanium(IV) oxide core-shell photocatalysts with UV/Vis light activity and magnetic separability, *Catalysis Today*. (2020); doi: 10.1016/j.cattod.2020.05.034;
- Zuzanna Bielan, Ewa Kowalska, Szymon Dudziak, Kunlei Wang, Bunsho Ohtani, Anna Zielińska-Jurek, Mono- and bimetallic (Pt/Cu) titanium(IV) oxide photocatalysts. Physicochemical and photocatalytic data of magnetic nanocomposites' shell, *Data in Brief*. 31 (2020) 105814;

In the above studies I have designed and conducted the experiments (photocatalysts preparation, XRD, DR-UV/Vis, BET surface area analysis as well as photocatalytic activity measurements), analyzed the data and wrote the manuscripts.

- Zuzanna Bielan, Agnieszka Sulowska, Szymon Dudziak, Daniel Pelczarski, Jacek Ryl, Anna Zielińska-Jurek, Preparation and characterization of defective TiO_2. The effect of the reaction environment on titanium vacancies formation, *Materials*. 13 (2020) 2763;
- Zuzanna Bielan, Agnieszka Sulowska, Szymon Dudziak, Jacek Ryl, Anna Zielińska-Jurek, Defective TiO_2 Core-Shell Magnetic Photocatalyst Modified with Plasmonic Nanoparticles for Visible Light-Induced Photocatalytic Activity, *Catalysts*. 10 (2020) 672;

In the above studies I have obtained and characterized three series of defective photocatalysts, investigated their photocatalytic activity under UV-Vis and Vis light and wrote the manuscripts.

- Anna Zielińska-Jurek, Zuzanna Bielan, Sposób otrzymywania fotokatalizatora magnetycznego warstwowego, *Polish Patent No*. PL. 233343, PL. 233344, PL. 233345 (2019)

In the above studies I have prepared the literature review, wrote the part of patent applications and took part in laboratory research on layered magnetic photocatalysts formation.

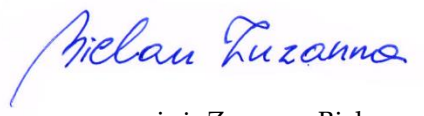

mgr inż. Zuzanna Bielan

GDAŃSK UNIVERSITY OF TECHNOLOGY
FACULTY OF CHEMISTRY

PhD DSc, Anna Zielińska-Jurek, Assoc. Prof. of GUT
Department of Process Engineering
and Chemical Technology
Faculty of Chemistry
Gdansk University of Technology
Gabriela Narutowicza 11/12
80-233 Gdańsk, Poland

Gdańsk, 04.09.2020

Statement of contribution

I have contributed to the publications, which constitute a part of the PhD dissertation of mgr inż. Zuzanna Bielan in the following way:

- Anna Zielińska-Jurek, Zuzanna Bielan, Izabela Wysocka, Judyta Strychalska, Marcin Janczarek, Tomasz Klimczuk, Magnetic semiconductor photocatalysts for the degradation of recalcitrant chemicals from flow back water, Journal of Environmental Management. 195 part 2 (2017) 157-165;
- Anna Zielińska-Jurek, Zuzanna Bielan, Szymon Dudziak, Izabela Wolak, Zuzanna Sobczak, Tomasz Klimczuk, Grzegorz Nowaczyk, Jan Hupka, Design and Application of Magnetic Photocatalysts for Water Treatment. The Effect of Particle Charge on Surface Functionality, *Catalysts*. 7 (2017) 360;

In the above studies, I have initiated the research topic (idea), conceived the concept, designed the experiments, analyzed the obtained data, drafted the manuscripts and designed the figures, prepare responses for reviewers, prepared the published versions of the manuscripts.

- Zuzanna Bielan, Ewa Kowalska, Szymon Dudziak, Kunlei Wang, Bunsho Ohtani, Anna Zielińska-Jurek, Mono- and bimetallic (Pt/Cu) titanium(IV) oxide core-shell photocatalysts with UV/Vis light activity and magnetic separability, *Catalysis Today*. (2020);
- Zuzanna Bielan, Ewa Kowalska, Szymon Dudziak, Kunlei Wang, Bunsho Ohtani, Anna Zielińska-Jurek, Mono- and bimetallic (Pt/Cu) titanium(IV) oxide photocatalysts. Physicochemical and photocatalytic data of magnetic nanocomposites' shell, *Data in Brief*. (2020);
- Zuzanna Bielan, Agnieszka Sulowska, Szymon Dudziak, Daniel Pelczarski, Jacek Ryl, Anna Zielińska-Jurek, Preparation and characterization of defective TiO_2. The effect of the reaction environment on titanium vacancies formation, *Materials*. (2020);
- Zuzanna Bielan, Agnieszka Sulowska, Szymon Dudziak, Jacek Ryl, Anna Zielińska-Jurek, Defective TiO_2 Core-Shell Magnetic Photocatalyst Modified with Plasmonic Nanoparticles for Visible Light-Induced Photocatalytic Activity, *Catalysts*. (2020);

In the above studies, I have conceived of the presented idea, conceived and planned the experiments, contributed materials and analysis tools, analyzed the obtained data, discussed the results and contributed to the final versions of the manuscripts.

Anna Zielińska-Jurek

PhD Dsc, Anna Zielińska-Jurek, Assoc. Prof. of GUT

GDAŃSK UNIVERSITY OF TECHNOLOGY
FACULTY OF CHEMISTRY

prof. dr hab. inż. Jan Hupka
Department of Process Engineering
and Chemical Technology
Faculty of Chemistry
Gdansk University of Technology
Gabriela Narutowicza 11/12
80-233 Gdańsk, Poland

July 7, 2020

Statement of contribution

I have contributed to the publications which constitute a part of the PhD dissertation of mgr inż. Zuzanna Bielan in the following way:

- Anna Zielińska-Jurek, Zuzanna Bielan, Izabela Wysocka, Judyta Strychalska, Marcin Janczarek, Tomasz Klimczuk, Magnetic semiconductor photocatalysts for the degradation of recalcitrant chemicals from flow back water, *Journal of Environmental Management*. 195 part 2 (2017) 157-165;

In the above study I have reviewed the manuscript.

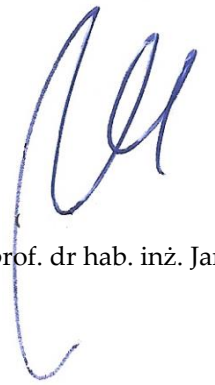

prof. dr hab. inż. Jan Hupka

GDAŃSK UNIVERSITY OF TECHNOLOGY
FACULTY OF CHEMISTRY

dr hab. inż. Marcin Janczarek
Institute of Chemical Technology and Engineering
Faculty of Chemical Technology
Poznan University of Technology
Berdychowo 4
60-965 Poznań, Poland

May 26, 2020

Statement of contribution

I have contributed to the publications which constitute a part of the PhD dissertation of mgr inż. Zuzanna Bielan in the following way:

- Anna Zielińska-Jurek, Zuzanna Bielan, Izabela Wysocka, Judyta Strychalska, Marcin Janczarek, Tomasz Klimczuk, Magnetic semiconductor photocatalysts for the degradation of recalcitrant chemicals from flow back water, *Journal of Environmental Management*. 195 part 2 (2017) 157-165;

In the above study I have performed the XRD analysis.

Marcin Janczarek

dr hab. inż. Marcin Janczarek

GDAŃSK UNIVERSITY OF TECHNOLOGY
FACULTY OF CHEMISTRY

dr inż. Izabela Wysocka
Department of Process Engineering
and Chemical Technology
Faculty of Chemistry
Gdansk University of Technology
Gabriela Narutowicza 11/12
80-233 Gdańsk, Poland

June 22, 2020

Statement of contribution

I hereby certify that my contribution to the article:

Anna Zielińska-Jurek, Zuzanna Bielan, Izabela Wysocka, Judyta Strychalska, Marcin Janczarek, Tomasz Klimczuk, Magnetic semiconductor photocatalysts for the degradation of recalcitrant chemicals from flow back water, *Journal of Environmental Management*. 195 part 2 (2017) 157-165; includes:

- Preparation of four samples Fe_3O_4@SiO_2/TiO_2 with different TiO_2 matrix – commercial TiO_2 P25 and ST-01, TiO_2 obtained via titanium butoxide and titanium isopropoxide hydrolysis,
- Characterization of the photocatalysts: crystal structure and phase composition, BET surface area and absorption properties analysis
- Investigation of the photocatalytic activity in degradation of pyridine, phenol and 4-heptanone under UV-Vis irradiation.

Wysocka Izabela

dr inż. Izabela Wysocka

GDAŃSK UNIVERSITY OF TECHNOLOGY
FACULTY OF CHEMISTRY

mgr inż. Judyta Strychalska-Nowak
Department of Solid State Physics
Faculty of Applied Physics and Mathematics
Gdansk University of Technology
Gabriela Narutowicza 11/12
80-233 Gdańsk, Poland

July 21, 2020

Statement of contribution

I have contributed to the publications which constitute a part of the PhD dissertation of mgr inż. Zuzanna Bielan in the following way:

- Anna Zielińska-Jurek, Zuzanna Bielan, Izabela Wysocka, Judyta Strychalska, Marcin Janczarek, Tomasz Klimczuk, Magnetic semiconductor photocatalysts for the degradation of recalcitrant chemicals from flow back water, *Journal of Environmental Management*. 195 part 2 (2017) 157-165;

In the above study I have performed hysteresis loops measurements, drawn the hysteresis loops graphs and helped with analysis of those results.

Judyta Strychalska-Nowak
mgr inż. Judyta Strychalska-Nowak

GDAŃSK UNIVERSITY OF TECHNOLOGY
FACULTY OF CHEMISTRY

mgr inż. Szymon Dudziak
Department of Process Engineering
and Chemical Technology
Faculty of Chemistry
Gdansk University of Technology
Gabriela Narutowicza 11/12
80-233 Gdańsk, Poland

May 21, 2020

Statement of contribution

I have contributed to the publications which constitute a part of the PhD dissertation of mgr inż. Zuzanna Bielan in the following way:

- Anna Zielińska-Jurek, Zuzanna Bielan, Szymon Dudziak, Izabela Wolak, Zuzanna Sobczak, Tomasz Klimczuk, Grzegorz Nowaczyk, Jan Hupka, Design and Application of Magnetic Photocatalysts for Water Treatment. The Effect of Particle Charge on Surface Functionality, *Catalysts*. 7 (2017) 360;

In the above study I have synthesized barium hexaferrite particles and was co-responsible with other authors for their physicochemical analysis and further surface modification with silica and TiO_2 layers.

- Zuzanna Bielan, Ewa Kowalska, Szymon Dudziak, Kunlei Wang, Bunsho Ohtani, Anna Zielińska-Jurek, Mono- and bimetallic (Pt/Cu) titanium(IV) oxide core-shell photocatalysts with UV/Vis light activity and magnetic separability, *Catalysis Today*. (2020) doi: 10.1016/j.cattod.2020.05.034;

- Zuzanna Bielan, Ewa Kowalska, Szymon Dudziak, Kunlei Wang, Bunsho Ohtani, Anna Zielińska-Jurek, Mono- and bimetallic (Pt/Cu) titanium(IV) oxide photocatalysts. Physicochemical and photocatalytic data of magnetic nanocomposites' shell, *Data in Brief.* 31 (2020) 105814;

In the above studies I have performed statistical analysis of the Cu and Pt modification on the photocatalytic activity of different TiO_2 species, together with their deposition on the surface of various magnetite particles. I have prepared relevant figures and wrote initial data interpretation, including interactions between all factors.

- Zuzanna Bielan, Szymon Dudziak, Agnieszka Sulowska, Daniel Pelczarski, Jacek Ryl, Anna Zielińska-Jurek, Preparation and characterization of defective TiO_2. The effect of the reaction environment on titanium vacancies formation, *Materials*. 13 (2020) 2763;
- Zuzanna Bielan, Agnieszka Sulowska, Szymon Dudziak, Katarzyna Siuzdak, Jacek Ryl, Anna Zielińska-Jurek, Defective TiO_2 Core-Shell Magnetic Photocatalyst Modified with Plasmonic Nanoparticles for Visible Light-Induced Photocatalytic Activity, *Catalysts.* 10 (2020) 672;

In the above studies I was co-responsible for the synthesis of the defective TiO_2 particles in different calcination temperatures and have also contributed to the data interpretation and the planning of electron paramagnetic resonance and x-ray photoelectron spectroscopy studies in order to confirm the structure of the photocatalyst.

Szymon Dudziak

mgr inż. Szymon Dudziak

GDAŃSK UNIVERSITY OF TECHNOLOGY
FACULTY OF CHEMISTRY

mgr inż. Zuzanna Ryżyńska
Department of Solid State Physics
Faculty of Applied Physics and Mathematics
Gdansk University of Technology
Gabriela Narutowicza 11/12
80-233 Gdańsk, Poland

May 22, 2020

Statement of contribution

I have contributed to the publications which constitute a part of the PhD dissertation of mgr inż. Zuzanna Bielan in the following way:

- Anna Zielińska-Jurek, Zuzanna Bielan, Szymon Dudziak, Izabela Wolak, Zuzanna Sobczak, Tomasz Klimczuk, Grzegorz Nowaczyk, Jan Hupka, Design and Application of Magnetic Photocatalysts for Water Treatment. The Effect of Particle Charge on Surface Functionality, *Catalysts*. 7 (2017) 360;

In the above study I have performed hysteresis loops measurements, drawn the hysteresis loops graphs and helped with analysis of those results.

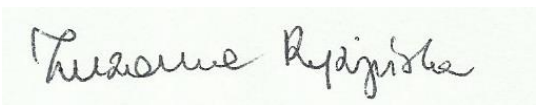

mgr inż. Zuzanna Ryżyńska

GDAŃSK UNIVERSITY OF TECHNOLOGY

FACULTY OF CHEMISTRY

GDAŃSK UNIVERSITY OF TECHNOLOGY

FACULTY OF APPLIED PHYSICS AND MATHEMATICS

Gdańsk, March 12th 2019

Re: Statement of contribution

I have contributed to the publications which constitute a part of the PhD dissertation of mgr inż. Zuzanna Bielan in the following way:

- Anna Zielińska-Jurek, Zuzanna Bielan, Izabela Wysocka, Judyta Strychalska, Marcin Janczarek, Tomasz Klimczuk,
  Magnetic semiconductor photocatalysts for the degradation of recalcitrant chemicals from flow back water,
  Journal of Environmental Management. 195 part 2 (2017) 157-165;
- Anna Zielińska-Jurek, Zuzanna Bielan, Szymon Dudziak, Izabela Wolak, Zuzanna Sobczak, Tomasz Klimczuk, Grzegorz Nowaczyk, Jan Hupka,
  Design and Application of Magnetic Photocatalysts for Water Treatment. The Effect of Particle Charge on Surface Functionality,
  Catalysts. 7 (2017) 360;

In the above studies I have supervised the magnetic properties measurements and revised the final versions of manuscripts.

Prof. Tomasz Klimczuk

GDANSK UNIVERSITY OF TECHNOLOGY
ul. G. Narutowicza 11/12
80-233 Gdańsk

tel. +48 58 348 6611

e-mail: tomasz.klimczuk@pg.edu.pl
www.mif.pg.gda.pl/homepages/tomek

GDAŃSK UNIVERSITY OF TECHNOLOGY
FACULTY OF CHEMISTRY

mgr inż. Izabela Malinowska
Department of Process Engineering
and Chemical Technology
Faculty of Chemistry
Gdansk University of Technology
Gabriela Narutowicza 11/12
80-233 Gdańsk, Poland

May, 24 2020

Statement of contribution

I have contributed to the publications which constitute a part of the PhD dissertation of mgr inż. Zuzanna Bielan in the following way:

- Anna Zielińska-Jurek, Zuzanna Bielan, Szymon Dudziak, Izabela Wolak, Zuzanna Sobczak, Tomasz Klimczuk, Grzegorz Nowaczyk, Jan Hupka, Design and Application of Magnetic Photocatalysts for Water Treatment. The Effect of Particle Charge on Surface Functionality, *Catalysts*. 7 (2017) 360;

In the above study I have prepared the cobalt spinel ferrites photocatalysts and characterized their physicochemical properties.

Izabela Malinowska

mgr inż. Izabela Malinowska

UNIWERSYTET IM. ADAMA MICKIEWICZA W POZNANIU
Centrum NanoBioMedyczne

dr Grzegorz Nowaczyk
NanoBioMedical Center
Adam Mickiewicz University
Wszechnicy Piastowskiej 3
61-614 Poznań, Poland

Date, 2020.07.10

Statement of contribution

I have contributed to the publications which constitute a part of the PhD dissertation of mgr inż. Zuzanna Bielan in the following way:

- Anna Zielińska-Jurek, Zuzanna Bielan, Szymon Dudziak, Izabela Wolak, Zuzanna Sobczak, Tomasz Klimczuk, Grzegorz Nowaczyk, Jan Hupka, Design and Application of Magnetic Photocatalysts for Water Treatment. The Effect of Particle Charge on Surface Functionality, *Catalysts*. 7 (2017) 360;

In the above study I have performed the TEM microscopy analysis.

dr Grzegorz Nowaczyk

ul. Wszechnicy Piastowskiej 3, 61-614 Poznań
NIP 777 00 06 350, REGON 000001293
tel. +48 61 829 5157, tel. /fax. +48 61 829 51 59
cnbm@amu.edu.pl
www.cnbm.amu.edu.pl

GDAŃSK UNIVERSITY OF TECHNOLOGY
FACULTY OF CHEMISTRY

Institute for Catalysis
Hokkaido University
Sapporo 001-0021, Japan
http://www.cat.hokudai.ac.jp

Sapporo, 2020.06.23

Statement of contribution

I have contributed to the following publications that constitute a part of the PhD dissertation of mgr inż. Zuzanna Bielan:

- Zuzanna Bielan, Ewa Kowalska, Szymon Dudziak, Kunlei Wang, Bunsho Ohtani, Anna Zielińska-Jurek, Mono- and bimetallic (Pt/Cu) titanium(IV) oxide core-shell photocatalysts with UV/Vis light activity and magnetic separability, *Catalysis Today*, in press (2020); https://doi.org/10.1016/j.cattod.2020.05.034.

- Zuzanna Bielan, Ewa Kowalska, Szymon Dudziak, Kunlei Wang, Bunsho Ohtani, Anna Zielińska-Jurek, Mono- and bimetallic (Pt/Cu) titanium(IV) oxide photocatalysts. Physicochemical and photocatalytic data of magnetic nanocomposites' shell, *Data in Brief*. 31 (2020) 105814;

In the above study I have supervised the research conducted in the Institute of Catalysis (ICAT), evaluated the literature review and results and reviewed the manuscripts.

Sincerely yours,

Ewa Kowalska
Associate Professor
& Leader of Research Cluster for Plasmonic Photocatalysis
Institute for Catalysis, Hokkaido University
kowalska@cat.hokudai.ac.jp

GDAŃSK UNIVERSITY OF TECHNOLOGY
FACULTY OF CHEMISTRY

Dr. Kunlei Wang
Institute for Catalysis (ICAT)
Hokkaido University
North 21, West 10
001-0021 Sapporo, Japan

June 24, 2020

Statement of contribution

I have contributed to the publications which constitute a part of the PhD dissertation of mgr inż. Zuzanna Bielan in the following way:

- Zuzanna Bielan, Ewa Kowalska, Szymon Dudziak, Kunlei Wang, Bunsho Ohtani, Anna Zielińska-Jurek, Mono- and bimetallic (Pt/Cu) titanium(IV) oxide core-shell photocatalysts with UV/Vis light activity and magnetic separability, *Catalysis Today*. (2020) doi: 10.1016/j.cattod.2020.05.034;
- Zuzanna Bielan, Ewa Kowalska, Szymon Dudziak, Kunlei Wang, Bunsho Ohtani, Anna Zielińska-Jurek, Mono- and bimetallic (Pt/Cu) titanium(IV) oxide photocatalysts. Physicochemical and photocatalytic data of magnetic nanocomposites' shell, *Data in Brief*. 31 (2020) 105814;

In the above study I have performed the XPS analysis and prepared XPS figures.

Kunlei W.

Dr. Kunlei Wang

GDAŃSK UNIVERSITY OF TECHNOLOGY
FACULTY OF CHEMISTRY

Prof. Bunsho Ohtani
Institute for Catalysis (ICAT)
Hokkaido University
North 21, West 10
001-0021 Sapporo, Japan

August 17, 2020

Statement of contribution

I have contributed to the publications which constitute a part of the PhD dissertation of mgr inż. Zuzanna Bielan in the following way:

- Zuzanna Bielan, Ewa Kowalska, Szymon Dudziak, Kunlei Wang, Bunsho Ohtani, Anna Zielińska-Jurek, Mono- and bimetallic (Pt/Cu) titanium(IV) oxide core-shell photocatalysts with UV/Vis light activity and magnetic separability, *Catalysis Today*. (2020) doi: 10.1016/j.cattod.2020.05.034;
- Zuzanna Bielan, Ewa Kowalska, Szymon Dudziak, Kunlei Wang, Bunsho Ohtani, Anna Zielińska-Jurek, Mono- and bimetallic (Pt/Cu) titanium(IV) oxide photocatalysts. Physicochemical and photocatalytic data of magnetic nanocomposites' shell, *Data in Brief*. 31 (2020) 105814;

In the above study I have provide the research resources and supervised the research conducted in the Institute of Catalysis (ICAT).

大谷文章

Prof. Bunsho Ohtani

GDAŃSK UNIVERSITY OF TECHNOLOGY
FACULTY OF CHEMISTRY

mgr inż. Agnieszka Sulowska
Department of Process Engineering
and Chemical Technology
Faculty of Chemistry
Gdansk University of Technology
Gabriela Narutowicza 11/12
80-233 Gdańsk, Poland

May 20, 2020

Statement of contribution

I have contributed to the publications which constitute a part of the PhD dissertation of mgr inż. Zuzanna Bielan in the following way:

- Zuzanna Bielan, Szymon Dudziak, Agnieszka Sulowska, Daniel Pelczarski, Jacek Ryl, Anna Zielińska-Jurek, Preparation and characterization of defective TiO_2. The effect of the reaction environment on titanium vacancies formation, *Materials*. 13 (2020) 2763;
- Zuzanna Bielan, Agnieszka Sulowska, Szymon Dudziak, Katarzyna Siuzdak, Jacek Ryl, Anna Zielińska-Jurek, Defective TiO_2 Core-Shell Magnetic Photocatalyst Modified with Plasmonic Nanoparticles for Visible Light-Induced Photocatalytic Activity, *Catalysts.* 10 (2020) 672;

In the above studies I have prepared a series of defective TiO_2 in the presence of iodic acid as an oxidizing agent, performed their characterization (XRD analysis, UV-Vis spectra, BET surface area analysis, photocatalytic activity) and prepared some figures.

Agnieszka Sulowska
mgr inż. Agnieszka Sulowska

GDAŃSK UNIVERSITY OF TECHNOLOGY
FACULTY OF CHEMISTRY

dr inż. Daniel Pelczarski
Department of Physics of Electronic Phenomena
Faculty of Applied Physics and Mathematics
Gdansk University of Technology
Gabriela Narutowicza 11/12
80-233 Gdańsk, Poland

June 22, 2020

Statement of contribution

I have contributed to the publications which constitute a part of the PhD dissertation of mgr inż. Zuzanna Bielan in the following way:

- Zuzanna Bielan, Szymon Dudziak, Agnieszka Sulowska, Daniel Pelczarski, Jacek Ryl, Anna Zielińska-Jurek, Preparation and characterization of defective TiO_2. The effect of the reaction environment on titanium vacancies formation, *Materials*. 13 (2020) 2763;

In the above study I have performed the photoluminescence (PL) spectra analysis.

Pelczarski Daniel

dr inż. Daniel Pelczarski

GDAŃSK UNIVERSITY OF TECHNOLOGY
FACULTY OF CHEMISTRY

dr hab. inż. Jacek Ryl
Department of Electrochemistry, Corrosion and Materials Engineering
Faculty of Chemistry
Gdansk University of Technology
Gabriela Narutowicza 11/12
80-233 Gdańsk, Poland

June 25, 2020

Statement of contribution

I have contributed to the publications which constitute a part of the PhD dissertation of mgr inż. Zuzanna Bielan in the following way:

- Zuzanna Bielan, Szymon Dudziak, Agnieszka Sulowska, Daniel Pelczarski, Jacek Ryl, Anna Zielińska-Jurek, Preparation and characterization of defective TiO_2. The effect of the reaction environment on titanium vacancies formation, *Materials*. 13 (2020) 2763;
- Zuzanna Bielan, Agnieszka Sulowska, Szymon Dudziak, Katarzyna Siuzdak, Jacek Ryl, Anna Zielińska-Jurek, Defective TiO_2 Core-Shell Magnetic Photocatalyst Modified with Plasmonic Nanoparticles for Visible Light-Induced Photocatalytic Activity, *Catalysts.* 10 (2020) 672;

In the above studies I have performed XPS and SEM analysis.

dr hab. inż. Jacek Ryl

INSTYTUT MASZYN PRZEPŁYWOWYCH
im. Roberta Szewalskiego
POLSKIEJ AKADEMII NAUK
80-231 Gdańsk ul. J. Fiszera 14

Tel. (centr.): 58 3460881
Tel. (sekr.): 58 3416071
Fax: 58 3416144
e-mail: imp@imp.gda.pl
www.imp.gda.pl

Gdańsk, 08.07.2020

PhD DSc, Katarzyna Siuzdak. Assoc. Prof. of IMP PAN
Head of the Laboratory of Functional Materials
Centre for Plasma and Laser Engineering
The Szewalski Institute of Fluid-Flow Machinery Polish Academy of Science
Fiszera 14, 80-231 Gdańsk, Poland

Statement of contribution

I have contributed to the publication which constitute a part of the PhD dissertation of mgr inż. Zuzanna Bielan in the following way:

- Zuzanna Bielan, Agnieszka Sulowska, Szymon Dudziak, Katarzyna Siuzdak, Jacek Ryl, Anna Zielińska-Jurek, Defective TiO_2 Core-Shell Magnetic Photocatalyst Modified with Plasmonic Nanoparticles for Visible Light-Induced Photocatalytic Activity, *Catalysts.* 10 (2020) 672;

In the above study I have performed the electrochemical measurements, prepare figure 11 and the discussion concerning flat-band potential.

dr hab. inż. Katarzyna Siuzdak
prof. IMP PAN

Kierownik
Pracowni Materiałów Funkcjonalnych
PhD DSc, Katarzyna Siuzdak. Assoc. Prof. of IMP PAN